

ABSTRACT

SHERBURN, KEITH DANIEL. Environments and Origins of Low-Level Vortices within High-Shear, Low-CAPE Convection. (Under the direction of Matthew D. Parker).

Environments characterized by large values of vertical wind shear and modest convective available potential energy (CAPE) are colloquially referred to as high-shear, low-CAPE (HSLC) environments. Convection within these environments represents a considerable operational forecasting challenge due to its associated low probability of detection of severe weather and high false alarm rate of tornado watch and warning products. The research herein has identified many key features that discriminate between severe and nonsevere HSLC events. Generally, it has been determined that large low-level wind shear and steep low-level lapse rates—along with deep, synoptic-scale forcing for ascent—are common to setups supporting severe HSLC convection. With these environmental factors in mind, this work studied the processes that lead to the development of strong, near-surface vortices in HSLC convection and how these processes are affected by varying low-level shear vector magnitudes and lapse rates. Through a matrix of high-resolution, idealized simulations, it was determined that the key factors in the development of a strong, near-surface vortex in HSLC convection are a) a strong low-to-midlevel mesocyclone, and b) a subsequent strong low-level updraft that results from the intense, upward-pointing dynamic perturbation pressure gradient acceleration. Sufficient low-level shear vector magnitudes are necessary for the development of low-to-midlevel vertical vorticity (factor a), while steeper low-level lapse rates provide stronger initial low-level updrafts, giving these environments an advantage in factor b. An ideal HSLC severe convection environment will exhibit both strong low-level shear vector magnitudes and lapse rates to maximize both of these factors.

© Copyright 2018 Keith Daniel Sherburn

All Rights Reserved

Environments and Origins of Low-Level Vortices within High-Shear, Low-CAPE Convection

by
Keith Daniel Sherburn

A dissertation submitted to the Graduate Faculty of
North Carolina State University
in partial fulfillment of the
requirements for the degree of
Doctor of Philosophy

Marine, Earth, and Atmospheric Sciences

Raleigh, North Carolina

2018

APPROVED BY:

Matthew D. Parker
Committee Chair

DelWayne R. Bohnenstiehl
Minor Representative

Gary M. Lackmann

Sandra E. Yuter

BIOGRAPHY

Keith was born in Kalamazoo, MI and now lives in Rapid City, SD. Everything in between is a bit of a mystery.

ACKNOWLEDGMENTS

I would first like to thank my advisor, Dr. Matthew Parker, for his patience over the past several years. The quality of my research—and abilities as a scientist in general—would have been considerably degraded without his guidance, and I am very grateful for his mentorship.

Additionally, I would like to acknowledge my remaining committee members—Drs. DelWayne Bohnenstiehl, Gary Lackmann, and Sandra Yuter—for their constructive criticisms in classes and throughout the evolution of this dissertation, which has encouraged more thoughtful and thorough research. Furthermore, I would like to thank my former coworkers at the Raleigh, NC NWS and current coworkers at the Rapid City, SD NWS for facilitating my development as a meteorologist and helping me achieve my professional goals. Also, I would like to thank past and present members of NC State’s Convective Storms Group (CSG) for their help and companionship during my time in Raleigh. A special kudos to CSG member Jessica King, who was a coauthor on the work presented in Chapter 1.

This research was funded by NSF grant AGS-1156123 and NOAA grants NA14NWS4680013, NA15OAR4590235, and NA16OAR4590213.

Taking a step back, my life as it is would not have been possible without my parents, Kevin and Nina Sherburn, and my sister, Sarah Jane. I am grateful for their love, and that of the rest of my family, which has supported me continuously over the years.

Finally, I would be remiss to not acknowledge my friends. Throughout my time as a student at NC State University, I am fortunate to have had a handful of individuals (both in Raleigh and elsewhere) that I could trust with my life; these individuals propped me up or pulled me along, even on the days that I didn’t want to get up. Although some of them have drifted out of my life in one way or another while others have entered my life, the memories and emotions will never fade. May our mutual love and support transcend borders, oceans, and decades, and may we never forget that we have one another.

TABLE OF CONTENTS

List of Tables	v
List of Figures	vi
Chapter 1: Composite Environments of Severe and Nonsevere High-Shear, Low-CAPE Convective Events	1
1.1 Introduction	1
1.2 Data and Methods for Environmental Analysis	5
1.3 HSLC Severe Climatology and Composites	9
1.4 Skill Score Tests	13
1.5 Synthesis and Discussion	20
Chapter 2: HSLC Idealized Simulations: Motivation and Experimental Design	60
2.1 Overview	60
2.2 Background	61
2.3 Primary Model Sensitivity Matrix	63
2.4 Example HSLC Cases	67
2.5 Analysis of Accelerations	68
2.6 Sensitivity to Hodograph Orientation	72
2.7 Object Tracking Algorithm	73
2.8 Parcel Trajectory Analysis	74
Chapter 3: HSLC Idealized Simulations: Results and Discussion	91
3.1 Control Simulation	91
3.2 Sensitivity Tests	98
Chapter 4: Summary and Conclusions	170
References	175

LIST OF TABLES

Table 1.1	Maximum HSS for ten most skillful individual ingredients and combination forecasting indices	24
Table 1.2	Skill scores and forecast skill metrics for the SHERBS3, SHERBE, MOSH, and MOSHE at discriminating between HSLC events and warning nulls within the entire Southeast dataset.	25
Table 1.3	Monte Carlo simulation results over the Southeast HSLC subset for chosen combination forecast indices.	26
Table 1.4	As in Table 1.2, but for the Northeast subset.	27
Table 1.5	As in Table 1.2, but for the 2012-2014 Southeast subset.	28
Table 2.1	Selected base-state environment variables for matrix of simulations	75

LIST OF FIGURES

Figure 1.1	(From Schneider and Dean 2008) Number of environmental hours represented by a given CAPE (abscissa) and 0-6 km shear vector magnitude (ordinate).	29
Figure 1.2	(From Dean et al. 2009) Conditional probability of severe weather by environment, 2003-2007.	30
Figure 1.3	(From Dean and Schneider 2012) False alarm area (top) and fraction of missed tornadoes (bottom) in SPC tornado watches by environment, 2003-2012.	31
Figure 1.4	(From Schneider et al. 2006) Map of 2004-2005 severe reports occurring in environments with mixed-layer (ML) CAPE < 1000 J kg ⁻¹ , ML lifted condensation levels (ML LCL) < 1000 m, 0-1 km shear vector magnitude ≥ 10 m s ⁻¹ , and 0-6 km shear vector magnitude ≥ 18 m s ⁻¹	32
Figure 1.5	(From Davis and Parker 2014) Time–height cross sections of median azimuthal shear for a) all tornadic vortices, b) all nontornadic vortices, c) tornadic supercell vortices, d) nontornadic supercell vortices, e) tornadic non-supercell vortices, and f) non-tornadic, non-supercell vortices within 60 km of radar.	33
Figure 1.6	(From Anderson-Frey et al. 2016) POD (left) and FAR (right) of tornado warnings binned by environment, 2003-2015.	34
Figure 1.7	Example of a higher-end HSLC event. NARR fields, as follows, are from 0600 UTC 4 March 2008. Panels show a) 300 hPa isotachs (shaded, kt), geopotential heights (black contours, every 120 m), and wind barbs (kt); b) 500 hPa absolute vorticity (shaded, 10 ⁻⁵ s ⁻¹), geopotential heights (black	

contours, every 60 m), and wind barbs (kt); c) 850 hPa temperatures (shaded, °C), geopotential heights (black contours, every 30 m), and wind barbs (kt); d) 2-m dew point (shaded, °C), mean sea-level pressure (PMSL, every 2 hPa), and 10-m wind barbs (kt). Filled circles represent locations of HSLC significant tornadoes (EF2 or greater, pink), EF1 tornadoes (red), and significant winds (65 kt or greater, blue) from 0430-0730 UTC 4 March 2008. 35

Figure 1.8 Comparisons of (left) SBCAPE and (right) mean sea-level pressure (PMSL) for SFCOA and NARR. SFCOA grid point used is that associated with the maximum 2-m θ_e in a 3 by 3 grid point box (approximately 80 km by 80 km) surrounding each respective Southeast HSLC EF1 or stronger tornado report and significant wind report. NARR grid point represents the maximum value in an approximate 160 km by 160 km box surrounding each report. Correlation is represented by r^2 values in the upper left of each panel. A 1:1 line (i.e., $y = x$) is included for ease of comparison. Note that significant hail reports were not included here, as discussed in Section 1.2a. 36

Figure 1.9 a) All EF1 or greater tornado reports (red dots) and significant wind reports (blue dots) occurring in HSLC environments from 2006-2011. Shading represents a kernel density estimation of significant severe reports; darker colors correspond to a higher density of reports (probability density function estimate contoured every 0.001); b) as in a), except only for springtime reports and excluding the kernel density estimation; c) as in b), but for summertime reports; d) as in b), but for autumn reports; e) as in b), but for wintertime reports. Insets show pie charts for percentage of reports that fall in the three subjectively-defined regions, as demarcated by the green lines in a): Southeast (SE), Northeast (NE), and West (W). Counts are shown in the bottom right of each panel. 37

Figure 1.10 Map showing locations of NWS WSR-88Ds used in constructing the radar-based nulls dataset (yellow dots). 41

- Figure 1.11** Fraction of EF1 or greater tornadoes and significant wind reports from 2006-2011 that occurred in HSLC environments by month and hour (shaded). Total number of EF1 or greater tornadoes and significant wind reports for the given hour/month are listed in each box. 42
- Figure 1.12** Regional comparisons of (panels a, d, and g) 300 hPa winds (shaded, kt), wind barbs (kt), and geopotential heights (black contours, every 120 m); (panels b, e, and h) 500 hPa absolute vorticity (shaded, 10^{-5} s^{-1}), wind barbs (kt), geopotential heights (black contours, every 60 m), and 700 hPa omega (blue contours, $\mu\text{bar s}^{-1}$); (panels c, f, and i) 2-m dew point (shaded, $^{\circ}\text{C}$), mean sea level pressure (black contours, every 2 hPa), and 10-m wind barbs (kt). Plots for the southeast region are in panels a)-c), northeast region are in panels d)-f), and western region are in panels g)-i). Maps are shown for a reference scale, with the white dot depicting the event-relative composite center point and the average latitude and longitude of each subset. The number of times in each composite is shown in a), d), and g) at bottom right. 43
- Figure 1.13** Regional comparisons of 0-3 km lapse rates (K km^{-1}) for (panels a, d, and g) severe events, defined as EF1 or greater tornadoes and significant wind reports (wind gusts ≥ 65 kt), (panels b, e, and h) warning nulls, and (panels c, f, and i) the difference field between events and nulls. All else is as in Fig. 1.12. 44
- Figure 1.14** Regional composite sounding comparisons. Data are color-coded by region, with southeast thermodynamic and kinematic profiles and derived indices in red, northeast profiles and indices in blue, and western profiles and indices in green. Vertical pressure levels where 25% or more of the data were below ground are set to missing. Note that only the upper right quadrant of the hodograph is shown to highlight differences between

regions. The plotted hodograph extends from the surface to 300 hPa. Storm-relative helicity (SRH) is calculated over the surface-to-3-km layer. 45

Figure 1.15 Mean (panels a-c) 300 hPa divergence (shaded, 10^{-5} s^{-1}), geopotential heights (black contours, every 120 m), isotachs (purple contours, every 5 kt), and wind barbs (kt); (panels d-f) 500 hPa absolute vorticity (shaded, 10^{-6} s^{-1}), geopotential heights (black contours, every 60 m), wind barbs (kt), and 700 hPa omega (blue contours, $\mu\text{bar s}^{-1}$); (panels g-i) 850 hPa divergence (shaded, 10^{-5} s^{-1}), geopotential heights (black contours, every 30 m), temperature advection (blue and red contours, K s^{-1}), and wind barbs (kt); (panels j-l) SBCAPE (shaded, J kg^{-1}), (black contours, every 2 hPa), and 10-m wind barbs for southeast (panels a, d, g, j) EF1 or greater tornadoes and significant wind reports, (panels b, e, h, k) warning nulls, and (panels c, f, i, l) radar-based nulls. Maps are shown for a reference scale, with the white dot depicting the event-relative composite center point and the average latitude and longitude of each subset. The number of times in each composite is shown in the top row at bottom right. 46

Figure 1.16 Mean of (panels a-c) 0-3 km SBCAPE (J kg^{-1}); (panels d-f) 0-3 km lapse rate (K km^{-1}); (panels g-i) 3 km surface-based lifted index (K); and (panels j-l) 3-5 km lapse rate (K km^{-1}) for southeast (panels a, d, g, j) EF1 or greater tornadoes and significant wind reports, (panels b, e, h, k) warning nulls, and (panels c, f, i, l) radar-based nulls. All else is as in Fig. 1.15. 47

Figure 1.17 Mean (panels a-c) SHERBS3 and (panels d-f) SHERBE for Southeast HSLC (panels a, d) events, (panels b, e) warning nulls, and (panels c, f) radar-based nulls. Note that the 3-5 km midlevel lapse rate is used here rather than the 700-500 hPa lapse rate, and this replacement is recommended for all further use. All else is as in Fig. 1.15. 48

Figure 1.18 Mean of (panels a-c) product of 3 km ω and 0-3 km $d\theta_e/dz$ ($\text{K Pa km}^{-1} \text{ s}^{-1}$); (panels d-f) product of 4.5 km ω and 0-4.5 km $d\theta_e/dz$ ($\text{K Pa km}^{-1} \text{ s}^{-1}$); (panels g-i) product of 6 km ω and 0-6 km $d\theta_e/dz$ ($\text{K Pa km}^{-1} \text{ s}^{-1}$); and (panels j-l) the maximum ω and $d\theta_e/dz$ product from 0-2 km through 0-6 km ($\text{K Pa km}^{-1} \text{ s}^{-1}$) for southeast (panels a, d, g, j) EF1 or greater tornadoes and significant wind reports, (panels b, e, h, k) warning nulls, and (panels c, f, i, l) radar-based nulls. All else is as in Fig. 1.15. 49

Figure 1.19 0-3 km lapse rate (shaded, K km^{-1}) and 0-3 km bulk shear vector (barbs, kt) for (panels a, d, g, j) autumn, (panels b, e, h, k) winter, and (panels c, f, i, l) spring (panels a-c) daytime events, as defined in the text, (panels d-f) daytime warning nulls, (panels g-i) nighttime events, and (panels j-l) nighttime warning nulls within the southeast subset. Counts for the respective subset are provided in the bottom right of each panel. 50

Figure 1.20 As in Fig. 1.19, but showing the significant tornado parameter (STP). Black contour denotes an STP value of 0.25. 51

Figure 1.21 Box-and-whisker plots for maximum (within a 160 km by 160 km box surrounding the respective report or null) LLLR, S15MG, ESHR, and MAXTEVV term contributions within the MOSHE (as defined in Equation 1.3; e.g., $[\{\text{LLLRR}-4\}2]/4 \text{ K}^2 \text{ km}^{-2}$) across Southeast events, warning nulls, and radar-based nulls. Purple line shows the median value, while the blue box encompasses the 25th (q_1) to 75th (q_3) percentile values. Black whiskers extend to values in the range $[q_1 - 1.5*(q_3-q_1), q_3 + 1.5*(q_3-q_1)]$. Outliers are excluded. 52

Figure 1.22 Mean (panels a-c) modified SHERB (MOSH) and (panels d-f) effective version of MOSH (MOSHE) for Southeast HSLC (panels a, d) events, (panels b, e) warning nulls, and (panels c, f) radar-based nulls. All else is as in Fig. 1.16. 53

Figure 1.23	As in Fig. 1.21, but for the SHERBS3, SHERBE, MOSH, and MOSHE value distributions.	54
Figure 1.24	As in Fig. 1.23, but for the independent 2012-2014 Southeast dataset.	55
Figure 1.25	a) NARR analysis, b) RAP 6-h forecast, c) GFS 6-h forecast, d) NAM 6-h forecast of the MOSH valid at 0600 UTC 30 January 2013 (models initialized 0000 UTC 30 January 2013). Black contours encompass MOSH values ≥ 1 . Black dots show locations of EF1 or greater tornadoes and significant wind reports in the surrounding 6 h (0300-0900 UTC 30 January 2013).	56
Figure 1.26	As in Fig. 1.25, but for the SHERBS3.	57
Figure 1.27	Contributions from the (panels a, d, g, j) low-level lapse rate term, (panels b, e, h, k) 0-1.5 km shear vector magnitude term, and (panels c, f, i, l) potential instability term (all as defined in Equation 3) for (panels a-c) NARR analysis valid at 0600 UTC 30 January 2013, (panels d-f) RAP 6-h forecast, (panels g-i) GFS 6-h forecast, and (panels j-l) NAM 6-h forecast, all valid for 0600 UTC 30 January 2013.	58
Figure 1.28	Conceptual models for composite HSLC significant severe (EF2 or stronger tornadoes and 65 kt or stronger winds) event (left) and non-severe event (right). “STP” refers to the Significant Tornado Parameter (e.g., Thompson et al. 2012), while “SCP” refers to the Supercell Composite Parameter (Thompson et al. 2004). Size of features are meant to represent their relative strength (e.g., surface low depicted by red “L” is larger in severe event conceptual model, consistent with a typically stronger surface cyclone in those cases).	59

Figure 2.1	From Markowski and Richardson (2010), adapted from Klemp (1987): Origins of rotation within a supercell, as discussed in the text. Panel (a) depicts the initial counter-rotating vortices resulting from updraft tilting of environmental vortex lines. Panel (b) shows the subsequent splitting of the initial storm into symmetric right- and left-moving supercells. This situation occurs when the wind profile is unidirectional.	76
Figure 2.2	From Markowski and Richardson (2010), adapted from Klemp (1987): Examples of the “updraft-in-shear” effect for (a) unidirectional wind shear and (b) a clockwise-turning wind profile with height. Panel (b) shows how high pressure upshear and low pressure downshear of the initial updraft can promote subsequent updraft development on a given flank of the initial storm; given this wind profile, as discussed in the text, an updraft is favored on the storm’s right flank.	77
Figure 2.3	(From Dahl et al. 2014) Schematic of barotropic and baroclinic vorticity vectors along the trajectory of a parcel acquiring appreciable near-surface vertical vorticity in a simulated supercell. Black line shows the parcel’s trajectory, while the dashed line shows its surface projection. Blue shaded region shows the cold pool of the parent supercell.	78
Figure 2.4	(From Trapp and Weisman 2003) Conceptual diagram of a proposed method of mesovortexgenesis that includes the formation of a cyclonic (red) and anticyclonic (purple) vortex couplet via downdraft tilting of baroclinically-generated horizontal vorticity. Vectors represent the direction and speed of wind flow. The green barbed line shows the relative position of the surface gust front.	79
Figure 2.5	(From Atkins and St. Laurent 2009b) Conceptual diagram of a proposed method of mesovortexgenesis that includes the formation of a cyclonic (north) and anticyclonic (south) vortex couplet via updraft tilting of	

baroclinically-generated horizontal vorticity. Vectors represent the direction and speed of wind flow. The black barbed line shows the relative position of the surface gust front. Yellow vectors represent the position of vortex lines and their sense of spin. 80

Figure 2.6 (From Atkins and St. Laurent 2009b) Conceptual diagram of a proposed method of mesovortexgenesis that is ultimately similar to low-level mesocyclogenesis in a supercell. Vectors represent the direction and speed of wind flow. The black barbed line shows the relative position of the surface gust front. Yellow vectors represent the position of vortex lines and their sense of spin. 81

Figure 2.7 (From Xu et al. 2015) Conceptual diagram of a proposed method of mesovortexgenesis that suggests the source of vorticity within the vortex is frictionally-induced horizontal vorticity. Vectors represent the direction and speed of wind flow. The blue barbed line shows the relative position of the surface gust front. Red lines represent the position of frictionally-induced vortex lines, with associated purple vectors showing their sense of spin. 82

Figure 2.8 Control base-state environment in HSLC matrix of simulations. 83

Figure 2.9 Base-state thermodynamic profiles for the (left) increased low-level lapse rate and (right) decreased low-level lapse rate simulations. 84

Figure 2.10 Base-state thermodynamic profiles for the (left) increased low-level shear vector magnitude and (right) decreased low-level shear vector magnitude simulations. 85

Figure 2.11 Regional mosaic of 1-km reflectivity over the Southeast for the 4-5 March 2008 severe HSLC event. Shortly after this time, several developed across

	the Carolinas and southern Virginia, while damaging straight-line winds were in progress. Image courtesy of UCAR and College of DuPage.	86
Figure 2.12	Regional mosaic of 1-km reflectivity over the Southeast for the 29-30 January 2013 severe HSLC event. Around this time, several QLCS tornadoes were in progress across middle Tennessee. Image courtesy of UCAR and College of DuPage.	87
Figure 2.13	Four-panel reflectivity imagery from the Raleigh, NC WSR-88D (KRAX) on 5 March 2008 at 0148 UTC showing four radar tilts (0.5°, 0.9°, 1.3°, and 1.8°) during an HSLC tornado event. Note that this is an embedded miniature supercell. Image courtesy of National Weather Service, Raleigh, NC.	88
Figure 2.14	As in Fig. 2.13, but for storm-relative velocity.	89
Figure 2.15	Radar reflectivity from the Nashville, TN WSR-88D (KOHX) on 30 January 2013 at 0900 UTC while an HSLC QLCS tornado outbreak was in progress. Note numerous hook-like appendages along the leading edge of the QLCS, many of which were associated with tornadoes.	90
Figure 3.1	Overview of 0-3 km lapse rates ($K km^{-1}$; shading, 1-km vertical velocity ($m s^{-1}$; black contours), and 1-km vertical vorticity (s^{-1} ; white contours) for the control simulation from $t=0$ min through $t=120$ min over 15-min intervals.	109
Figure 3.2	Overview of 1-km reflectivity (dBZ; rainbow shading), surface potential temperature perturbation (K; tan to dark blue shading), 1-km vertical velocity ($m s^{-1}$; black contours), and 1-km vertical vorticity (s^{-1} ; white contours) for the control simulation from $t=150$ min through $t=270$ min over 15-min intervals.	110

Figure 3.3	As in Fig. 3.2, but zoomed out to show the initiating cold pool’s retreat relative to the evolving convection.	111
Figure 3.4	Hovmöller plot of 2-5 km updraft helicity (m^2s^{-2} ; shaded) and near-surface vertical vorticity (s^{-1} ; contours) tracks for the control simulation over the time period $t=150$ min to $t=270$ min.	112
Figure 3.5	Zoomed-in plot of 1-km reflectivity (dBZ; rainbow shading), surface potential temperature perturbation (K; tan to dark blue shading), 1-km vertical velocity ($m s^{-1}$; black contours), and 1-km vertical vorticity (s^{-1} ; white contours) for the control simulation’s strongest updraft from $t=230$ min through $t=270$ min over 5-min intervals.	113
Figure 3.6	Plot of surface vertical vorticity (s^{-1} ; rainbow shading) and maximum (black contours) and minimum (brown contours) vertical velocity in the lowest 1 km ($m s^{-1}$) for the control simulation’s strongest updraft from $t=247$ min through $t=263$ min over 2-min intervals.	114
Figure 3.7	As in Fig. 3.6, but zoomed in and including surface wind vectors ($m s^{-1}$). Note change in color bar meant to highlight lower values of vertical vorticity. Red “P”s and blue “N”s in first two panels show alternating positive and negative bands of vertical vorticity appearing to emanate from the downdraft.	115
Figure 3.8	As in Fig. 3.6 for $t = 253$ min, but zoomed in and including surface wind vectors ($m s^{-1}$). Pink dashed lines show two apparent “rivers” of vorticity feeding the developing vortex.	116
Figure 3.9	Trajectories, (left) vertical vorticity (s^{-1}) and (right) height (m) of parcels contributing to a strong, near-surface vortex in the control simulation.	117

Figure 3.10	As in Fig. 3.9, but for the y-z plane and showing vertical velocity (m s^{-1}) rather than height. Also note that this figure represents a longer time period (including the time after parcels exit the vortex).....	118
Figure 3.11	Scatter plot of updraft duration (min) against maximum vertical velocity (m s^{-1}) for each updraft object tracked for at least 5 minutes in the control simulation.	119
Figure 3.12	As in Fig. 3.11, but for the maximum vertical vorticity (s^{-1}) of tracked vortex objects.	120
Figure 3.13	Scatter plot of maximum vertical vorticity (s^{-1}) of each tracked vortex object compared to the strongest overlying updraft (m s^{-1}) during its lifetime. Blue line shows the best-fit line, with correlation coefficient (r) and p-value provided in the top right corner.	121
Figure 3.14	As in Fig. 3.5, but showing 1-km ACCD ($10^{-2} \times \text{m s}^{-2}$; shading), surface-to-1-km maximum (black contours) and minimum (blue contours) vertical velocity (m s^{-1}), and lowest level vertical vorticity (s^{-1} ; green to red contours).	122
Figure 3.15	As in Fig. 3.14, but for 1-km ACCB ($10^{-2} \times \text{m s}^{-2}$; shading).	123
Figure 3.16	Time series of ACCB (green, m s^{-2}), ACCD (blue m s^{-2}), and vertical velocity (red, m s^{-1}) for a sampling of parcels that entered the strongest updraft in the control simulation. Time is adjusted such that $t=0$ min is the time at which maximum vertical velocity was achieved for the given parcel. Only a subset of the parcels that entered the updraft are shown for clarity, but they enter the updraft along a similar trajectory to the remaining parcels and are representative of the population as a whole.	124

Figure 3.17	ACCD (m s^{-2}) and trajectories of parcels entering the strongest updraft in the control simulation, looking south-southwest.	125
Figure 3.18	ACCB (m s^{-2}) and trajectories of parcels entering the strongest updraft in the control simulation, looking south-southwest.	126
Figure 3.19	As in Fig. 3.17, but looking towards the west-northwest.	127
Figure 3.20	As in Fig. 3.14, but for 1-km ACCDNL ($10^{-2} \text{ x m s}^{-2}$; shading).	128
Figure 3.21	As in Fig. 3.14, but for 1-km ACCDL ($10^{-2} \text{ x m s}^{-2}$; shading).	129
Figure 3.22	As in Fig. 3.21, but for 3-km ACCDL ($10^{-2} \text{ x m s}^{-2}$; shading).	130
Figure 3.23	As in Fig. 3.20, but for 3-km ACCDNL ($10^{-2} \text{ x m s}^{-2}$; shading).	131
Figure 3.24	Vertical time series of maximum vertical vorticity (10^{-2} x s^{-1} ; shading), vertical velocity (m s^{-1} , black contours), and ACCDNL (10 x m s^{-2} , blue contours) within a 10 km by 10 km box surrounding the strongest updraft, leading to the development of the strongest vortices in the control simulation.	132
Figure 3.25	Plan-view images of (top row) low-to-midlevel vertical vorticity (shaded; 10^{-2} s^{-1}), (middle row) low-level ACCDNL (shaded; 10^{-2} m s^{-2}), and (bottom row) low-level vertical velocity (shaded; m s^{-1}) for the updraft and vortex shown in Fig. 3.24. Green, brown, and red contours show constant values of vertical velocity (10 m s^{-1}), ACCDNL (0.1 m s^{-2}), and vertical vorticity (0.03 s^{-1}), respectively. Times shown are $t=230 \text{ min}$, $t=235 \text{ min}$, and $t=240 \text{ min}$ from left to right, respectively.	133

Figure 3.26	As in Fig. 3.25, but for $t=245$ min, $t=250$ min, and $t=255$ min from left to right, respectively.	134
Figure 3.27	As in Fig. 3.2, but for (top row) +01s, (second row) -01s, (third row) +03lr, and (bottom row) -03lr for (left to right columns) $t=180$ min, 225 min, and 270 min.	135
Figure 3.28	As in Fig. 3.4, but for -01s.	136
Figure 3.29	As in Fig. 3.4, but for +01s.	137
Figure 3.30	As in Fig. 3.4, but for -03lr.	138
Figure 3.31	As in Fig. 3.4, but for +03lr.	139
Figure 3.32	Scatter plot of median updraft duration (min) against median maximum updraft intensity (m s^{-1}) for the tracked updraft features in each simulation. Error bars extend to the 25th and 75th percentiles of each distribution.	140
Figure 3.33	As in Fig. 3.32, but for duration and intensity (Okubo-Weiss parameter, s^{-2}) of tracked vortex features in each simulation.	141
Figure 3.34	(Top) Scatter plot of ACCD and ACCB for each minute of tracked long-lived updrafts within the respective simulations. (Bottom) A kernel density estimate encompassing 50% of the total distribution, extending from the densest bin.	142
Figure 3.35	Exceedance frequency for vertical vorticity of 0.03 s^{-1} for all simulations. ..	143
Figure 3.36	Exceedance frequency for ACCDNL of 0.3 m s^{-2} for all simulations.	144

Figure 3.37	Exceedance frequency for vertical velocity of 20 m s^{-1} for all simulations. ..	145
Figure 3.38	As in Fig. 3.14, but for -01s.	146
Figure 3.39	As in Fig. 3.20, but for -01s.	147
Figure 3.40	As in Fig. 3.24, but for -01s.	148
Figure 3.41	As in Fig. 3.24, but for +01s.	149
Figure 3.42	As in Fig. 3.24, but for +03lr.	150
Figure 3.43	As in Fig. 3.24, but for -03lr.	151
Figure 3.44	As in Fig. 3.24, but for a second -03lr updraft that occurs at a closer simulation time to that in Fig. 3.42 for a more direct comparison between -03lr and +03lr.	152
Figure 3.45	As in Fig. 3.15, but for -03lr.	153
Figure 3.46	As in Fig. 3.15, but for +03lr.	154
Figure 3.47	As in Fig. 3.14, but for -03lr.	155
Figure 3.48	As in Fig. 3.14, but for +03lr.	156
Figure 3.49	As in Fig. 3.4, but including anticyclonic lowest-level vortices.	157
Figure 3.50	As in Fig. 3.49, but for the non-Coriolis control simulation.	158

Figure 3.51	Hovmöller plot of near-surface vertical vorticity (s^{-1} ; shaded) and 1-km vertical velocity ($m s^{-1}$; contours) tracks for the control simulation over the time period $t=150$ min to $t=270$ min.	159
Figure 3.52	As in Fig. 3.51, but for the non-Coriolis control run.	160
Figure 3.53	As in Fig. 3.2, but showing surface potential temperature perturbation (K; shaded) and surface wind vectors.	161
Figure 3.54	As in Fig. 3.53, but for the non-Coriolis control simulation.	162
Figure 3.55	As in Fig. 3.3, but for the non-Coriolis control simulation.	163
Figure 3.56	As in Fig. 3.5, but for the control, no Coriolis run.	164
Figure 3.57	As in Fig. 3.2, but for the control simulation with the hodograph rotated 30° clockwise.	165
Figure 3.58	As in Fig. 3.2, but for the control simulation with the hodograph rotated 60° clockwise.	166
Figure 3.59	As in Fig. 3.57, but zoomed in on the development of an updraft and zone of near-surface vertical vorticity between two discrete convective cells.	167
Figure 3.60	As in Fig. 3.4, but for the rotated 60° control simulation.	168
Figure 3.61	Lowest level vertical vorticity (s^{-1} ; shaded), 1-km updraft ($m s^{-1}$; black contours), and 40-dBZ simulated reflectivity contour (blue) for the strongest updraft in the rotated 60° control simulation from $t=210$ min through $t=250$ min.	169

CHAPTER 1

Composite Environments of Severe and Nonsevere High-Shear, Low-CAPE Convective Events

Note that Chapter 1 is a slightly updated version of the following published manuscript: Sherburn, K. D., M. D. Parker, J. R. King, and G. M. Lackmann, 2016: Composite environments of severe and nonsevere high-shear, low-CAPE convective events. Wea. Forecasting, 31, 1899-1927.

1.1 Introduction

Environments characterized by limited CAPE and large vertical wind shear (colloquially referred to as high-shear, low-CAPE, or “HSLC” environments) are common across the contiguous U.S. (Dean and Schneider 2008; Fig. 1.1) and can be associated with severe convection, particularly during the cool season and overnight hours (e.g., Johns et al. 1993; Sherburn and Parker 2014). HSLC severe weather, including significant (EF2 or greater on the enhanced Fujita scale) tornadoes, occurs worldwide and is recognized as a considerable forecasting challenge (e.g., Hanstrum et al. 2002; Tyrrell 2007; Romero et al. 2007; Clark 2009, 2011; Gatzen et al. 2011; Inoue et al. 2011; Clark and Parker 2014; Mulder and Schultz 2015). To date, the peer-reviewed literature on HSLC convection within the U.S. is largely confined to case studies (e.g., Kennedy et al. 1993; Markowski and Straka 2000) and climatologies (Evans 2010; Davis and Parker 2014; Sherburn and Parker 2014), with a few related modeling studies primarily focused on tropical storm environments (McCaul and Weisman 1996, 2001). The goal of Chapter 1 is to build upon the methods and metrics of recent HSLC studies (e.g., Sherburn and Parker 2014, explored in further detail shortly) and to identify features discriminating between severe and non-severe HSLC episodes, thereby improving existing forecasting techniques.

Across the continental U.S., HSLC environments are present considerably more frequently than “high-shear, high-CAPE” (HSHC) environments (Dean and Schneider 2008; Schneider and Dean 2008; Fig. 1.1). However, given the occurrence of lightning, the probability of severe weather is nearly an order of magnitude lower in HSLC environments

than in environments with comparable deep-layer shear vector magnitudes but 2500 J kg^{-1} of most unstable (MU) CAPE (Dean et al. 2009, Fig. 1.2). Accordingly, the skill of NOAA Storm Prediction Center's tornado watches is substantially lower in HSLC environments, with false alarm area and fraction of missed tornadoes maximized in this zone of the parameter space (Dean and Schneider 2012; Fig. 1.3).

A large fraction¹ of U.S. tornadoes (and significant tornadoes) occur in HSLC regimes (e.g., Schneider et al. 2006; Guyer and Dean 2010; Dean and Schneider 2012; Fig. 1.4). HSLC significant tornadoes tend to be concentrated in the Mississippi, Tennessee, and Ohio Valleys (e.g., Sherburn and Parker 2014). These locations coincide with the typical locations of significant cool season and overnight tornadoes and tornado outbreaks (e.g., Vescio and Thompson 1998; Guyer et al. 2006; Kis and Straka 2010). Additionally, given the compact spatial (tornadic mesocyclone or mesovortex depths and diameters of approximately 2-4 km; Davis and Parker 2014; Fig. 1.5) and temporal dimensions of HSLC convection (e.g., McCaul 1987), resolving rotation may be challenging, delayed, or even impossible, particularly far from radar (e.g., McCaul 1993; Lane and Moore 2006; Davis and Parker 2014). Thus, the climatology of HSLC tornadoes also exhibits considerable overlap with time periods known for poor tornado warning skill and correspondingly high normalized fatality totals (e.g., Ashley et al. 2008; Brotzge and Erickson 2010; Brotzge et al. 2011). Further, recent work highlights low probability of detection (POD) and high false alarm rate (FAR) specifically in association with HSLC tornado warnings (Anderson-Frey et al. 2016; Fig. 1.6).

Given the aforementioned operational challenges, there has been some emphasis on the large-scale environments accompanying HSLC severe weather. Figure 1.7 provides an example of the 4 March 2008 HSLC event, illustrating several features identified in prior

¹ Guyer and Dean (2010) found that approximately 28% of all 2003-2009 tornadoes occurred in environments characterized by mixed-layer CAPE (MLCAPE) $\leq 500 \text{ J kg}^{-1}$. Schneider et al. (2006) showed that 54% of EF2 or greater tornadoes in 2004-2005 were associated with MLCAPE $\leq 1000 \text{ J kg}^{-1}$ and 0-6 km shear vector magnitude $\geq 18 \text{ m s}^{-1}$.

case studies. HSLC environments producing severe convection tend to be associated with potent upper-level troughs, surface cyclones, and cold fronts (e.g., McAvoy et al. 2000; Cope 2004; Lane and Moore 2006; Wasula et al. 2008). Moisture is typically abundant in the low levels and through much of the troposphere, contributing to low lifted condensation levels (LCLs; as in Schneider et al. 2006 and Lane 2008; Fig. 1.7d). Winds over the depth of the troposphere tend to be intense, with low-level jets (LLJs) and deep-layer shear vector magnitudes commonly reaching upwards of 25-30 m s⁻¹ (e.g., Lane and Moore 2006; Konarik and Nelson 2008; note 70-75 kt 850 hPa jet in Fig. 1.7c). Numerous case studies have also noted dry intrusions aloft coincident with the development or strengthening of convection (Kennedy et al. 1993; Lane and Moore 2006; Wasula et al. 2008; Evans 2010; Gatzen et al. 2011). These features could be indicative of a cold front aloft (e.g., Hobbs et al. 1990; note strong 850 hPa cold front in Fig. 1.7c) or an approaching upper-level jet streak (Gatzen et al. 2011; Fig. 1.7a). Either way, dry air aloft suggests the presence of potential instability, which could be released by ascent, thus supplementing the apparently low ambient CAPE values.

Because CAPE is by definition low in HSLC environments, forecasting parameters that include CAPE as a constituent [including the Significant Tornado Parameter (STP; Thompson et al. 2003; Thompson et al. 2004; Thompson et al. 2012), Energy Helicity Index (EHI; e.g., Davies 1993), Vorticity Generation Parameter (VGP; e.g., Rasmussen and Blanchard 1998), and Craven-Brooks significant severe parameter (Craven and Brooks 2004)] struggle to adequately represent the risk for severe hazards in HSLC environments (Guyer and Dean 2010; Sherburn and Parker 2014). In fact, Sherburn and Parker (2014) showed that all of the aforementioned indices had their maximum skill values well below those values recommended as operational guidance (e.g., Rasmussen and Blanchard 1998; Craven and Brooks 2004; Thompson et al. 2004).

To address these concerns, Sherburn and Parker (2014) developed the Severe Hazards in Environments with Reduced Buoyancy (SHERB) parameter. This combination of lapse rates (0-3 km and 700-500 hPa in the original formulation) and shear vector magnitudes

(particularly 0-3 km and effective bulk shear magnitudes) was statistically shown to improve the discrimination between significant severe convection and non-severe convection. However, because it does not directly rely on CAPE, the SHERB is subject to large false alarm areas, as values often climb above its severe guidance threshold of 1 in environments where convection is not expected (Sherburn and Parker 2014; R. Thompson, personal communication). This is particularly a concern in locations where low-level lapse rates are climatologically steeper than those in the Southeast (for which the parameter was developed), such as in the Plains, or in elevated terrain where the two lapse rate layers overlap. Additionally, values are often observed to rise above the threshold behind cold fronts. Other parameters, such as the combination of lifted index, low-level shear vector magnitude, and near-surface convergence suggested by Hanstrum et al. (2002) or the TQ index (Henry 2000)—a modified version of the total totals index using the 700 hPa temperature rather than the 500 hPa temperature—have not been subject to rigorous statistical tests but have shown practical operational utility in other regions.

Despite a recent uptick in the number of studies investigating HSLC environments, several gaps in the knowledge base associated with the dynamics and predictability (both long- and short-term) of severe HSLC convection remain. As a first step towards addressing these knowledge gaps, we seek an understanding of the climatology of severe HSLC convection within the scope of the entire severe weather spectrum. Next, we explore the range of synoptic patterns conducive to severe HSLC convection. We find that considerable information and context is added by focusing on spatial patterns of fields instead of individual grid point values (i.e., as explored by Sherburn and Parker 2014). Thorough interrogation of 3D reanalysis fields suggests a highly effective forecast parameter for the prediction of HSLC convection. A novel aspect of this parameter is a proxy measure for the in-situ generation of instability through the release of potential instability. Results indicate that this parameter is a useful discriminator between severe events and nulls (the latter is defined in Section 1.2b). The results of this climatology subsequently motivate process studies aimed toward establishing a physical understanding of severe HSLC convection and how environmental variables can affect its intensity and longevity. The ultimate goals of this

research are to determine a) the chain of processes that extend from the development of HSLC convection to its ultimate production of tornadoes or damaging straight-line winds and b) *how* the favorable environmental parameters identified in Chapter 1 and prior studies physically influence the potential for these processes to succeed.

1.2 Data and Methods for Environmental Analysis

a. Definition of events

Nationwide EF1 or greater tornado reports and significant wind reports (wind gusts ≥ 65 kt or 33.44 m s^{-1}) from 2006-2011 were gathered from the Storm Prediction Center (SPC). For each report, archived SPC Surface Objective Analysis (SFCOA; i.e., Mesoscale Analysis or Mesoanalysis; Bothwell et al. 2002) data for several fields at the nearest grid point and previous hour were available. For this work, the SFCOA data were only utilized to determine if the report occurred within an HSLC environment (i.e., did it meet our HSLC criteria, as defined in Sherburn and Parker 2014: surface-based CAPE (SBCAPE) $\leq 500 \text{ J kg}^{-1}$, MUCAPE $\leq 1000 \text{ J kg}^{-1}$, and 0-6 km bulk wind difference $\geq 18 \text{ m s}^{-1}$). As will be discussed in Section 1.2c, the majority of analysis within this work is performed utilizing North American Regional Reanalysis (NARR; Mesinger et al. 2006) data. Comparisons between SFCOA² and NARR data suggest the two datasets can vary considerably for a given event, particularly for parameters relevant to this study (see and compare scatter plots for SBCAPE and mean sea-level pressure, or PMSL, in Fig. 1.8). Detailed verification of the representativeness of SFCOA vs. NARR is beyond the scope of this work (given that there are few, if any, “ground truth” measurements of thermodynamic and wind profiles in HSLC environments). However, given the aforementioned differences and the observation that

² In Fig. 1.8, the SFCOA grid point with the neighborhood maximum (within a 3-by-3 grid point box surrounding the report) 2-m θ_e was used. Given that these cases all met HSLC criteria using the nearest grid point, it is clear that some cases had very large gradients of CAPE over a small (i.e., < 100 km) area.

NARR CAPE tended to be higher than that of the SFCOA (consistent with the positive bias noted by Gensini et al. 2014), we used an additional constraint requiring NARR SBCAPE and mixed-layer CAPE (MLCAPE) $\leq 1000 \text{ J kg}^{-1}$ to ensure that truly high-CAPE environments were excluded. Reports that met the above criteria were included in our HSLC dataset.

We chose to exclude significant hail reports, which comprised a small percentage of the overall dataset, due to concerns that some of these may have been associated with elevated convection that bypassed our HSLC thresholds (as discussed in Sherburn and Parker 2014). However, analysis including significant hail reports showed no appreciable differences. In addition, EF0 tornado reports and non-significant wind reports were excluded from our analyses. Generally, these reports are considered less reliable due to the non-meteorological factors affecting their inclusion in the official Storm Data database (e.g., Brooks et al. 2003; Smith et al. 2013), including diurnal occurrence, population density (e.g., Doswell et al. 2009), land use dependencies (Weiss et al. 2002; Trapp et al. 2006), and poorly estimated wind speeds (Doswell et al. 2005). Further discussion on these caveats can be found in Smith et al. (2012) and Sherburn and Parker (2014). The authors acknowledge that this approach excludes a portion of the convective spectrum, including measured, non-significant wind reports; the present work focuses on high-end tornado and wind events that ultimately have the largest impact on life and property. Hereafter, the 1447 reports meeting these criteria (Fig. 1.9a; separated by season in Figs. 1.9b-e) will be referred to as “events”.

b. Definition of nulls

Because binary forecasting statistics can be sensitive to how a null case is defined, two different null datasets (here, generally referring to non-severe convection) were utilized in this study for comparison. The first set of nulls is defined as in Sherburn and Parker (2014): “the initial latitude-longitude point [i.e., the subjectively-defined location of the storm’s area of interest, as determined by the NWS warning meteorologist] of a severe thunderstorm or tornado warning that was issued in an HSLC environment [as defined in Section 1.2a] when

there were no severe reports from the Storm Data archives in the corresponding CWA [NWS county warning area] throughout that convective day (1200-1200 UTC).” As in that work, the null dataset spans October 2006 through April 2011 and encompasses the contiguous U.S. The SFCOA and NARR CAPE and shear constraints were again used to determine which nulls occurred within an HSLC environment. Using these criteria, 925 nulls were identified, and these are hereafter referred to as “warning nulls”.

The primary concern in basing null identifications on warnings is their inherent subjectivity—the severity of a given cell is judged by the forecaster on shift, and he or she may have a warning threshold that differs from a peer. To address such concerns of objectivity, the second set of nulls is defined based upon the WSR-88D’s storm cell identification and tracking algorithm (SCIT; Johnson et al. 1998), which identifies cells based upon given spatial and temporal thresholds of radar reflectivity and predicts their subsequent motion. The purpose of this alternative null dataset is to identify non-severe convection without the requirement of warning issuance. To this end, only the diagnostic portion of the SCIT (i.e., the identification of cells) was utilized, and a minimum reflectivity threshold of 45 dBZ was enforced. SCIT data were gathered for January-April and October-December in 2011, encompassing the typical period of HSLC convective activity across the southeastern U.S. Only radars in the Southeast (Fig. 1.10) and cells within five minutes of a NARR data time (e.g., for 0300 UTC, data from 0255 to 0305 UTC) were utilized for this null subset.

To ensure a clean radar-based null population, only cells clearly lacking severe weather reports (no reports in their CWA or any adjacent CWA during the given convective day³) were retained for analysis. Then, the aforementioned SFCOA and NARR filters were

³ Note that this varies from the spatial criterion used to define warning nulls. Warning nulls, on the other hand, could be from within a CWA that is adjacent to a neighboring CWA represented by events on the same convective day. For example, if a tornado warning was issued by the Raleigh, NC WFO on a given day when no severe weather occurred in the Raleigh CWA, that tornado warning would be considered a warning null. However, if an EF1 tornado occurred in the adjacent Wakefield, VA CWA on the same day, that tornado would be included in the events subset.

again utilized to ensure the detected cells were within HSLC environments. Additionally, to ensure that non-convective cells were not included, minimal buoyancy (i.e., at least 10 J kg^{-1} of CAPE in SFCOA or NARR) was required. Finally, only the cell with the highest reflectivity for a given NARR data time was retained to prevent oversampling of a given environment. Using this definition, 1301 nulls were identified. These are hereafter referred to as “radar-based nulls”.

c. Composites

Composite maps and soundings were generated using NARR data from the National Centers for Environmental Information (NCEI). The NARR has a horizontal grid spacing of approximately 32 km with 29 vertical levels and is available every 3 h. Though its resolution is not ideal, recent studies (e.g., Gensini and Ashley 2011; Walters et al. 2014) suggest that the NARR is practical for climatological analyses, even for mesoscale phenomena. Further, the NARR has several research benefits over the SFCOA, including its full three-dimensionality and the ability to derive additional variables from its grids. For each report or null, a 20° latitude by 20° longitude box centered on the report or null was created using the nearest NARR data time. Data within these boxes were then averaged over the number of sample times to create report- or null-relative composites.

Regional, seasonal, and diurnal subsets of the HSLC population of events and warning nulls were created to further assess potential differences. Regions were defined by latitude and longitude, as shown in Fig. 1.9a. While these regions were defined subjectively, it is shown later that the majority of HSLC activity occurs in the Southeast subset, while cases in the West exhibit markedly dissimilar synoptic-scale characteristics to those in the East. Spring, summer, autumn, and winter were defined as March-May, June-August, September-November, and December-February, respectively. Daytime cases were those occurring between 8 AM and 5 PM LST, while nighttime cases were limited to the time period of 8 PM to 5 AM LST. Compound subsets (e.g., nighttime winter events) were also created to determine the seasonal differences in diurnal variability.

1.3 HSLC Severe Climatology and Composites

Previous studies have noted that HSLC events peak in the cool season and overnight (e.g., Evans 2010; Guyer and Dean 2010; Sherburn and Parker 2014). Our data further show that the majority of significant wind reports and EF1 or greater tornadoes from winter through mid-spring occur within HSLC environments, particularly during the overnight and morning hours (Fig. 1.11). As was shown by Sherburn and Parker (2014), HSLC significant wind reports and EF1 or greater tornadoes are most common in the Ohio, Tennessee, and Mississippi Valleys but can occur in any region (Fig. 1.9a). A clear annual shift in this distribution is apparent, with an increasing number of reports in northern and western portions of the country during the warm season (Figs. 1.9b-e). However, the majority of HSLC events occur in the Southeast during the winter or spring (Figs. 1.9b, 1.9e).

Comparing the three regions via typical synoptic scale fields⁴ (Fig. 1.12), it becomes apparent that western HSLC events are fundamentally dissimilar from those in the Southeast and Northeast. The composite event in the West is characterized by weaker upper-level flow (cf. Figs. 1.12a-b, 1.12d-e, 1.12g-h) and appears closer to a surface triple-point or upslope setup than the warm sector/cold front-driven pattern common in the East (cf. Figs. 1.12c, 1.12f, 1.12i). This is likely attributable to both the relative climatology of events in the West (biased towards the warm season) and greater case-to-case variability in the region. As noted in Section 1.1, lapse rates are climatologically steeper in the West than the East; however, lapse rates across the West are also far less useful indicators than in the East (Fig. 1.13), with steeper lapse rates observed in the null environments than in the events (Figs. 1.13g-i). This suggests that techniques developed to improve the forecasting of HSLC environments utilizing lapse rates as ingredients [e.g., Sherburn and Parker (2014)'s SHERB parameters, reviewed in Section 1] may lack utility across the West and may be more subject to large

⁴ Recall that the composite maps are presented in a *report- or null-relative framework*. Background maps are primarily meant to provide a sense of scale, though they also show the *mean report or null location* for each subset.

false alarm areas in this region. Additionally, although compositing vertical profiles smooths features considerably, western soundings (interpolated to the composite center) are characterized by much lower relative humidity in the lower troposphere than in the East (Fig. 1.14), leading to higher LCLs and larger downdraft CAPE. Hodographs in the West are also relatively straight compared to those in the East (Fig. 1.14). These sounding features corroborate the comparatively higher percentage of straight-line winds in the western U.S. sample of HSLC significant severe reports (approximately 50% of eastern U.S. events are straight-line wind reports compared to 83% of western U.S. events).

Given the apparent differences between western and eastern HSLC events and our desire to focus on the cool season phenomenon that appears to be relatively absent from the West, we exclude western cases from our subsequent analysis. Additionally, because Southeast and Northeast events appear fundamentally rather similar (cf. soundings in Fig. 1.14 and respective panels in Figs. 1.12, 1.13), we chose to focus on the Southeast subset, which encompasses the majority of the density “bull’s eye” exhibited in Fig. 1.9a and contains the vast majority of significant tornadoes. Focusing the discussion on a single region allows for easier segmentation of the data and a clearer depiction of what processes and features show operational utility at discriminating between events and nulls. The Northeast subset returns later as an independent verification dataset following the development of new forecasting techniques using the Southeast subset.

There are several recurring themes in the Southeast cases. First, events are characterized by especially strong synoptic-scale forcing for ascent, including intense upper-level divergence and low-level convergence, a potent upstream vorticity maximum at 500 hPa, strong low-level warm air advection, and a surface cyclone centered just north of the composite center (Figs. 1.15a, 1.15d, 1.15g, 1.15j). A coupled jet feature aloft is also noted, with the composite report occurring near the right entrance region of a northern jet streak and the exit region of a southern jet streak. The warning null composite—centered approximately 100 km south of the event composite—reveals similar features (e.g., a coupled jet feature aloft, an upstream trough at all levels, upper-level divergence atop low-level convergence, a

closed surface cyclone), but these are displaced slightly northwest with respect to the composite center and have substantially weaker magnitudes, particularly in the lower levels (Figs. 1.15b, 1.15e, 1.15h, 1.15k). On the other hand, radar-based nulls show a similar jet streak focused north of the composite center, but the upper-level divergence, low-level convergence, and surface cyclone are much more benign (Figs. 1.15c, 1.15f, 1.15i, 1.15l). Radar-based nulls further lack any hint of a southern upper-level jet streak and, compared to the warning nulls, show a considerably less amplified lower- and upper-level trough. Combined, these features contribute to much weaker synoptic scale forcing for ascent in the radar-based nulls, as reflected in 700 hPa ω (vertical velocity with respect to pressure) fields. Overall, on the mean, there is generally a decrease in forcing strength from severe events to warning nulls to radar-based nulls.

Instability is inherently limited in both the events and nulls⁵ (Figs. 1.15j-l); however, a tongue of enhanced low-level instability is apparent in 0-3 km surface-based CAPE, lapse rate, and lifted index fields in the events (Figs. 1.16a-i). While the zone of enhanced lapse rates extends well upstream of the composite event center (Figs. 1.16d-f), relatively large magnitudes of low-level CAPE are confined to areas near and just upstream of the event center, with a local maximum apparently detached from the region of higher CAPE to the south (Figs. 1.16a-c). This zone is oriented roughly linearly along the mean surface trough, suggesting a narrow unstable sector ahead of an approaching cold front. Large interquartile ranges relative to mean values (not shown), however, suggest that the distribution of low-level CAPE values (in particular) within HSLC environments is wide, meaning that this feature—though noteworthy on the mean—may not be apparent in all events and may be present in some nulls, as well.

Low-level lapse rate distributions have relatively small interquartile ranges (not shown), and the lapse rates are overall less variable than low-level CAPE. Given that low-

⁵ Note that SBCAPE near the composite report is actually above the HSLC threshold of 500 J kg^{-1} , representing differences between the NARR and SF COA, as shown in Figure 1.8.

level lapse rates tend to be steeper in events than in nulls (Fig. 1.16), values of the SHERB utilizing the 0-3 km bulk wind difference (SHERBS3) and effective bulk wind difference (SHERBE) are accordingly higher in events (Fig. 1.17). Compared to the other two SHERB ingredients, the midlevel lapse rate term (using the 3-5 km layer, which we recommended for future use given that it is independent of surface height above sea level) appears to be a less practical discriminator between events and nulls (Figs. 1.16j-l); in fact, in several subsets, this mid-level lapse rate is higher in nulls than events. This suggests that a) the midlevel lapse rate's skill is conditional, perhaps only in a portion of the parameter space; and b) a modified version of the SHERB parameters with new ingredients replacing or supplementing the midlevel lapse rate may be more operationally advantageous.

The orientation of locally enhanced low-level CAPE relative to a zone of enhanced synoptic-scale forcing for ascent suggests the possibility that potential instability is being released in-situ as forcing arrives in a given location. To address this hypothesis, a product of $d\theta_e/dz$ (i.e., the change of equivalent potential temperature with height, indicating potential instability when negative) and ω was calculated and plotted over several layers. As shown in Fig. 1.18, there is a robust discriminatory signal in this product, particularly when comparing events and radar-based nulls. Additionally, there is reasonable overlap between the maxima in these fields and the enhanced area of low-level CAPE, implying that the release of potential instability could be the mechanism responsible for this feature. The practical utility of these features and ingredients in discriminating between events and nulls will be assessed in a more rigorous quantitative framework in Section 1.4.

Individual ingredients show substantial variability through the diurnal cycle. There is clear evidence of steeper lapse rates during the day and stronger shear vector magnitude at night, regardless of whether the event or null dataset is being investigated (Fig. 1.19)⁶. There is also a variability (albeit weaker) in both parameters on the seasonal cycle. This implies that

⁶ Transition periods (i.e., 5 AM-8 AM and 5 PM-8PM LST, the latter of which encompasses the climatological peak of tornado occurrence across the CONUS; e.g., Kelly et al. 1978) were excluded from the diurnal analyses to more clearly represent the unique characteristics of daytime and nocturnal cases.

a single value or threshold of lapse rates, for example, is unlikely to be equally skillful for nighttime versus daytime cases. However, forecasting indices that include several individual ingredients are somewhat more resistant to seasonal and diurnal variability. One such combination is the significant tornado parameter (STP; Thompson et al. 2012). A “reservoir” of enhanced effective STP values (albeit still below the operational guidance value of 1) is observed upstream of the composite event in all six diurnal/annual cycle event subsets, while such a feature is practically absent in all null subsets (Fig. 1.20). These findings suggest that multi-ingredient forecast indices have a higher potential to be consistently discriminatory regardless of season or time of day.

1.4 Skill Score Tests

In addition to the creation of report-relative composites, NARR data were used in a series of skill score tests to determine the most statistically skillful combination of ingredients among a selection of fields included within NARR grids and additional parameters calculated from them. A set of over 250 potential ingredients was assessed. Here, each ingredient or combination of ingredients was tested independently for its ability to discriminate between HSLC events and warning nulls within the Southeast. Four possible formulations of each ingredient (X) were tested:

- 1) $X - a$, or the ingredient minus some constant value a ;
- 2) X , or the ingredient itself;
- 3) $b - X$, or the ingredient subtracted from some constant value b ; and
- 4) X^2 , or the ingredient squared.

This builds upon the work of Sherburn and Parker (2014), who only used formulation 2 and who applied a tiered skill score test that first identified the most skillful ingredient, then explored the conditional skill of additional ingredients.

Herein, only data from the Southeast subset were utilized, and skill was defined by correctly discriminating between events and warning nulls. This analysis was also performed on radar-based nulls. However, comparing radar-based nulls with events may be of less practical utility, given that the former were not necessarily associated with convection that subjectively appeared severe. The maximum (or minimum, depending on the particular ingredient) grid point value in an approximate 160 km by 160 km box surrounding the composite center was utilized in the skill score tests in an attempt to capture the most representative fields available given that small-scale evolution at a point may not be captured by the relatively coarse temporal resolution of the NARR. The two compound metrics used to determine skill were the Heidke Skill Score (HSS), calculated by

$$\text{HSS} = 2 * (ad - bc) / [(a + c)(c + d) + (a + b)(b + d)], \quad (1)$$

and True Skill Statistic (TSS; Wilks 1995), given by

$$\text{TSS} = (ad - bc) / [(a + c)(b + d)], \quad (2)$$

where a is a correct forecast of an event, b is a false alarm, c is a missed event, and d is a correct null. Preference was given to the HSS based upon its consistency regardless of event rarity (Doswell et al. 1990). Traditional forecasting metrics such as POD and FAR were also calculated.

Initial tests determined the skill of individual ingredients using the entire set of parameters. Subsequent tests then assessed the skill of multi-ingredient combinations of parameters consisting of those that had exhibited skill on their own or in conjunction with one other ingredient. Tests with multiple ingredients allowed for the inclusion of more than one term of a given type but were subjectively checked to avoid redundancy of ingredients. It is possible that some ingredients or combinations of parameters exhibit statistical skill but little practical skill. For example, PMSL may be statistically skillful, as events tend to be

associated with deeper surface cyclones than nulls; however, in practice, this would imply that the threat would increase along a cold front as one travels closer to the cyclone center, which is not necessarily true. Thus, only those composite parameters judged to have a robust physical basis were considered for further analysis.

As shown in Table 1.1, the 0-3 km lapse rate was the most skillful individual thermodynamic ingredient, consistent with findings from Sherburn and Parker (2014). Most of the other independent terms that exhibited skill were kinematic fields, including the effective shear vector magnitude [also consistent with Sherburn and Parker (2014)] and its zonal component, as well as the meridional component and magnitude of the 10-m wind speed (perhaps highlighting the importance of low-level θ_e advection). Finally, frontogenesis within the 750 hPa to 700 hPa layer was also skillful, perhaps suggesting that the depth of linear forcing or the presence of a cold front aloft may be important for determining the potential severity of an event.

The SHERBE and SHERBS3 parameters developed by Sherburn and Parker (2014; here using the recommended 3-5 km lapse rate instead of the 700-500 hPa lapse rate) showed the most skill among existing combination indices [a group that also included the STP, Supercell Composite Parameter (Thompson et al. 2003; Thompson et al. 2004), Craven-Brooks significant severe parameter, 0-3 km EHI, and 0-3 km VGP], followed by several low-level turbulent kinetic energy (TKE) terms (Table 1.1). Although statistically skillful, TKE terms are dependent on model configuration and parameterizations (here, these terms are outputted from the NARR grid, not calculated manually). As a result, these terms were excluded from further investigation. However, in general, large low-level TKE would result from large low-level lapse rates and low-level vertical shear (e.g., low Richardson numbers). In this sense, it provides rather similar information to the SHERBS3 and SHERBE. Products of ω and $d\theta_e/dz$, meant to approximate the release of potential instability, also showed relatively high skill, consistent with the spatial footprint noted in Fig. 1.16. While ω is also dependent on model configuration (primarily grid spacing), it is an explicitly-represented

field (unlike TKE, which is parameterized). Thus, it was retained for the multi-ingredient tests.

Low-level lapse rates and bulk wind differences appear in nearly every combination of skillful ingredients, suggesting they are crucial in discriminating between HSLC events and nulls. Steep low-level lapse rates can promote downward momentum transfer of strong flow aloft (e.g., Johns and Hirt 1987; Johns 1993; Evans and Doswell 2001) or the strengthening of low-level vortices (e.g., Parker 2012). Meanwhile, larger low-level shear vector magnitudes also promote the strengthening of low-level mesocyclones (e.g., Markowski and Richardson 2014; Coffey and Parker 2015) or mesovortices (e.g., Weisman and Trapp 2003) and are representative of stronger environmental flow that could potentially be transported to the surface via convective downdrafts. Combining the two terms, rather than looking at each in isolation, helps preserve their discriminatory skill while diminishing each term's respective diurnal cycle (as shown in Fig. 1.19). In particular, the effective shear vector magnitude appeared in many skillful combinations. The effective layer is approximately defined as the lower half of the vertical layer exhibiting CAPE (Thompson et al. 2007); the inclusion of the effective bulk shear magnitude therefore adds an inherent CAPE mask that may be a useful contributor to an index lacking an explicit buoyancy term.

When combined with instability and shear ingredients, the most skillful synoptic forcing ingredient was typically either a product of ω and $d\theta_e/dz$ or near-surface wind magnitude, showing that potential instability or low-level advection may be critical in some cases. This idea is supported by complementary modeling work (e.g., King et al. 2017) and will be discussed further in Section 1.5. Midlevel lapse rates, despite not showing skill on their own, do exhibit skill when combined with other ingredients, as found by Sherburn and Parker (2014); this suggests potential non-linear interaction with other ingredients or compensation in some portion of the parameter space.

After testing all combinations of up to five ingredients, an index including the 0-3 km lapse rate (low-level lapse rate, or LLLR), 0-1.5 km bulk shear vector magnitude (S15MG), the maximum $d\theta_e/dz * \omega$ product calculated from the 0-2 km layer through the 0-6 km layer

at 0.5 km intervals (MAXTEVV), and (optionally, as discussed shortly) the effective bulk shear magnitude (ESHR) was found to outperform all other combinations. The most skillful formulation including the effective bulk shear magnitude [hereafter referred to as the Modified SHERB (effective version), or MOSHE] is:

$$MOSHE = \frac{(LLLR-4 K km^{-1})^2}{4 K^2 km^{-2}} * \frac{(S15MG-8 m s^{-1})}{10 m s^{-1}} * \frac{(ESHR-8 m s^{-1})}{10 m s^{-1}} * \frac{(MAXTEVV+10 K Pa km^{-1}s^{-1})}{9 K Pa km^{-1}s^{-1}}, \quad (3)$$

where LLLR is in $K km^{-1}$ (a positive value indicates decreasing temperature with height), S15MG and ESHR are in $m s^{-1}$, and MAXTEVV is in $K Pa km^{-1} s^{-1}$ (and signed such that θ_e decreasing with height multiplied by upward motion yields a positive value). If any ingredient is negative (e.g., $LLLR < 4 K km^{-1}$), MOSHE is set to 0. MOSHE was set to missing when the environment lacked an effective layer (e.g., there was little or zero diagnosed MUCAPE). The given denominators were chosen such that the most skillful discriminating value of the MOSHE within the Southeast HSLC events subset would approximately equal 1 (using the NARR dataset). Further, the subtracted constants and squared lapse rate term result in the most skillful formulation of the MOSHE, while maintaining approximately equivalent interquartile ranges and contributions from each term (Fig. 15). Physically, in addition to the MUCAPE consideration above, the subtracted constants lead to a MOSHE of 0 when the low levels are especially stable (i.e., when $LLLR \leq 4 K km^{-1}$) or when the low-level shear is especially weak (i.e., when $S15MG \leq 8 m s^{-1}$), both of which are not conducive for the production of severe weather in HSLC environments. The version of this index excluding the effective bulk shear vector magnitude (hereafter referred to as simply the Modified SHERB, or MOSH) is given by:

$$MOSH = \frac{(LLLR-4 K km^{-1})^2}{4 K^2 km^{-2}} * \frac{(S15MG-8 m s^{-1})}{10 m s^{-1}} * \frac{(MAXTEVV+10 K Pa km^{-1}s^{-1})}{9 K Pa km^{-1}s^{-1}}. \quad (4)$$

As with the MOSHE, if any ingredient is negative, MOSH is set to 0. Likewise, denominators were determined in a similar fashion. The MOSH and MOSHE have comparable maximum HSS and TSS. The MOSHE may be desired to further reduce false alarm area where convection is not anticipated (i.e., locations where CAPE is near zero), and the MOSH may especially be a desired aid when the analyzed or forecast CAPE is suspected

to be too low, which could lead to an underestimate of the severe threat by the MOSHE⁷ (as shown by POD and FAR in Table 1.2).

Spatially, the MOSH composite maps reveal much clearer delineation of the threat area in events compared to the rather broad SHERB signals (cf. Figs. 1.17, 1.22), largely attributable to the inclusion of the MAXTEVV term. In addition, the MOSH parameters show clear separation between events and nulls due to their larger fundamental range of values as compared to the SHERB parameters (Fig. 1.23). Overall, the MOSH parameters show an improvement over the SHERB parameters, both in statistical skill (Table 1.2) and spatial accuracy, while maintaining the core emphasis on low-level lapse rates and shear vector magnitude.

MOSH and MOSHE maximum skill scores are comparable to the SHERBS3 and SHERBE, with the MOSH showing a lower FAR than the SHERBS3 (Table 1.2). Monte Carlo simulations (Wilks 1995) utilizing 1000 iterations of 50 random events and warning nulls within the Southeast subset showed that the MOSH consistently outperformed all other combination forecast indices at their traditional guidance values (Table 1.3). Generally similar maximum skill scores were calculated using the independent Northeast subset, though the value where the maximum skill occurred varied (Table 1.4). As a final verification of the robustness of the MOSH parameters, independent 2012-2014 event and null datasets were generated for the Southeast region, subject to the same criteria as the original 2006-2011 datasets. Parameter distributions (Fig. 1.24) and calculated skill scores (Table 1.5) reveal similar characteristics of the MOSH parameters within the 2012-2014 dataset, though in a similar fashion to the Northeast subset, the parameter value associated with maximum skill varied. This suggests that the guidance value of 1 should not be used as a hard threshold; rather, it can be expected that the conditional threat for HSLC severe hazards will increase as MOSH progressively exceeds 1.

⁷ Recall that ESHR is based on the layer exhibiting sufficient CAPE. Thus, if CAPE is low or zero, that layer can become vanishingly small, or ESHR can be zero.

Consistent with the SHERB parameters (Sherburn and Parker 2014), formulations of MOSH including the midlevel lapse rate showed a modest increase in skill over the formulations listed above (maximum HSSs of 0.410 and 0.377, respectively, for MOSH and MOSHE with the midlevel lapse rate term included). However, results of a principal component analysis (not shown) revealed that the midlevel lapse rate contributed far less variance than the other MOSH ingredients, implying that its role is minor compared to other terms. Additionally, the practical importance of the midlevel lapse rate remains in question, given the concerns posed in Section 1.3. Finally, the MOSH and MOSHE formulations excluding the midlevel lapse rate still exhibit the key improvements over the SHERBS3 and SHERBE: a spatial focusing of enhanced values near the location of reports in addition to an increase in statistical skill. Thus, for simplicity, the midlevel lapse rate was excluded from the presented version of the MOSH and MOSHE indices herein.

We have heretofore addressed the skill of parameters in the reference frame of gridded analyses, but it is worth considering their value in numerical weather prediction forecasts. Additional tests will be necessary to determine the sensitivity of MOSH ingredients—particularly the MAXTEVV field—to model setup, including grid spacing. For example, ω values will locally be considerably larger within high-resolution models due to their ability to resolve convective updrafts. Thus, the most skillful values of MOSH and MOSHE may be sensitive to horizontal grid spacing. Future work could examine the potential of “capping” the MAXTEVV contribution (e.g., as done with ESHR, among other ingredients, in the STP) on higher-resolution grids or working with spatially smoothed vertical motion fields (to capture synoptic or frontal-scale updrafts rather than convective updrafts) to alleviate this concern. Philosophically, the use of the MOSH and MOSHE fields is most practical in numerical weather prediction models with coarser grid spacing; after all, these indices are designed to diagnose a favorable environment for severe HSLC convection. In contrast, convection-allowing models should theoretically be capable of resolving the severe convection itself. This is corroborated by real-case model simulations of HSLC severe and non-severe convection (King et al. 2017), while previous studies have noted improved

forecasts of convection in strongly-forced regimes (e.g., Duda and Gallus 2013), which are present in most HSLC cases.

As a preliminary step towards examining the sensitivity of MOSH fields to model configuration, MOSH and MOSHE values were calculated using archived forecasts from the Global Forecast System (GFS; 0.5° horizontal grid spacing), North American Mesoscale (NAM; 12-km horizontal grid spacing), and Rapid Refresh (RAP; 13-km horizontal grid spacing) models for an HSLC event on January 30, 2013. For this case, 6-h forecasts valid at 0600 UTC 30 January 2013 show enhanced MOSH values focused over a smaller area than the SHERBS3 (cf. Figs. 1.25, 1.26), consistent with the NARR event composites. The corridors of enhanced MOSH values do vary somewhat more than those of the SHERBS3 values based upon the chosen analysis; however, it is difficult to determine if these distinctions are artifacts of the model setup or simply due to differing forecast and analysis accuracy. By breaking the MOSH down into its respective components (Fig. 1.27), it appears that the contribution from the low-level shear vector magnitude term is rather consistent among all forecasts and analyses; the low-level lapse rate term and, especially, the potential instability term appear to be responsible for the varying modeled threat areas. For example, the RAP appears to underestimate the threat across northern portions of the report area (Fig. 1.25b); this is coincident with a relatively low potential instability term contribution in the RAP (Fig. 1.27f). Overall, however, the forecasts of MOSH depict the region where severe weather occurred in the surrounding 6 h with reasonable accuracy. A more robust evaluation of the sensitivity of the MOSH and MOSHE to grid spacing and model configuration will be left for future work.

1.5 Synthesis and Discussion

High-shear, low-CAPE (HSLC) severe convection remains a forecasting challenge across time scales ranging from days to minutes in advance. These environments comprise a

majority of the EF1 or greater tornado and significant wind report population during the cool season, especially during the overnight hours (Fig. 1.11). This population corresponds to time periods where climatological conditions are generally unfavorable for severe convection and, accordingly, the performance of severe weather watches and warnings is notably decreased. HSLC severe convection occurs across all regions of the contiguous U.S.; however, the majority of significant tornadoes and winds occur within the Southeast (Fig. 1.9). Across the West, HSLC environments are characterized by a drier lower troposphere and a surface triple point or upslope setup, which suggest they may be fundamentally dissimilar from HSLC events in the East that are typically associated with low lifted condensation levels and occur in the warm sector or along a cold front (Figs. 1.12 and 1.14). However, middle and upper tropospheric synoptic scale features across all regions are fairly similar, with strong forcing for ascent exhibited at all levels (Fig. 1.12).

Much of the analysis herein focused on the Southeast subset, given that it comprises a large fraction of the severe HSLC convection climatology. Through the analysis of composite maps and skill score tests, several features were shown to exhibit discrimination between events and nulls, including (but not limited to) intense upper-level divergence and low-level convergence (Fig. 1.15), a localized maximum of low-level CAPE (Fig. 1.16), conditions for release of potential instability, which could supplement low values of ambient CAPE (Fig. 1.18), and enhanced near-surface flow (Fig. 1.15). Additionally, plan-view maps showed that events tended to occur on the northern nose of a surface-based unstable sector, where SBCAPE values exceeded the 500 J kg^{-1} threshold (Fig. 1.15) and STP values were marginally enhanced to the near south (Fig. 1.20). Overall, it appears that both the magnitude and relative positioning of the aforementioned features is important in determining whether an HSLC setup will produce severe or non-severe convection, with stronger, more closely collocated features conducive to severe HSLC events. Future work could examine how these features differ in location and intensity with convective mode (e.g., as in work conducted by the Sterling, VA WFO; M. Kramar, personal communication), particularly given the propensity of HSLC tornadoes occurring within quasi-linear convective systems (e.g., Thompson et al. 2012).

The SHERB parameters (Sherburn and Parker 2014) continue to exhibit skill at discriminating between Southeast HSLC events and nulls (Table 1.2; Figs. 1.17, 1.23; note that the 3-5 km lapse rate is used and recommended to replace the 700-500 hPa lapse rate). However, this study provides evidence that skill could be further improved when interrogating additional fields or incorporating other ingredients. Shear vector magnitudes over shallower layers than those utilized in the SHERBS3 exhibit higher skill than the original formulation. Additionally, skill score tests suggest that including a term meant to represent the release of potential instability further improves skill while also focusing the spatial footprint of parameter maximum values. These ingredients were combined into a Modified SHERB, or MOSH, introduced in Section 4 (Table 1.2; Figs. 1.22, 1.23). Another version of this index including the effective bulk shear magnitude (MOSHE, also introduced in Section 4) provides similar skill while alleviating concerns of enhanced values where there is little or no chance for convection. While the spatial (Fig. 1.22) and statistical (Tables 1.2-1.5) skill of these indices are robust, future work must address the sensitivity of these new combination parameters to model setup, particularly grid resolution, to determine if the distributions of values presented herein are consistent across all platforms. Using an ensemble approach (e.g., assessing the ensemble mean MOSH or MOSHE) may ultimately be preferable, given the potential sensitivity of the ingredients to model physics choices and resolution.

These results, which are summarized as conceptual diagrams in Figure 1.28, are consistent with the modeling study of King et al. (2017), who found that the release of potential instability—a process by which instability is generated in-situ due to the arrival of synoptic-scale forcing for ascent—or strong low-level advection of warm, moist air—which generally scales with the strength of the attendant cyclone—were responsible for rapid destabilization preceding convection in severe HSLC cases. Combined, these studies suggest that some continuous external forcing may be necessary to support vigorous convection in environments with limited CAPE. Additionally, the destabilization in these cases tended to occur on very fine spatial and temporal scales—potentially at scales unresolvable by conventional numerical weather prediction guidance. However, King et al. (2017) also found

that convection-allowing models with grid spacing as coarse as 3 km are capable of providing useful guidance in discriminating between severe and nonsevere HSLC convection. In particular, in their simulations, all severe events were characterized by broad areas of 10-m wind speeds of at least 16 m s^{-1} or updraft helicity of at least $95 \text{ m}^2 \text{ s}^{-2}$, which had comparatively much smaller footprints in nonsevere events (Fig. 1.28). Furthermore, although some nonsevere events experienced SBCAPE increases over 100 J kg^{-1} in the 3 h preceding convection, the overall distribution of 3-h CAPE increases was lower in nonsevere events, suggesting more rapid destabilization in severe events, as noted above. Additionally, SBCAPE increases in nonsevere events due to low-level moistening were typically countered by stabilization near the surface, as noted by decreases in surface potential temperature.

The results here indicate that our ability to discriminate between severe and nonsevere HSLC convection is improving. We have shown that a favorable environment, as determined by low-level lapse rates and shear vector magnitudes, along with strong synoptic scale forcing for ascent, discriminate well between severe and nonsevere HSLC convective events. However, our understanding of the processes that lead to the development of strong low-level vortices or damaging straight-line winds in HSLC convection remains limited due to a lack of observations and modeling studies associated with these environments. Thus, a logical next step—which will be addressed in Chapter 2—is to conduct an idealized numerical simulation study that aims to isolate the processes responsible for the production of severe hazards in HSLC convection. Following from the results of the environmental study here, we can then begin to assess the dynamics behind the discriminatory skill of low-level lapse rates and shear vector magnitudes.

TABLES

Table 1.1. Maximum HSS for ten most skillful individual ingredients and combination forecasting indices

<i>Ingredient</i>	<i>Maximum HSS</i>
<i>U</i> -component of effective bulk shear vector	0.329
<i>U</i> -component of 0-2 km shear vector	0.302
Planetary boundary layer height	0.294
725 hPa frontogenesis	0.292
Effective shear vector magnitude	0.291
750 hPa frontogenesis	0.288
10-m wind magnitude	0.277
<i>V</i> -component of 10-m wind vector	0.275
700 hPa frontogenesis	0.273
0-3 km lapse rate	0.262
<i>Combination Index</i>	<i>Maximum HSS</i>
SHERBE	0.374
SHERBS3	0.366
950 hPa TKE	0.347
900 hPa TKE	0.335
925 hPa TKE	0.332
875 hPa TKE	0.284
700 hPa ω * 1000-700 hPa $d\theta_e/dz$	0.257
4.5 km ω * 0-4.5 km $d\theta_e/dz$	0.248
3 km ω * 0-3 km $d\theta_e/dz$	0.247
500 hPa ω * 1000-500 hPa $d\theta_e/dz$	0.246

Table 1.2. Skill scores and forecast skill metrics for the SHERBS3, SHERBE, MOSH, and MOSHE at discriminating between HSLC events and warning nulls within the entire Southeast dataset.

<i>Index</i>	<i>Maximum HSS</i>	<i>Maximum TSS</i>	<i>POD at max HSS</i>	<i>FAR at max HSS</i>	<i>Max HSS threshold</i>	<i>HSS at threshold = 1</i>
SHERBS3	0.366	0.363	0.861	0.515	0.90	0.343
SHERBE	0.374	0.415	0.690	0.275	0.80	0.222
MOSH	0.402	0.446	0.799	0.392	1.00	0.402
MOSHE	0.377	0.412	0.709	0.297	1.00	0.377

Table 1.3. Monte Carlo simulation results over the Southeast HSLC subset for chosen combination forecast indices.

<i>Index</i>	<i>Mean HSS</i>	<i>Minimum HSS</i>	<i>25th Percentile HSS</i>	<i>Median HSS</i>	<i>75th Percentile HSS</i>	<i>Maximum HSS</i>	<i>Tested Threshold</i>
Craven-Brooks Significant Severe	0.076	-0.120	0.035	0.080	0.120	0.260	20000
EHI (0-3 km)	0.124	-0.100	0.080	0.120	0.180	0.380	1.0
MOSH	0.407	0.100	0.360	0.400	0.480	0.680	1.0
MOSHE	0.412	0.120	0.360	0.400	0.480	0.700	1.0
SCP	0.237	-0.060	0.180	0.240	0.300	0.520	1.0
SHERBS3	0.367	0.100	0.300	0.360	0.420	0.620	1.0
SHERBE	0.300	0.060	0.240	0.300	0.360	0.520	1.0
STP	0.088	-0.060	0.060	0.080	0.120	0.240	1.0
VGP (0-3 km)	0.120	-0.080	0.080	0.120	0.160	0.340	0.2

Table 1.4. As in Table 1.2, but for the Northeast subset.

<i>Index</i>	<i>Maximum HSS</i>	<i>Maximum TSS</i>	<i>POD at max HSS</i>	<i>FAR at max HSS</i>	<i>Max HSS threshold</i>	<i>HSS at threshold = 1</i>
SHERBS3	0.426	0.424	0.809	0.385	0.95	0.418
SHERBE	0.377	0.379	0.588	0.209	0.80	0.207
MOSH	0.396	0.398	0.638	0.241	1.45	0.366
MOSHE	0.390	0.394	0.528	0.134	1.30	0.331

Table 1.5. As in Table 1.2, but for the 2012-2014 Southeast subset.

<i>Index</i>	<i>Maximum HSS</i>	<i>Maximum TSS</i>	<i>POD at max HSS</i>	<i>FAR at max HSS</i>	<i>Max HSS value</i>	<i>HSS at index = 1</i>
SHERBS3	0.398	0.401	0.709	0.310	1.15	0.266
SHERBE	0.440	0.445	0.619	0.173	1.00	0.400
MOSH	0.451	0.450	0.760	0.310	1.50	0.407
MOSHE	0.461	0.464	0.691	0.227	1.85	0.425

FIGURES

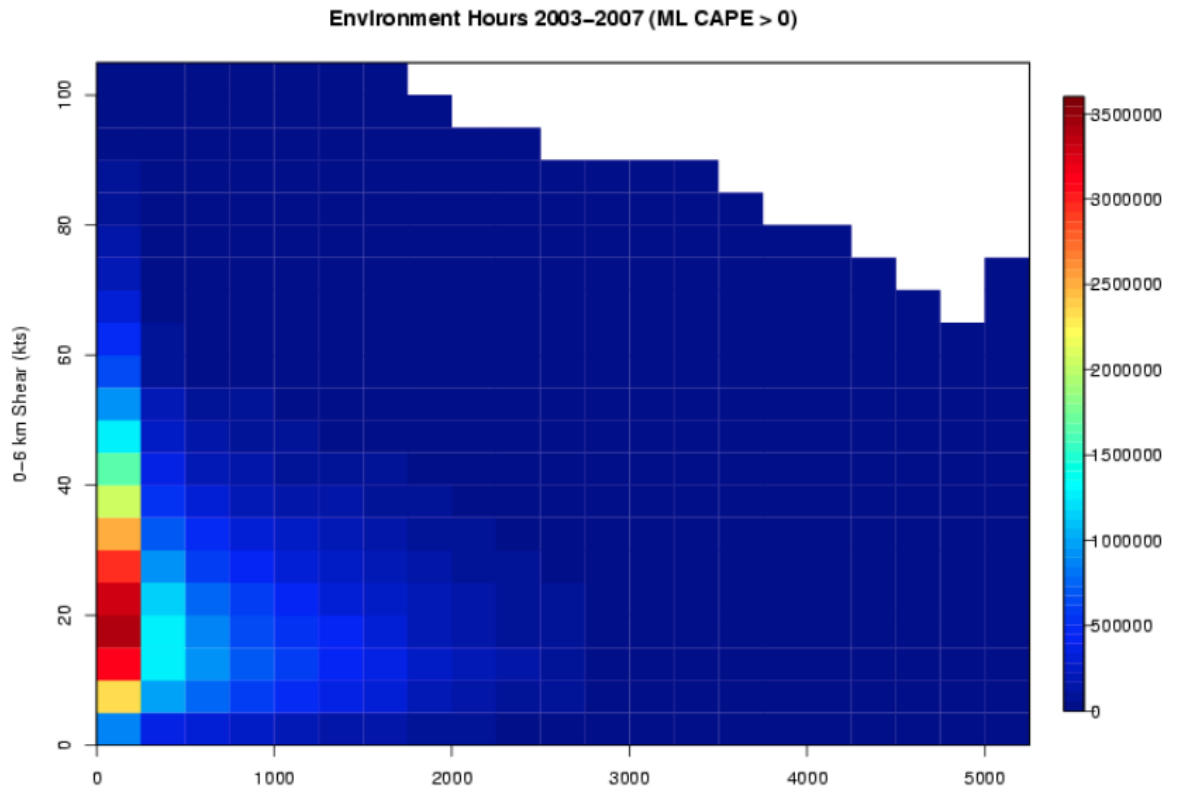


Figure 1.1. (From Schneider and Dean 2008) Number of environmental hours represented by a given CAPE (abscissa) and 0-6 km shear vector magnitude (ordinate).

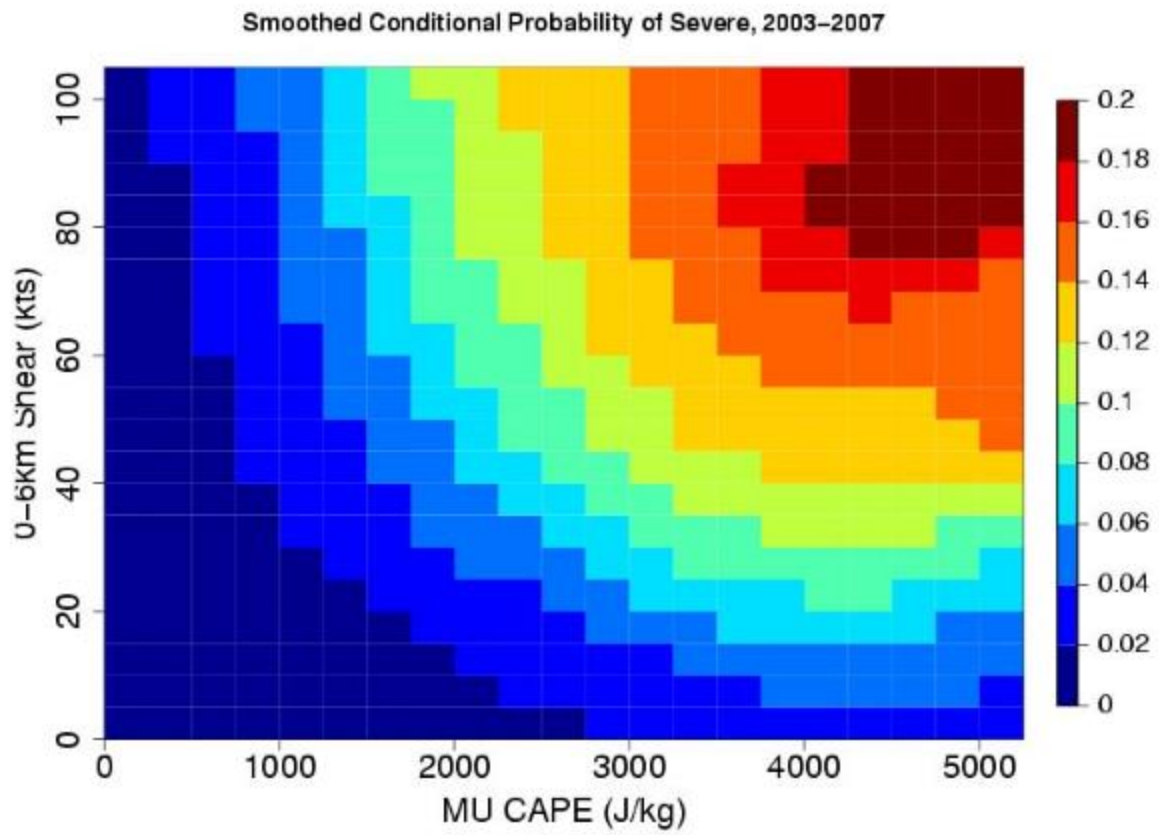


Figure 1.2. (From Dean et al. 2009) Conditional probability of severe weather by environment, 2003-2007.

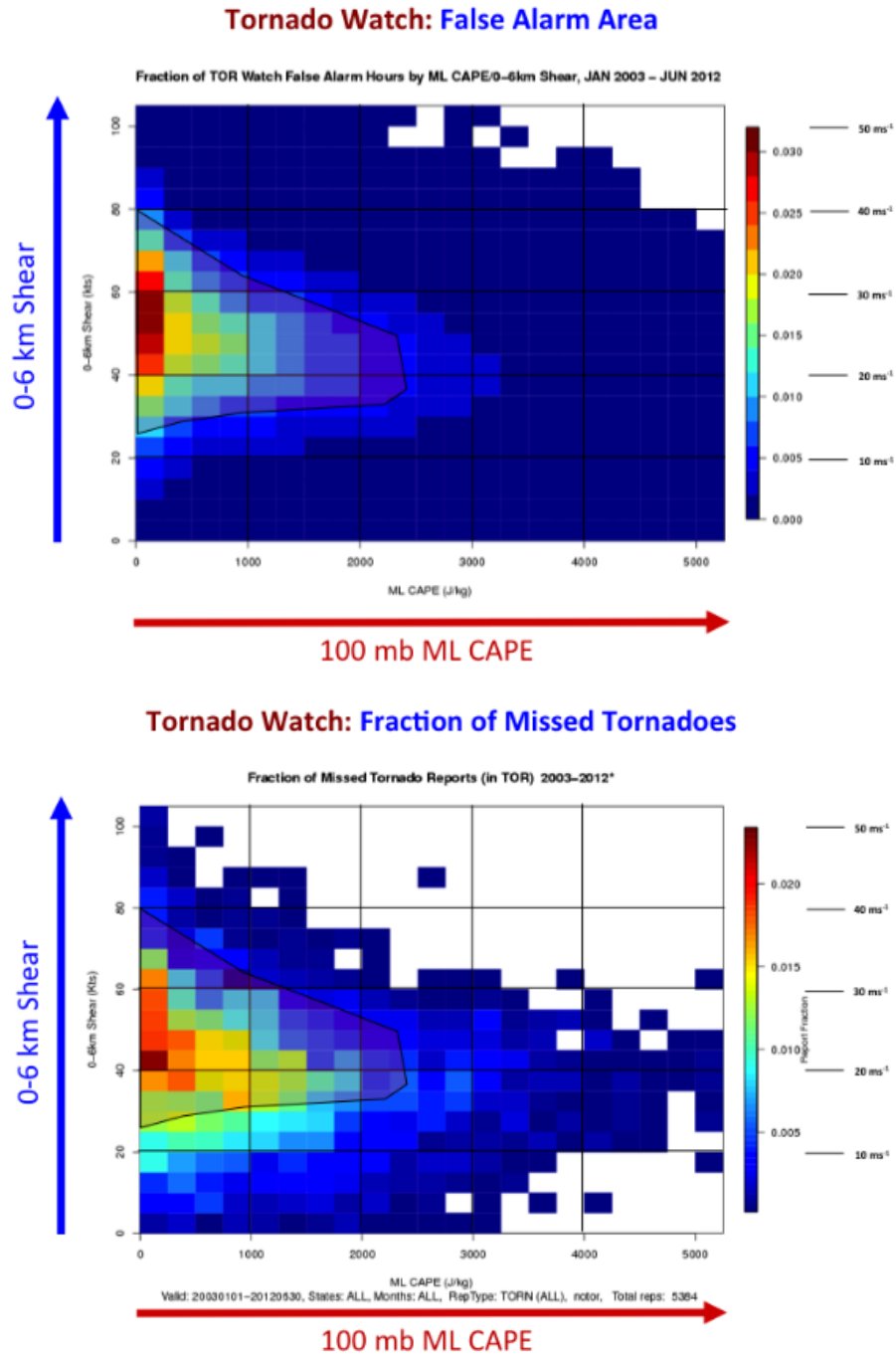


Figure 1.3. (From Dean and Schneider 2012) False alarm area (top) and fraction of missed tornadoes (bottom) in SPC tornado watches by environment, 2003-2012.

Figure 4b

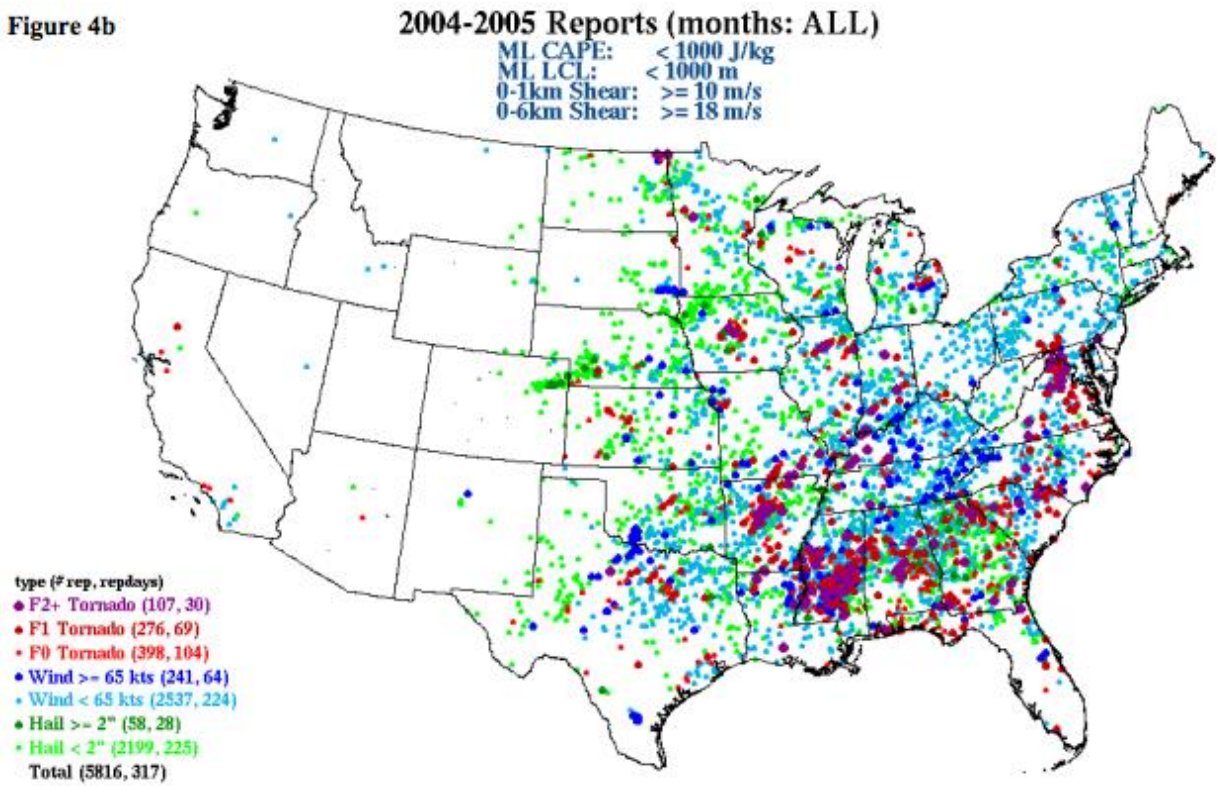


Figure 1.4. (From Schneider et al. 2006) Map of 2004-2005 severe reports occurring in environments with mixed-layer (ML) CAPE $< 1000 \text{ J kg}^{-1}$, ML lifted condensation levels (ML LCL) $< 1000 \text{ m}$, 0-1 km shear vector magnitude $\geq 10 \text{ m s}^{-1}$, and 0-6 km shear vector magnitude $\geq 18 \text{ m s}^{-1}$.

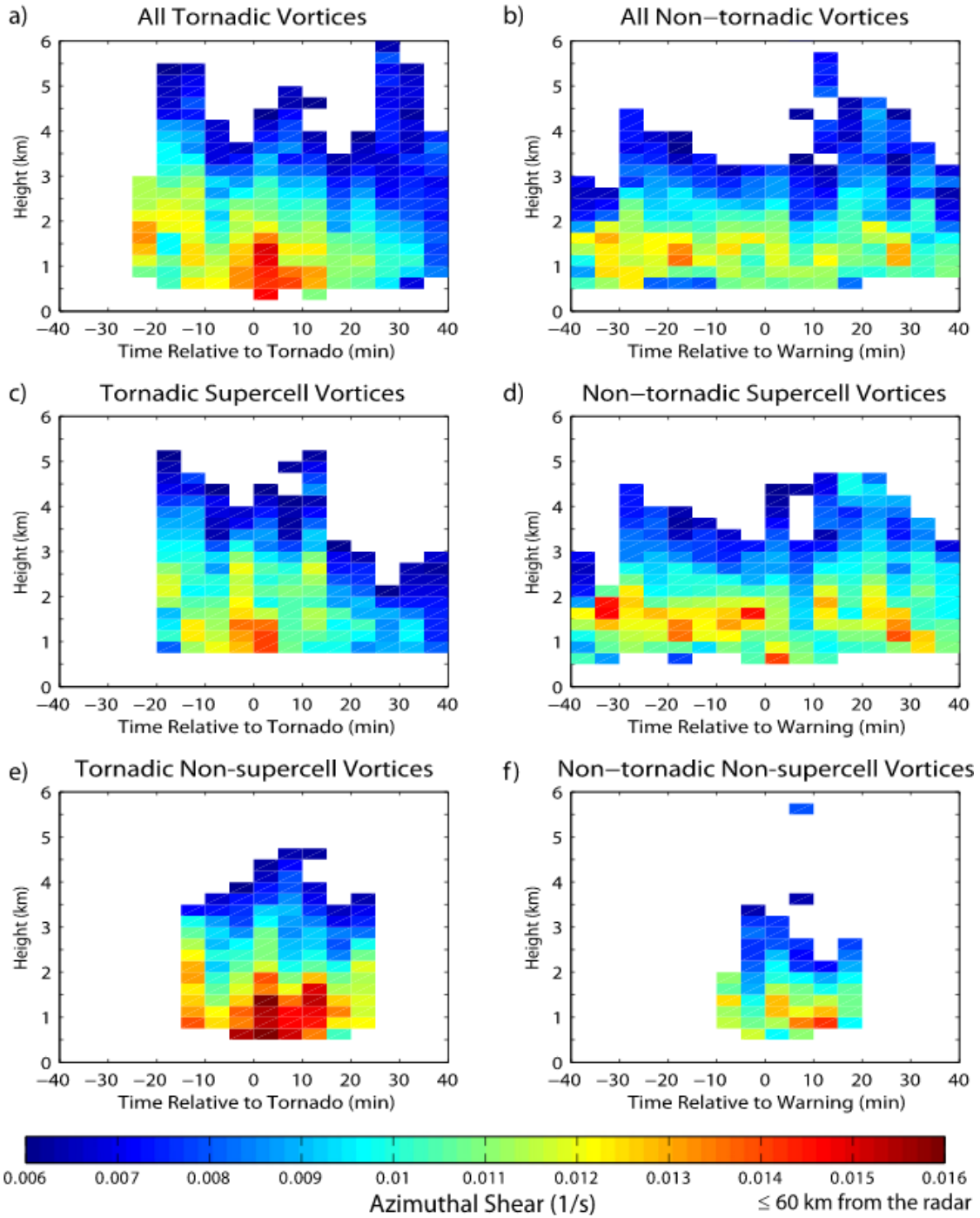


Figure 1.5. (From Davis and Parker 2014) Time–height cross sections of median azimuthal shear for a) all tornadoic vortices, b) all nontornadoic vortices, c) tornadoic supercell vortices, d) nontornadoic supercell vortices, e) tornadoic non-supercell vortices, and f) non-tornadoic, non-supercell vortices within 60 km of radar.

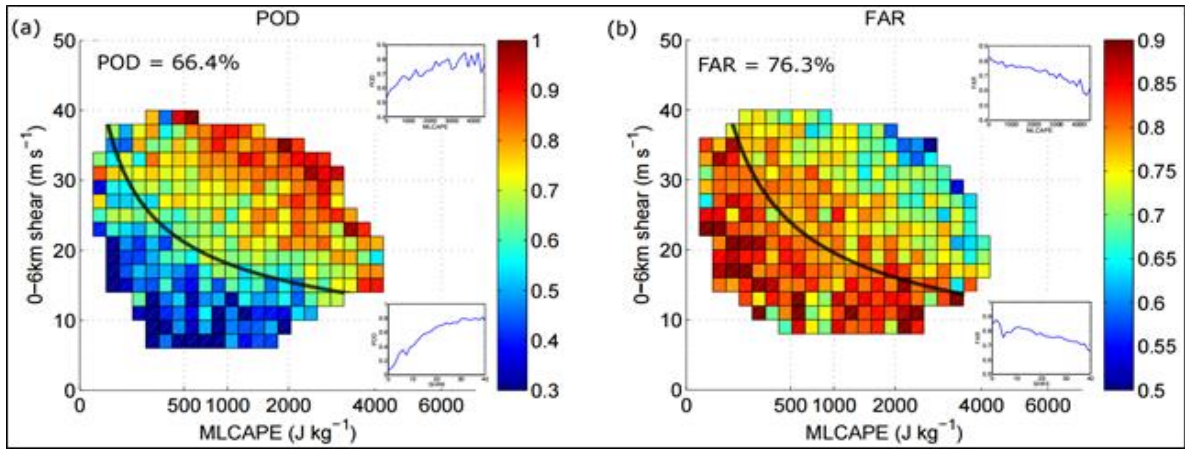
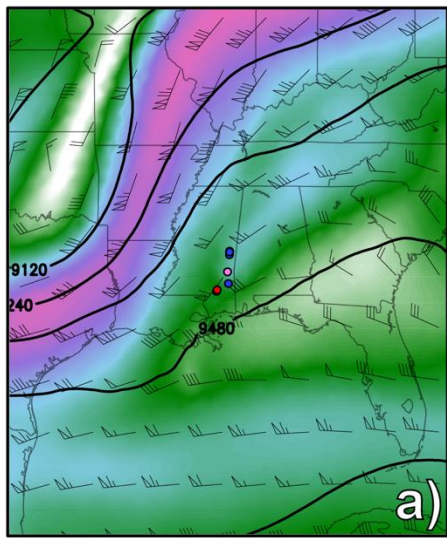


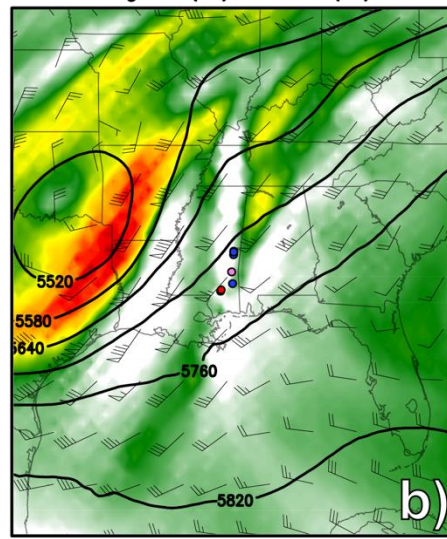
Figure 1.6. (From Anderson-Frey et al. 2016) POD (left) and FAR (right) of tornado warnings binned by environment, 2003-2015.

300 hPa winds (kt) and heights (m)



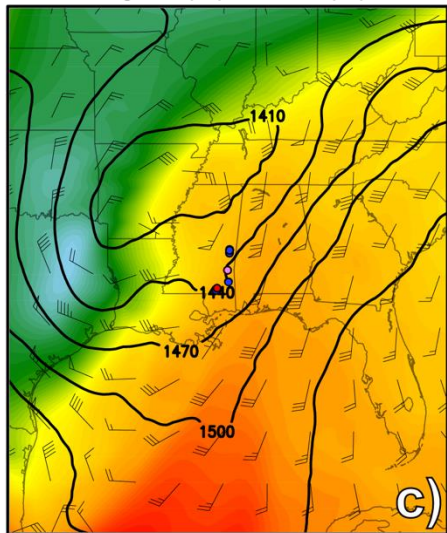
300 hPa winds (kt)

500 hPa abs vort (10^{-5} s^{-1}), heights (m), winds (kt)



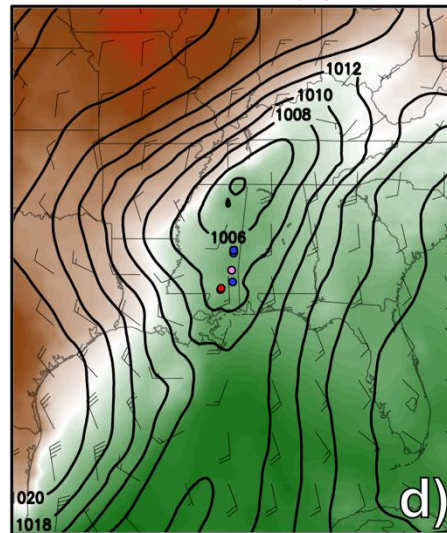
500 hPa abs vort (10^{-5} s^{-1})

850 hPa temperature ($^{\circ}\text{C}$), heights (m), winds (kt)



850 hPa temperature ($^{\circ}\text{C}$)

PMSL (hPa), 2-m dew point ($^{\circ}\text{C}$), 10-m winds (kt)



2-m dew point ($^{\circ}\text{C}$)

Figure 1.7. Example of a higher-end HSLC event. NARR fields, as follows, are from 0600 UTC 4 March 2008.

Panels show a) 300 hPa isotachs (shaded, kt), geopotential heights (black contours, every 120 m), and wind barbs (kt); b) 500 hPa absolute vorticity (shaded, 10^{-5} s^{-1}), geopotential heights (black contours, every 60 m), and wind barbs (kt); c) 850 hPa temperatures (shaded, $^{\circ}\text{C}$), geopotential heights (black contours, every 30 m), and wind barbs (kt); d) 2-m dew point (shaded, $^{\circ}\text{C}$), mean sea-level pressure (PMSL, every 2 hPa), and 10-m wind barbs (kt). Filled circles represent locations of HSLC significant tornadoes (EF2 or greater, pink), EF1 tornadoes (red), and significant winds (65 kt or greater, blue) from 0430-0730 UTC 4 March 2008.

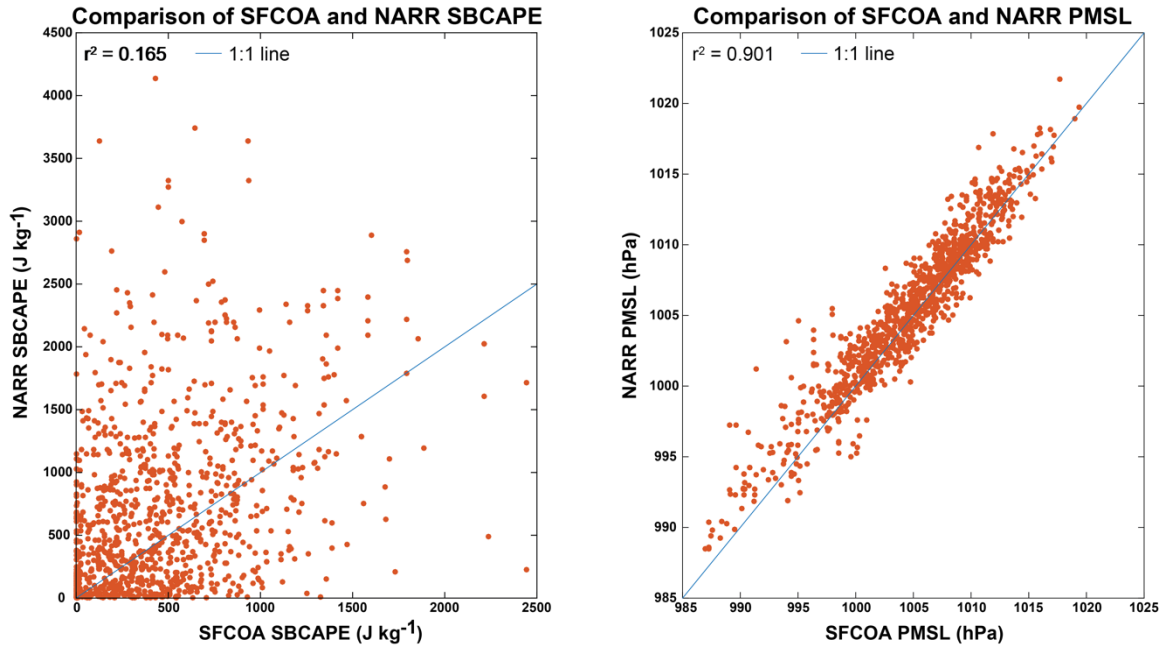
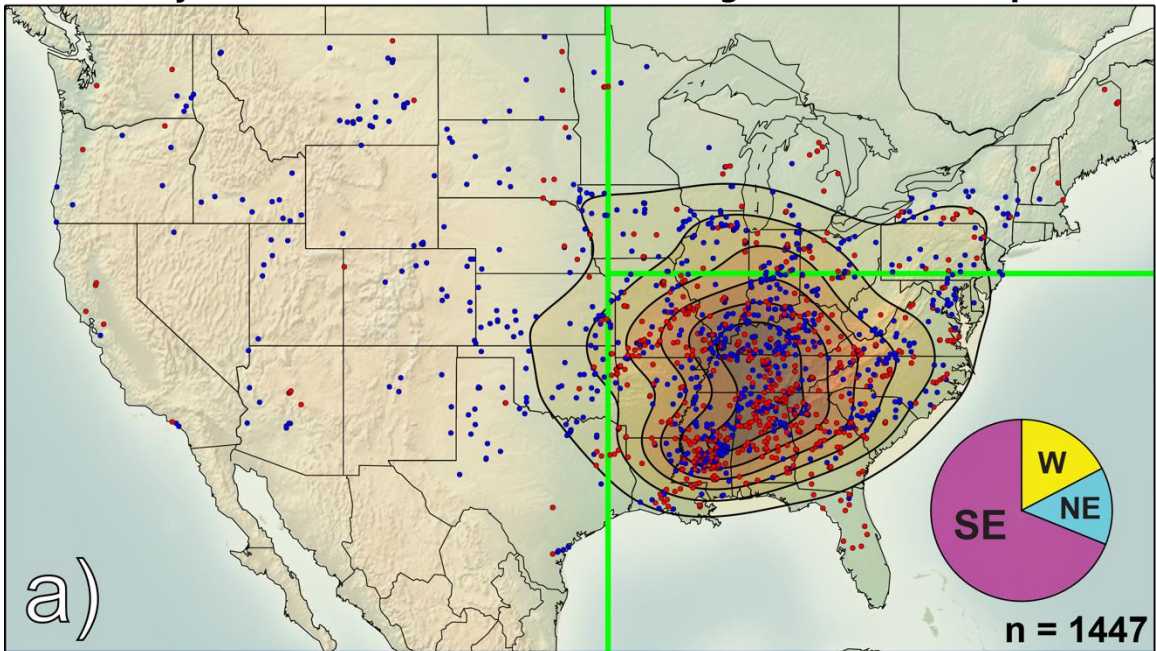


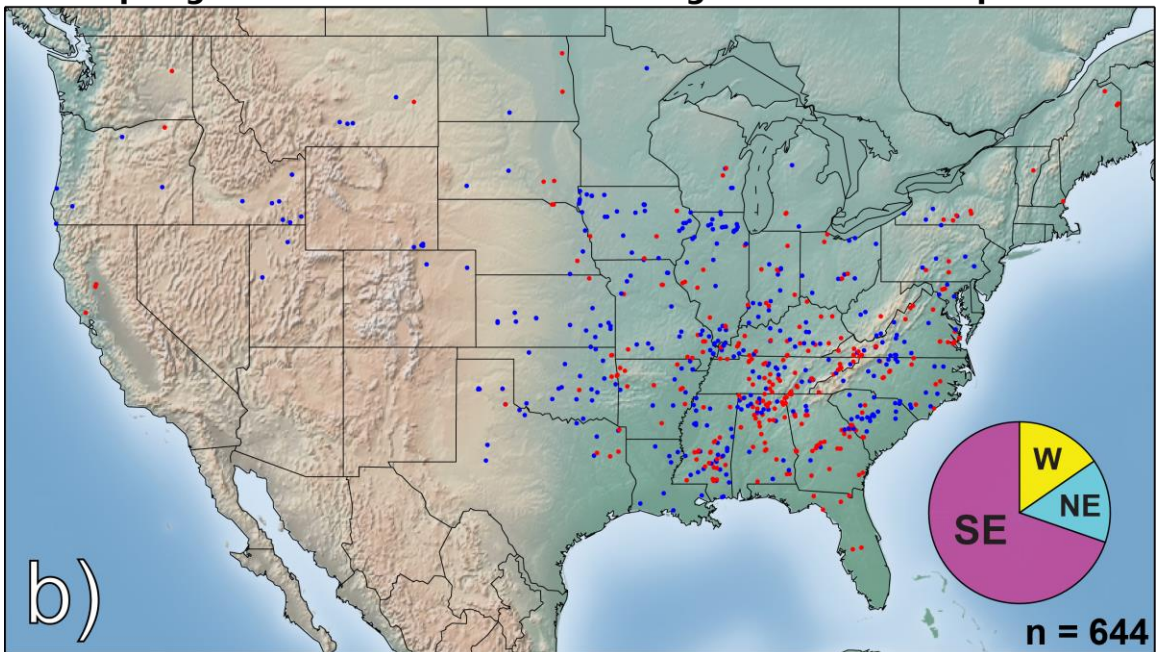
Figure 1.8. Comparisons of (left) SBCAPE and (right) mean sea-level pressure (PMSL) for SFCOA and NARR. SFCOA grid point used is that associated with the maximum 2-m θ_e in a 3 by 3 grid point box (approximately 80 km by 80 km) surrounding each respective Southeast HSLC EF1 or stronger tornado report and significant wind report. NARR grid point represents the maximum value in an approximate 160 km by 160 km box surrounding each report. Correlation is represented by r^2 values in the upper left of each panel. A 1:1 line (i.e., $y = x$) is included for ease of comparison. Note that significant hail reports were not included here, as discussed in Section 2a.

Figure 1.9. a) All EF1 or greater tornado reports (red dots) and significant wind reports (blue dots) occurring in HSLC environments from 2006-2011. Shading represents a kernel density estimation of significant severe reports; darker colors correspond to a higher density of reports (probability density function estimate contoured every 0.001); b) as in a), except only for springtime reports and excluding the kernel density estimation; c) as in b), but for summertime reports; d) as in b), but for autumn reports; e) as in b), but for wintertime reports. Insets show pie charts for percentage of reports that fall in the three subjectively-defined regions, as demarcated by the green lines in a): Southeast (SE), Northeast (NE), and West (W). Counts are shown in the bottom right of each panel.

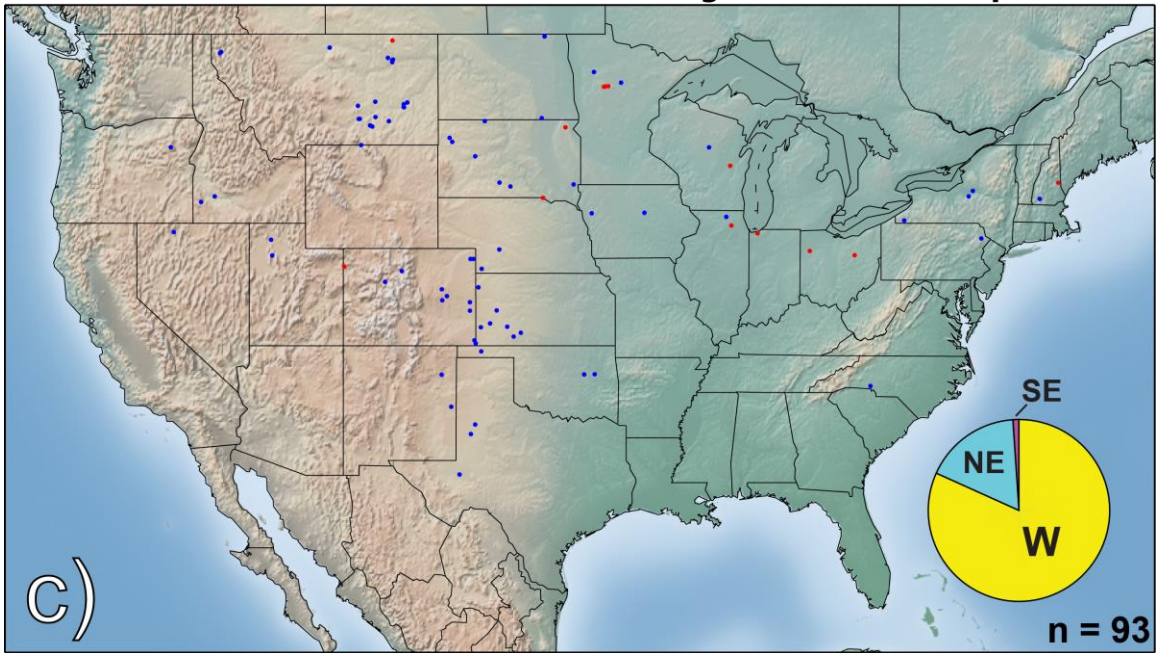
Density of HSLC EF1+ Tornadoes and Significant Wind Reports



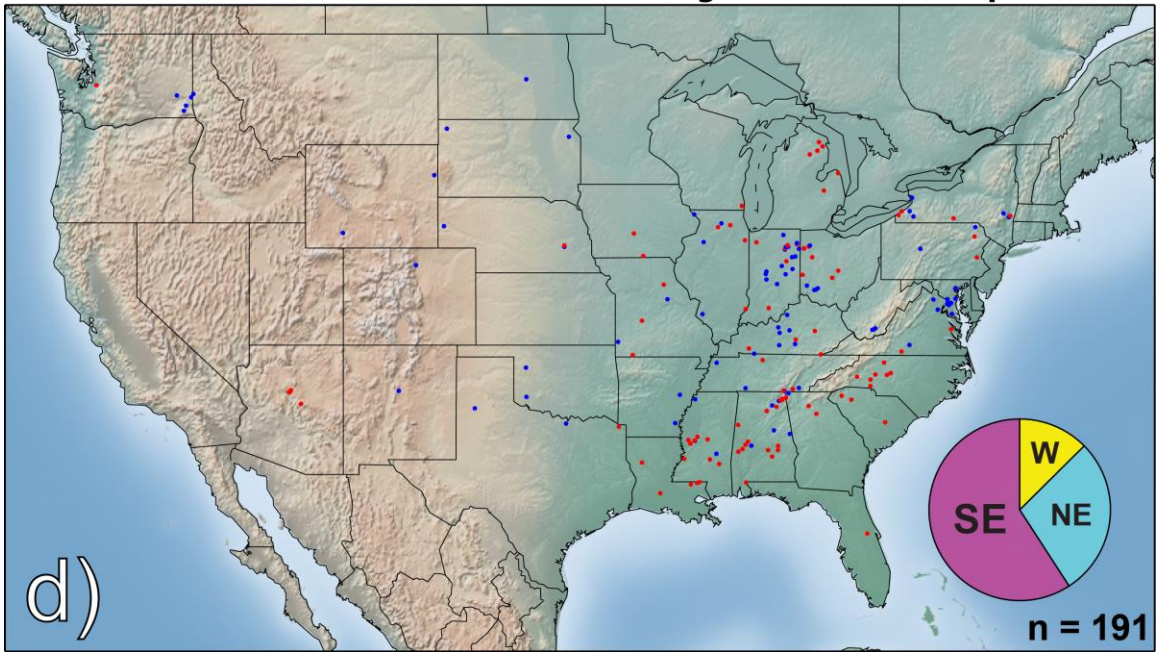
Spring HSLC EF1+ Tornadoes and Significant Wind Reports



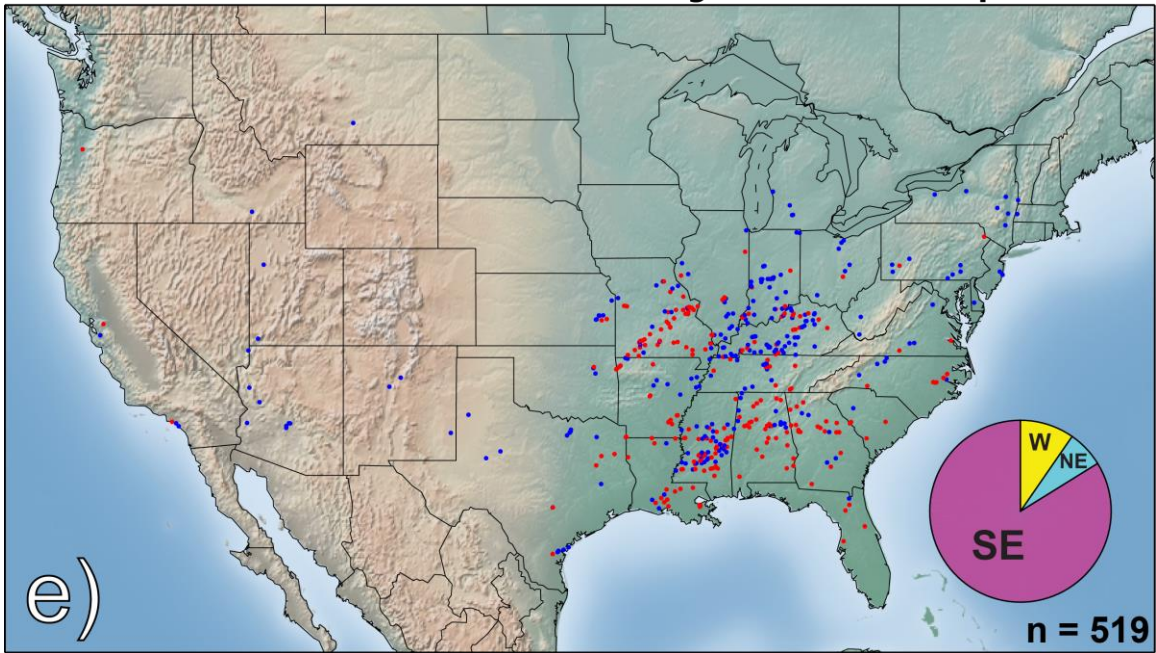
Summer HSLC EF1+ Tornadoes and Significant Wind Reports



Autumn HSLC EF1+ Tornadoes and Significant Wind Reports



Winter HSLC EF1+ Tornadoes and Significant Wind Reports



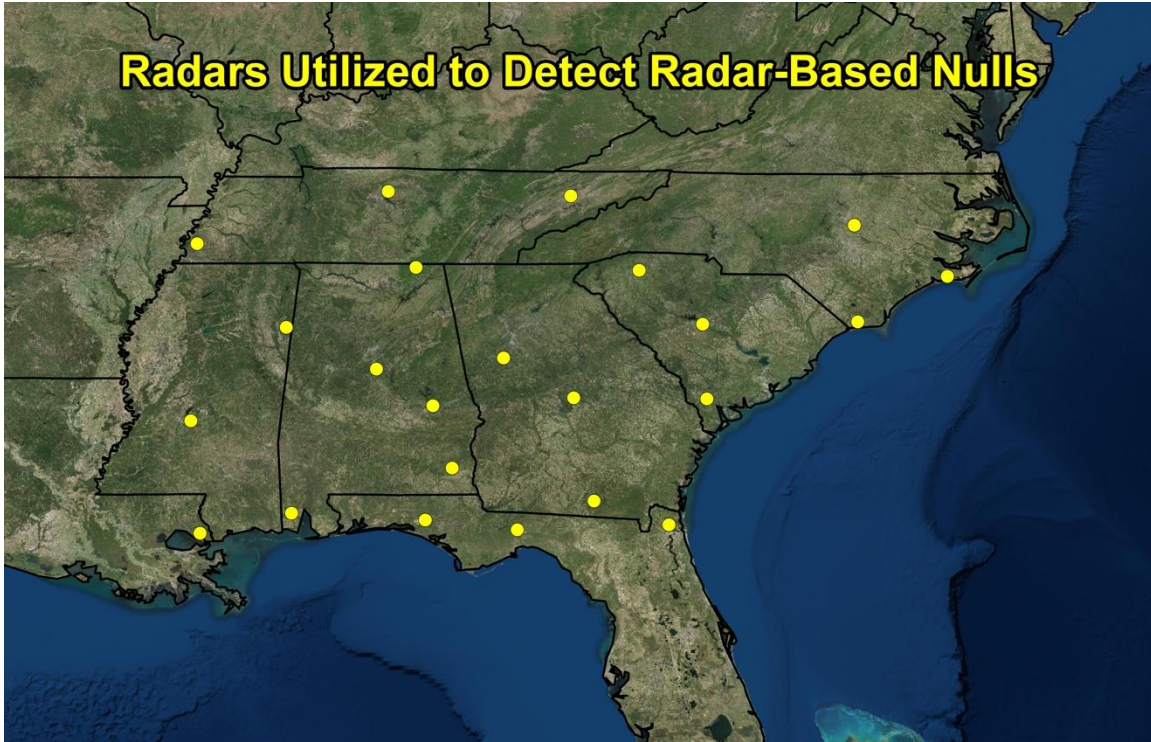


Figure 1.10. Map showing locations of NWS WSR-88Ds used in constructing the radar-based nulls dataset (yellow dots).

Fraction of EF1+ tornadoes and significant wind reports in HSLC environments

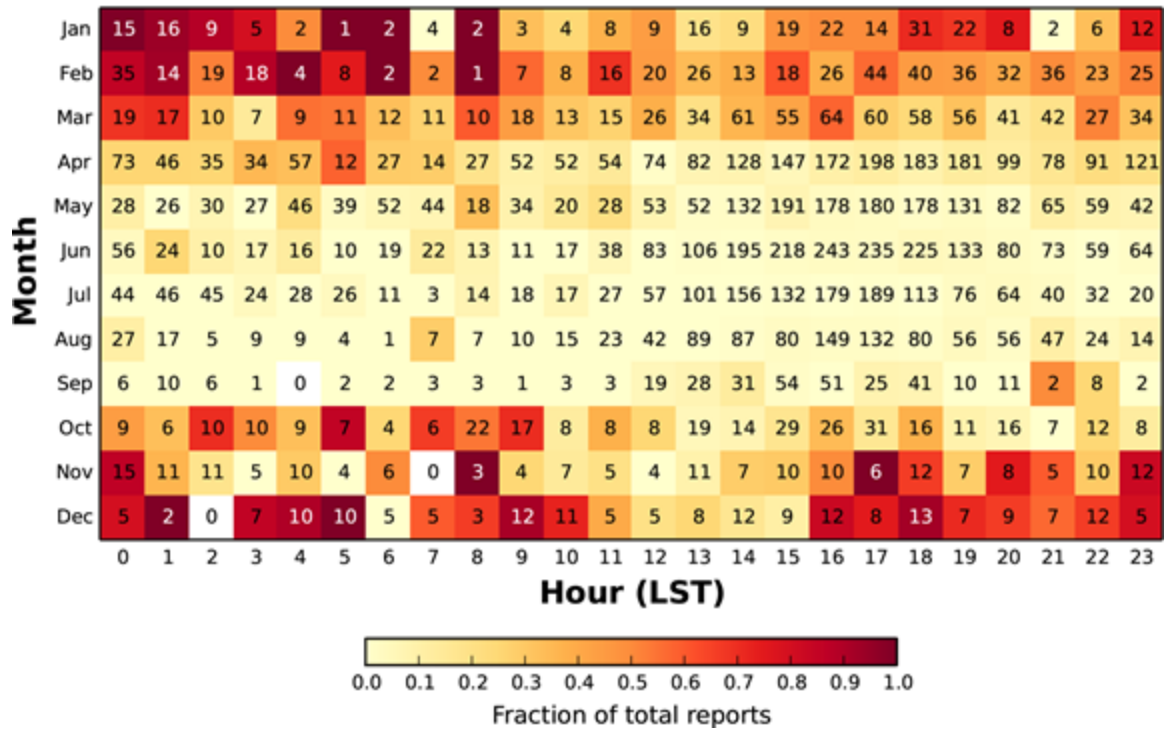


Figure 1.11. Fraction of EF1 or greater tornadoes and significant wind reports from 2006-2011 that occurred in HSLC environments by month and hour (shaded). Total number of EF1 or greater tornadoes and significant wind reports for the given hour/month are listed in each box.

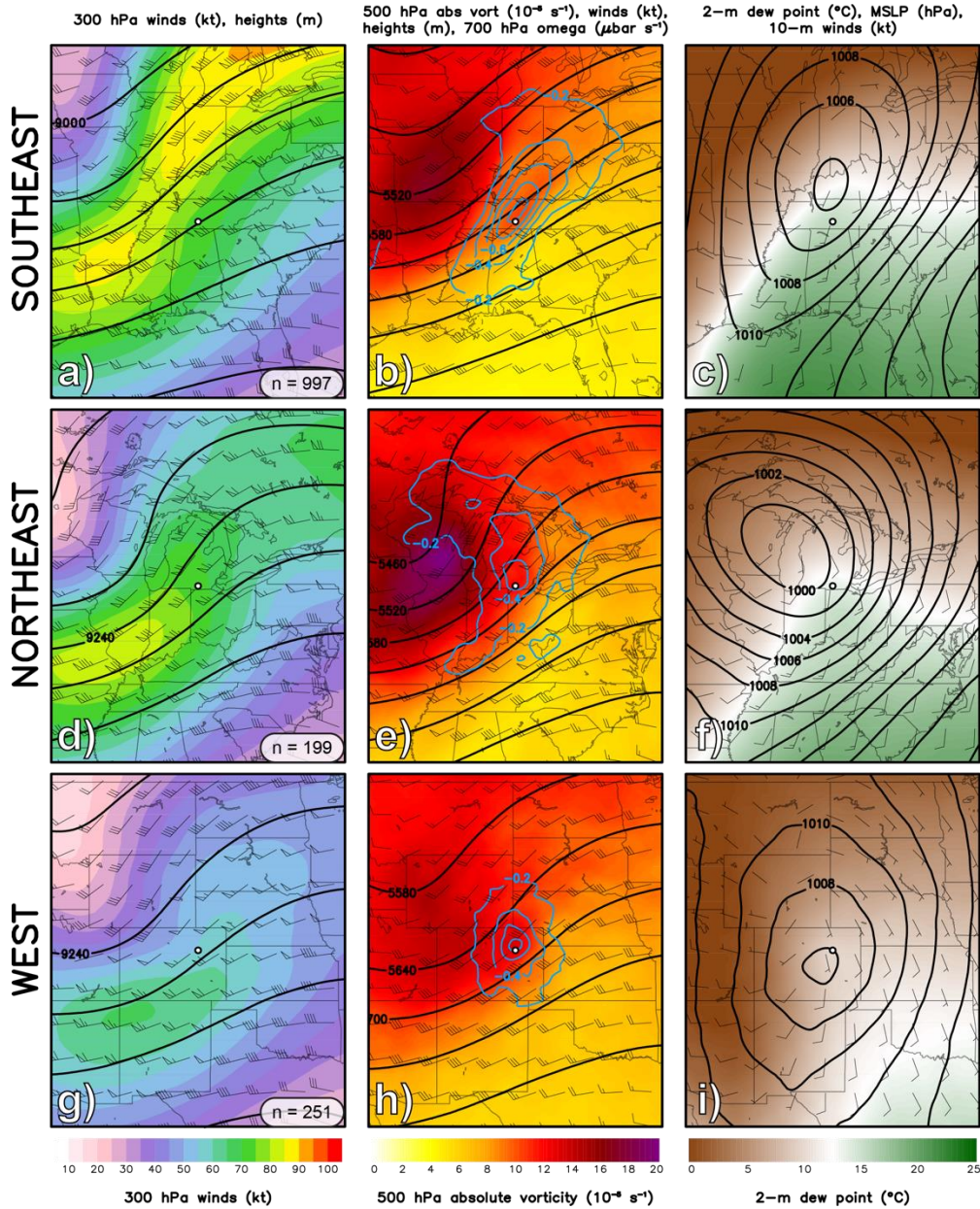


Figure 1.12. Regional comparisons of (panels a, d, and g) 300 hPa winds (shaded, kt), wind barbs (kt), and geopotential heights (black contours, every 120 m); (panels b, e, and h) 500 hPa absolute vorticity (shaded, 10^{-5} s^{-1}), wind barbs (kt), geopotential heights (black contours, every 60 m), and 700 hPa omega (blue contours, $\mu\text{bar s}^{-1}$); (panels c, f, and i) 2-m dew point (shaded, $^{\circ}\text{C}$), mean sea level pressure (black contours, every 2 hPa), and 10-m wind barbs (kt). Plots for the southeast region are in panels a-c), northeast region are in panels d-f), and western region are in panels g-i). Maps are shown for a reference scale, with the white dot depicting the event-relative composite center point and the average latitude and longitude of each subset. The number of times in each composite is shown in a), d), and g) at bottom right.

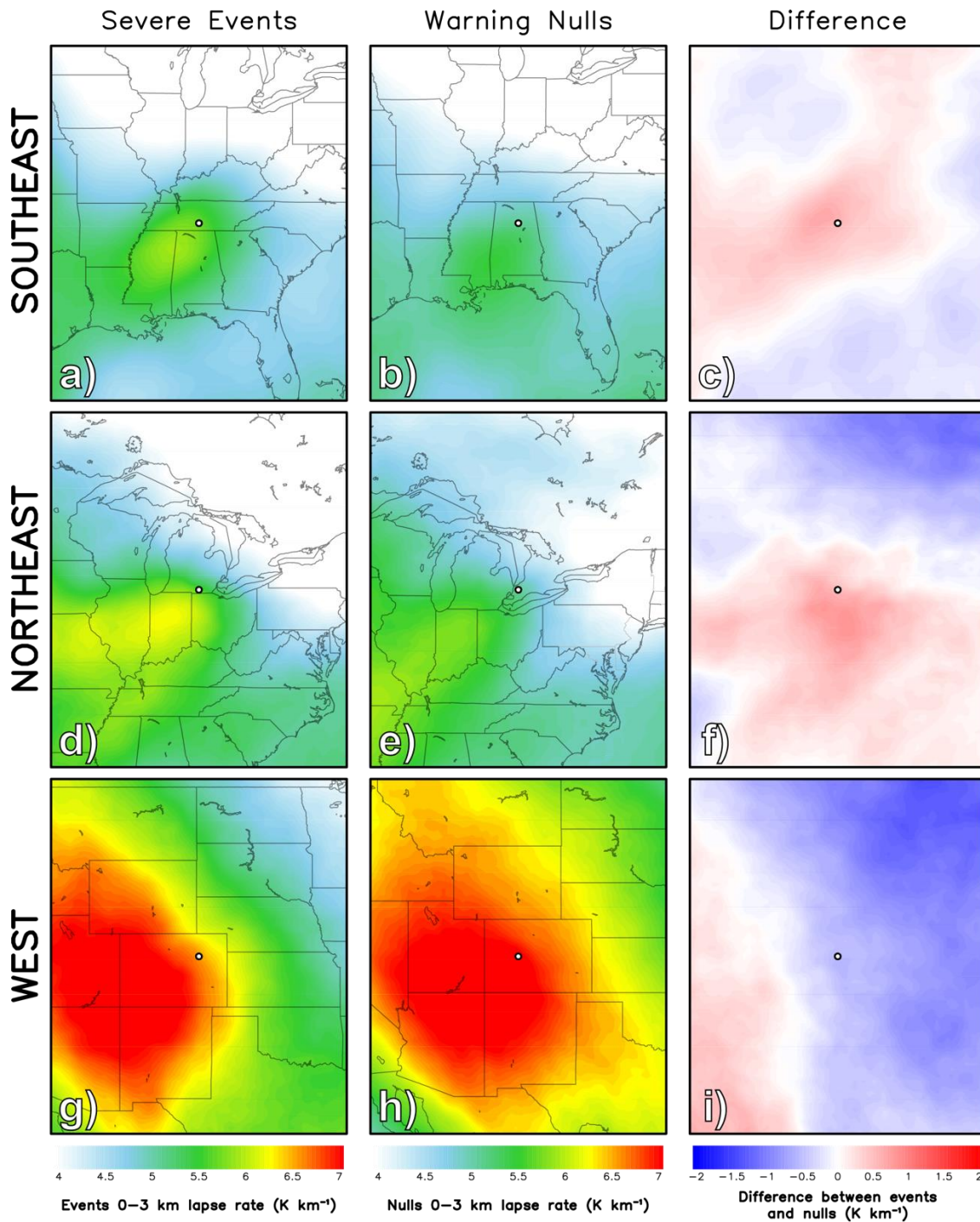


Figure 1.13. Regional comparisons of 0-3 km lapse rates ($K km^{-1}$) for (panels a, d, and g) severe events, defined as EF1 or greater tornadoes and significant wind reports (wind gusts ≥ 65 kt), (panels b, e, and h) warning nulls, and (panels c, f, and i) the difference field between events and nulls. All else is as in Fig. 1.12.

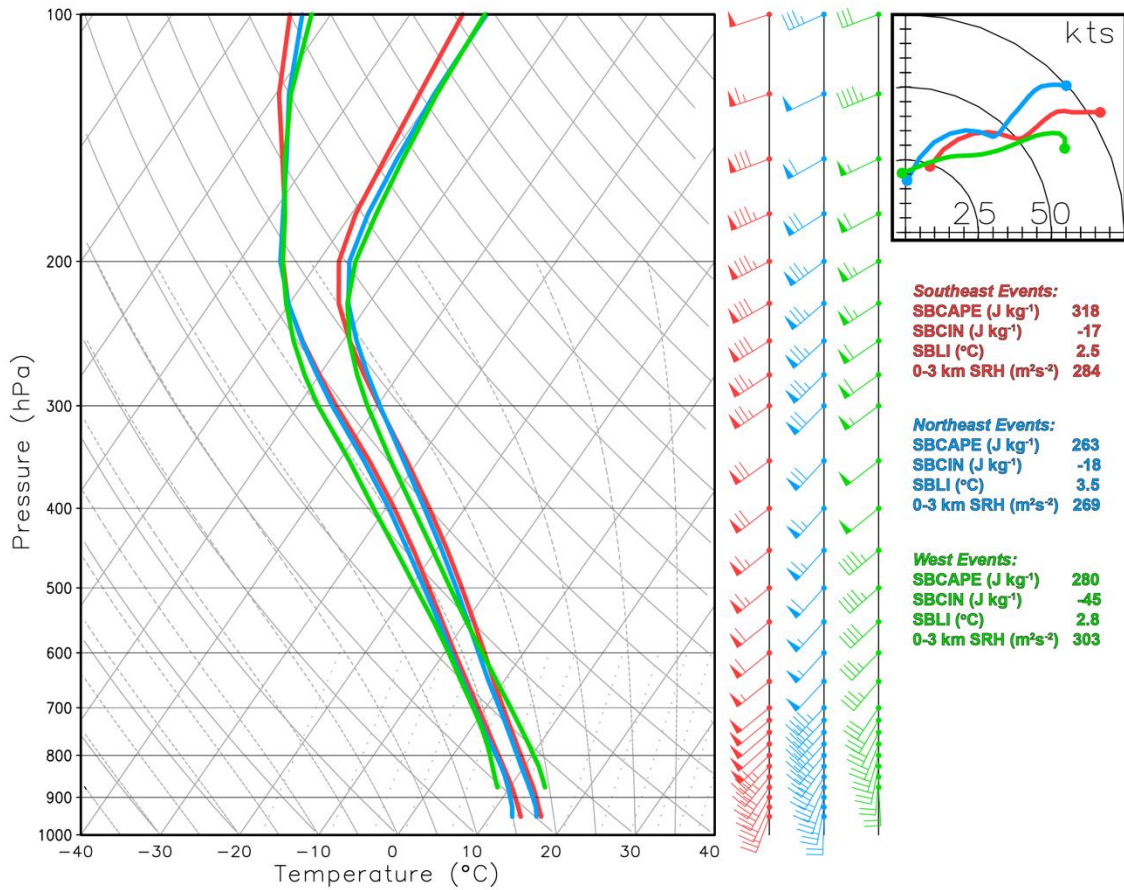


Figure 1.14. Regional composite sounding comparisons. Data are color-coded by region, with southeast thermodynamic and kinematic profiles and derived indices in red, northeast profiles and indices in blue, and western profiles and indices in green. Vertical pressure levels where 25% or more of the data were below ground are set to missing. Note that only the upper right quadrant of the hodograph is shown to highlight differences between regions. The plotted hodograph extends from the surface to 300 hPa. Storm-relative helicity (SRH) is calculated over the surface-to-3-km layer.

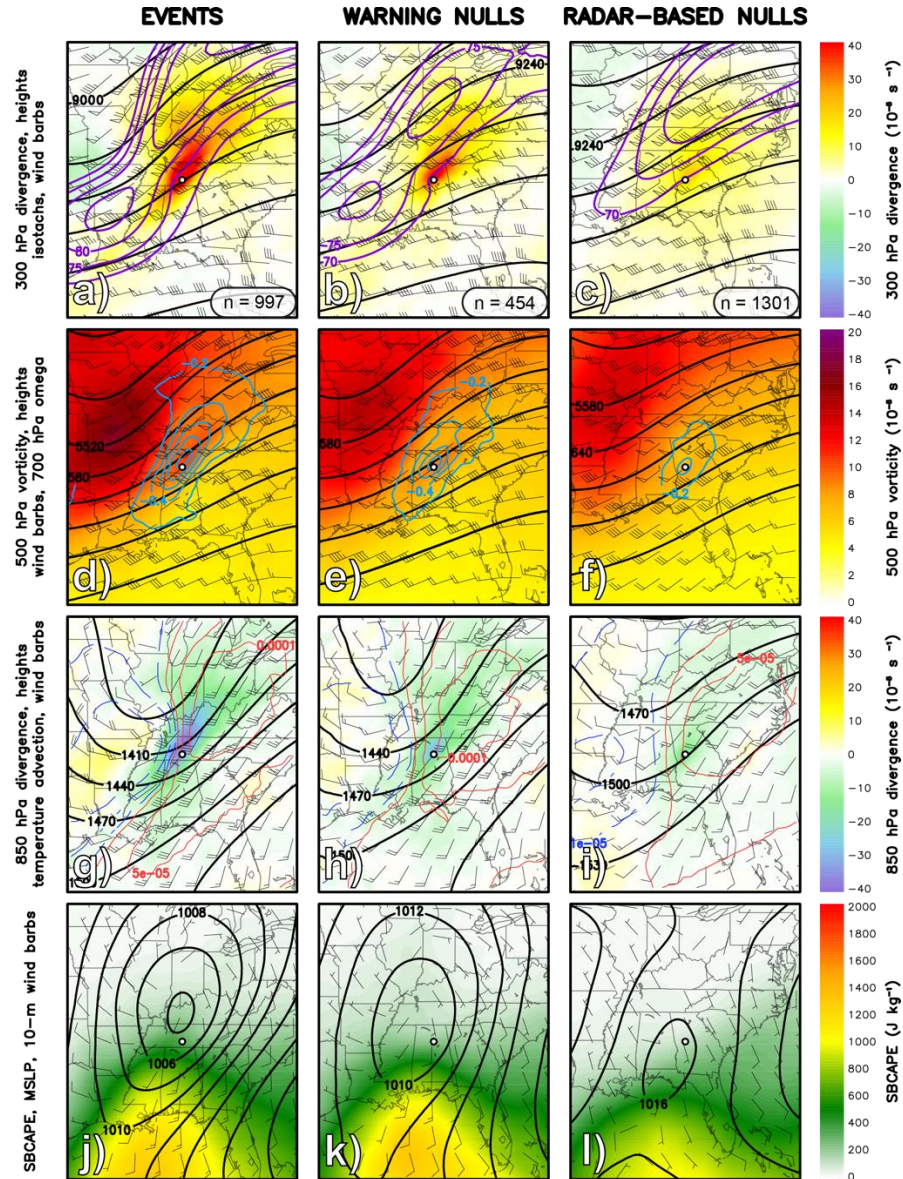


Figure 1.15. Mean (panels a-c) 300 hPa divergence (shaded, 10^{-5} s^{-1}), geopotential heights (black contours, every 120 m), isotachs (purple contours, every 5 kt), and wind barbs (kt); (panels d-f) 500 hPa absolute vorticity (shaded, 10^{-6} s^{-1}), geopotential heights (black contours, every 60 m), wind barbs (kt), and 700 hPa omega (blue contours, $\mu\text{bar s}^{-1}$); (panels g-i) 850 hPa divergence (shaded, 10^{-5} s^{-1}), geopotential heights (black contours, every 30 m), temperature advection (blue and red contours, K s^{-1}), and wind barbs (kt); (panels j-l) SBCAPE (shaded, J kg^{-1}), (black contours, every 2 hPa), and 10-m wind barbs for southeast (panels a, d, g, j) EF1 or greater tornadoes and significant wind reports, (panels b, e, h, k) warning nulls, and (panels c, f, i, l) radar-based nulls. Maps are shown for a reference scale, with the white dot depicting the event-relative composite center point and the average latitude and longitude of each subset. The number of times in each composite is shown in the top row at bottom right.

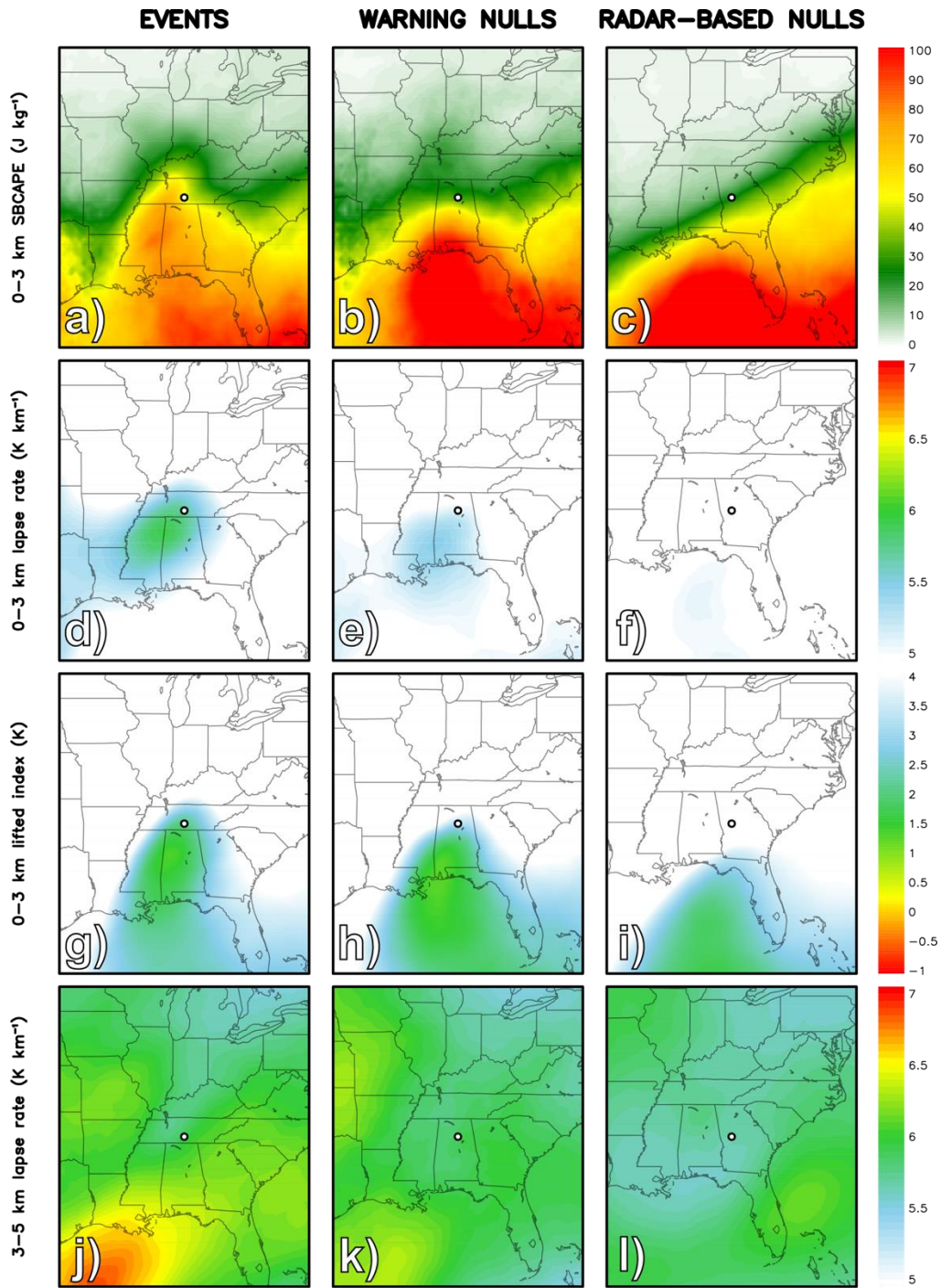


Figure 1.16. Mean of (panels a-c) 0-3 km SBCAPE (J kg^{-1}); (panels d-f) 0-3 km lapse rate (K km^{-1}); (panels g-i) 3 km surface-based lifted index (K); and (panels j-l) 3-5 km lapse rate (K km^{-1}) for southeast (panels a, d, g, j) EF1 or greater tornadoes and significant wind reports, (panels b, e, h, k) warning nulls, and (panels c, f, i, l) radar-based nulls. All else is as in Fig. 1.15.

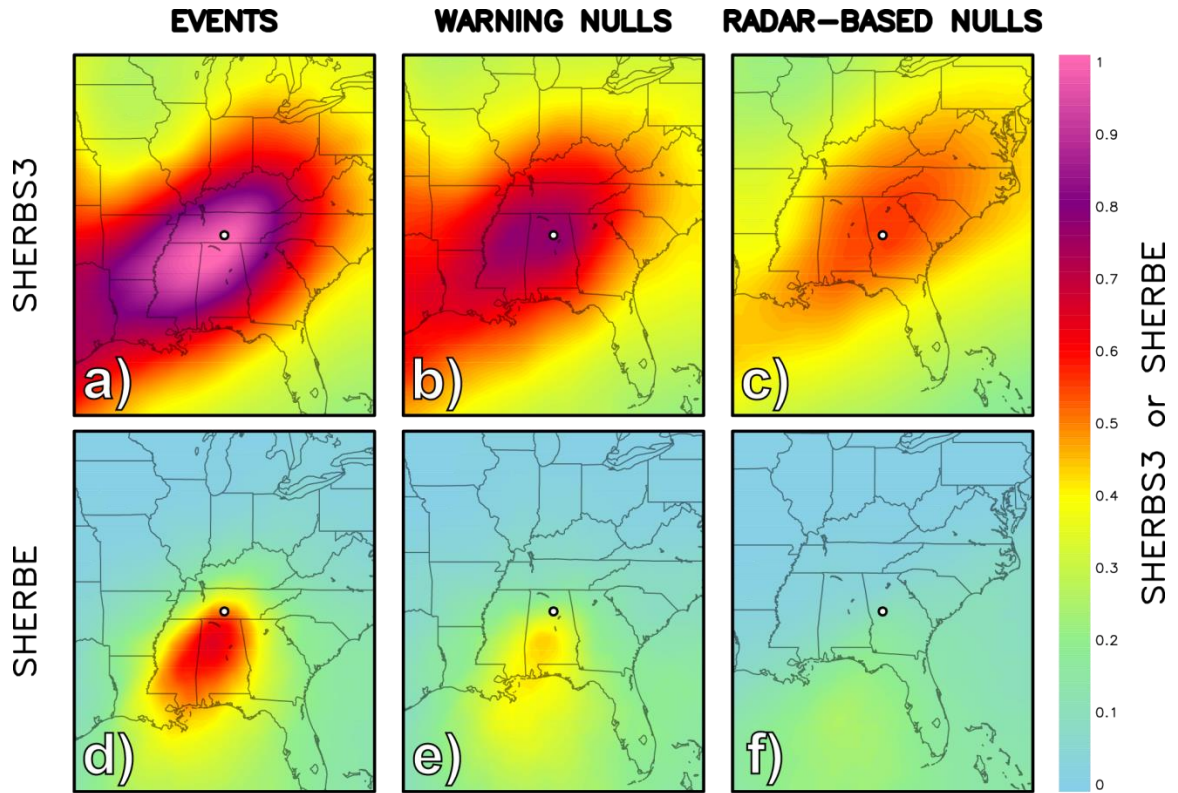


Figure 1.17. Mean (panels a-c) SHERBS3 and (panels d-f) SHERBE for Southeast HSLC (panels a, d) events, (panels b, e) warning nulls, and (panels c, f) radar-based nulls. Note that the 3-5 km midlevel lapse rate is used here rather than the 700-500 hPa lapse rate, and this replacement is recommended for all further use. All else is as in Fig. 1.15.

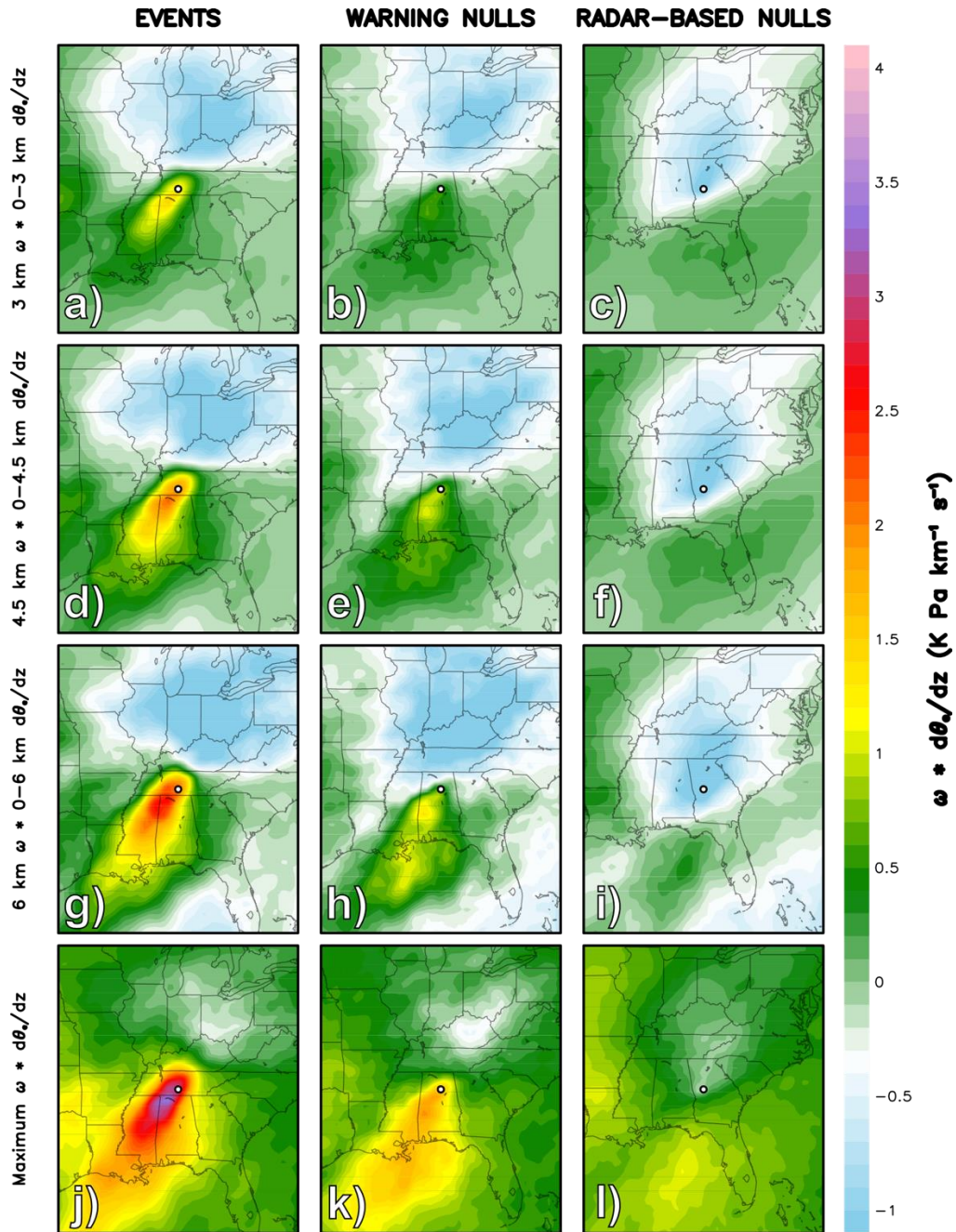


Figure 1.18. Mean of (panels a-c) product of 3 km ω and 0-3 km $d\theta_e/dz$ ($\text{K Pa km}^{-1} \text{s}^{-1}$); (panels d-f) product of 4.5 km ω and 0-4.5 km $d\theta_e/dz$ ($\text{K Pa km}^{-1} \text{s}^{-1}$); (panels g-i) product of 6 km ω and 0-6 km $d\theta_e/dz$ ($\text{K Pa km}^{-1} \text{s}^{-1}$); and (panels j-l) the maximum ω and $d\theta_e/dz$ product from 0-2 km through 0-6 km ($\text{K Pa km}^{-1} \text{s}^{-1}$) for southeast (panels a, d, g, j) EF1 or greater tornadoes and significant wind reports, (panels b, e, h, k) warning nulls, and (panels c, f, i, l) radar-based nulls. All else is as in Fig. 1.15.

0-3 km lapse rate (shaded, $K km^{-1}$) and bulk shear vectors (kt)

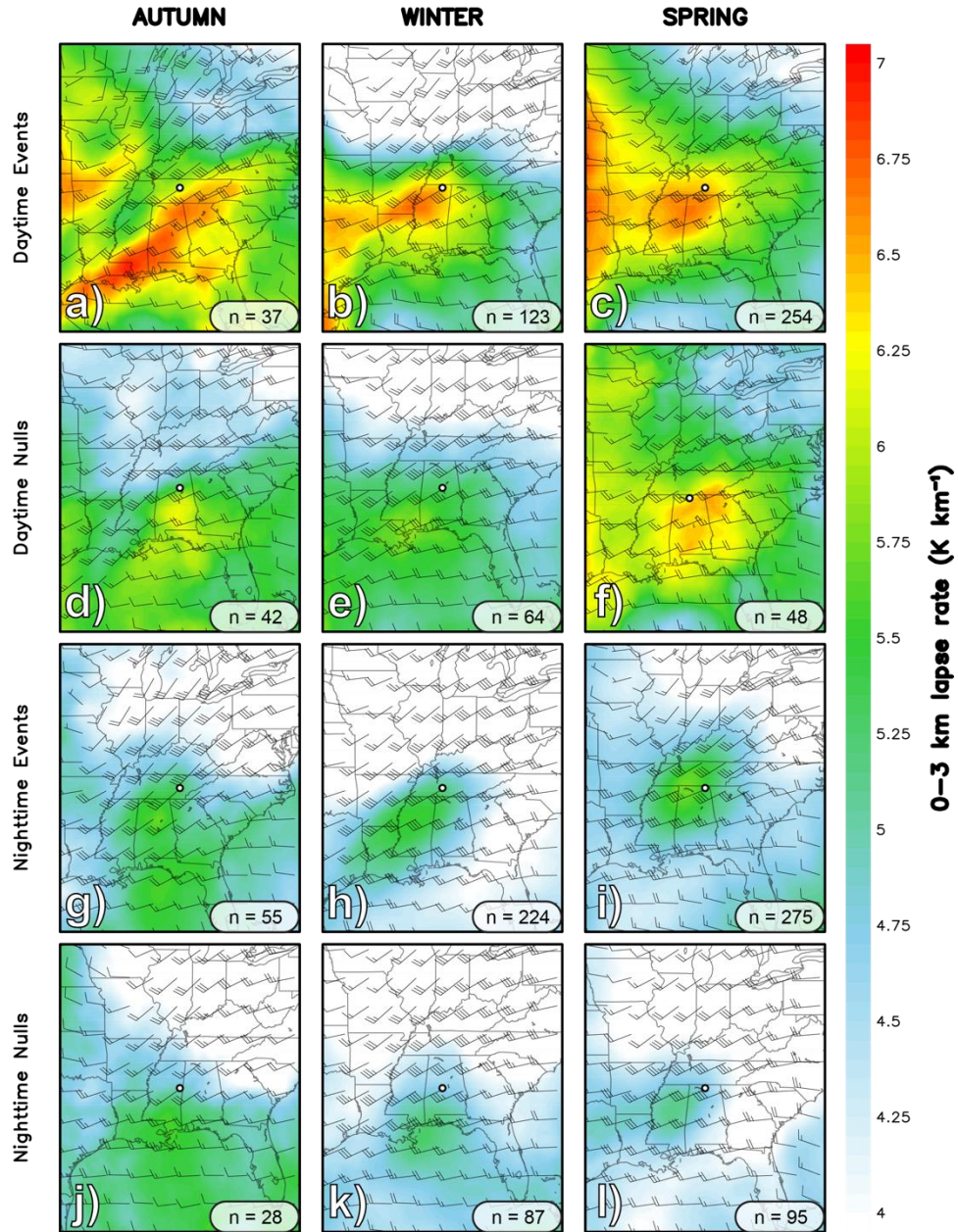


Figure 1.19. 0-3 km lapse rate (shaded, $K km^{-1}$) and 0-3 km bulk shear vector (barbs, kt) for (panels a, d, g, j) autumn, (panels b, e, h, k) winter, and (panels c, f, i, l) spring (panels a-c) daytime events, as defined in the text, (panels d-f) daytime warning nulls, (panels g-i) nighttime events, and (panels j-l) nighttime warning nulls within the southeast subset. Counts for the respective subset are provided in the bottom right of each panel.

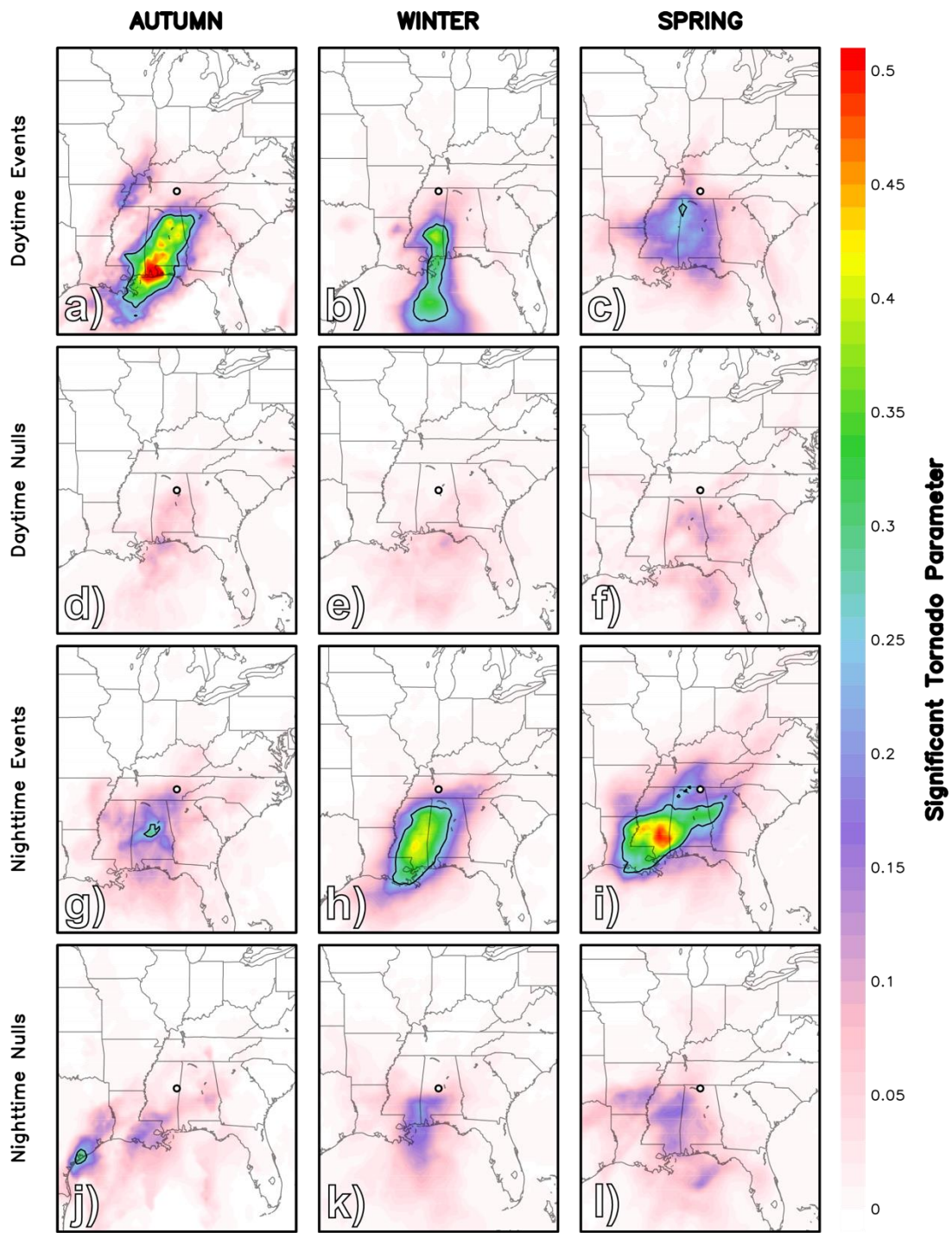


Figure 1.20. As in Fig. 1.19, but showing the significant tornado parameter (STP). Black contour denotes an STP value of 0.25.

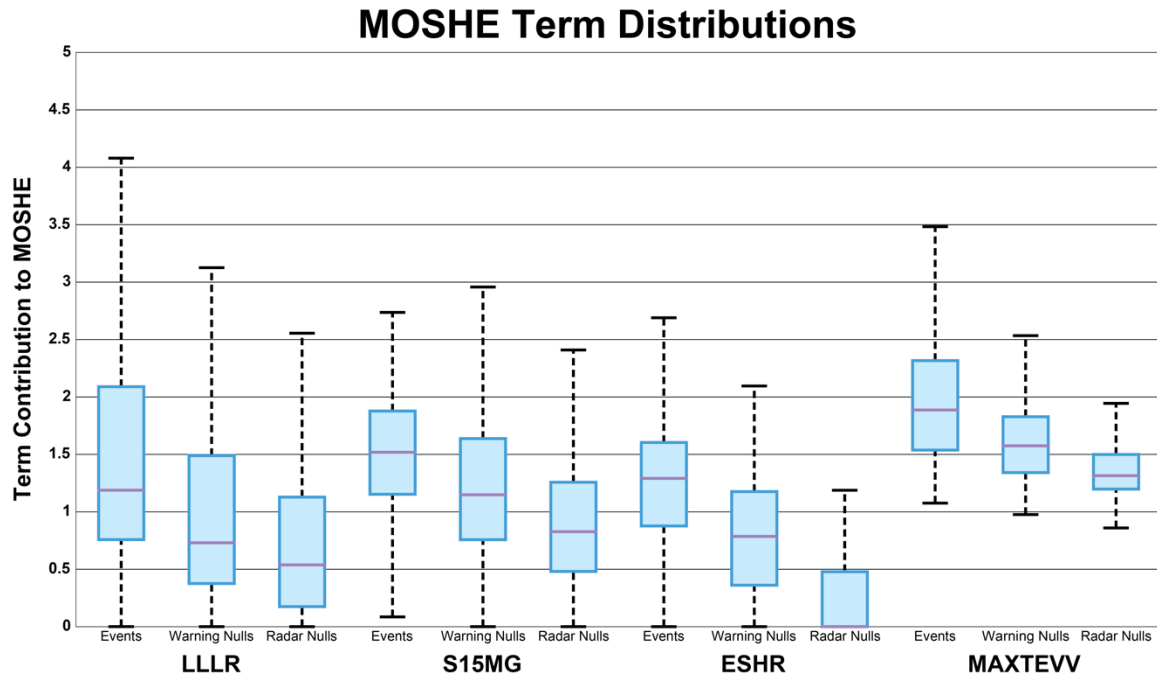


Figure 1.21. Box-and-whisker plots for maximum (within a 160 km by 160 km box surrounding the respective report or null) LLLR, S15MG, ESHR, and MAXTEVV term contributions within the MOSHE (as defined in Equation 1.3; e.g., $[\{\text{LLLRR}-4\}^2]/4 \text{ K}^2 \text{ km}^{-2}$) across Southeast events, warning nulls, and radar-based nulls. Purple line shows the median value, while the blue box encompasses the 25th (q_1) to 75th (q_3) percentile values. Black whiskers extend to values in the range $[q_1 - 1.5*(q_3-q_1), q_3 + 1.5*(q_3-q_1)]$. Outliers are excluded.

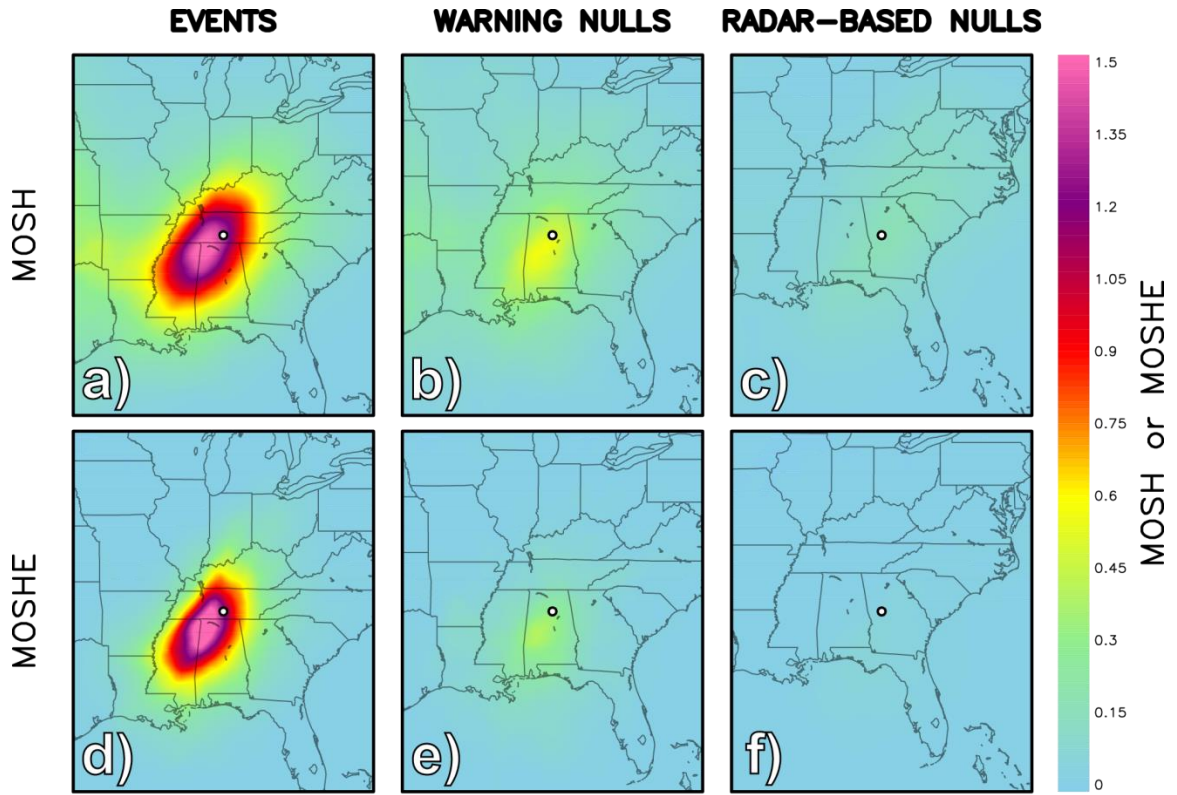


Figure 1.22. Mean (panels a-c) modified SHERB (MOSH) and (panels d-f) effective version of MOSH (MOSHE) for Southeast HSLC (panels a, d) events, (panels b, e) warning nulls, and (panels c, f) radar-based nulls. All else is as in Fig. 1.16.

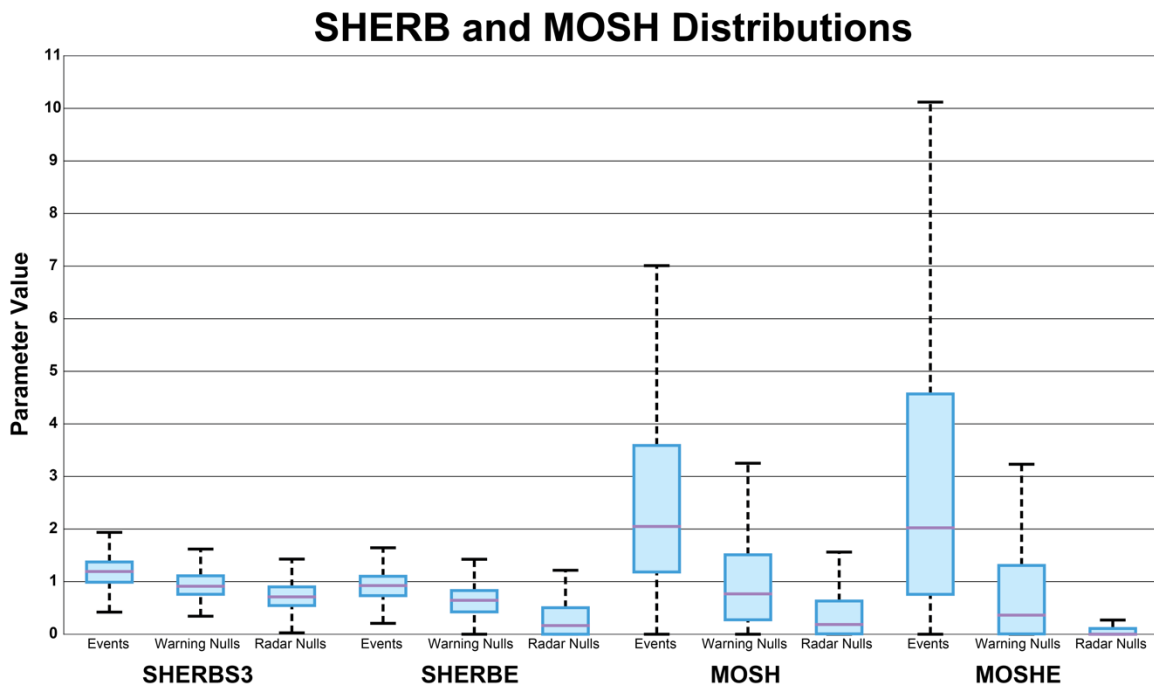


Figure 1.23. As in Fig. 1.21, but for the SHERBS3, SHERBE, MOSH, and MOSHE value distributions.

SHERB and MOSH Distributions, 2012-2014 Dataset

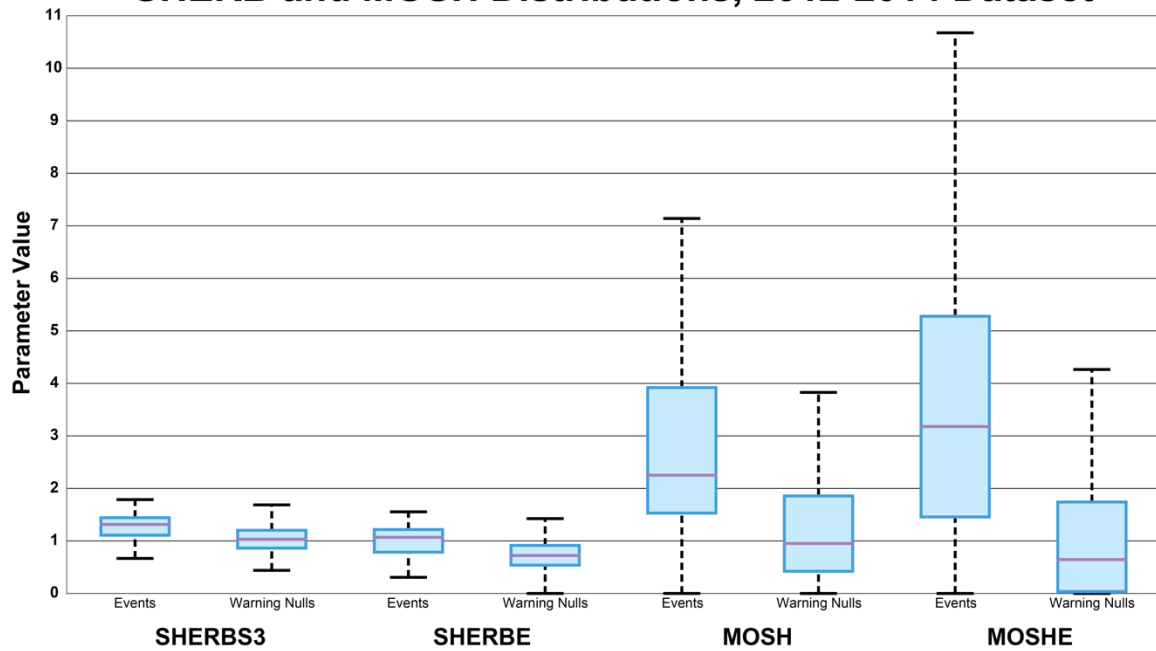


Figure 1.24. As in Fig. 1.23, but for the independent 2012-2014 Southeast dataset.

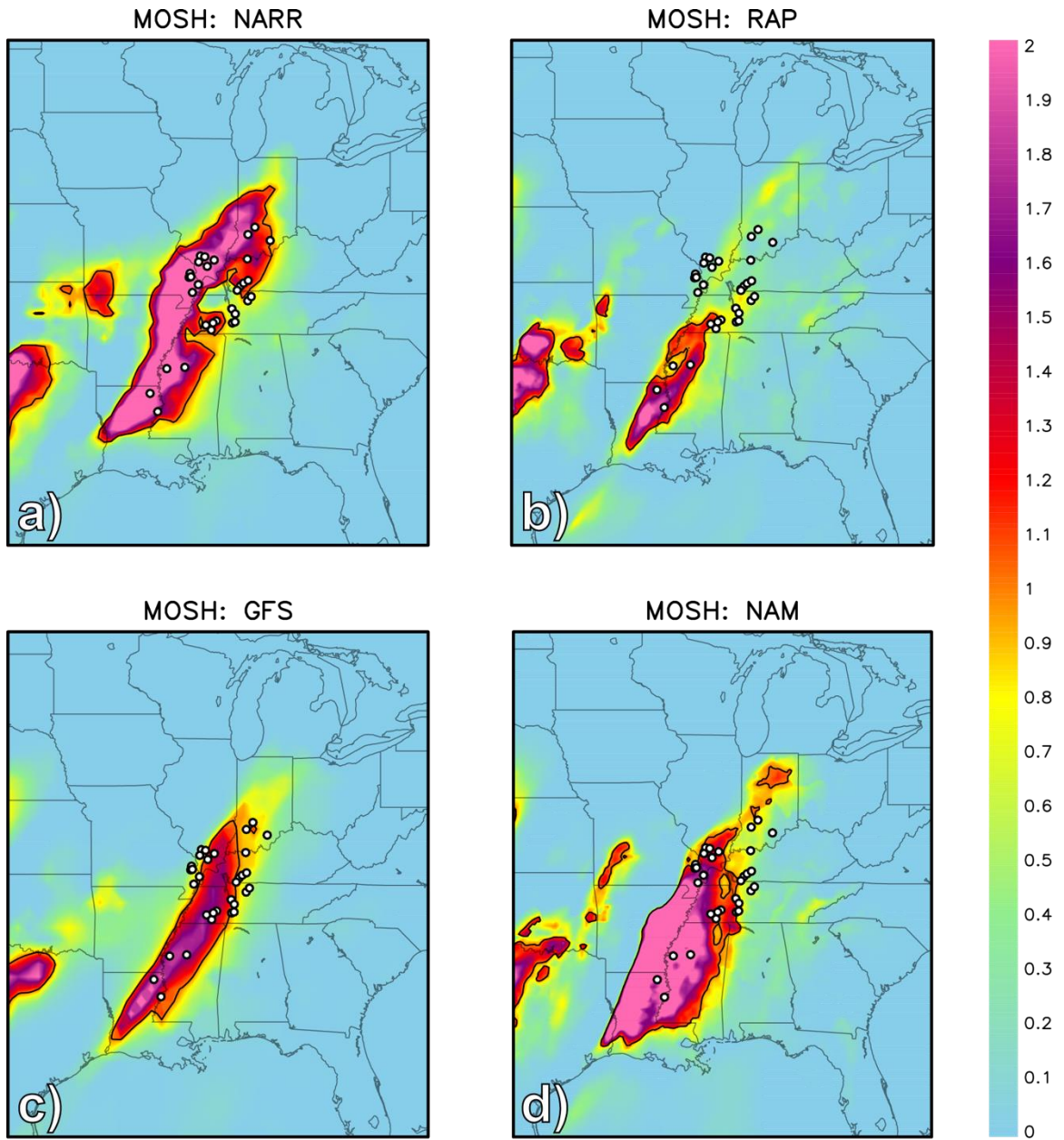


Figure 1.25. a) NARR analysis, b) RAP 6-h forecast, c) GFS 6-h forecast, d) NAM 6-h forecast of the MOSH valid at 0600 UTC 30 January 2013 (models initialized 0000 UTC 30 January 2013). Black contours encompass MOSH values ≥ 1 . Black dots show locations of EF1 or greater tornadoes and significant wind reports in the surrounding 6 h (0300-0900 UTC 30 January 2013).

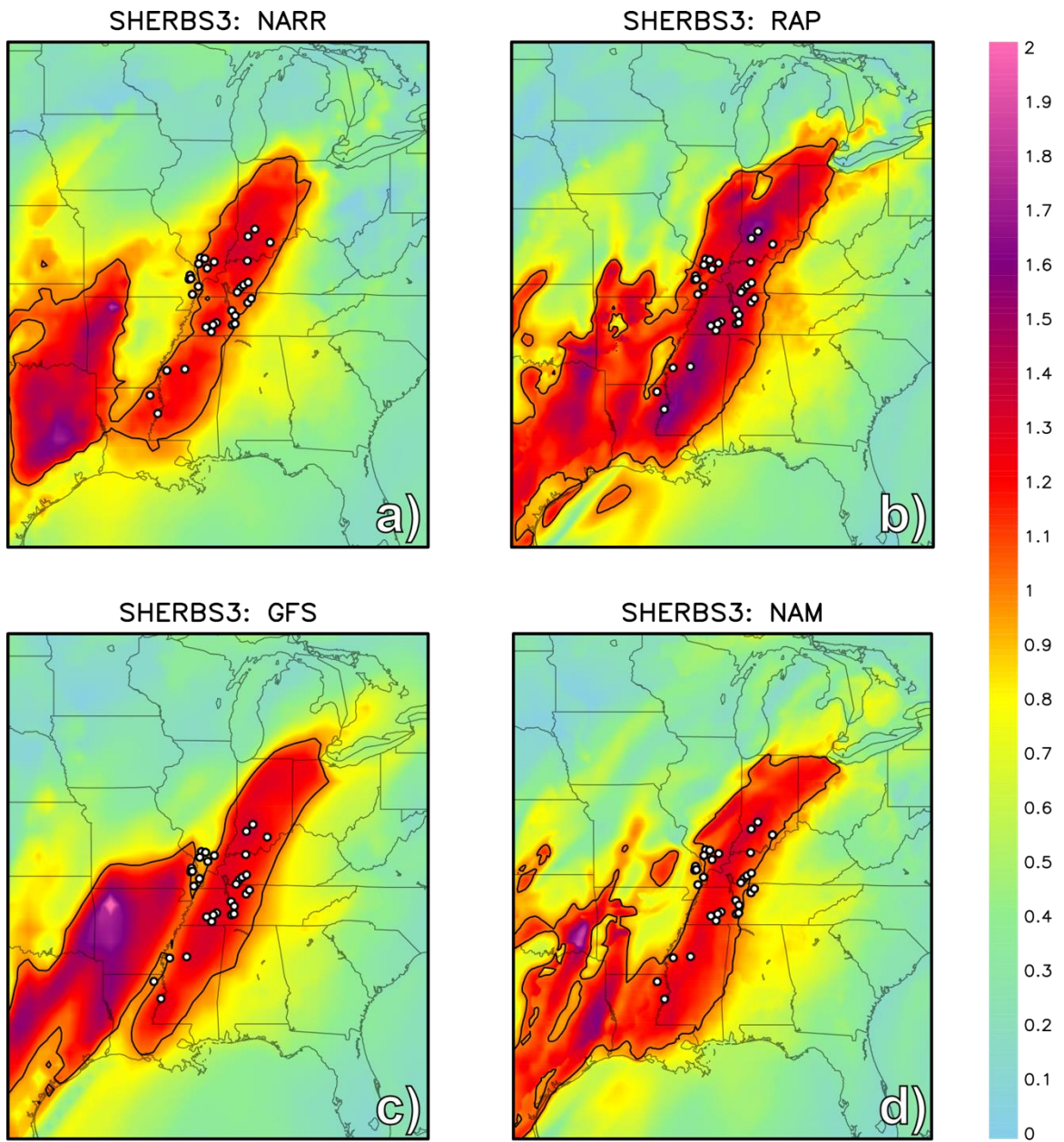


Figure 1.26. As in Fig. 1.25, but for the SHERBS3.

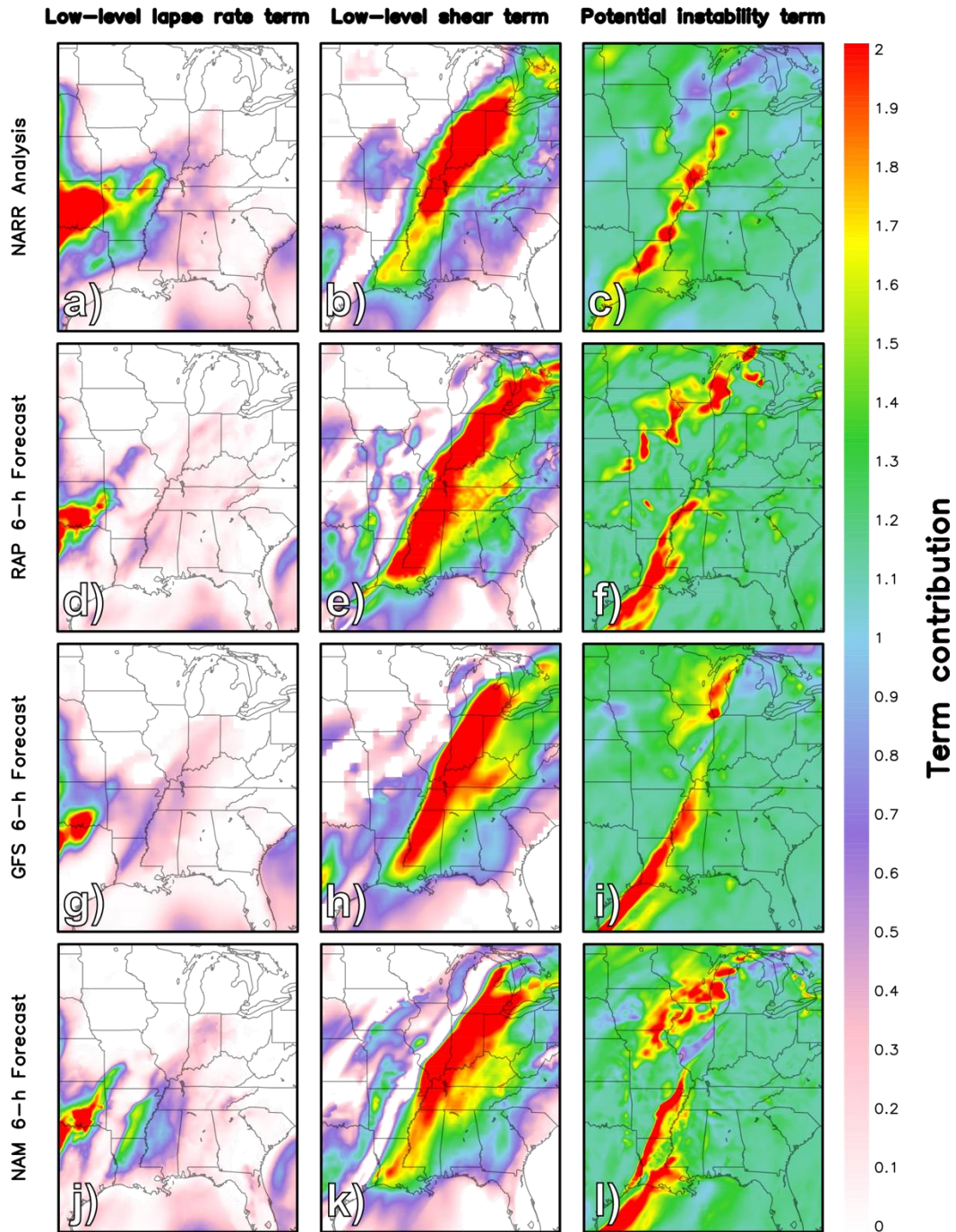


Figure 1.27. Contributions from the (panels a, d, g, j) low-level lapse rate term, (panels b, e, h, k) 0-1.5 km shear vector magnitude term, and (panels c, f, i, l) potential instability term (all as defined in Equation 3) for (panels a-c) NARR analysis valid at 0600 UTC 30 January 2013, (panels d-f) RAP 6-h forecast, (panels g-i) GFS 6-h forecast, and (panels j-l) NAM 6-h forecast, all valid for 0600 UTC 30 January 2013.

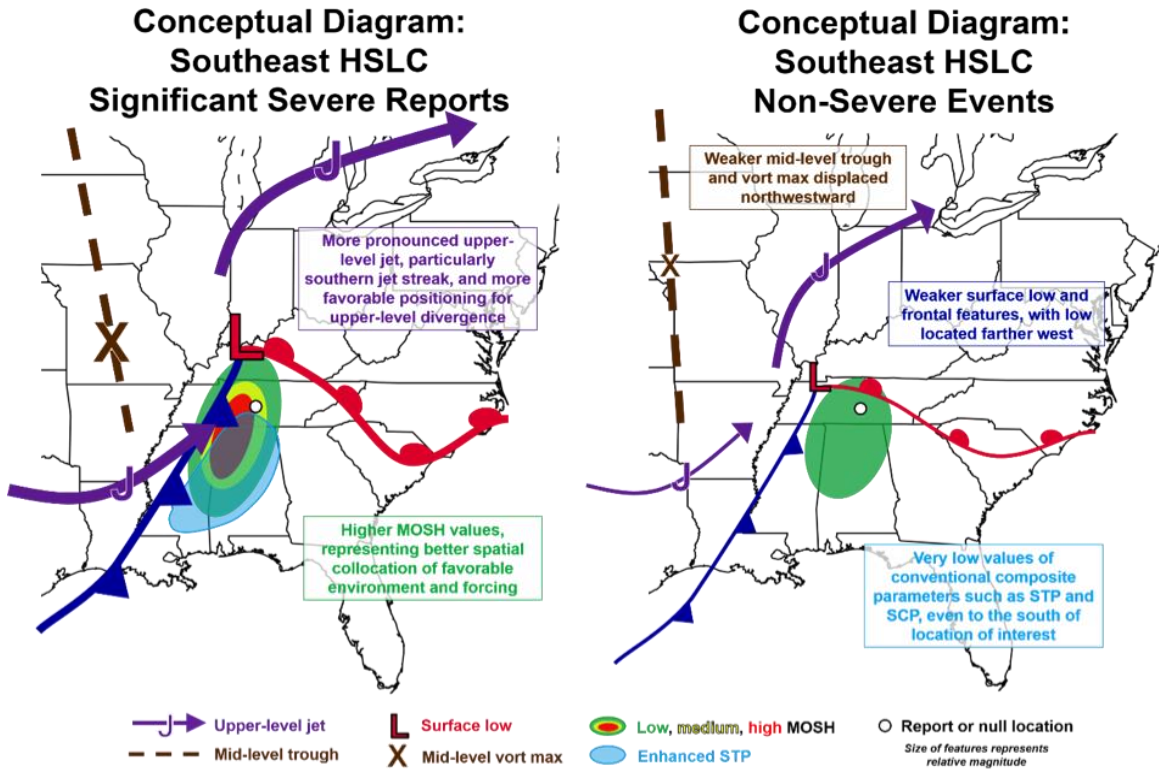


Figure 1.28. Conceptual models for composite HSLC significant severe (EF2 or stronger tornadoes and 65 kt or stronger winds) event (left) and non-severe event (right). “STP” refers to the Significant Tornado Parameter (e.g., Thompson et al. 2012), while “SCP” refers to the Supercell Composite Parameter (Thompson et al. 2004). Size of features are meant to represent their relative strength (e.g., surface low depicted by red “L” is larger in severe event conceptual model, consistent with a typically stronger surface cyclone in those cases).

CHAPTER 2

HSLC Idealized Simulations: Motivation and Experimental Design

2.1 Overview

The aforementioned recent work has improved our understanding of HSLC convection and discrimination between severe and nonsevere HSLC convective events. However, there have been very few targeted observations or high-resolution numerical simulations of HSLC events. As a result, there remain many gaps in our knowledge regarding the dynamics that govern the differences between severe and nonsevere HSLC convection, particularly in the minutes prior to the development of severe hazards. There have been no general sensitivity studies aimed at understanding the portions of the HSLC parameter space where severe weather can be expected, nor have process studies investigated the means by which HSLC convection produces damaging winds and tornadoes. In particular, the origins of strong, low-level vortices capable of producing tornadoes and damaging straight-line winds—in addition to the updrafts that support them—remain an open question. These lingering questions motivate the research presented here, as an understanding of the processes leading to the development of tornadoes or damaging winds within HSLC convection, along with their potential precursors, are critical for operational forecasting and nowcasting success. The primary aim of the following idealized simulations is to understand the links in the chain that lead from the development of a strong updraft to the subsequent genesis of a strong, low-level vortex in a typical HSLC severe convection environment. Once an understanding of these processes is established, it will be possible to assess what links in this chain are “broken” in some portions of the parameter space.

2.2 Background

For the most part, research on the genesis mechanisms of low-level vortices and tornadoes has been focused on high-CAPE environments supportive of supercells, which are common in the U.S. Great Plains. Generally, tornadoes develop within high-CAPE supercells following the development of a midlevel mesocyclone—the vorticity of which is acquired from the tilting of environmental horizontal vorticity, present as a result of sufficient vertical wind shear—and the development of a separate area of vertical vorticity near the surface. Subsequently, this near-surface vertical vorticity is stretched, leading to the development of a tornado (Davies-Jones and Brooks 1993; Davies-Jones 2015). The first step in this process is fairly well understood. In a strongly-sheared environment with predominantly crosswise environmental vorticity, an updraft produces counter-rotating vortices of either sign on its right (relative to the shear vector; cyclonic) and left (anticyclonic) sides (Fig. 2.1; Klemp 1987). When environmental vorticity is streamwise, the updraft is instead correlated with vertical vorticity. In the Northern Hemisphere, the right-moving updraft is typically dominant as a result of a clockwise-turning shear vector with height, which promotes ascent on the right flank of the updraft and descent on the left flank via the so-called “updraft-in-shear effect” (Fig. 2.2; Klemp 1987; Bunkers et al. 2000), which will be explored further shortly. Thus, this wind profile favors a right-moving (relative to the hodograph), cyclonically-rotating updraft as the updraft ingests streamwise vorticity; in other words, the sense of spin of the vorticity is in the same direction as the flow entering the storm (Davies-Jones 1984; Weisman and Rotunno 2000). The typical environmental wind profile associated with HSLC severe convection exhibits clockwise turning of the hodograph, particularly in the low levels (e.g., Figure 1.14).

Furthermore, recent research has elucidated the mechanisms by which near-surface vertical vorticity arises within these storms and how it is intensified to tornadic strength (e.g., Markowski and Richardson 2014; Dahl et al. 2014), although there remains some debate regarding the relative contribution of terms to low-level vertical vorticity, particularly

vorticity generated via the baroclinic (e.g., Dahl 2015) and frictional (e.g., Schenkman et al. 2014; Markowski 2016; Roberts et al. 2016) mechanisms. Baroclinic generation of horizontal vorticity arises due to density differences in the horizontal, such as within the downdraft or along an outflow boundary, while frictionally-generated vorticity is a consequence of surface drag. Via trajectory analysis, these studies have also identified the general pathways by which parcels approach and contribute to intense low-level vortices. By and large, the majority of parcels contributing to near-surface vortices arrive from storm-relative north or northwest, acquiring a vertical component of vorticity as they descend in the downdraft (e.g., Dahl et al. 2014; Fig. 2.3). More recent numerical simulations with lowest model levels very close to the ground (e.g., Rotunno et al. 2017) suggest that vertical vorticity may arise due to tilting of baroclinically-generated horizontal vorticity very close to the surface, without a need for the development of vertical vorticity in the downdraft itself. At any rate, the *source* of near-surface vertical vorticity does not appear to be of utmost importance; rather, the ability for the storm's updraft to converge and stretch this vorticity is the deciding factor in whether or not it produces a tornado (e.g., Coffey et al. 2017). Therefore, *the strength of low-level vertical accelerations—and subsequently, low-level updrafts—is of utmost importance in distinguishing tornadic from nontornadic supercells.*

Mesovortices within quasi-linear convective systems (QLCSs) may be shallow and lack accompanying mid-level rotation (Weisman and Trapp 2003), contrary to supercell mesocyclones and their associated low-level vortexgenesis. QLCS mesovortices tend to be classified as separate from system-scale book-end vortices (e.g., Weisman 1993), although they can also develop as cyclonic-anticyclonic couplets (e.g., Trapp and Weisman 2003; Wakimoto et al. 2006; Atkins and St. Laurent 2009b; Figs. 2.4 and 2.5). The eventual asymmetry of these couplets appears to be dependent on the Coriolis force, which allows cyclonic members to become dominant over time and stronger than without the inclusion of Coriolis (Trapp and Weisman 2003). Accordingly, the control simulation in this study will also be run *without* Coriolis forcing to assess the role that planetary vorticity plays in the development of strong, low-level vortices within HSLC convection or in the convection itself. Cyclonic QLCS mesovortices have also been documented to form in the absence of

anticyclonic partners (Atkins and St. Laurent 2009b; Xu et al. 2015; Figs. 2.6 and 2.7). Severe mesovortices, those that produce tornadoes or damaging straight-line winds, tend to be longer-lived, taller, and stronger than nonsevere mesovortices (e.g., Atkins et al. 2004; Atkins et al. 2005), characteristics which may in turn depend upon the low-level shear vector magnitude (Weisman and Trapp 2003; Schaumann and Przybylinski 2012). The typically large values of low-to-midlevel shear vector magnitude in HSLC environments may explain the propensity of QLCS tornadoes within HSLC convection (Smith et al. 2012; Davis and Parker 2014), as they could support deeper, longer-lived mesovortices.

Based on this prior research of supercells and QLCSs, the strength of low-level updrafts and associated rotation—in the form of mesocyclones or mesovortices—appear to determine the likelihood of tornadogenesis. Next, we will explore the means by which our environmental variables with documented discriminatory skill could impact each of these features.

2.3 Primary Model Sensitivity Matrix

Given the results of Chapter 1, it is clear there are three key considerations that distinguish those HSLC events that produce severe weather from those that do not: low-level shear, low-level instability (or lapse rates), and the magnitude of large-scale forcing⁸. The sensitivity of vortexgenesis to low-level shear vector magnitude has been documented in both QLCSs and supercells within high-CAPE environments. The strength and lifetime of QLCS mesovortices—and, accordingly, their potential to produce severe hazards—appears to *primarily* be dictated by the low-level environmental shear vector magnitude (Weisman and

⁸ Despite being a critical discriminator between severe and nonsevere HSLC convective events, the magnitude of synoptic-scale forcing is not systematically tested in this modeling study. The idealized framework of the experimental design does attempt to mimic synoptic-scale forcing, but it is not explicitly represented. As such, sensitivity studies associated with synoptic forcing cannot be performed within this framework and will be left for future work.

Trapp 2003; Schaumann and Przybylinski 2012). Meanwhile, shear vector magnitude and storm-relative helicity over the lowest 500 to 1000 m above ground has been shown to be a key discriminator between tornadic and nontornadic supercells (Brooks et al. 2003; Adleman and Droegemeier 2005; Markowski and Richardson 2014; Coffey and Parker 2015; Coffey and Parker 2017). Vortex sensitivity to low-level lapse rates is less definitive, though highly idealized simulations suggest that steeper lapse rates facilitate stronger vortices (Leslie and Smith 1978; Parker 2012). Increased lapse rates and low-level shear vector magnitude can also contribute to momentum transfer, which could produce damaging *straight-line* winds (Johns and Hirt 1987; Johns 1993; Evans and Doswell 2001). Before we can better prepare for potential severe hazards within HSLC environments, we must understand the sensitivity of convection therein to these parameters with documented discriminatory skill.

The specific question guiding this research is: why (physically) do changes in low-level lapse rates and shear vector magnitudes influence the evolution and severity of HSLC storms? To address this question, a multi-member model sensitivity matrix was developed to examine how variations in 0-1 km shear vector magnitude (01s) and 0-3 km lapse rates (03lr) affect the structure, evolution, and intensity of HSLC convection. The control base-state environment is shown in Figure 2.8⁹ and exhibits 493 J kg⁻¹ of surface-based (SB) CAPE, 21 J kg⁻¹ of 0-3 km CAPE, and 30 kt (1 kt = 0.51 m s⁻¹), 45 kt, and 83 kt of 0-1 km, 0-3 km, and 0-6 km shear vector magnitude, respectively. The control thermodynamic and kinematic profiles are based upon prior HSLC composites (as in Chapter 1) and preliminary radiosonde data from the Verifications of the Origins of Rotation in Tornadoes Experiment-Southeast (VORTEX-SE) field experiment and HSLC-focused radiosonde launches from NC State University, which tended to exhibit a nearly moist-neutral thermodynamic profile, moist boundary layer, and strongly-sheared wind profile in advance of HSLC convection.

⁹ It could be argued that the base state hodograph inherently includes effects of surface drag and Coriolis, given that it is based on real-world profiles.

The four primary experimental simulations are characterized by adjustments to the base-state 01s or 03lr over ranges of 20 kt (-01s) to 40 kt (+01s) and 6.0 K km^{-1} (-03lr) to 6.5 K km^{-1} (+03lr)¹⁰, respectively. Table 2.1 shows the variability in chosen convective ingredients from the control base-state environment to the other simulations. Skew-T/log-p diagrams for the 03lr variations are provided in Figure 2.9, while Figure 2.10 shows hodographs for the 01s variations. Note that changes in 03lr do not alter the SBCAPE but do lead to minor differences in mixed-layer (ML) CAPE. Because the moisture profile is constant across all cases, differences in CAPE are attributable to changes in both the 0-3 km and 3-6 km lapse rates. Storm-relative helicity (SRH) values change considerably with variations in 01s, as expected, with minor changes between the 03lr simulations¹¹. Note that the 0-1 km, 0-3 km, and 0-6 km shear vector orientations remain constant across all simulations in this matrix. Future work could instead explore modifying both 01s and 03lr simultaneously, using factor separation (e.g., Stein and Alpert 1993) to assess their respective roles. This study focuses on the first-order effects of varying each parameter, which should be determined sufficiently by studying each in isolation.

Simulations were performed with the Bryan Cloud Model (CM1; Bryan and Fritsch 2002; Bryan and Rotunno 2009), release 18, and initialized with a cold pool meant to mimic a cold front or outflow boundary. The cold pool was characterized by a minimum potential temperature perturbation of -10 K, decreasing as a cosine function eastward and upward from the western and bottom edge of the domain. Although vertical motion due to synoptic-scale and mesoscale heterogeneity is not thoroughly depicted in this idealized framework, this initiating cold pool is meant to represent linear forcing similar to an outflow boundary or cold front, along which HSLC severe convection tends to form and/or evolve. Further, by

¹⁰ This range of lapse rates seems fairly modest; however, climatologically, the inner 50% of 03lr associated with severe HSLC convection for any given region tends to encompass a range of only about 1 K km^{-1} (Sherburn and Parker 2014). Using SPC mesoanalysis data for the Southeast U.S., 25th and 75th percentile values are around 5 to 6 K km^{-1} .

¹¹ These changes result from the chosen storm motion estimate (Bunkers et al. 2014), which was used to be consistent with typical analysis and model fields. Actual storm motions between the simulations show minor differences, so true SRH is approximately the same.

virtue of the cold pool's structure, realistic destabilization through cooling aloft occurs east of the surface cold pool owing to advection of the mid-level temperature perturbation. This leads to rather organic evolution of convection, which is a benefit of this particular approach. It is worth noting here that other initialization techniques—such as one or more warm bubbles and forced convergence—were tested, as well, but no other initialization technique led to the development of sustained convection. The implications of these findings will be discussed in Chapter 4, but in general, this is consistent with prior studies suggesting that continuous forcing may be necessary to maintain strong HSLC convection (e.g., Chapter 1; King et al. 2017).

Horizontal grid spacing was 250 m, with the x-domain stretched outside of the inner 100 km to lower the computational demand. Note that the horizontal grid spacing here is fairly coarse given the scale of HSLC vortices (e.g., Davis and Parker 2014), and simulation results here are presented with the caveat that near-surface vortices are likely not entirely resolved. However, the focus here is on the processes leading to the development of these vortices, which should be reasonably represented given that comparable grid spacing has been used in prior similar studies (e.g., Dahl et al. 2014). Given the size disparity between HSLC and higher-CAPE convection, it is reasonable to question if HSLC convection can be adequately simulated using similar model configurations. Through preliminary tests, it was observed that there is little difference in storm structure or characteristics when the horizontal grid spacing is cut in half to 125 m. Therefore, to reduce computational demand, all simulations analyzed here maintained the 250-m grid spacing.

The vertical grid spacing was stretched from 10 m at the lowest model level (5 m) to 250 m from approximately 9.875 km to the top of the domain. The domain moved with a constant speed that varied slightly depending upon the base-state environment to ensure that convection remained near the center of the domain within the unstretched x grid. Boundaries were open in the x-direction and periodic in the y-direction. Coriolis forcing was included on the perturbation winds only, which is equivalent to assuming geostrophic balance in the base-state wind field (Roberts et al. 2016; Coffey and Parker 2017). The simulations were

initialized with modest, random potential temperature perturbations throughout the domain to encourage development of three-dimensional convective structures. The NSSL double-moment microphysics scheme (Mansell et al. 2010) is used, with both graupel and hail densities predicted. Although surface drag is a plausible source of near-surface horizontal vorticity that could potentially influence the development of low-level vortices, the bottom boundary is free-slip, consistent with the majority of prior QLCS mesovortex and supercell tornadogenesis studies. Additionally, surface fluxes of heat and moisture—which are thought to influence HSLC environments only modestly (e.g., King et al. 2017)—and radiation are excluded for simplicity.

Note that this is considered a “zero-order” attempt at modeling HSLC convection. Many of the aforementioned choices were made for simplicity, in order to focus on the processes of primary interest, or to reduce computational demand. Future work should take advantage of finer grid spacing, in particular, to assess how the important processes examined here are affected at higher resolution and to begin to study the details of the vortex dynamics. Additionally, a more realistic boundary layer including surface drag could be utilized to assess the role of neglected near-ground processes in the vortexgenesis process, though this should only be included at scales capable of resolving turbulent eddies to prevent unrealistic low-level shear profiles (Markowski and Bryan 2016). Despite these caveats, we are confident that the given model setup accurately depicts the processes that govern HSLC convection.

2.4 Example HSLC Cases

As will be shown in Section 3, the general structure and evolution of the control run’s convection resembled typical HSLC events. Two examples of regional radar reflectivity imagery associated with the severe HSLC QLCS cases of 4-5 March 2008 and 29-30 January 2013 are provided in Figs. 2.11 and 2.12, respectively. Each of these QLCSs persisted for

several hours and produced multiple tornadoes and instances of damaging straight-line winds. The case of 4-5 March 2008 exhibited embedded miniature supercells, one of which is shown in Figs. 2.13 and 2.14. The characteristic features of a supercell, including a hook echo and mesocyclone, were evident in this storm but not well-defined. This lack of definition was a consequence of the poor radar resolution of the relatively small HSLC convection¹². The 29-30 January 2013 case was more representative of a typical QLCS, as associated rotation was relatively short-lived and shallow. However, embedded radar reflectivity signatures at the time of tornado occurrence appear similar to that of a supercell, with several hook echo-like appendages evident along the system's leading edge (Fig. 2.15). Interestingly, many of these vortices developed at approximately the same time and with fairly regular spacing (of approximately 15-20 km) along the cold pool's leading edge. Given that this occurred 18 to 24 hours into the event, it is plausible that the convergence of planetary vorticity played a part in this process; the role of Coriolis in our control simulation will be explored further in Section 3.2b. While the simultaneous development of multiple strong vortices was not found in our simulations, the radar reflectivity structures and associated rotation were consistent with those observed in these two cases.

2.5 Analysis of Accelerations

In order to isolate cause from effect in these sensitivity experiments, we seek to quantify the specific impacts of 01s and 03lr upon the low-level updrafts of the simulated storms.

Regardless of associated convective mode, *a strong low-level vortex cannot develop and be maintained without low-level stretching of vertical vorticity, which is driven by low-level vertical accelerations*. Thus, careful analysis of low-level accelerations was a primary focus

¹² A recent upgrade to super-resolution radar imagery may improve the depiction of these small-scale features in HSLC convection, though this remains dependent upon the convection's distance from radar.

of this study. When the Boussinesq approximation is valid and frictional and viscous forces are ignored, vertical accelerations are governed by the following expression:

$$\frac{Dw}{Dt} = -\frac{1}{\rho_0} \frac{\partial p'}{\partial z} + B, \quad (2.1)$$

where the first term on the right-hand side is the vertical perturbation pressure gradient acceleration, and the second term is the buoyancy. Vertical accelerations can subsequently be broken down into *buoyant* and *dynamic* components (Wilhelmson and Ogura 1972; Rotunno and Klemp 1982), which involves decomposing the total pressure perturbation (p') into its buoyant (p'_b) and dynamic (p'_d) components. Within the simulations, differences in updraft production and strengths across simulations were assessed by calculating these components. By doing so, it is possible to determine not only which processes are dominant in forcing HSLC convective updrafts (and downdrafts) but also how changes in the ambient environment influence these processes. In turn, these resultant updrafts directly impact the tilting and stretching of vorticity in the simulated storms.

Following a similar methodology to Parker and Johnson (2004a,b), Parker (2007b, 2010, 2017), Davenport and Parker (2015), and Coffey and Parker (2015, 2017), the first step in decomposing the perturbation pressure equation is to solve p'_b iteratively using

$$\alpha_0 \nabla^2 p'_b = \frac{\partial B}{\partial z}, \quad (2.2)$$

then p'_d is treated as the residual. By definition, in low-CAPE environments, the buoyant term tends to be small, as a lifted parcel has a density relatively close to that of the ambient environment. Therefore, vertical accelerations resulting from the dynamic perturbation pressure gradient likely dominate in HSLC convection (e.g., McCaul and Weisman 1996; Markowski and Richardson 2014). The dynamic component of the perturbation pressure is given by

$$\nabla^2 p'_d = -\rho_0 \left[\left(\frac{du}{dx} \right)^2 + \left(\frac{dv}{dy} \right)^2 + \left(\frac{dw}{dz} \right)^2 \right] - w^2 \frac{\partial^2}{\partial z^2} (\ln \rho_0) - 2\rho_0 \left(\frac{dv}{dx} \frac{du}{dy} + \frac{du}{dz} \frac{dw}{dx} + \frac{dv}{dz} \frac{dw}{dy} \right), \quad (2.3)$$

where u , v , and w are the 3D wind components and ρ_0 is density. For incompressible, storm-scale motions, this expression can be simplified, and p'_D can be approximated as

$$p'_D \propto e'_{ij}{}^2 - \frac{1}{2}|\omega'|^2 + 2 \left(\frac{\partial w'}{\partial x} \frac{\partial \bar{u}}{\partial z} + \frac{\partial w'}{\partial y} \frac{\partial \bar{v}}{\partial z} \right), \quad (2.4)$$

where e'_{ij} , ω' , and w' are the perturbations of deformation, vorticity, and vertical velocity, respectively, and $\frac{\partial \bar{u}}{\partial z}$ and $\frac{\partial \bar{v}}{\partial z}$ are components of the mean wind shear vector (Markowski and Richardson 2010). Here, the first two terms on the right-hand side are referred to as the *nonlinear* dynamic pressure perturbation, and the last term is the *linear* dynamic pressure perturbation. Much as in the first step of decomposing the perturbation pressure equation, in our solver, the nonlinear dynamic term (p'_{dnl}) is treated as the residual of the total dynamic acceleration following the calculation of p'_{dl} . In terms of these three components, the equation for vertical accelerations is then¹³

$$\frac{Dw}{Dt} = B - \underbrace{\frac{1}{\rho_0} \frac{\partial p'_B}{\partial z}}_{ACCB} - \underbrace{\frac{1}{\rho_0} \frac{\partial p'_{DL}}{\partial z}}_{ACCDL} - \underbrace{\frac{1}{\rho_0} \frac{\partial p'_{DNL}}{\partial z}}_{ACCDNL}. \quad (2.5)$$

The linear term of the dynamic pressure perturbation (p'_{dl}) is colloquially referred to as the “updraft-in-shear” effect, and its primary footprint is a low pressure perturbation *downshear* of an updraft and a high pressure perturbation *upshear* (Fig. 2.2; Klemp 1987). One key implication of this term is that it explains the deviate motion of supercells with curved hodographs owing to the development of an upward-pointing dynamic acceleration on either the right (with a clockwise-turning wind profile) or left flank (with a counterclockwise-turning wind profile) of a supercell (Fig. 2.2; Rotunno and Klemp 1982; Klemp 1987). This term could conceivably be quite large in HSLC convective environments given the large speed and directional shear of the typical wind profile (as shown in Chapter 1).

¹³ Note that B within our pressure solver includes the effects of hydrometeor loading.

The nonlinear term (p'_{dnl}) corresponds to either low-pressure perturbations resulting from any flow dominated by “spin” (i.e., rotation) or high pressure perturbations in regions dominated by “splat” (i.e., divergence, convergence, or deformation). The nonlinear term can be quite significant in tornadic convection. In particular, within supercells—which are characterized by a rotating updraft—nonlinear dynamic accelerations can substantially augment vertical velocities in the updraft and have in fact been shown to be the primary contributor to vertical accelerations in numerical studies of supercells (e.g., Coffey and Parker 2017). Additionally, *downward* dynamic accelerations attributable to the nonlinear term have been suggested as the primary driver for the so-called occlusion downdraft¹⁴ within supercells, which arise as the strength of the near-surface rotation begins to surpass that of the low-to-mid-level mesocyclone (Klemp and Weisman 1983; Markowski 2002). Because low-level shear vector magnitude plays a significant role in the strength of low-level mesocyclones in supercells (Brooks et al. 2003; Adlerman and Droegemeier 2005; Markowski and Richardson 2014; Coffey and Parker 2015; Coffey and Parker 2017) and QLCS mesovortices (Weisman and Trapp 2003; Schaumann and Przybylinski 2012), it is likely that low-level vertical accelerations due to the nonlinear components of the perturbation pressure gradient could be significant in HSLC convection, particularly when coupled with the near-surface “splat” associated with a system-generated or larger-scale cold pool.

Rather than strictly focusing on the origins and lifetimes of strong near-surface vortices in these simulations, much of the analysis will instead focus on the origins of strong, low-level updrafts that have been shown to facilitate and maintain these vortices. The reasoning for this choice is twofold: 1) As noted throughout this section and Section 2.3, the most important consideration in whether or not a near-surface vortex intensifies is not necessarily the availability of vertical vorticity at the surface but instead the ability for vorticity near the surface to be tilted and stretched, a process made possible through a strong

¹⁴ More generally referred to as the “vortex valve” effect.

low-level updraft; and 2) convective updrafts are well-resolved on the chosen model domain, while vortices are only marginally resolved on the 250-m horizontal grid. This analysis will lead to an understanding of the processes that precede the intensification of near-surface vortices; additionally, this will allow for the identification of any storm-scale precursors that could be observed in real cases, potentially aiding operational meteorologists in detection of severe hazards and improving lead time of warnings.

2.6 Sensitivity to Hodograph Orientation

Prior studies have indicated that the wind profile's orientation relative to a boundary has significant ramifications on the convection's ultimate convective mode and its potential hazards (e.g., Bluestein and Weisman 2000; French and Parker 2008; Dial et al. 2010). Cursory investigation into high-impact HSLC tornado and wind events across the Southeast supports these findings, as it was determined that events with 20 or more tornadoes tended to have a larger *cross*-boundary component of shear vectors than in primarily wind events, which were dominated by *along*-boundary shear (Sherburn 2013). The varying wind profiles explored in this study lead to disparate storm motion and development locations relative to the initiating cold pool and subsequent system-generated outflow boundaries. Though not systematically studied in the *primary* matrix of simulations, the wind profile and, thus, storm development and motion relative to the boundary is undoubtedly important in determining the severe potential of HSLC convection.

Given these considerations, an additional two simulations are performed to investigate the impact of rotating the control wind profile 30° and 60° clockwise relative to the initiating boundary. The goal here was to assess any changes in convection's organization, evolution, or potential for producing strong low-level vorticity. Other than the hodograph rotation, these simulations had an identical model setup to the primary matrix described above.

2.7 Object Tracking Algorithm

To analyze the characteristics of low-level updrafts and vortices within each simulation, an algorithm to objectively detect and track these features was developed. 3D fields were compressed to 2D by taking the maximum value of either vertical velocity or vertical vorticity over the lowest 1.5 km. Then, an object detection tool was used to identify 2D closed contours within which a vertical velocity of 5 m s^{-1} or Okubo-Weiss parameter (Okubo 1970; Weiss 1991)¹⁵ of 0.001 s^{-2} was satisfied over an area of at least 1.5 km^2 . In addition to identifying updraft and vortex features meeting these thresholds, the algorithm was able to objectively determine the maximum and mean values of the chosen fields and the area, centroid, orientation, and aspect ratios of the features. The updrafts were subject to a depth criterion (i.e., how many points in the vertical where the threshold magnitude is exceeded) of 12 grid points (8 for vortices), meaning that threshold values of vertical velocity (or vorticity) had to be met over 12 (8) grid points in the lowest 1.5 km to be considered. These criteria were incorporated to prevent the oversaturation of small, inconsequential features in the population of updrafts and vortices. Note that additional criteria were tested, but these choices provided the most useful populations of updrafts and vortices for further analysis.

Once features were detected, the algorithm then searched the same grids over the next time step to determine the new location of these features. The algorithm searched within a 10-grid point (4-grid points for vortices) box surrounding the feature's centroid during the previous time step, starting with the grid point nearest the prior centroid. Because the domain was moving at a speed generally close to that of the convection, the centroid tended to move little between time steps; thus, features of interest were tracked readily. Features were

¹⁵ The Okubo-Weiss parameter [$OW = \left(\frac{dv}{dx} - \frac{du}{dy}\right)^2 - \left(\frac{du}{dx} - \frac{dv}{dy}\right)^2 - \left(\frac{dv}{dx} + \frac{du}{dy}\right)^2$] is sometimes preferred over vertical vorticity because it effectively removes deformation from vertical vorticity, thus providing a focus on the location where rotation is dominant.

subsequently subject to a longevity requirement of 5 minutes, as transient updrafts and vortices were not the intended subject of analysis.

By detecting and tracking updrafts and vortices, it was possible to analyze the distribution of these features—including their typical sizes, intensities, and durations—and how these characteristics varied across base-state environments. The distributions of values for a population of objectively-identified objects over time is much more representative than a single maximum value, the latter of which was at times inconclusive or even misleading.

2.8 Parcel Trajectory Analysis

For each primary matrix simulation, a restart run was performed in which tracer parcels are seeded within the model. Parcels are initiated at each grid point within a 50 km (in x) by 100 km (in y) by 1.4 km (in z) box ahead, and in the vicinity, of the location where the strongest or longest-lived updraft developed, and then integrated forward in time. Parcel trajectories were calculated at every large model time step, with output—calculated via trilinear interpolation of 3D model fields—written every ten seconds in the simulation. Candidate parcels entering low-level updrafts and vortices were then identified to determine the origins and key accelerations contributing to the strongest features. These trajectories offered insight into the Lagrangian characteristics of the parcels that contributed to strong updrafts and vortices—particularly how the accelerations affecting their motion changed as they approached and entered the updrafts—while also allowing for comparisons of these characteristics among the environmental sensitivity simulations.

Table 2.1. Selected base-state environment variables for matrix of simulations

<i>Variable</i>	<i>Control</i>	<i>+01s</i>	<i>-01s</i>	<i>+03lr</i>	<i>-03lr</i>	<i>No Coriolis</i>	<i>Rotated 30°</i>	<i>Rotated 60°</i>
<i>SBCAPE (J kg⁻¹)</i>	493	493	493	493	493	493	493	493
<i>MLCAPE (J kg⁻¹)</i>	274	274	274	276	288	274	274	274
<i>0-3 km CAPE (J kg⁻¹)</i>	21	21	21	40	6	21	21	21
<i>0-1 km shear (kt)</i>	30	40	20	30	30	30	30	30
<i>0-1 km SRH (m²s⁻²)</i>	253	352	160	236	264	253	253	253
<i>0-3 km shear (kt)</i>	45	45	45	45	45	45	45	45
<i>0-3 km SRH (m²s⁻²)</i>	369	451	304	366	370	369	369	369
<i>0-6 km shear (kt)</i>	83	83	83	83	83	83	83	83

FIGURES

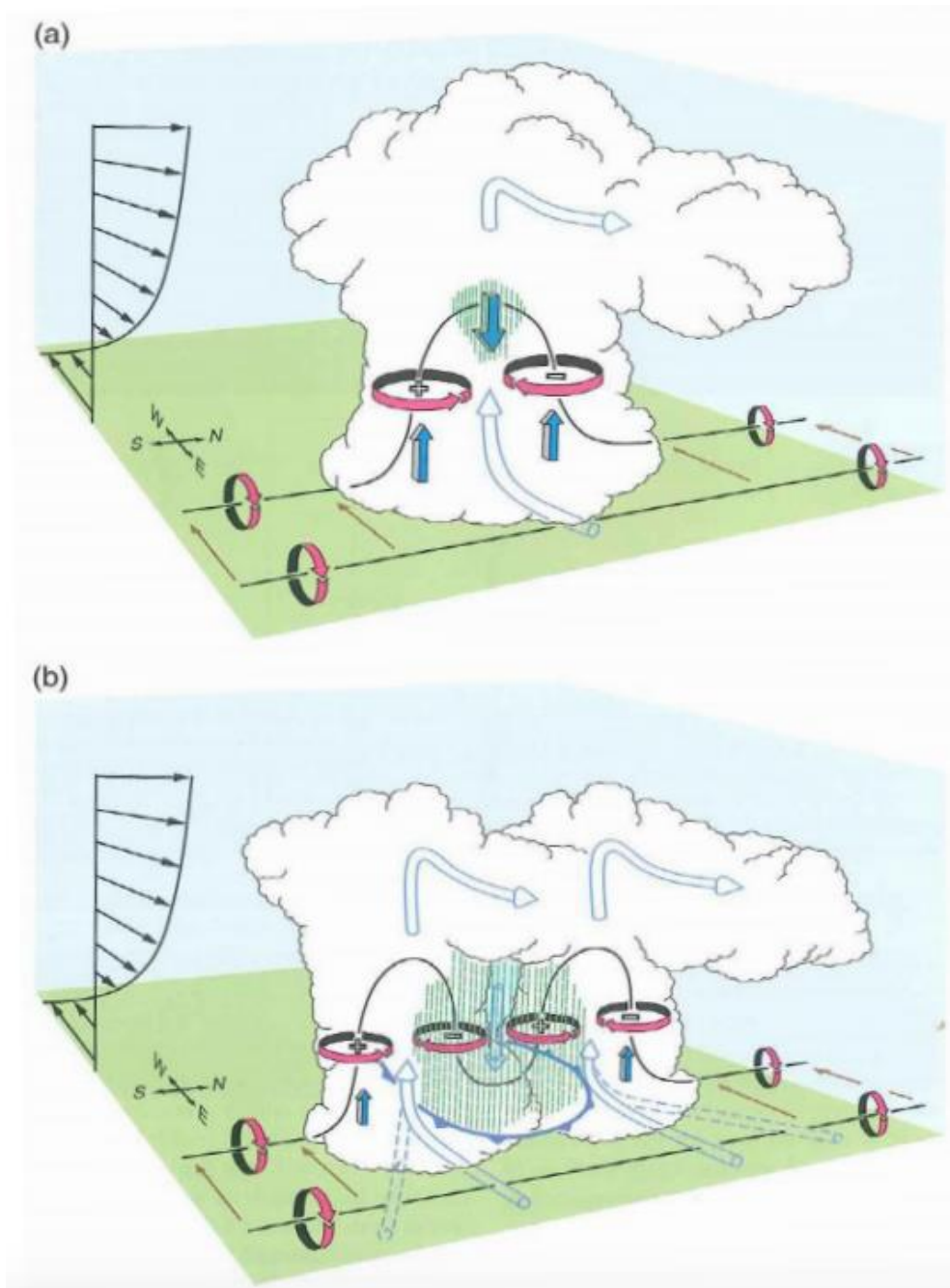


Figure 2.1. From Markowski and Richardson (2010), adapted from Klemp (1987): Origins of rotation within a supercell, as discussed in the text. Panel (a) depicts the initial counter-rotating vortices resulting from updraft tilting of environmental vortex lines. Panel (b) shows the subsequent splitting of the initial storm into symmetric right- and left-moving supercells. This situation occurs when the wind profile is unidirectional.

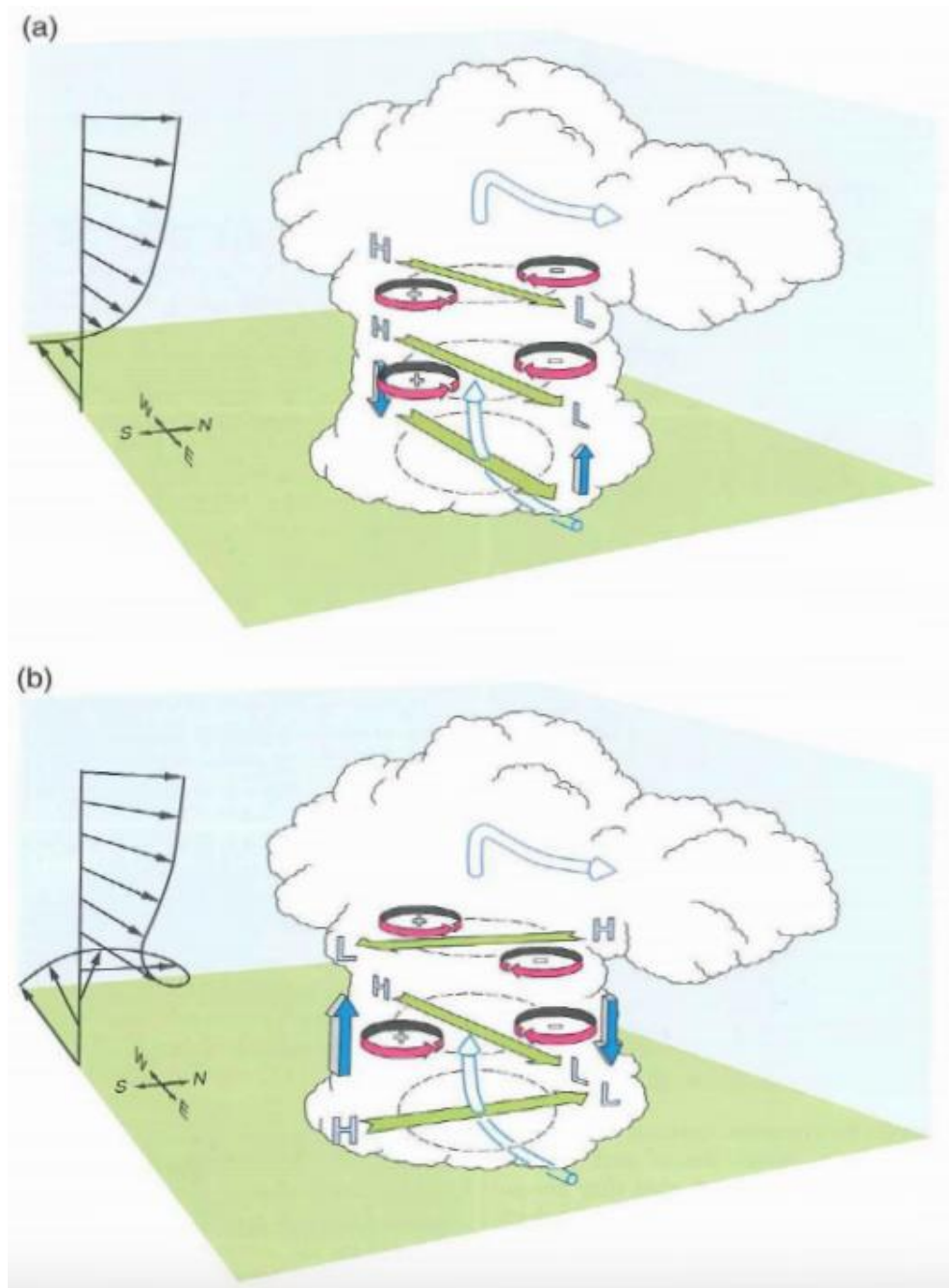


Figure 2.2. From Markowski and Richardson (2010), adapted from Klemp (1987): Examples of the “updraft-in-shear” effect for (a) unidirectional wind shear and (b) a clockwise-turning wind profile with height. Panel (b) shows how high pressure upshear and low pressure downshear of the initial updraft can promote subsequent updraft development on a given flank of the initial storm; given this wind profile, as discussed in the text, an updraft is favored on the storm’s right flank.

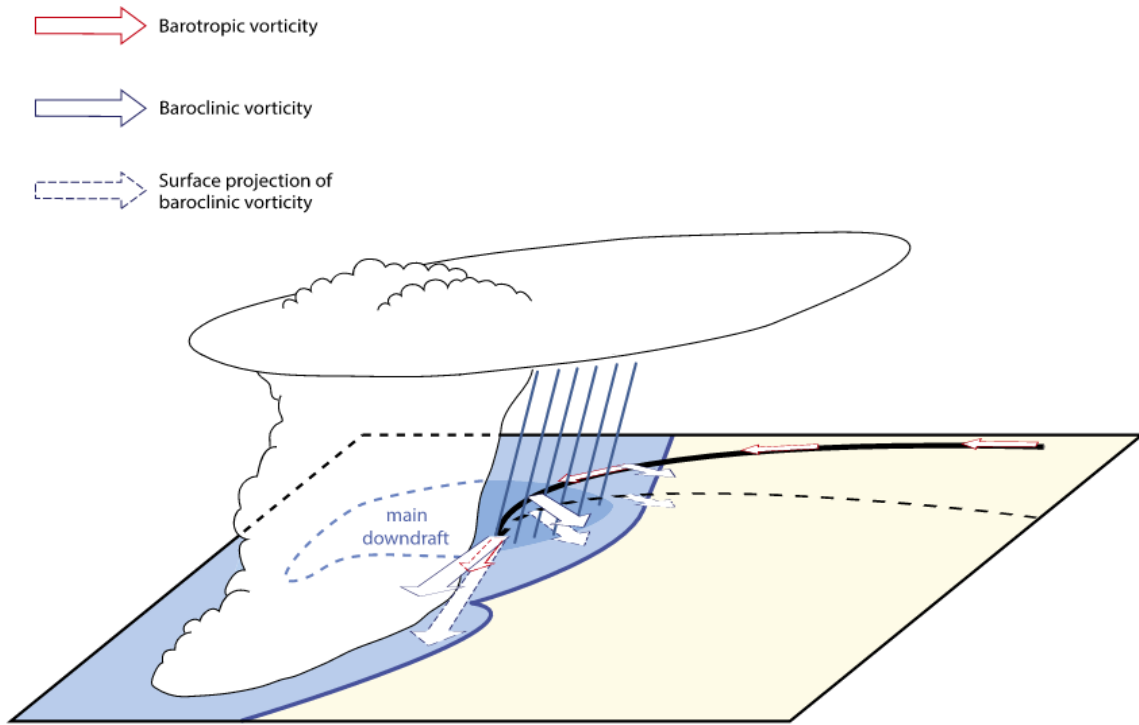


Figure 2.3. (From Dahl et al. 2014) Schematic of barotropic and baroclinic vorticity vectors along the trajectory of a parcel acquiring appreciable near-surface vertical vorticity in a simulated supercell. Black line shows the parcel's trajectory, while the dashed line shows its surface projection. Blue shaded region shows the cold pool of the parent supercell.

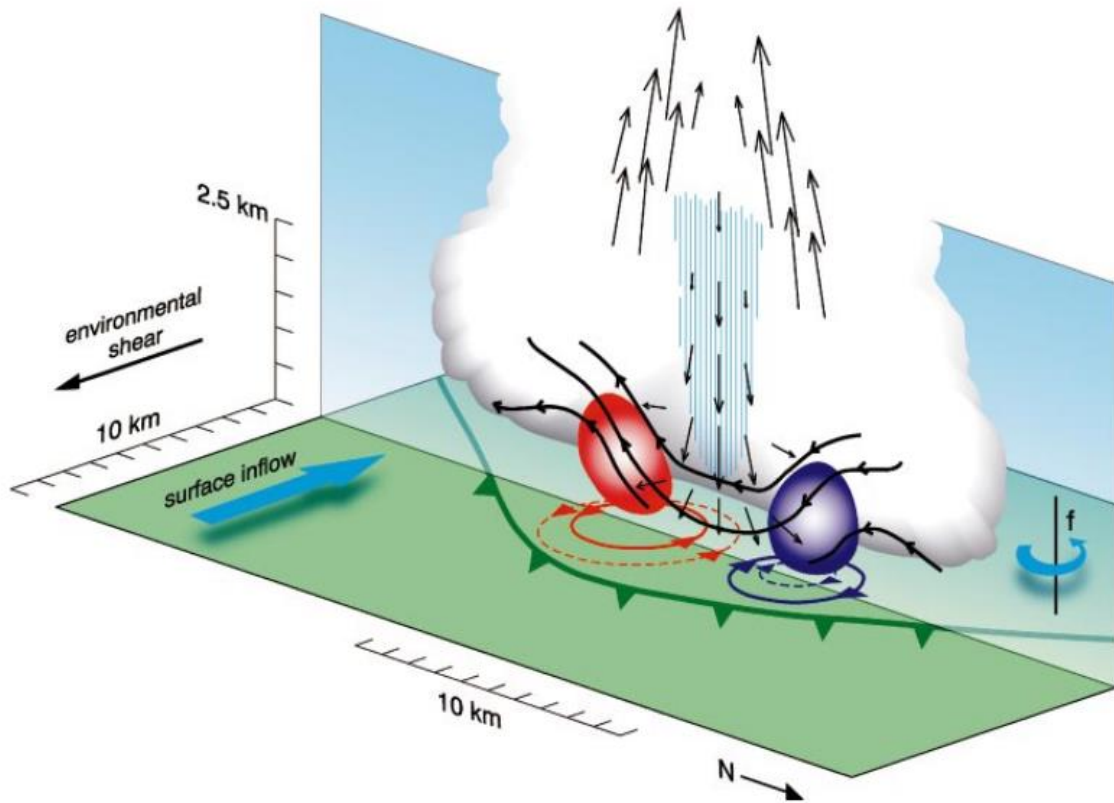


Figure 2.4. (From Trapp and Weisman 2003) Conceptual diagram of a proposed method of mesovortexgenesis that includes the formation of a cyclonic (red) and anticyclonic (purple) vortex couplet via downdraft tilting of baroclinically-generated horizontal vorticity. Vectors represent the direction and speed of wind flow. The green barbed line shows the relative position of the surface gust front.

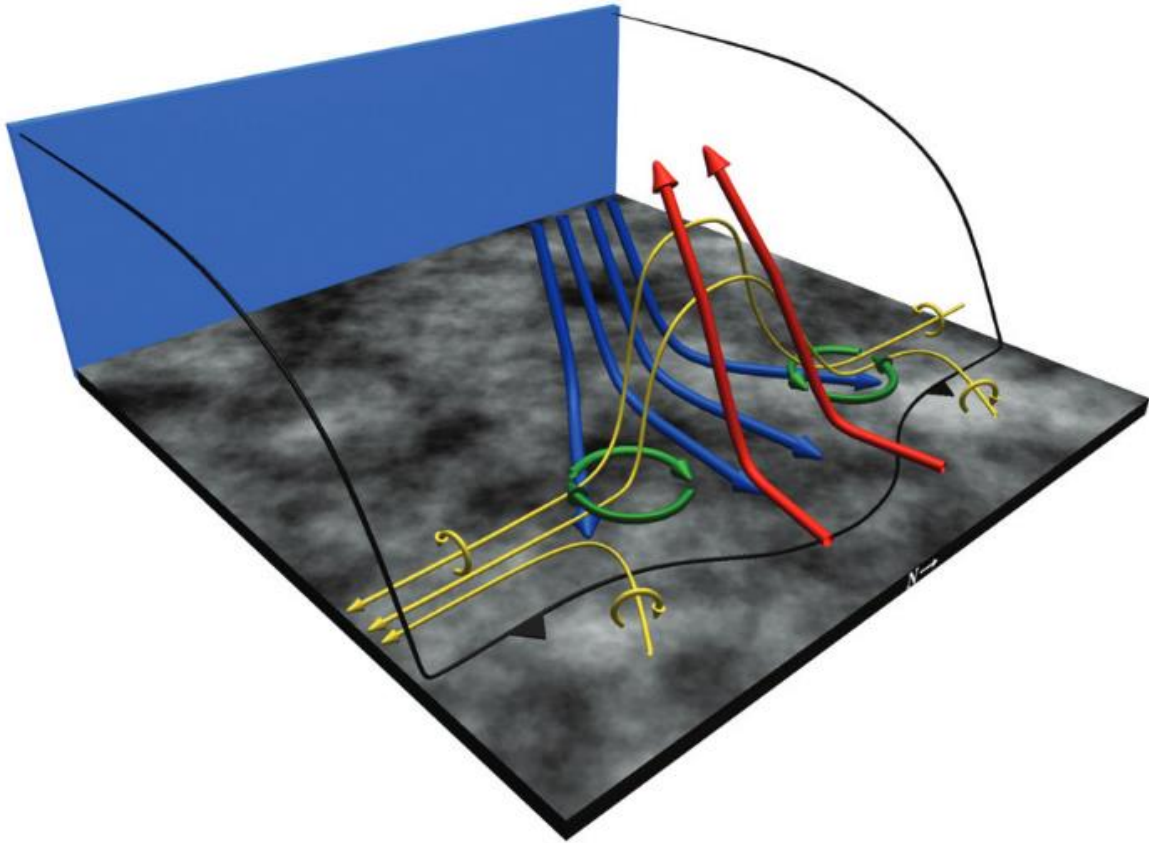


Figure 2.5. (From Atkins and St. Laurent 2009b) Conceptual diagram of a proposed method of mesovortexgenesis that includes the formation of a cyclonic (north) and anticyclonic (south) vortex couplet via updraft tilting of baroclinically-generated horizontal vorticity. Vectors represent the direction and speed of wind flow. The black barbed line shows the relative position of the surface gust front. Yellow vectors represent the position of vortex lines and their sense of spin.

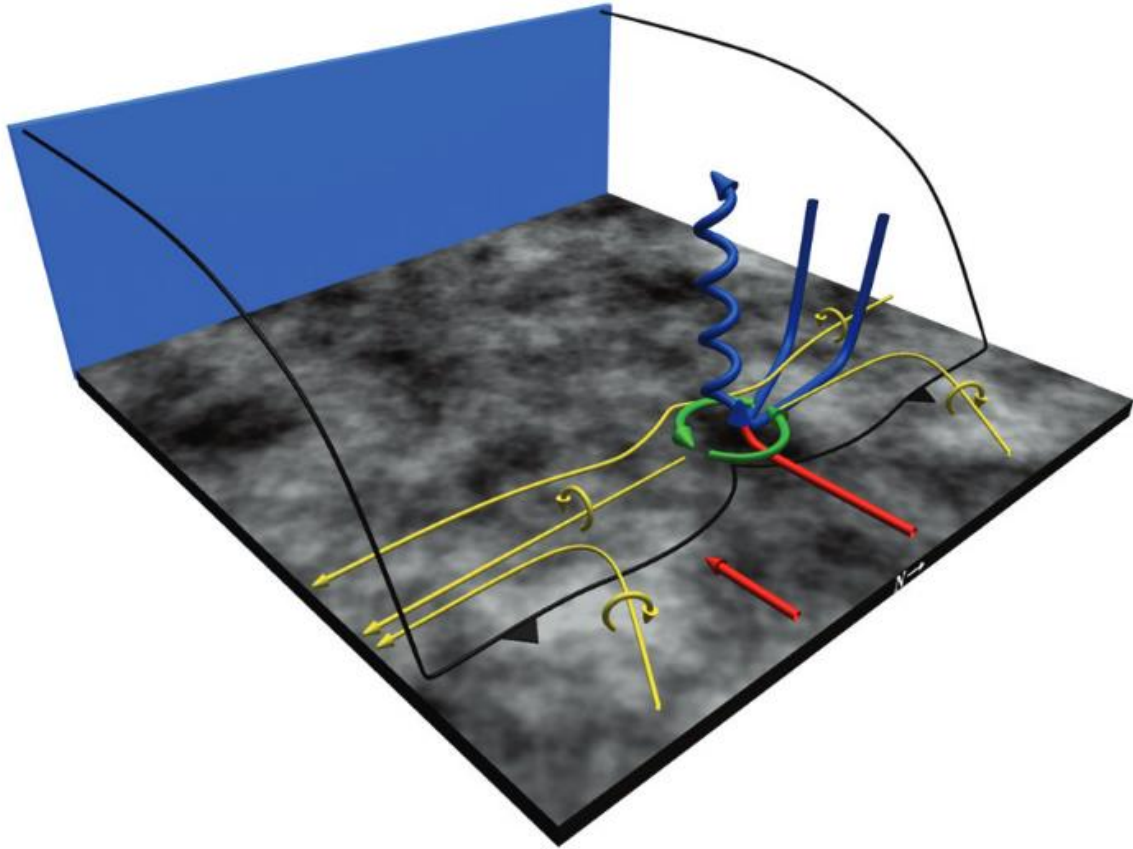


Figure 2.6. (From Atkins and St. Laurent 2009b) Conceptual diagram of a proposed method of mesovortexgenesis that is ultimately similar to low-level mesocyclogenesis in a supercell. Vectors represent the direction and speed of wind flow. The black barbed line shows the relative position of the surface gust front. Yellow vectors represent the position of vortex lines and their sense of spin.

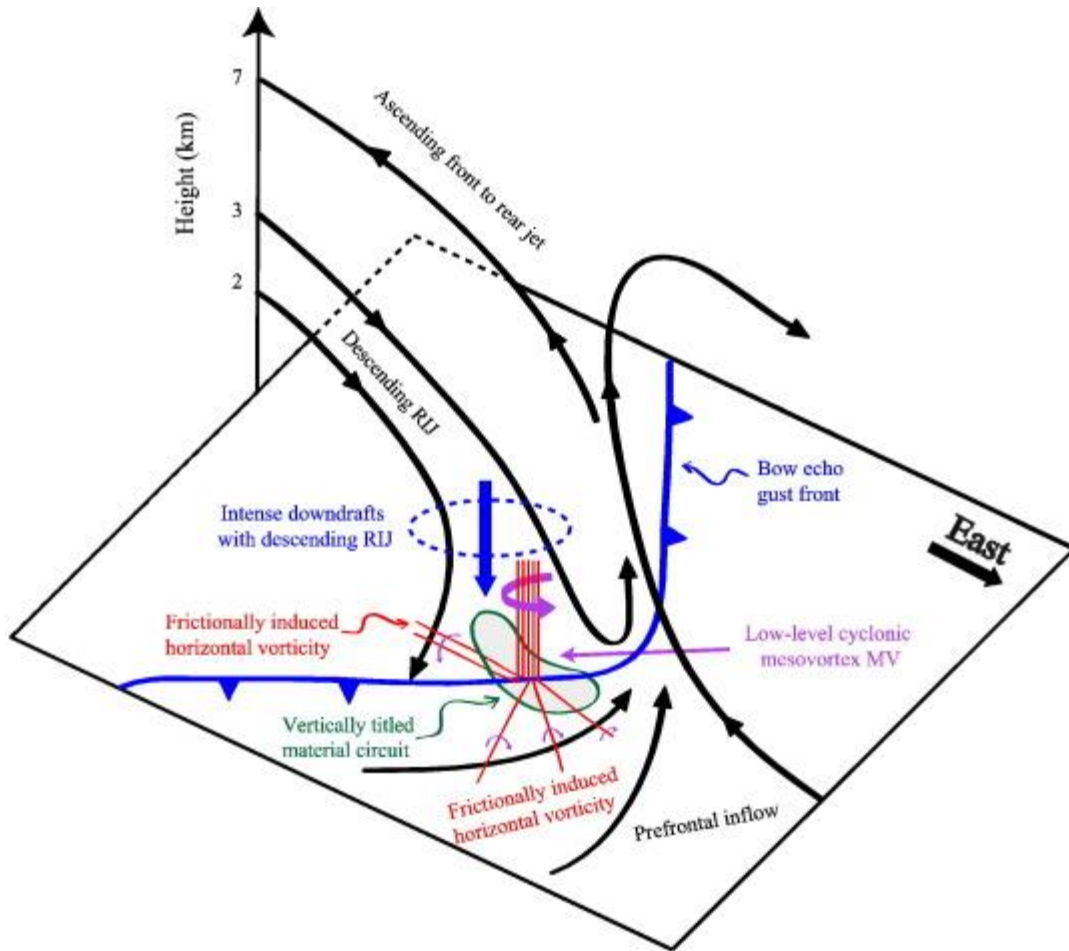


Figure 2.7. (From Xu et al. 2015) Conceptual diagram of a proposed method of mesovortexgenesis that suggests the source of vorticity within the vortex is frictionally-induced horizontal vorticity. Vectors represent the direction and speed of wind flow. The blue barbed line shows the relative position of the surface gust front. Red lines represent the position of frictionally-induced vortex lines, with associated purple vectors showing their sense of spin.

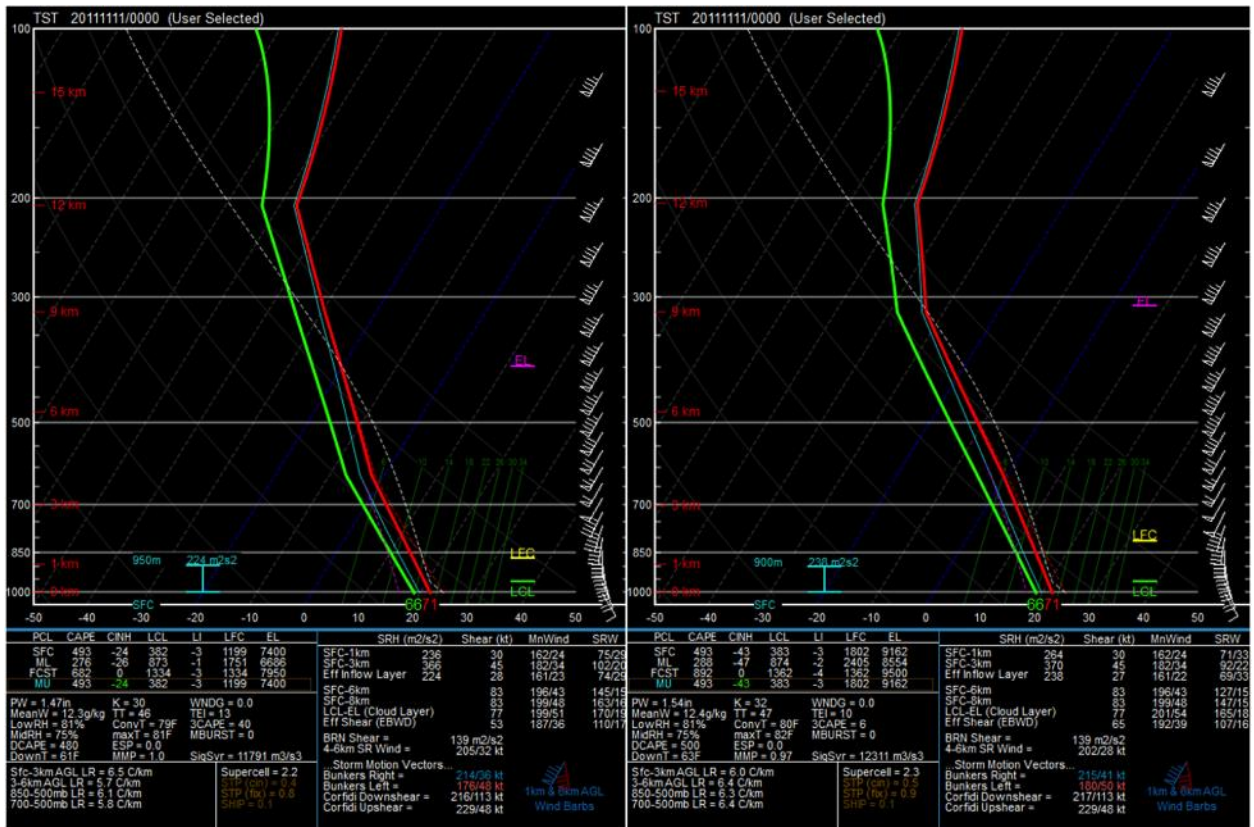


Figure 2.9. Base-state thermodynamic profiles for the (left) increased low-level lapse rate and (right) decreased low-level lapse rate simulations.

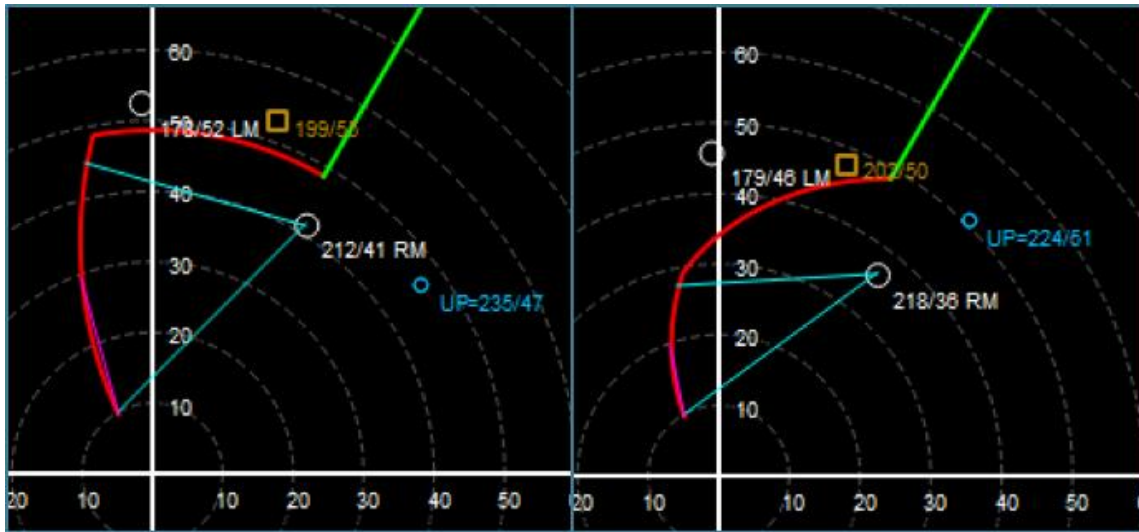


Figure 2.10. Base-state thermodynamic profiles for the (left) increased low-level lapse rate and (right) decreased low-level lapse rate simulations.

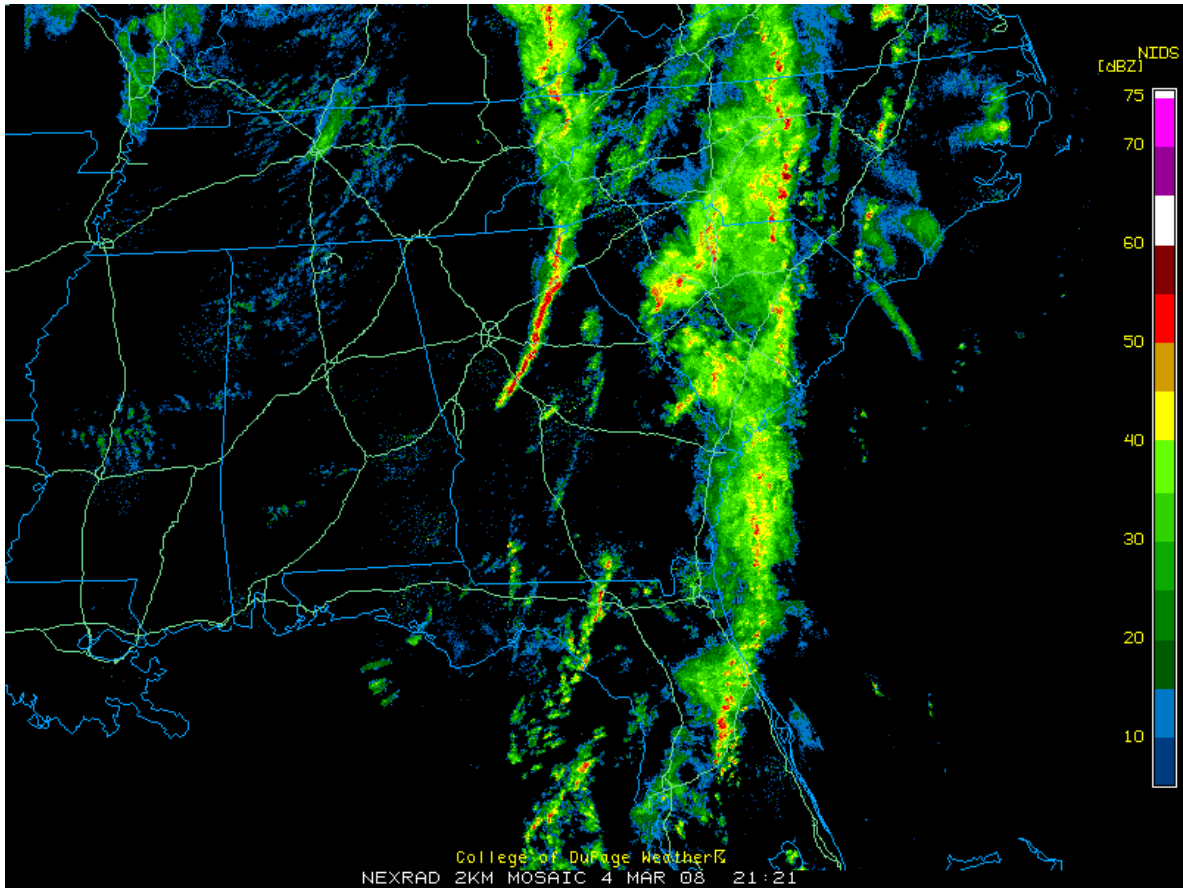


Figure 2.11. Regional mosaic of 1-km reflectivity over the Southeast for the 4-5 March 2008 severe HSLC event. Shortly after this time, several developed across the Carolinas and southern Virginia, while damaging straight-line winds were in progress. Image courtesy of UCAR and College of DuPage.

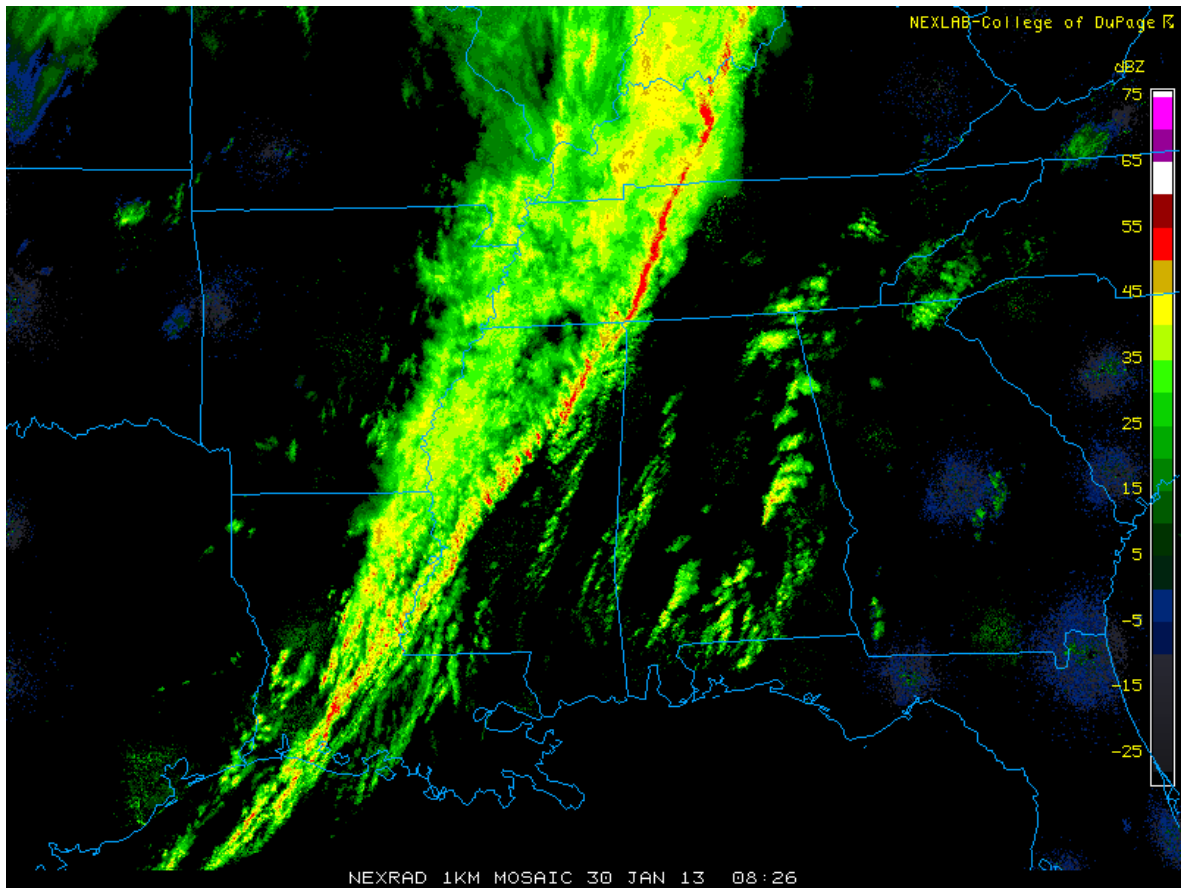


Figure 2.12. Regional mosaic of 1-km reflectivity over the Southeast for the 29-30 January 2013 severe HSLC event. Around this time, several QLCS tornadoes were in progress across middle Tennessee. Image courtesy of UCAR and College of DuPage.

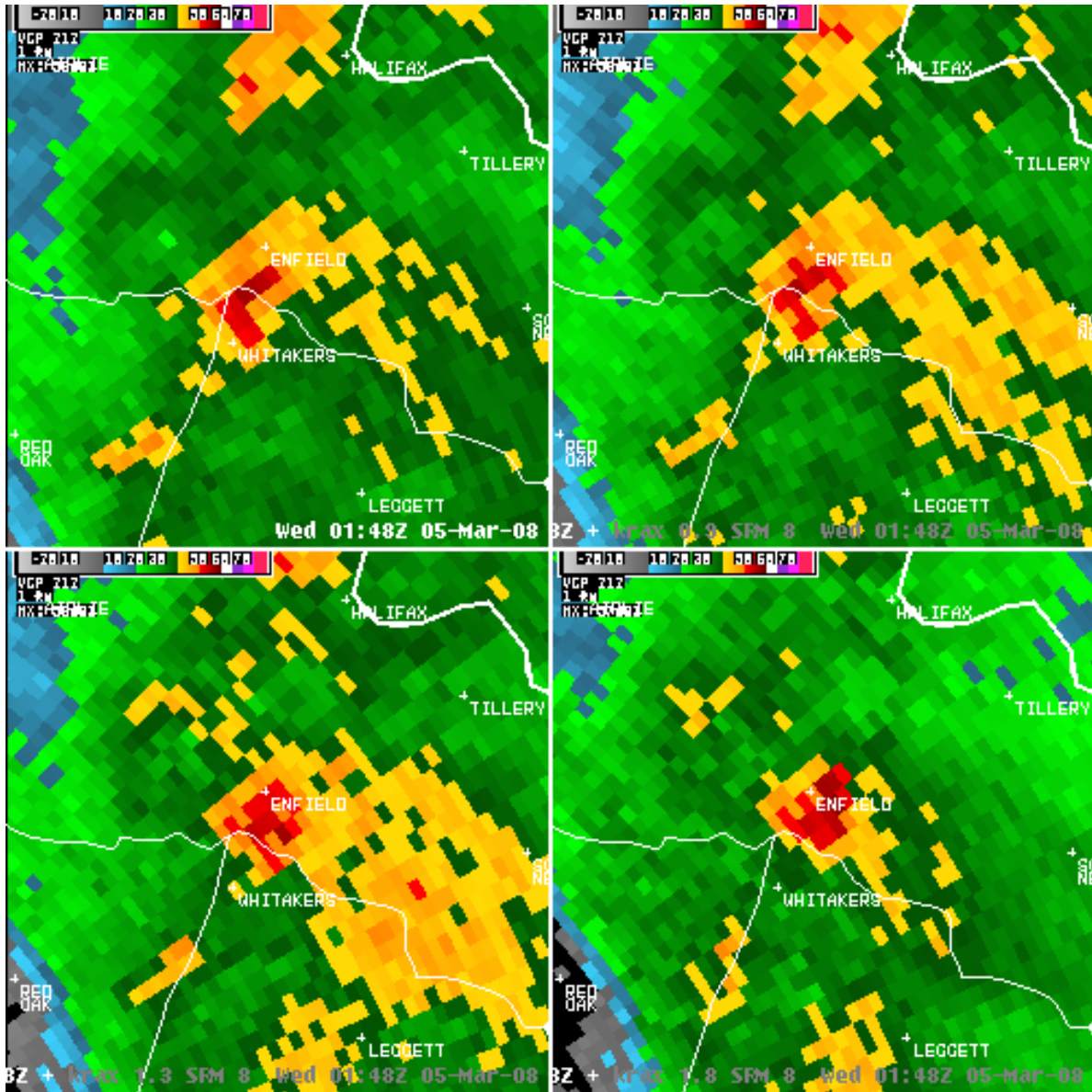


Figure 2.13. Four-panel reflectivity imagery from the Raleigh, NC WSR-88D (KRAX) on 5 March 2008 at 0148 UTC showing four radar tilts (0.5° , 0.9° , 1.3° , and 1.8°) during an HSLC tornado event. Note that this is an embedded miniature supercell. Image courtesy of National Weather Service, Raleigh, NC.

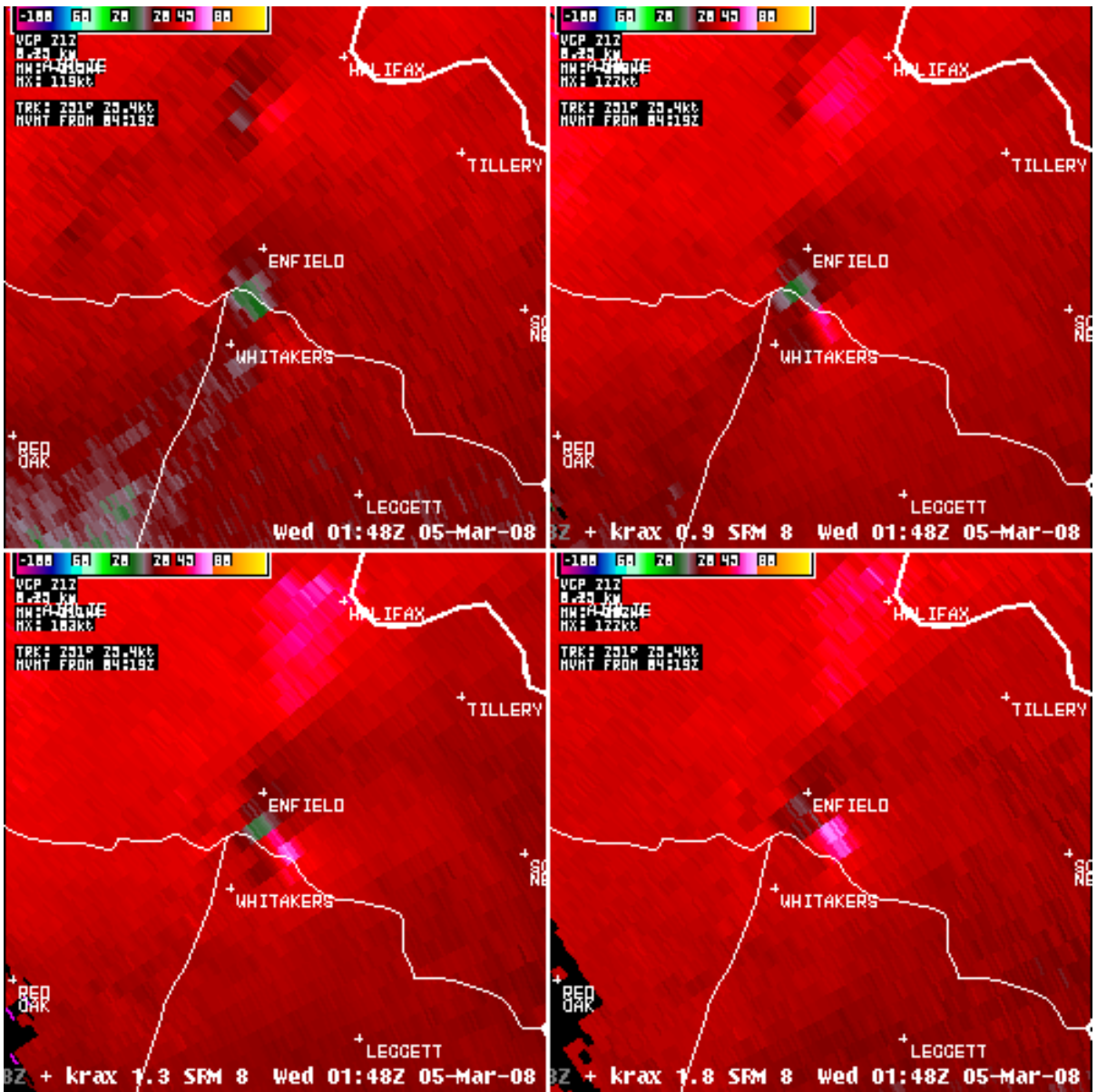


Figure 2.14. As in Fig. 2.13, but for storm-relative velocity.

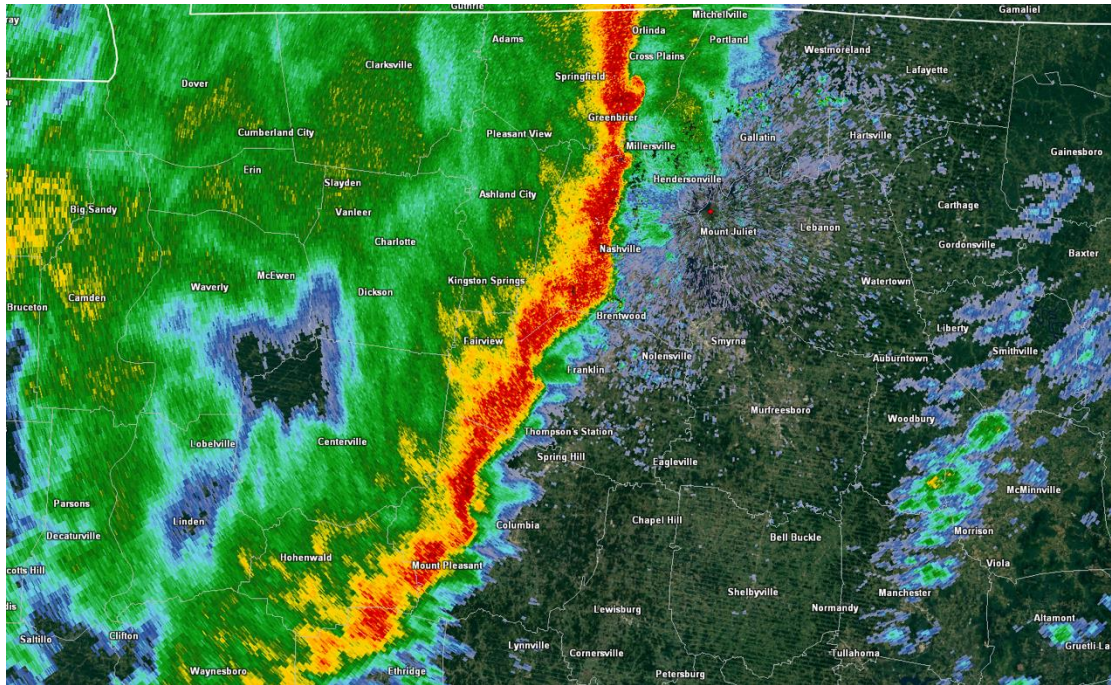


Figure 2.15. Radar reflectivity from the Nashville, TN WSR-88D (KOHX) on 30 January 2013 at 0900 UTC while an HSLC QLCS tornado outbreak was in progress. Note numerous hook-like appendages along the leading edge of the QLCS, many of which were associated with tornadoes.

CHAPTER 3

HSLC Idealized Simulations: Results and Discussion

3.1 Control Simulation

a. Overview

The purpose of the control run is to establish a baseline for behavior in a typical HSLC environment. As a reminder, the base-state profile used in the control simulation is provided in Figure 2.8. This environment exhibits 30 kt of 0-1 km shear vector magnitude and a 0-3 km lapse rate of 6.3 K km^{-1} , which lie near the most skillful discriminatory values of each parameter based on prior HSLC studies (e.g., Sherburn and Parker 2014). Within the control simulation, convection was fairly slow to develop, with appreciable updrafts (i.e., $w \geq 10 \text{ m s}^{-1}$) first appearing nearly two hours¹⁶ after the model was started. Convective updrafts tended to originate within 10 km of the leading edge of the initiating cold pool, which retreated westward relative to the domain's motion prior to the development of convection. Initial updrafts were likely aided—and perhaps organized—by convective rolls that developed as midlevel cool air was advected eastward atop relatively warm near-surface air due to strong low-to-midlevel shear, leading to destabilization in the lowest 3 km (Fig. 3.1). Although the details of the physical mechanisms may differ, this rapid destabilization in the one or two hours leading to HSLC convection is reminiscent of that shown in real-case simulations by King et al. (2017). Following initiation, convective evolution proceeded rapidly, with upscale growth into a QLCS occurring over the next 30-60 min (Fig. 3.2). Convection then progressively moved east of the initiating boundary due to the ambient environmental flow and the establishment of a system-generated cold pool (Fig. 3.3).

¹⁶ This time scale was somewhat unexpected, but the environmental evolution that provided organic development of convection was important and worth the upfront computational demand.

Beyond 3 h, embedded rotating updrafts became apparent, as shown in Hovmöller diagrams of 2-5 km updraft helicity and near-surface¹⁷ vertical vorticity (Fig. 3.4). These features correspond to embedded supercellular structures within the predominant QLCS mode, which are supported by the favorable lower and middle tropospheric wind profile. The co-existence of QLCS and supercellular structures suggests that the magnitude of the forcing, and the orientation of the wind profile relative to the forcing, may both be key elements in dictating the ultimate mode of convection. This point will be explored further in Section 3.2c. In addition to rotating updrafts, numerous weak, near-surface vortices became established along the leading edge of the system-generated cold pool, which was distinct from the initiating cold pool farther to the west. New updrafts occasionally developed near and just ahead of this QLCS, including the strongest updraft of the simulation that became dominant just prior to 4 h into the simulation (Fig. 3.5; can also be identified at approximately $y = -10$ km after $t = 200$ min in Figs. 3.2 and 3.4). This updraft exhibited persistent rotation and a hook echo and eventually supported a series of strong, near-surface vortices (Fig. 3.4, beyond $t = 250$ min between $y = -20$ km and $y = -10$ km) before weakening near the end of simulation time (270 min).

Over the last 30 minutes of the control simulation, positive vertical vorticity is essentially ubiquitous along the cold pool's leading edge¹⁸ north of the dominant updraft (Fig. 3.11). Meanwhile, additional, subtle maxima and minima of vertical vorticity appear to be emanating from the convective downdrafts (Fig. 3.12; note alternating positive and negative bands of vorticity south of the primary downdraft, annotated by "P" and "N"). In terms of their basic positioning, these two zones of vertical vorticity (Fig. 3.13) somewhat resemble the "rivers" feeding a near-surface vortex in a high-CAPE supercell simulated by Dahl et al. (2014). Trajectory analysis confirms that there are indeed two primary source regions for the air parcels that are eventually converged into a strong vortex (Fig. 3.14).

¹⁷ "Near-surface" here and throughout refers to the bottom physical model level.

¹⁸ Note also a secondary zone of vertical vorticity farther west, potentially demarcating an internal boundary.

Parcels initially contributing to the strong vortex in the control run had very little vertical vorticity (i.e., $\leq 0.01 \text{ s}^{-1}$) as they approached the updraft from the two aforementioned source regions. In the ten to fifteen minutes prior to contributing to the vortex, these parcels approached the updraft along or very near the bottom model level. Tilting of vorticity into the vertical was fairly modest as parcels entered the updraft. As in prior tornadogenesis studies, stretching was the primary contributor to the rapid development of vertical vorticity as the parcels ascended within updraft (Fig. 3.15). Vertical vorticity typically¹⁹ exceeded 0.1 s^{-1} by an altitude of 180 m, and the vast majority of stretching (and thus enhancement of vertical vorticity) occurred in the lowest 0.5 to 1 km above ground (Fig. 3.15), which provides evidence that strong low-level updrafts were critical for the intensification of near-surface HSLC vortices.

In light of the importance of stretching to the most intense low-level vortices, it is worthwhile to isolate and study the strongest low-level updrafts that occur in the control simulation. The updraft tracking algorithm introduced in Section 2.6 identified over 30 low-level updrafts that persisted for five or more minutes in the control simulation (Fig. 3.16). Five of these had lifetimes of over 20 minutes, including the strongest that is explored in more detail throughout this section. In addition to a count of updraft features tracked, the algorithm identified their mean duration and mean maximum intensity. For the control simulation, the mean maximum intensity was approximately 18 m s^{-1} , while the mean duration was about 12 minutes. While this lifetime may seem short based on conventional thinking of the updraft life cycle (e.g., Byers and Braham 1948), the algorithm was designed to specifically identify updrafts in the lowest 1.5 km AGL, which were shown above to be particularly important for the development of near-surface vortices. These tended to be shorter-lived than the core convective updrafts aloft. Additionally, the way in which the algorithm treats updraft mergers may overstate the number of short-lived features. For example, if there were two distinct centers of vertical velocity in close proximity within a

¹⁹ Using the 75th percentile of lowest height at which each parcel acquired vertical vorticity of 0.1 s^{-1} .

developing updraft and these two features “merged” as the updraft strengthened, only one feature would then continue to be tracked, giving the other feature a relatively short reported “lifetime”. Despite these caveats, tracking statistics are still useful for identifying updrafts worthy of study and for comparisons among the different sensitivity tests.

Likewise, the vortex tracking algorithm was useful in determining which environments were the most prolific vortex producers. In the control simulation, 35 low-level vortices were identified (Fig. 3.17). These tended to be a bit shorter-lived, with a typical duration of approximately seven minutes for the control run. The short vortex durations are unsurprising, given operational anecdotal evidence of rapid strengthening and demise of HSLC vortices. However, some longer-lived vortices with lifetimes over 15 minutes were also identified. The strongest vortices were not necessarily the longest lived; instead, vortex strength again appeared to be more dependent upon the strength of the overlying low-level updraft (Fig. 3.18). This provides further support for the contention that the strength of low-level updrafts appears to be a considerable factor in the potential intensification of near-surface vortices. The forcing mechanisms for these low-level updrafts will be explored next.

b. Vertical accelerations

For the purposes of this discussion, we will focus on the strongest updraft in the control simulation, which also supported the longest-lived vortex. Focusing on this one particular updraft allows for a clear depiction and discussion of the processes that lead to low-level vortexgenesis. However, this updraft was not the only strong updraft in the simulation. Within the control run, low-level updrafts frequently exceeded 20 m s^{-1} . Given that these values existed very close to the height of the LFC, it is likely that any buoyant accelerations were augmented by other processes. Indeed, within mature updrafts, positive low-level accelerations attributable to the dynamic perturbation pressure gradient acceleration components (ACCD; Fig. 3.19) appear to be more critical for low-level accelerations than the buoyant perturbation pressure gradient acceleration (ACCB), which are generally much more modest (Fig. 3.20). Additionally, ACCD maxima correlate well with the strongest embedded

updraft (Fig. 3.19). This was further supported by examining the characteristics of parcels entering the updraft, the accelerations for which were dominated by ACCD (Fig. 3.21; cf. Figs. 3.22 and 3.23). Parcels approaching the updraft exhibited predominantly horizontal motion prior to reaching the region of strong upward-pointing ACCD, confirming that this acceleration was necessary for the appreciable low-level updrafts (Fig. 3.24).

By breaking ACCD down into its linear (ACCDL) and nonlinear (ACCDNL) components, it becomes clear that the ACCDNL terms are most important for strengthening and maintenance of the core of this updraft. Indeed, ACCDNL maxima through time are correlated well with the maxima in vertical velocity (Fig. 3.25), while ACCDL maxima and minima generally straddle the maximum updraft (Fig. 3.26). These findings are in line with theory, given that high and low pressure perturbations attributable to the linear dynamic terms develop on the upshear and downshear sides of the updraft; additionally, those associated with the nonlinear terms tend to be located beneath areas of rotation, which are maximized near the updraft in this case. In addition, this finding is consistent with prior investigations of supercell simulations (e.g., Weisman and Rotunno 2000; Markowski and Richardson 2014; Coffey and Parker 2017), particularly those in environments with limited CAPE (e.g., McCaul and Weisman 1996), who found that ACCD—and particularly ACCDNL—was dominant in supercell updrafts.

At 3 km above the ground, the dynamic accelerations flip sign, with both ACCDL and ACCDNL becoming *downward* (e.g., cf. Figs. 3.26 and 3.27 at $t=255$ min to the northeast and southwest of the updraft or cf. Figs 3.25 and 3.28 at the same time near the updraft core; also see trajectories in Figs. 3.22-3.24). For ACCDL, the sign flip is likely associated with a rotation of the shear vector from southwesterly to northwesterly around 3 km above ground. Regardless, the magnitude of ACCDL remains well below that of ACCDNL, while the maxima and minima continue to straddle the updraft core. Thus, its overall effect on the updraft strength appears to be secondary. For ACCDNL, this sign flip results from a decrease in vertical vorticity between 2 km and 3 km in height (Fig. 3.29 note loss in orange shading above 3 km beginning after $t=240$ min); in other words, the embedded

mesocyclone is strongest below 3 km. This change in sign could have ramifications on storm depth, as the updraft top within HSLC environments may be somewhat influenced by the height of maximum vertical vorticity.

The updraft explored throughout this section represented the strongest and one of the longest-lived within the control simulation and, subsequently, supported its strongest near-surface vortex. A key contributor to the longevity and intensity of these features is the associated upward-pointing ACCDNL, which is associated with relatively persistent and organized low-to-midlevel vertical vorticity within the embedded supercell. The physical processes linking the strength of the updraft to that of its associated near-surface vortex will be explored in more detail next, followed by a discussion of how these processes vary as low-level lapse rates and shear vector magnitudes change.

c. Processes leading to near-surface vortexgenesis

As noted in Chapter 2, establishing the chain of processes leading from mature convection to the development of strong, near-surface vortices is critical in order to establish physical explanations for the sensitivities associated with varying environmental lapse rates and shear. By determining this chain of processes, we can then assess what processes are hindered in some portions of the parameter space. In Section 3.1a, we identified the importance of a strong low-level updraft in the stretching of vertical vorticity that led to the development of near-surface vortices. In the following section, it was determined that enhanced ACCDNL resulting from the increase in low-to-midlevel vertical vorticity was the key term in strengthening low-level updrafts. Through these analyses, we can then offer the following processes that lead to near-surface vortexgenesis in the control run:

- a) Low-to-midlevel (0.5-km to 2-km) vertical vorticity begins to generally increase as the developing midlevel updraft strengthens;
- b) In response to a), low-level, upward-pointing ACCDNL increases;

c) In response to b), low-level vertical velocities are enhanced, bringing strong updrafts closer to the ground; and

d) Resulting from c), the potential for tilting horizontal vorticity into the vertical and stretching vertical vorticity increases.

Note that these processes exhibit a positive feedback between one another and may not necessarily occur in this order at all times. For example, a strengthening updraft provides the impetus for midlevel vertical vorticity to strengthen early in the storm's life. Thus, these processes should be viewed as working in concert to increase the potential for near-surface vortexgenesis, rather than always a strictly direct sequence of events.

The processes explored above correspond to those that explain the evolution to tornadogenesis in high-CAPE supercell thunderstorms (Markowski and Richardson 2014; Coffey and Parker 2017). Despite the similarities to tornadogenesis in supercells, the interior of this control QLCS seems to possess far more transient and rapidly-evolving features than the long-lived discrete supercells that have historically been studied in tornadogenesis research. In the control run, the primary updraft (explored herein previously) strengthened to over 20 m s^{-1} between 0.5 and 1 km in the minutes preceding rapid intensification of the near-surface vortices (Fig. 3.29). This was a result of ACCDNL exceeding 0.35 m s^{-2} , which followed an enhancement of low-level vertical vorticity to several mesocyclone units (i.e., greater than $0.03\text{-}0.04 \text{ s}^{-1}$; Fig. 3.29). This chain of processes appears to begin several minutes prior to the development of the near-surface vortex. In fact, approximately 20 minutes passes from the initial enhancement of 1-2 km vertical vorticity to the rapid intensification of the near-surface vortex. This suggests the potential for lead time during real-time warning operations of these events, assuming radar coverage is sufficient to observe the trends of low-to-midlevel rotation and that the model is accurately representing the real within-storm processes. However, this chain of processes is also likely associated with a nonzero, yet-to-be-determined false alarm rate.

Potential failure points in the series of processes leading to vortexgenesis will be examined in the following section across the varying environmental base states. It is

theorized that, among other sensitivities, the decreased low-level lapse rate (-03lr) simulation may struggle to support initially strong low-level updrafts given extremely modest instability in the lowest 3 km above ground. In this case, the initial updraft may simply be too weak to support the ultimate development of a strong, near-surface vortex. With decreased 0-1 km shear vector magnitude (-01s), it is suspected that the production of low-to-midlevel vertical vorticity will be limited, given the documented sensitivity of low-level vertical vorticity production to low-level shear in both supercells and QLCSs. This could preclude the strengthening of a low-level updraft that precedes vortexgenesis. It is also plausible that vertical vorticity may not exist at the surface in some cases and may struggle to be generated via some internal storm dynamics. This would obviously preclude convergence and stretching of vorticity and, thus, the development of a vortex. However, *assuming the convection can produce and maintain a sufficiently strong cold pool*, it is suspected that each environment will produce near-surface vertical vorticity that could potentially be converged and stretched. This follows the control simulation detailed above, which showed plentiful vertical vorticity within the cold pool, and Coffey and Parker (2017), who posited that this final step in the process of tornadogenesis was nearly entirely dependent on *above-ground* (i.e., not surface) storm characteristics, given that sufficient near-surface vertical vorticity was present in both tornadic and nontornadic supercells. With these hypotheses in mind, we can now begin to evaluate their validity via the various sensitivity simulations.

3.2 Sensitivity Tests

a. Impact of varying lapse rates and shear vector magnitude

In our preceding environmental studies of HSLC convection, low-level lapse rates and shear vector magnitudes have consistently shown skill at discriminating between severe and nonsevere events. Specifically, severe events are more likely to occur in environments with steeper low-level lapse rates and increased low-level shear vector magnitudes. A primary

goal of these sensitivity studies is to elucidate the physical mechanisms governing this documented skill.

Convective mode generally differs little across the matrix of five simulations (cf. Fig. 3.2 and Fig. 3.30), even as the areal coverage of convection varies somewhat. However, Hovmöller plots reveal considerable differences in rotational characteristics between the runs. In particular, it appears that low-level shear vector magnitude plays a substantial role in both the number of incipient near-surface vortices that develop and the strength and longevity of rotating updrafts. With a decreased 0-1 km shear vector magnitude (-01s), the number of near-surface vortex tracks decreases greatly (Fig. 3.31), while the opposite is true when the 0-1 km shear vector magnitude is increased (+01s; Fig. 3.32). Additionally, +01s supports a long-lived rotating updraft, while rotating updrafts in -01s tend to be transient compared to the control simulation or +01s. Similarly, with a stabilized 0-3 km lapse rate (-03lr), rotating updrafts are fairly weak and short-lived (Fig. 3.33), whereas with an increased 0-3 km lapse rate (+03lr), the strongest updrafts and vortices across the matrix of simulations were observed (Fig. 3.34). The most prominent sensitivities in the lapse rate tests appear to be associated with the *number* of strong, rotating updrafts and the typical *strength* of near-surface vortices; both of these decrease as 0-3 km lapse rate decreases.

Results from the tracking algorithms corroborate these findings (Figs. 3.35, 3.36). Compared to the control simulation, the number, strength, and longevity of updrafts and vortices decrease in -03lr and -01s, while they generally increase or are comparable to the control run for +03lr and +01s. Additionally, as either 0-1 km shear vector magnitude or 0-3 km lapse rates increase, the distributions of ACCD and ACCB within long-lived (i.e., duration ≥ 20 min) updrafts shift towards higher values (Fig. 3.37). Notably, ACCD is almost always larger than ACCB within these updrafts, regardless of the associated environment, as was documented in the control run. To further compare the simulations in their entirety, we use plots of exceedance frequency; in other words, we calculate the number of times a given threshold value of a field was met or exceeded over the course of each simulation. Here, we use thresholds of 0.03 s^{-1} , 0.3 m s^{-2} , and 20 m s^{-1} for vertical vorticity (Fig. 3.38), ACCDNL

(Fig. 3.39), and vertical velocity (Fig. 3.40), respectively. Given that the processes of utmost importance appeared to be limited to the low levels, we focus our analysis on the surface to 1.5 km above ground layer.

Low-level vertical vorticity appears to be largely dependent on the magnitude of low-level shear, given approximately an order of magnitude increase in the number of occurrences of vertical vorticity of at least 0.03 s^{-1} across the lowest 1 km in +01s compared to -01s (Fig. 3.38). This gives +01s a considerable advantage over -01s in the chain of processes leading to near-surface vortexgenesis and contributes to increased ACCDNL (Fig. 3.39) and, accordingly, vertical velocity (Fig. 3.40) in the lowest 1 km. The primary difference between +03lr and -03lr lies in the vertical velocity, where an order of magnitude increase is again noted in +03lr throughout most of the lowest 1.5 km when compared to -03lr (Fig. 3.40). Comparable differences are noted in ACCDNL (Fig. 3.39), while exceedance frequencies for vertical vorticity are a bit more similar (Fig. 3.38). Interestingly, the +01s vertical vorticity exceedance frequencies outpace those in +03lr, while +03lr has larger exceedance frequencies at most heights for ACCDNL; this is likely because +01s has *more* low-level vortices, but those that form in +03lr tend to be *stronger*. Altogether, this analysis supports the contention that steeper low-level lapse rates support stronger low-level updrafts, while low-level shear vector magnitude affects the number and strength of embedded rotation centers within the updrafts (i.e., low-level mesocyclones). The ideal HSLC environment for the development of severe hazards would exhibit both steep low-level lapse rates and large low-level shear vector magnitude in order to benefit from both of these sensitivities. With these broad differences in the distributions in mind, we can shift our analysis to the strongest updraft in each case to investigate the relevant processes in more detail.

Within the strongest updraft of -01s, low-level ACCD is considerably weaker than in the control simulation (Fig. 3.41). This can be attributed primarily to ACCDNL (Fig. 3.42), which is limited due to a lack of low-level vertical vorticity (Fig. 3.43). Thus, as suggested above, the failure point as low-level shear vector magnitude decreases appears to be a lack of

sufficient dynamic forcing for ascent due to decreased low-to-midlevel vertical vorticity. This limits the strength of low-level updrafts and precludes the convergence and stretching of near-surface vertical vorticity, which is generally present once a cold pool is established in all of the primary matrix simulations. Therefore, there is likely a minimum value of 0-1 km shear vector magnitude necessary for the development of strong, long-lived, low-level vortices capable of producing tornadoes or damaging straight-line winds within HSLC environments. However, it is important to note that even with this less favorable base-state environment, convection-induced modifications to the environment over time (such as localized backing of the winds and broadening of the hodograph, thus increasing low-level shear vector magnitude and storm-relative helicity) can lead to localized potential for the development of rotating updrafts and near-surface vortices late in the simulation.

As low-level shear vector magnitude increases beyond the control value, the response is not entirely straightforward. The number of near-surface vortices indeed increases in +01s (as shown in Fig. 3.36), but embedded rotating updrafts become less organized. As the 0-1 km shear vector magnitude increases, the environmental Richardson number within this idealized framework falls well below the critical value of 0.25, leading to the development of widespread turbulence. Within +01s, this does not disrupt the convection to a point where near-surface vortices are precluded. Low-level ACCD fields associated with the strongest updraft remain sufficient to produce appreciable updrafts in the lowest 1 km, facilitating the development of an intense surface vortex, albeit one that is weaker and shallower than in the control simulation (Fig. 3.44). However, in a supplemental simulation with 0-1 km shear vector magnitude of 50 kt (i.e., 10 kt stronger than in +01s), tracked updrafts become shorter-lived and weaker on the mean (not shown). Thus, in addition to the minimum threshold of 0-1 km shear vector magnitude for the development of severe hazards in HSLC environments, it is possible that there is a threshold beyond which increasing low-level shear no longer improves the potential for the production of severe hazards. It may also be that, in such strongly sheared environments with low Richardson numbers, a fully turbulent representation of the atmospheric boundary layer is essential in order to acquire a statistically steady

ambient environment; this would avoid the possibility that the convection is being inhibited by the sporadic release of Kelvin-Helmholtz instability on the model grid.

Based on Figs. 3.35 and 3.36, steepening 0-3 km lapse rates clearly leads to an increase in the severe potential of HSLC convection, given the environment's ability to produce stronger and longer-lived low-level updrafts and vortices. This is supported by a vertical time series of the strongest updraft (Fig. 3.45), which shows a rapid increase in low-level vertical vorticity and the subsequent development of an intense near-surface vortex. Interestingly, the strongest updraft from -03lr appears fairly similar to that in +03lr via the vertical time series (Fig. 3.46), but there is a key distinguishing feature: There is a distinct lack of vertical vorticity *at the surface* in -03lr. This could be a result of the updraft's timing within the evolution of the greater convective system, as the updraft developed early in the simulation and approximately 90 minutes prior to the strongest updraft in +03lr. At this time, the cold pool was not yet mature in -03lr, and any vertical vorticity along its leading edge was very weak. Comparing updrafts at similar times in the simulation, another sensitivity becomes apparent: the initial strength of updrafts in -03lr tend to be weaker (Fig. 3.47), which hinders the remaining processes in their ability to produce a strong, near-surface vortex. Generally, the weaker *initial* updrafts can likely be attributed to weaker buoyancy in -03lr compared to the ambient environment (cf. Figs. 3.48 and 3.49), although ACCD is notably weaker early in the lifetime, as well (and particularly later in the lifetime; cf. Figs. 3.50 and 3.51). Taking the points made here together, it appears that both the associated environment *and* the availability of near-surface vorticity both play a role in the potential severity of HSLC convection.

Across the five preceding simulations, the most intense vortices are associated with the largest lowest-level wind speeds and vertical vorticity, and these vortices tend to be affiliated with the updrafts that are the strongest. The results suggest that decreasing either low-level lapse rates or low-level shear vector magnitude decreases the potential for stronger, longer-lived, and more numerous low-level updrafts and near-surface vortices through both the initial baseline updraft strengths and feedbacks associated with the ACCDNL that

develops beneath rotation aloft. These basic sensitivities help explain the parameters identified as the most skillful in the environmental study of Sherburn and Parker (2014) and the results from Chapter 1 (i.e., the potential for tornadoes and damaging straight-line winds increases statistically with steepening lapse rates and increased shear vector magnitudes).

b. Role of Coriolis forcing

As discussed in the overview of the 29-30 January 2013 severe HSLC QLCS case, it is plausible that the convergence of planetary vorticity may augment the production of surface vorticity in particularly long-lived HSLC QLCSs. Further, as noted in Chapter 2, the inclusion of Coriolis has been suggested to be necessary for the dominance of cyclonic vortices within numerical studies of QLCSs. Thus, an additional simulation using the control base state but *excluding* Coriolis was performed to assess any changes in convective mode and the production of near-surface vortices. The non-Coriolis control simulation produced a similar convective mode to the original control simulation—a QLCS with embedded rotating updrafts—but also exhibited several key differences, many of which are difficult to isolate from one another. It is worth noting, however, that (unlike in the studies by Weisman and Trapp 2003 and Trapp and Weisman 2003) the strongest and longest-lived vortices were still cyclonic even when Coriolis forcing was excluded. Thus, findings from prior QLCS studies that determined Coriolis was *necessary* for the dominance of cyclonic vortices appear to not hold here. Presumably, this is because the hodographs employed here possess realistic clockwise curvature, which favors the development of cyclonically-rotating updrafts and vortices and could be argued to inherently include the effects of Coriolis in the base state; prior idealized work on QLCSs has largely utilized straight-line hodographs, which would not have favored either cyclonic or anticyclonic vortices (e.g., Trapp and Weisman 2003).

A lack of Coriolis—predictably—plays a role in the availability of low-level vertical vorticity. Indeed, the number of incipient near-surface vortices drastically decreases in the non-Coriolis control run when compared to the original (cf. Figs. 3.52 and 3.53). In fact,

appreciable vertical vorticity ($\geq 0.01 \text{ s}^{-1}$) is essentially ubiquitous in the Coriolis simulation (Fig. 3.54), while it is much more localized in the vicinity of stronger updrafts in the non-Coriolis simulation (Fig. 3.55). Even in supplementary idealized simulations without moisture included, this sensitivity holds, as no appreciable near-surface vertical vorticity emerges without the inclusion of Coriolis (not shown). This sensitivity is likely attributable to the convergence of planetary vorticity through time via the perturbation winds.

One additional impact of Coriolis is its role in outflow motion. When Coriolis is included, westerly perturbation winds—such as those associated with outflow or an eastward-progressing cold pool—are subject to a southward deflection (cf. Figs. 3.56 and 3.57). Over time, this slows progression of the initiating cold pool, which ultimately leads to convection outpacing this boundary as it matures in the original control run (and subsequently evolving along its own, system-generated cold pool; Fig. 3.3). Without this rightward deflection and subsequent slower movement, the initiating cold pool remains closer to the QLCS as it evolves (cf. Figs. 3.3 and 3.58). This could promote linear development and restrict the ability for any particular updraft to become discrete. These characteristics are also impacted by hodograph orientation relative to the boundary, which will be explored in the next section.

The differences between the Coriolis and non-Coriolis simulations appear to be primarily attributable to the convergence of planetary vorticity. The convergence of planetary vorticity augments the near-surface vorticity that develops via other means and contributes to widespread appreciable vertical vorticity at the lowest model level, a sensitivity that persists even in highly idealized simulations without moisture. This ultimately supports stronger low-level updrafts and vortices in the simulation with Coriolis. However, it is worth reiterating that *both simulations produce embedded supercell features within the QLCS, and both simulations support the development of a long-lived, near-surface vortex* (cf. Figs. 3.5 and 3.59). Furthermore, Coriolis forcing within the model is not necessary for cyclonic vortices to dominate in simulated convection, contrary to the results of prior QLCS studies.

c. Role of shear vector orientation

Prior research has suggested that shear vector orientation relative to an initiating boundary plays a large role in convective mode and the potential for severe hazards, both in high- and low-CAPE environments. Generally, a larger cross-boundary component of the shear vector is conducive to more discrete convective elements, while a shear vector with a large along-boundary component tends to promote linear convective organization (Bluestein and Weisman 2000; French and Parker 2008; Dial et al. 2010). The orientation of the shear vector may also play a role in the most likely severe hazards within HSLC convection. Sherburn (2013) found that HSLC severe weather outbreaks with more than 20 tornadoes tended to have larger cross-boundary shear vector components, while those that produced primarily straight-line winds had larger along-boundary components. Therefore, two additional simulations were conducted with the control hodograph rotated 30° and 60° clockwise to assess the effect on convective strength and evolution. As noted in Section 3.1a, the control environment is suitable for the production of supercells, given the development of embedded rotating updrafts within the simulated QLCS. These sensitivity tests will determine if that contention holds as the hodograph is rotated to produce a larger cross-boundary component of the winds (and shear vectors) compared to the largely along-boundary wind profile in the original control simulation.

The change in convective evolution upon rotating the hodograph relative to the initiating boundary generally conformed to the aforementioned prior research: a larger *cross*-boundary component led to increasingly discrete convection (Figs. 3.60 and 3.61). However, all three simulations (original control and two rotated runs) produce rotating updrafts of comparable strengths, confirming that the environment is favorable for supercells and that their potential strength does not necessarily change regardless of hodograph orientation. Despite their similarly rotating updrafts, the strengths and lifetimes of associated near-surface vortices varies across the simulations. Additionally, the *locations* of these vortices appear to vary. The strongest vortices that develop in the rotated 30° simulation seem to occur at the interface of cold pools from two separate discrete storms, as shown in Figure 3.62. Curiously,

this interaction leads to the development of strong vortices—and low-level updrafts—in regions devoid of appreciable low-level reflectivity (precipitation can develop as the updraft matures and fall farther downstream). This phenomenon is unique to the rotated 30° simulation and is potentially concerning, as it implies that the development of strong, near-surface vortices is plausible even in non-traditional storm-relative locations. This could pose substantial detection difficulties in warning operations during HSLC events, particularly in cases without a clearly-defined, system-generated cold pool that can act as a continuous source of vorticity in the vicinity of developing and maturing updrafts.

Within the rotated 60° simulation, a single discrete cell dominates for much of the run. Via updraft helicity, a continuous rotating updraft is tracked for approximately 150 min within this simulation (Fig. 3.63). This updraft exhibits the longest continuous track of any across the simulations studied here, suggesting that discrete HSLC convection is more favorable for *long-lived* rotating updrafts than HSLC QLCSs. Despite producing a particularly long-lived updraft, any near-surface vortices that form in association with this updraft are relatively weak and short-lived compared to the original control simulation. The reasoning for this sensitivity is tied to the location of near-surface vertical vorticity with respect to the updrafts in each case. As was documented previously, the original control simulation has a persistent zone of vertical vorticity along the leading edge of its cold pool. This zone is well-correlated spatially with updrafts that develop and evolve along the cold pool (Fig. 3.11), proving apt for the convergence and stretching of near-surface vertical vorticity. Outflow associated with the strongest updraft in the rotated 60° run is ill-defined and largely relegated to the rear of the storm due to rapid storm motion (Fig. 3.64). Thus, while the updrafts in this simulation benefit from being discrete, the sources of near-surface vertical vorticity become spatially offset from their convergence and stretching mechanisms, preventing the development of strong, long-lived vortices.

In terms of convective mode, the results of the hodograph rotation tests were consistent with expectations. As winds throughout the troposphere became increasingly perpendicular to the initiating boundary, updrafts became increasingly discrete. Owing to

strong curvature in the hodograph, cyclonically-rotating updrafts were dominant, and with no nearby cells to disrupt the updrafts, these strongest updrafts were longer-lived than those in the original QLCS. In spite of these longer-lived updrafts, however, near-surface vortices were *weaker*. This underscores an important point: Strong, long-lived updrafts cannot support intense near-surface vortices unless they are spatially collocated with one another. As the hodograph is rotated, updrafts were unable to take advantage of the persistent zone of vertical vorticity along the leading edge of the system-generated cold pool. Instead, any vertical vorticity that was generated by the storms' downdrafts existed at the rear of the storm—well behind the strong updrafts. This precluded the strengthening of any near-surface vortices as the hodograph was rotated 60° clockwise. In the rotated 30° simulation, strong vortices only appeared to develop along the interface of colliding outflow boundaries associated with separate downdrafts, where vertical vorticity and brief, strong, low-level updrafts were collocated. Thus, one benefit of a QLCS convective mode in HSLC environments is that it provides a continuous source of near-surface vorticity along the leading edge of its outflow that can be stretched by updrafts that form and mature there.

The rotated hodograph simulations confirm that the control base-state environment is suitable for the production of supercells, given that rotating updrafts occurred in the control simulation along with these two rotated simulations. This is a critical point, as it implies that even in a QLCS, embedded low-to-midlevel rotation is capable of locally enhancing updrafts via increased ACCDNL. Given the height of maximum vertical vorticity in some of these updrafts (i.e., below 3 km), it is plausible that these embedded rotational elements will appear innocuous on radar prior to the development of an intense near-surface vortex, particularly far from radar. However, the results of these simulations are not necessarily consistent with prior cursory studies conducted by the author (Sherburn 2013), which suggested that larger cross-boundary shear components (in isolation) may be associated with a greater potential for tornadoes in these environments. This implies that some process not considered in our idealized framework may be responsible for this environmental sensitivity. In particular, it is possible that the relatively coarse horizontal grid spacing employed here may be insufficient to capture the processes that eventually lead to tornadogenesis within HSLC miniature

supercells or that the prior study identified shear vector orientation as a red herring. Future work should examine these potential concerns by conducting finer resolution simulations of HSLC miniature supercells.

FIGURES

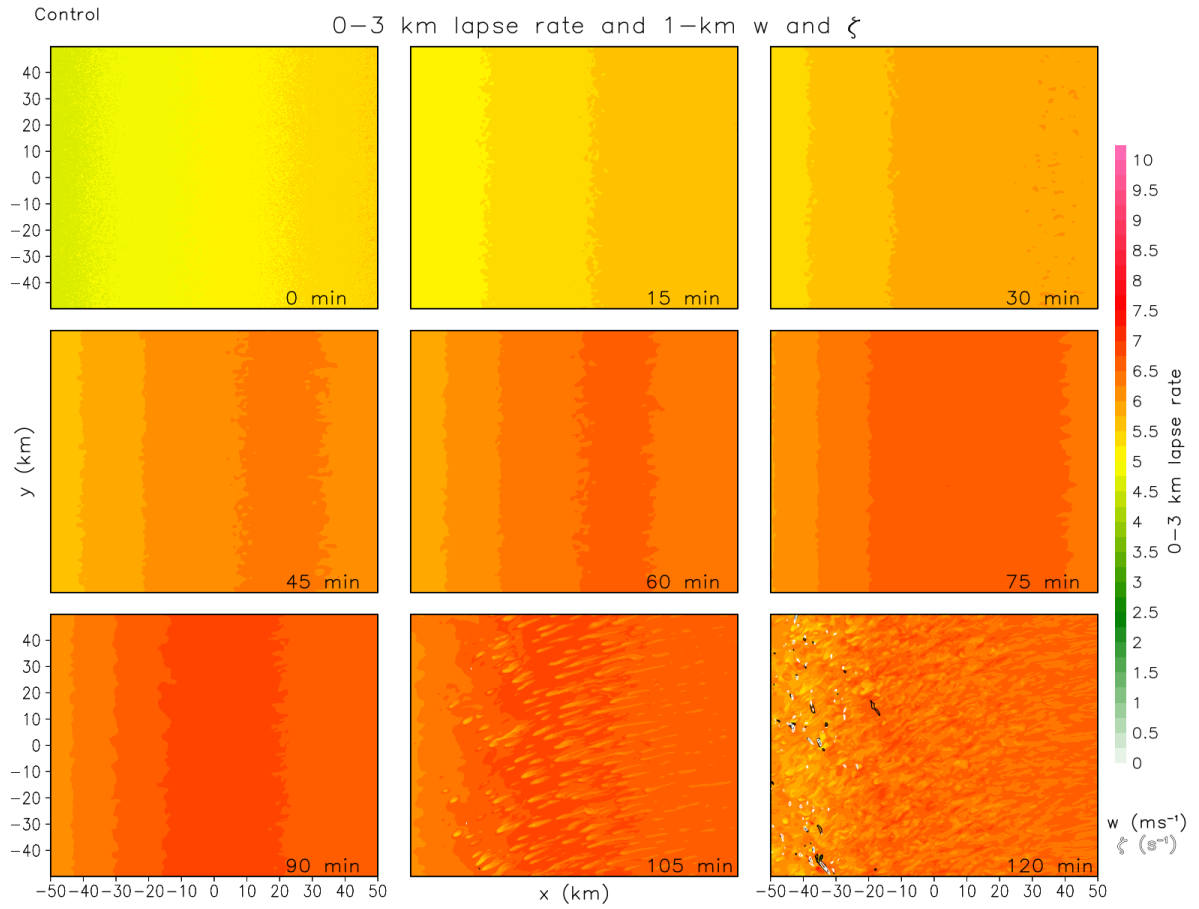


Figure 3.1. Overview of 0–3 km lapse rates (K km^{-1} ; shading, 1-km vertical velocity (m s^{-1} ; black contours), and 1-km vertical vorticity (s^{-1} ; white contours) for the control simulation from $t=0$ min through $t=120$ min over 15-min intervals.

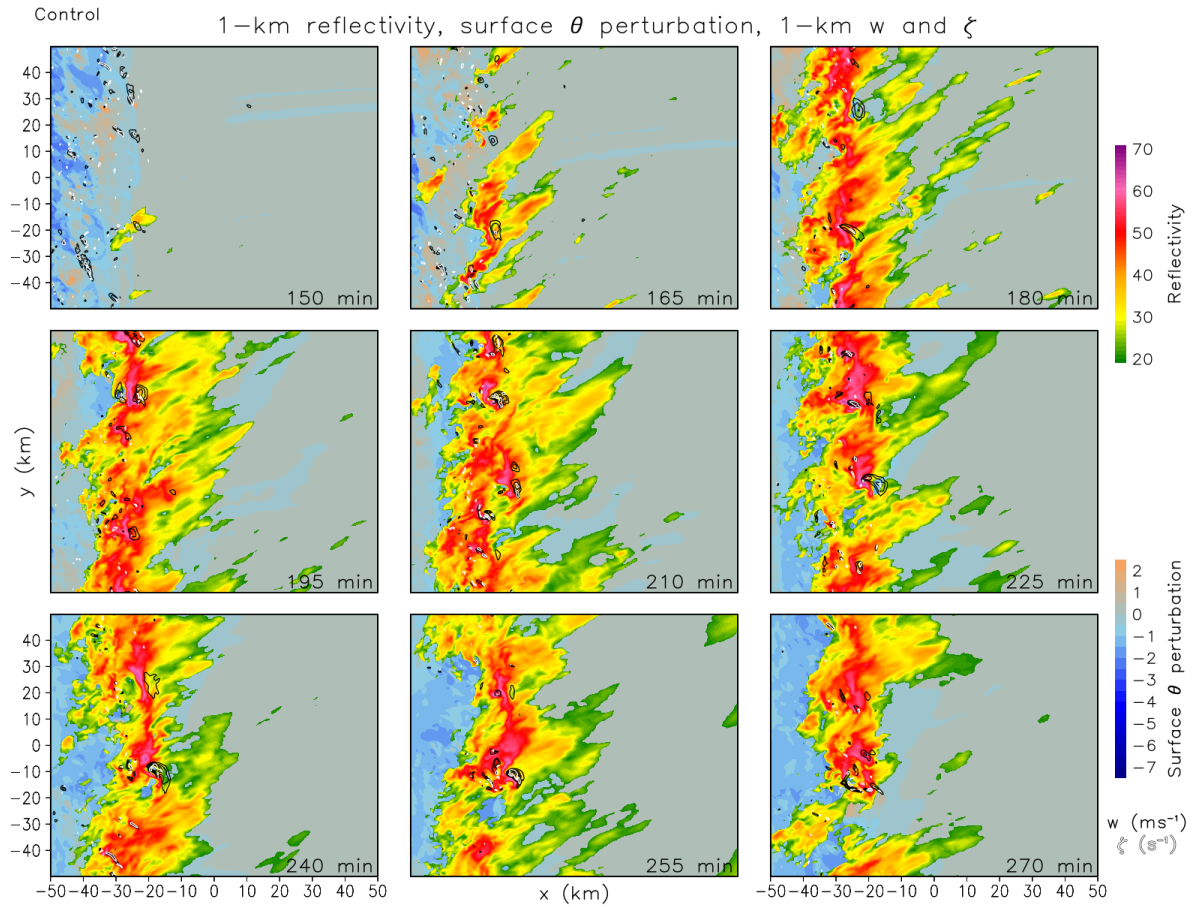


Figure 3.2. Overview of 1-km reflectivity (dBZ; rainbow shading), surface potential temperature perturbation (K; tan to dark blue shading), 1-km vertical velocity (m s^{-1} ; black contours), and 1-km vertical vorticity (s^{-1} ; white contours) for the control simulation from $t=150$ min through $t=270$ min over 15-min intervals.

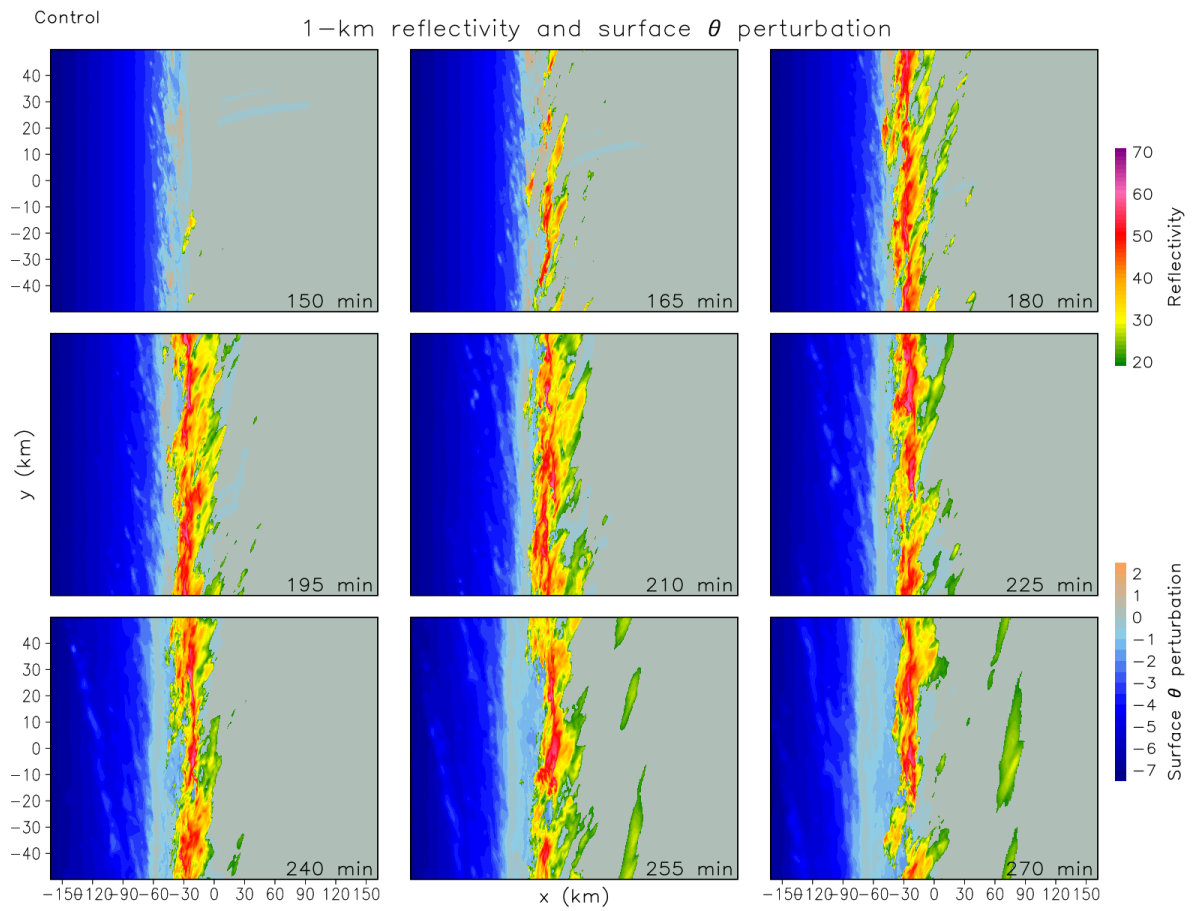


Figure 3.3. As in Fig. 3.2, but zoomed out to show the initiating cold pool's retreat relative to the evolving convection.

Updraft Helicity and Near-Surface Vortex Tracks, Control

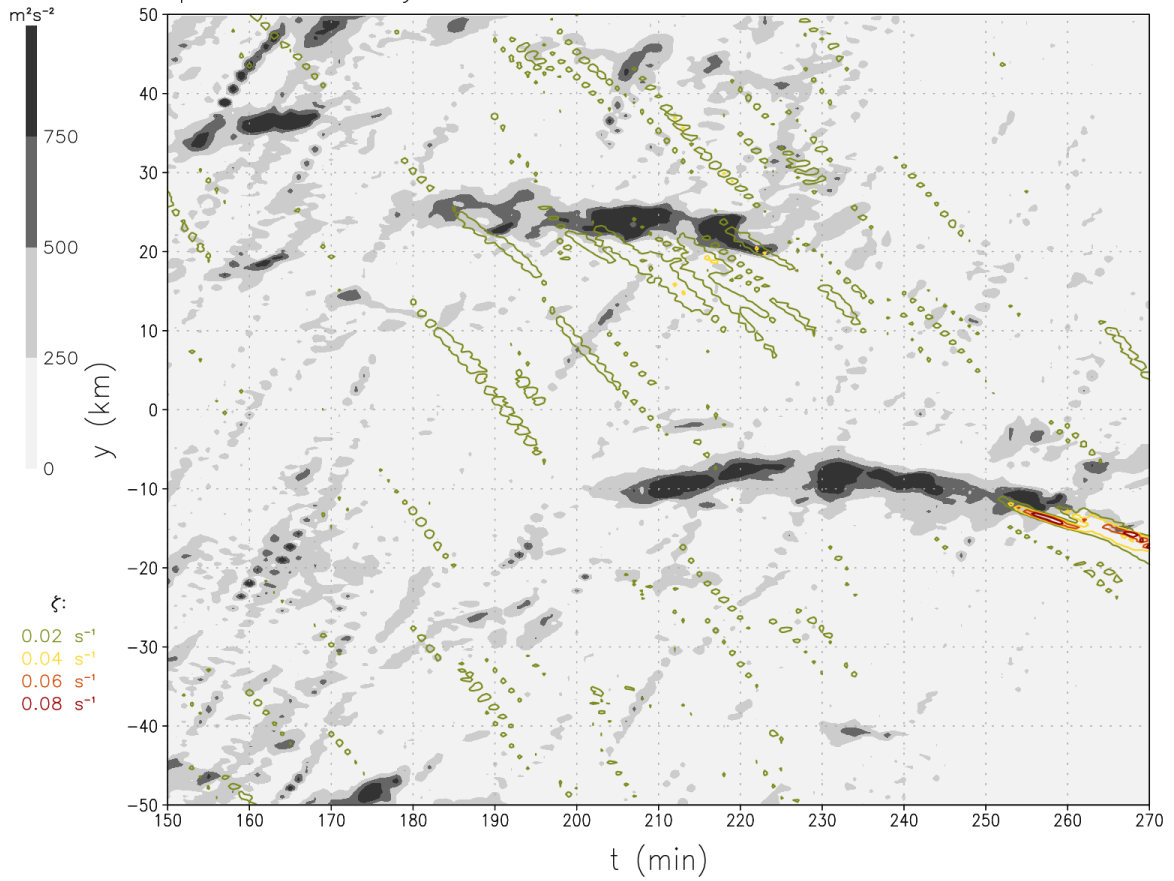


Figure 3.4. Hovmöller plot of 2-5 km updraft helicity (m^2s^{-2} ; shaded) and near-surface vertical vorticity (s^{-1} ; contours) tracks for the control simulation over the time period $t=150$ min to $t=270$ min.

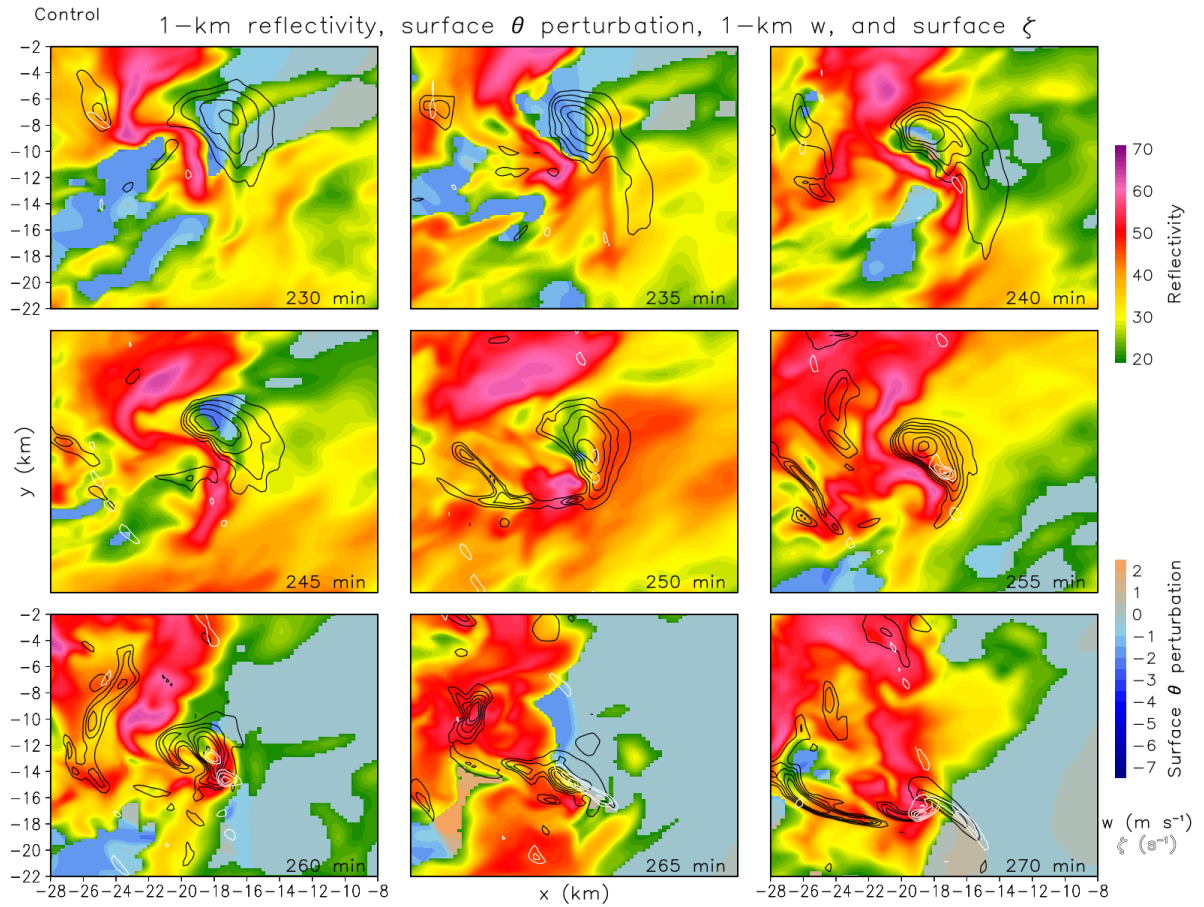


Figure 3.5. Zoomed-in plot of 1-km reflectivity (dBZ; rainbow shading), surface potential temperature perturbation (K; tan to dark blue shading), 1-km vertical velocity (m s^{-1} ; black contours), and 1-km vertical vorticity (s^{-1} ; white contours) for the control simulation's strongest updraft from $t=230$ min through $t=270$ min over 5-min intervals.

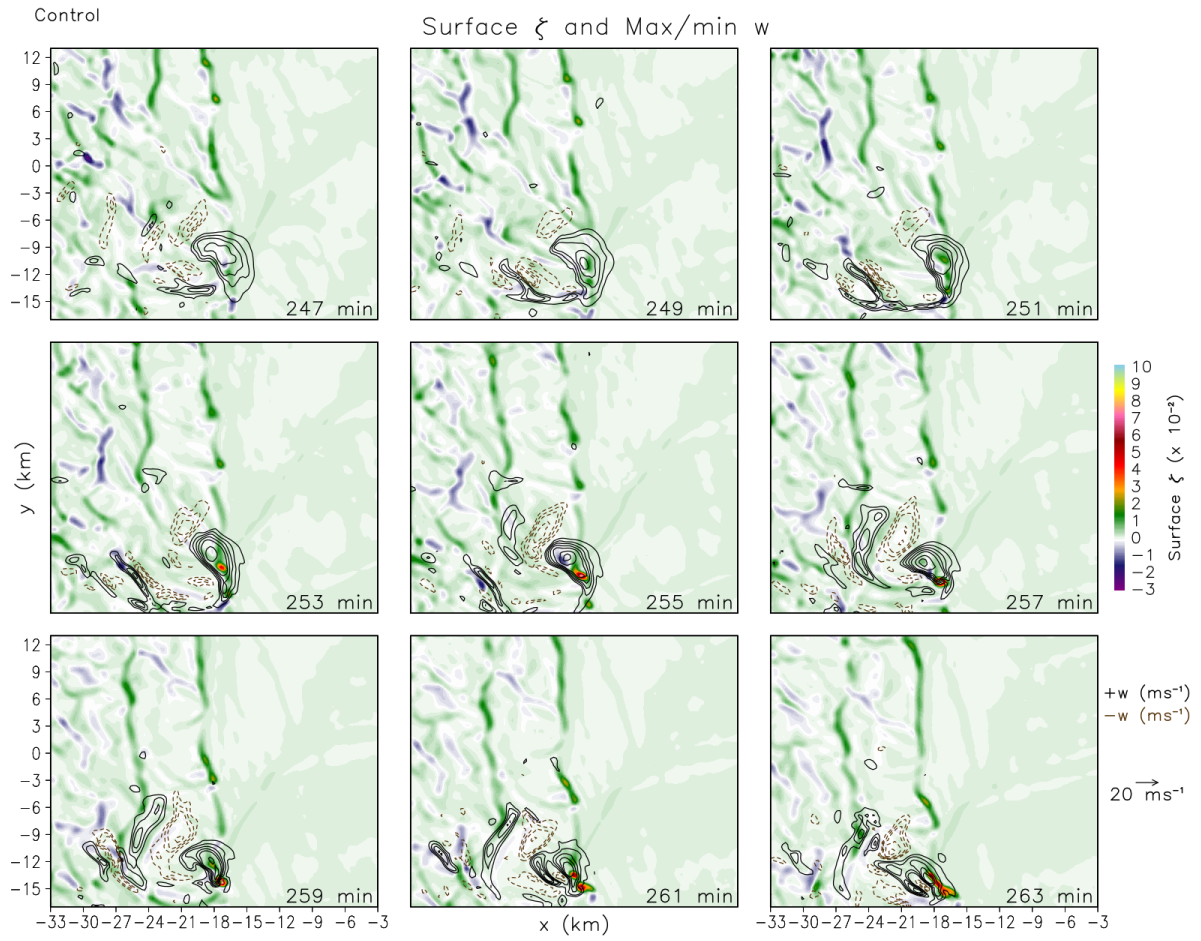


Figure 3.6. Plot of surface vertical vorticity (s^{-1} ; rainbow shading) and maximum (black contours) and minimum (brown contours) vertical velocity in the lowest 1 km (m s^{-1}) for the control simulation's strongest updraft from $t=247$ min through $t=263$ min over 2-min intervals.

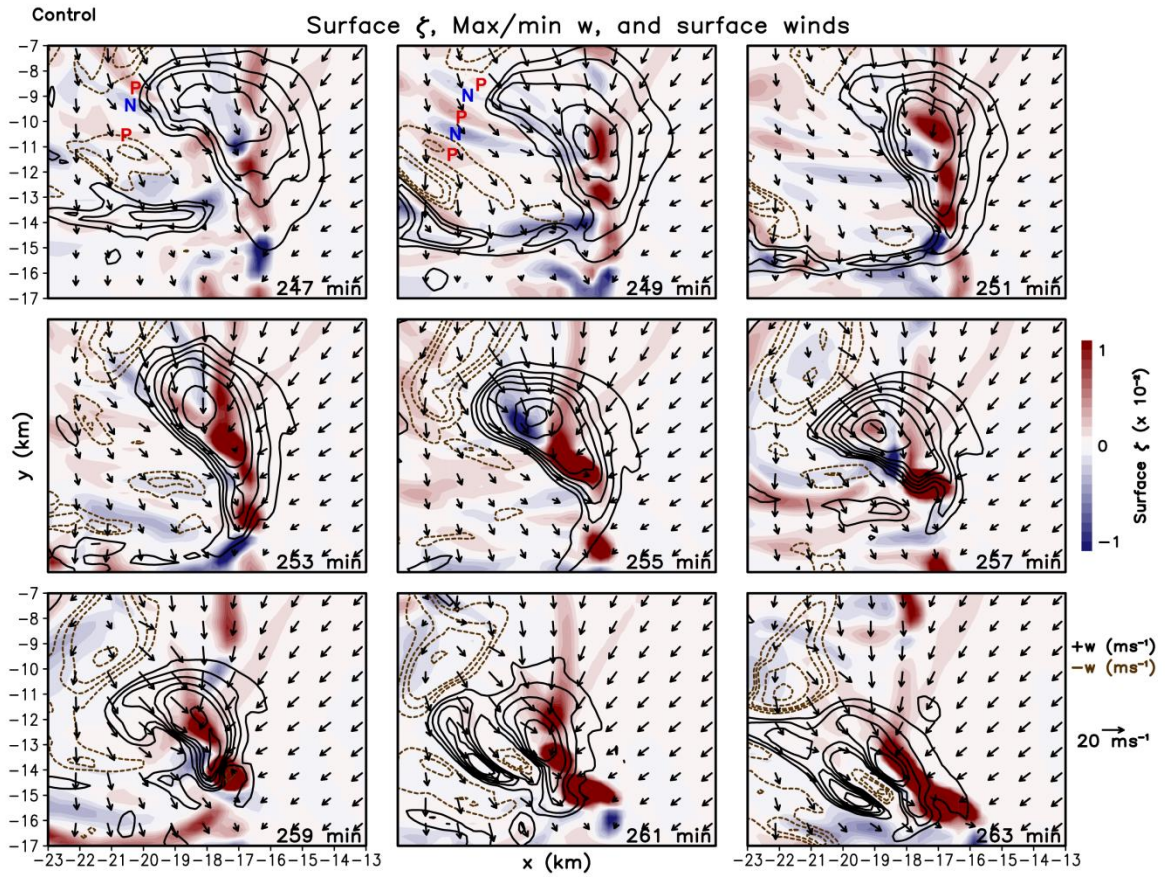


Figure 3.7. As in Fig. 3.6, but zoomed in and including surface wind vectors (m s^{-1}). Note change in color bar meant to highlight lower values of vertical vorticity. Red “P”s and blue “N”s in first two panels show alternating positive and negative bands of vertical vorticity appearing to emanate from the downdraft.

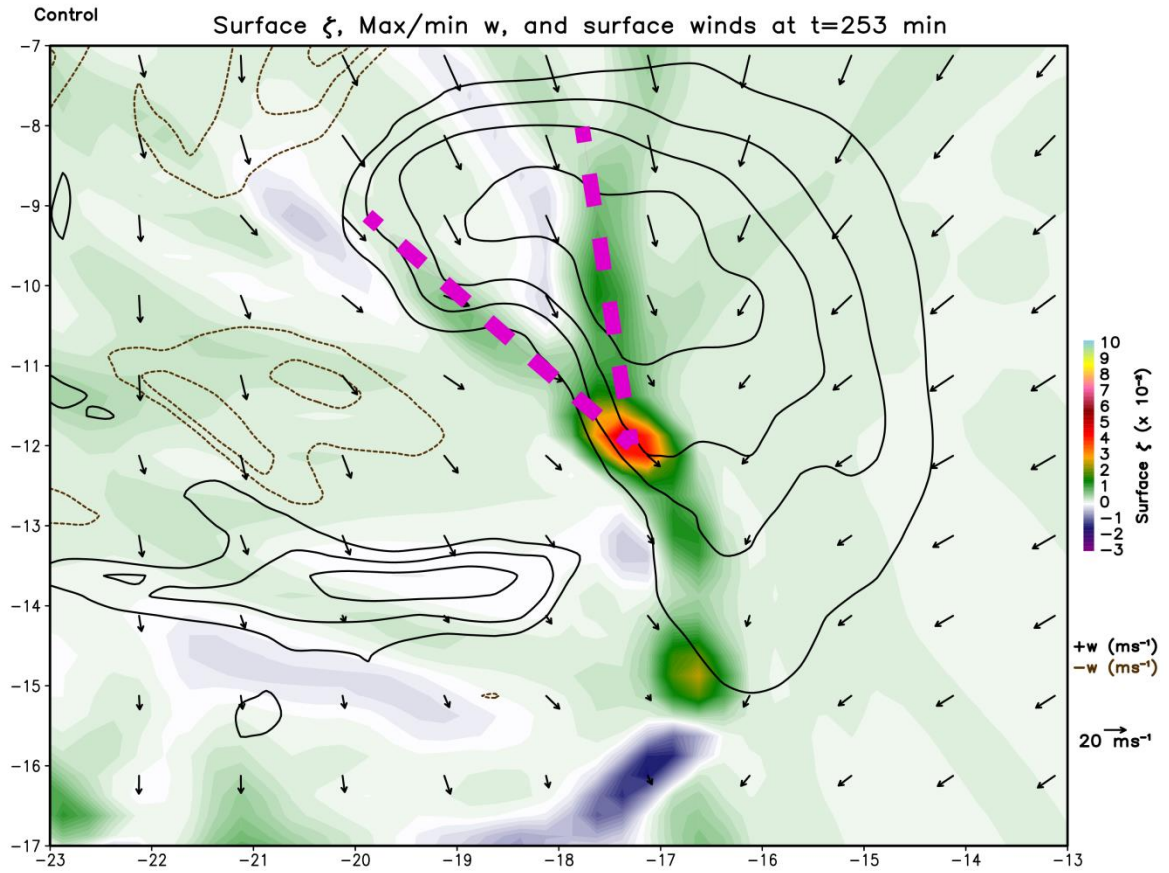


Figure 3.8. As in Fig. 3.6 for $t = 253$ min, but zoomed in and including surface wind vectors (m s^{-1}). Pink dashed lines show two apparent “rivers” of vorticity feeding the developing vortex.

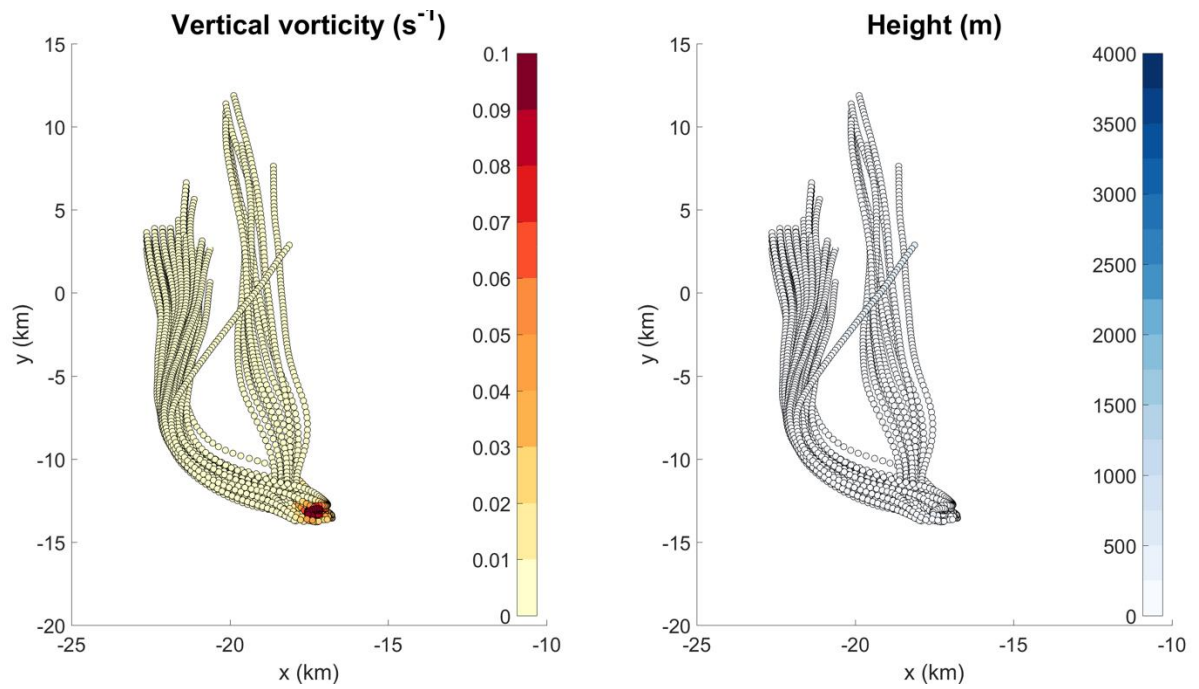


Figure 3.9. Trajectories, (left) vertical vorticity (s^{-1}) and (right) height (m) of parcels contributing to a strong, near-surface vortex in the control simulation.

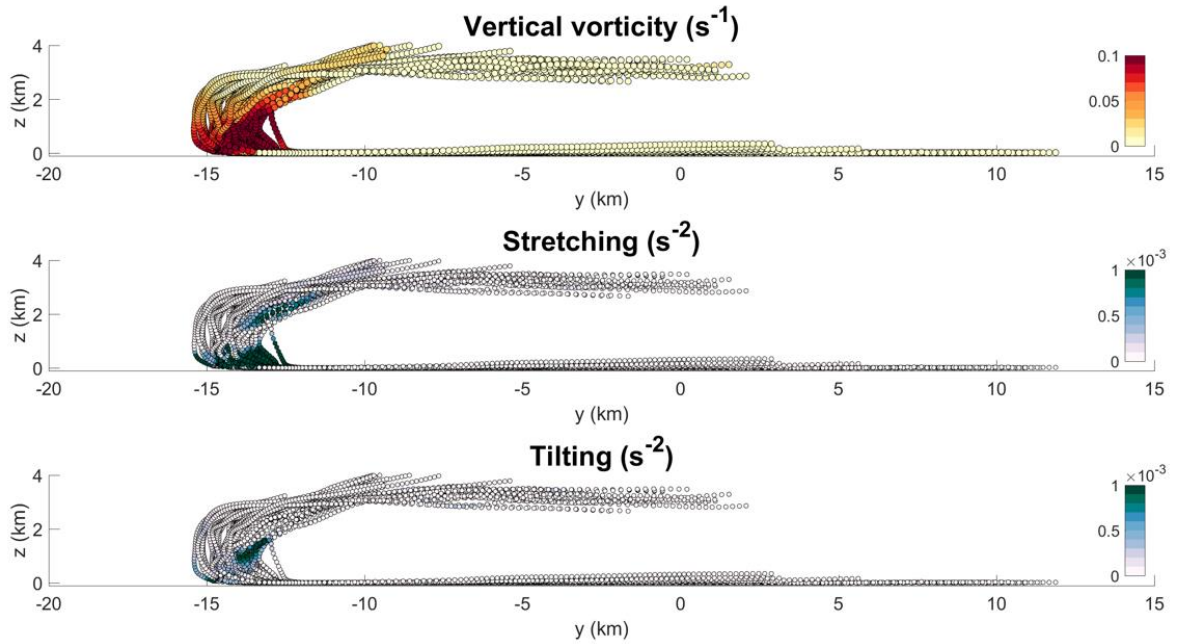


Figure 3.10. As in Fig. 3.9, but for the y - z plane and showing vertical velocity ($m s^{-1}$) rather than height. Also note that this figure represents a longer time period (including the time *after* parcels *exit* the vortex).

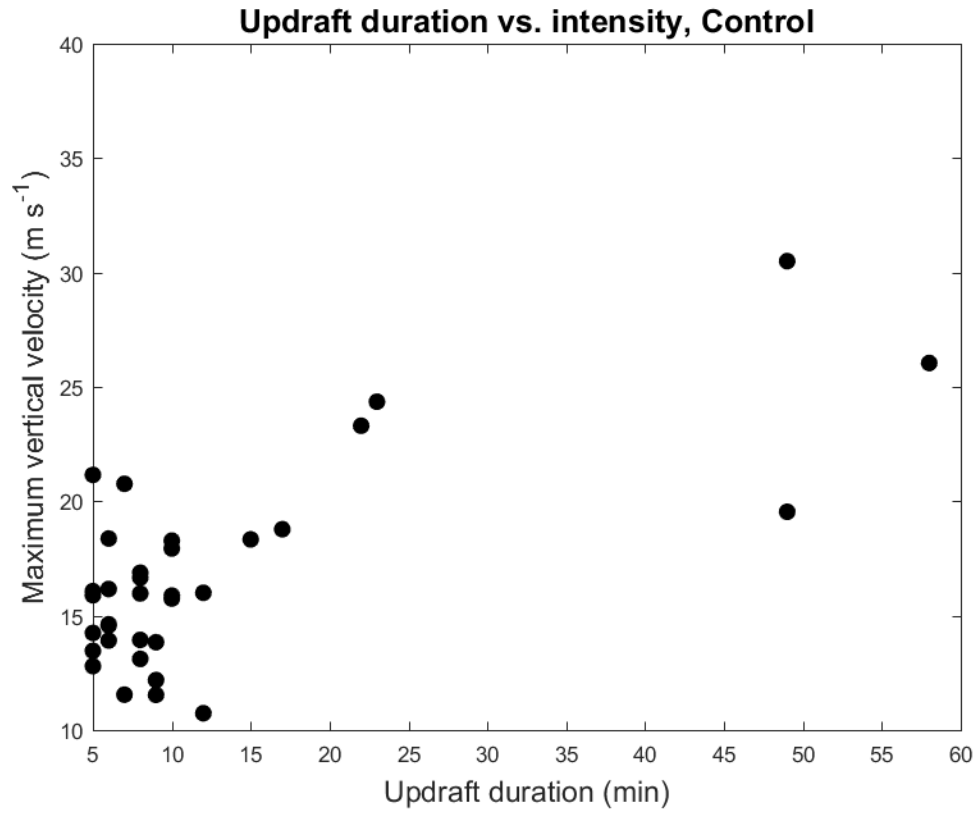


Figure 3.11. Scatter plot of updraft duration (min) against maximum vertical velocity (m s^{-1}) for each updraft object tracked for at least 5 minutes in the control simulation.

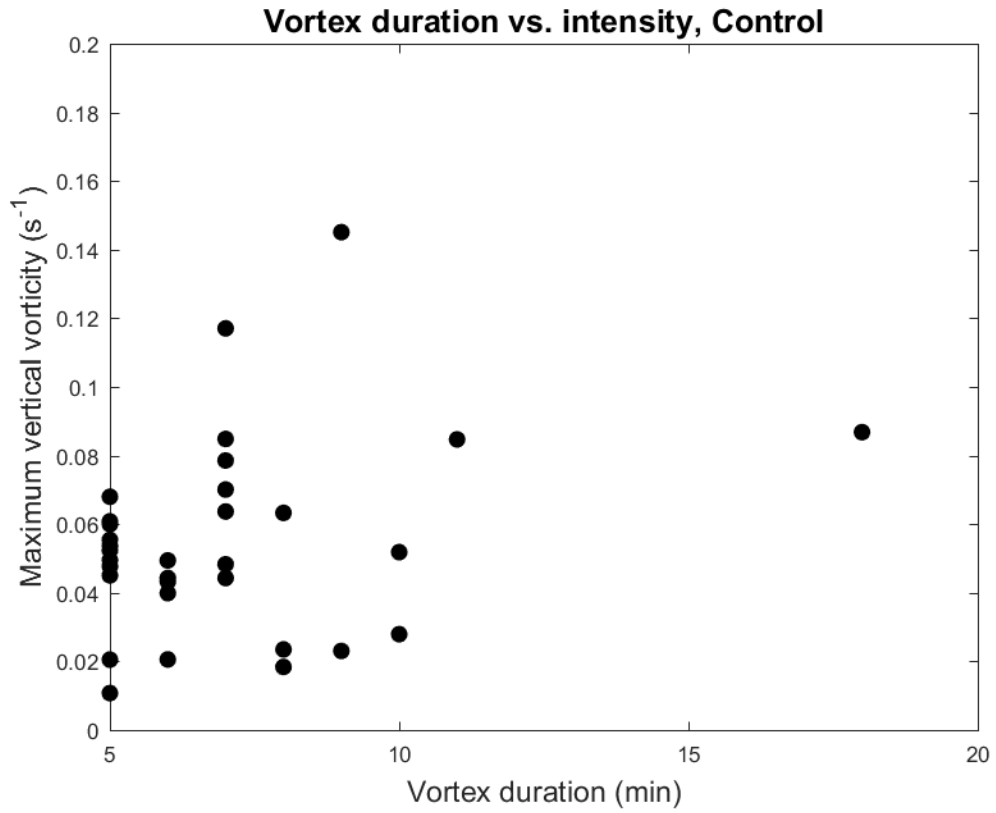


Figure 3.12. As in Fig. 3.11, but for the maximum vertical vorticity (s^{-1}) of tracked vortex objects.

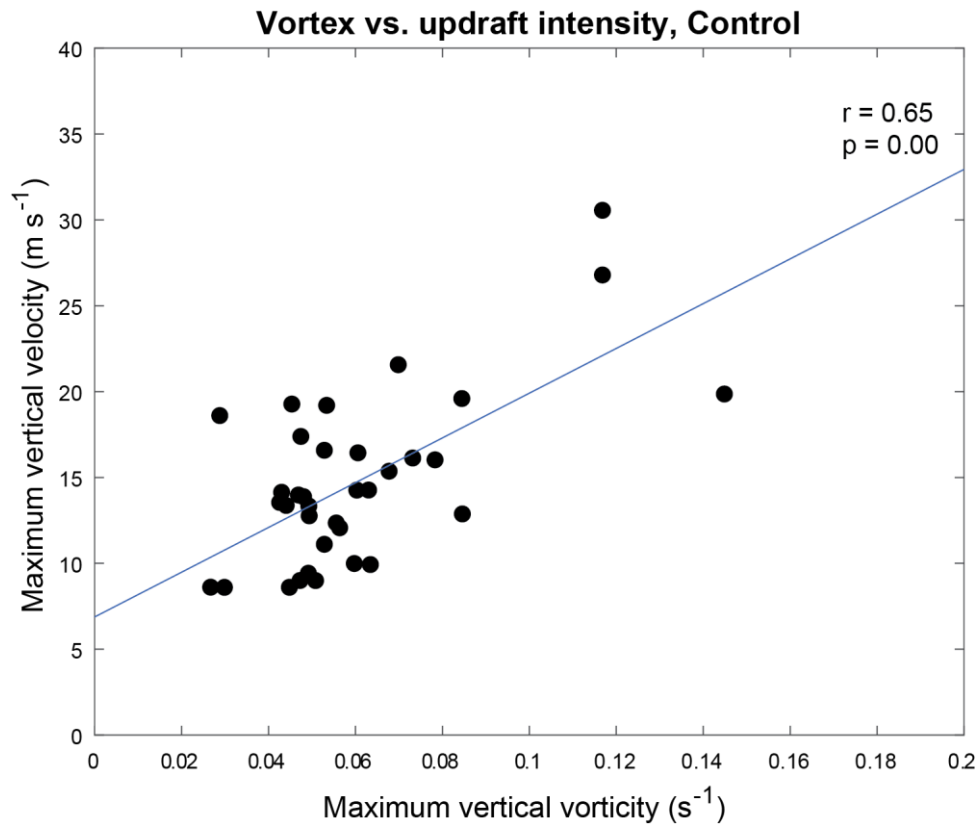


Figure 3.13. Scatter plot of maximum vertical vorticity (s⁻¹) of each tracked vortex object compared to the strongest overlying updraft (m s⁻¹) during its lifetime. Blue line shows the best-fit line, with correlation coefficient (r) and p -value provided in the top right corner.

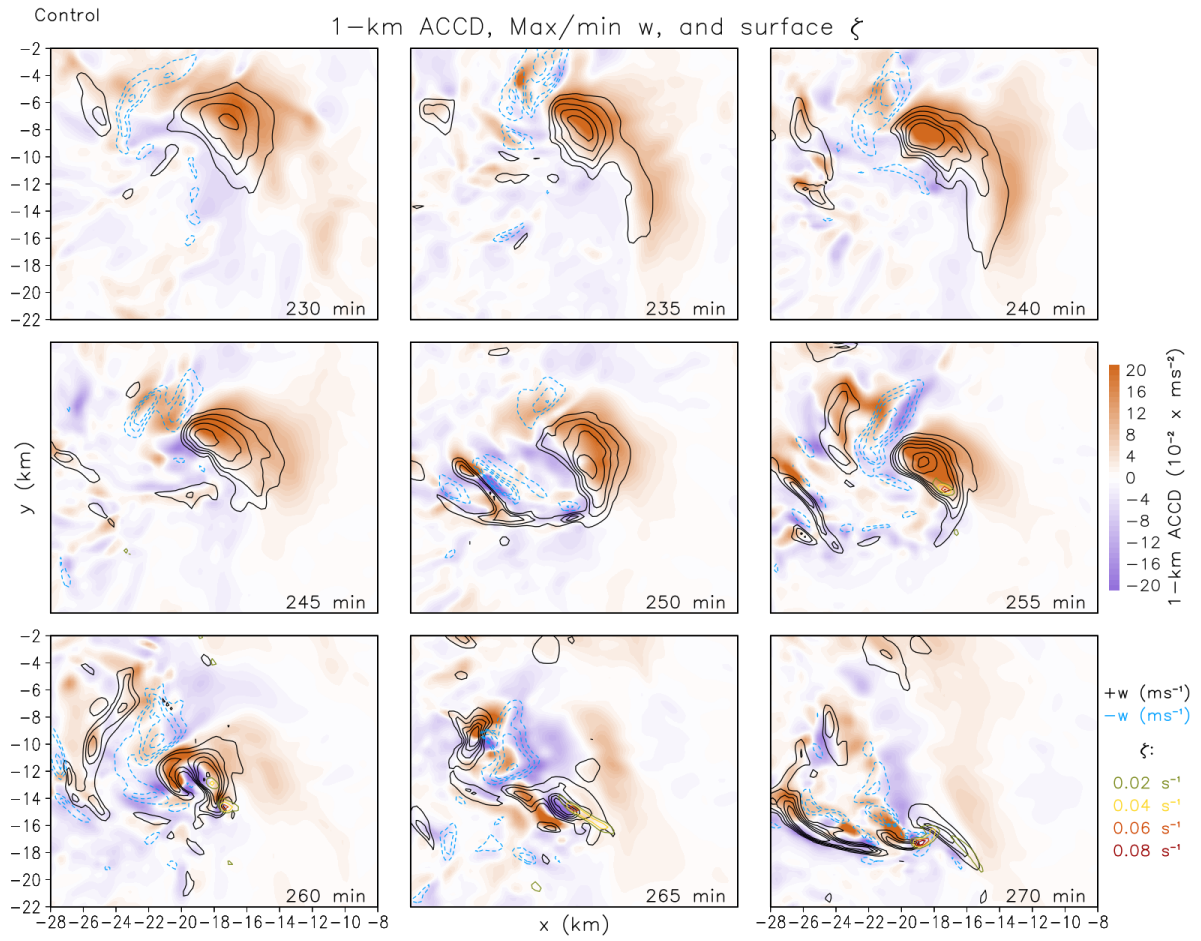


Figure 3.14. As in Fig. 3.5, but showing 1-km ACCD ($10^{-2} \times \text{m s}^{-2}$; shading), surface-to-1-km maximum (black contours) and minimum (blue contours) vertical velocity (m s^{-1}), and lowest level vertical vorticity (s^{-1} ; green to red contours).

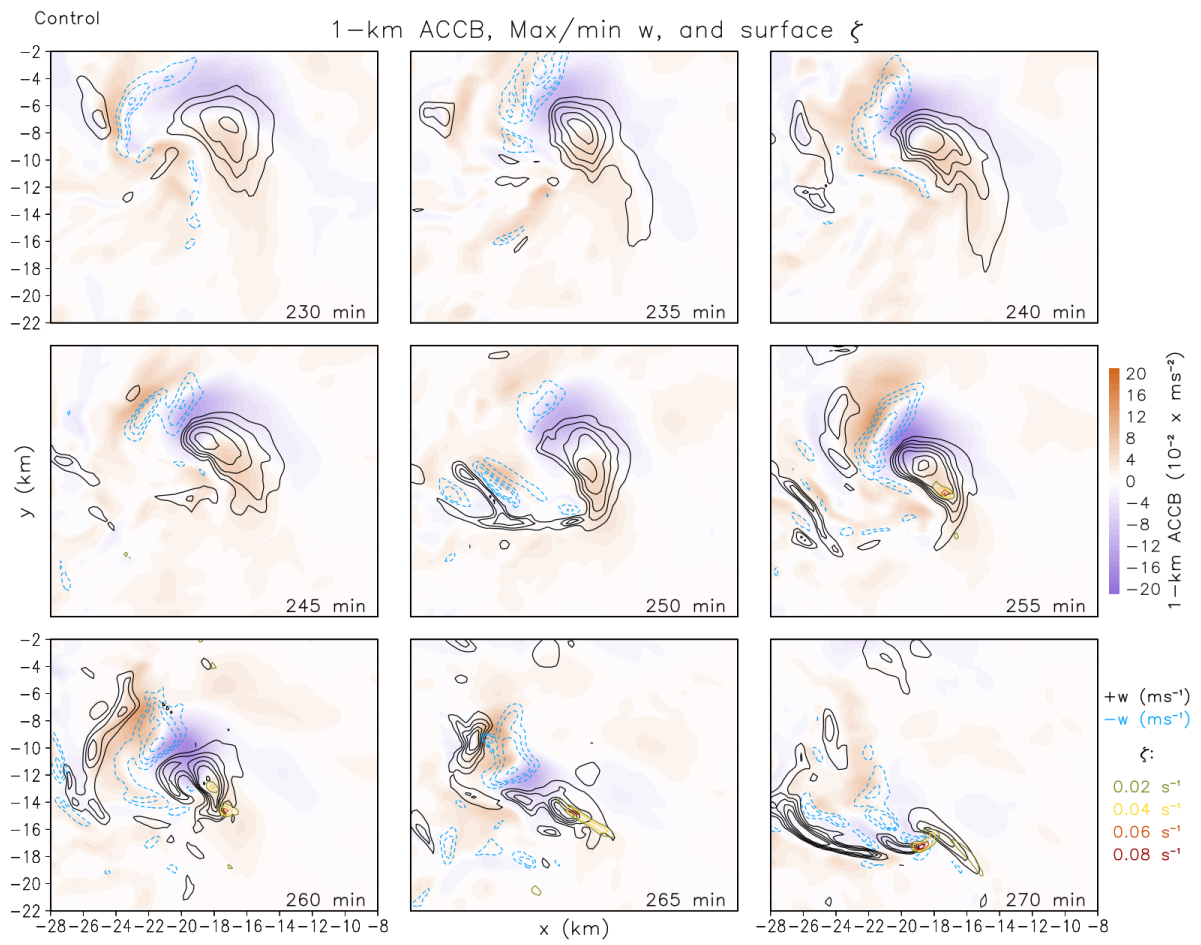


Figure 3.15. As in Fig. 3.14, but for 1-km ACCB ($10^{-2} \times \text{m s}^{-2}$; shading).

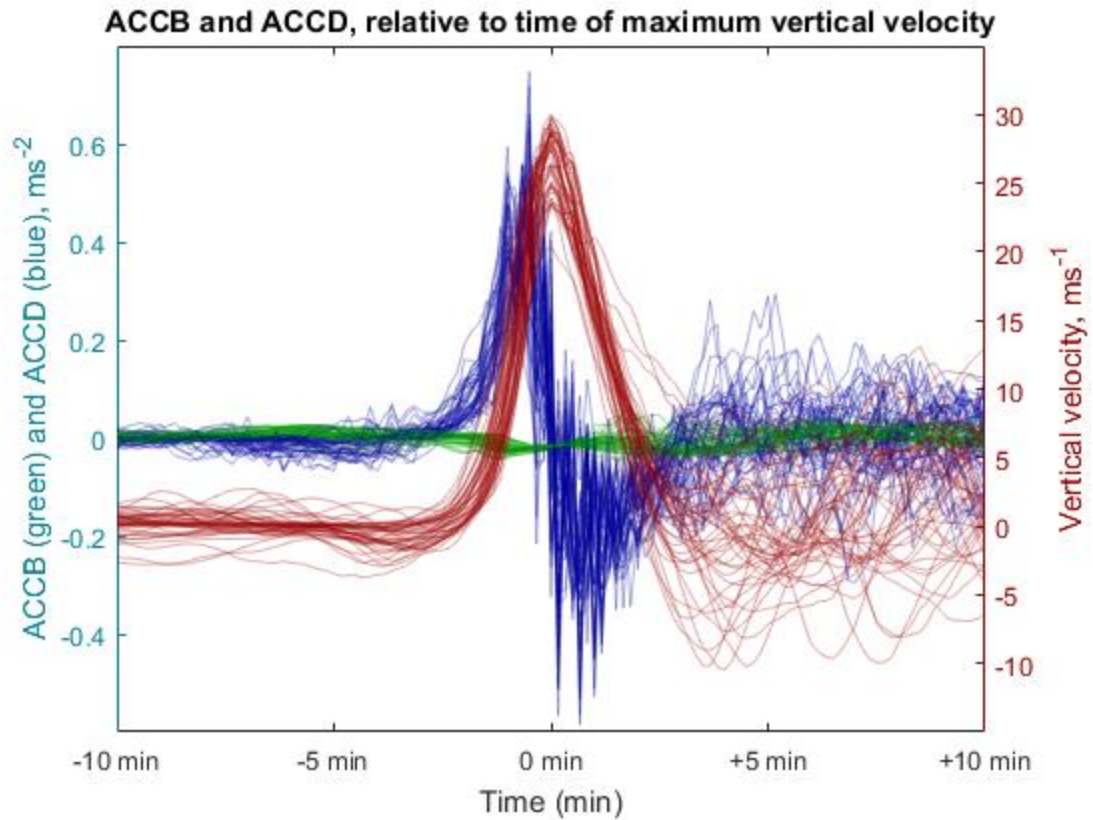


Figure 3.16. Time series of ACCB (green, m s^{-2}), ACCD (blue m s^{-2}), and vertical velocity (red, m s^{-1}) for a sampling of parcels that entered the strongest updraft in the control simulation. Time is adjusted such that $t=0$ min is the time at which maximum vertical velocity was achieved for the given parcel. Only a subset of the parcels that entered the updraft are shown for clarity, but they enter the updraft along a similar trajectory to the remaining parcels and are representative of the population as a whole.

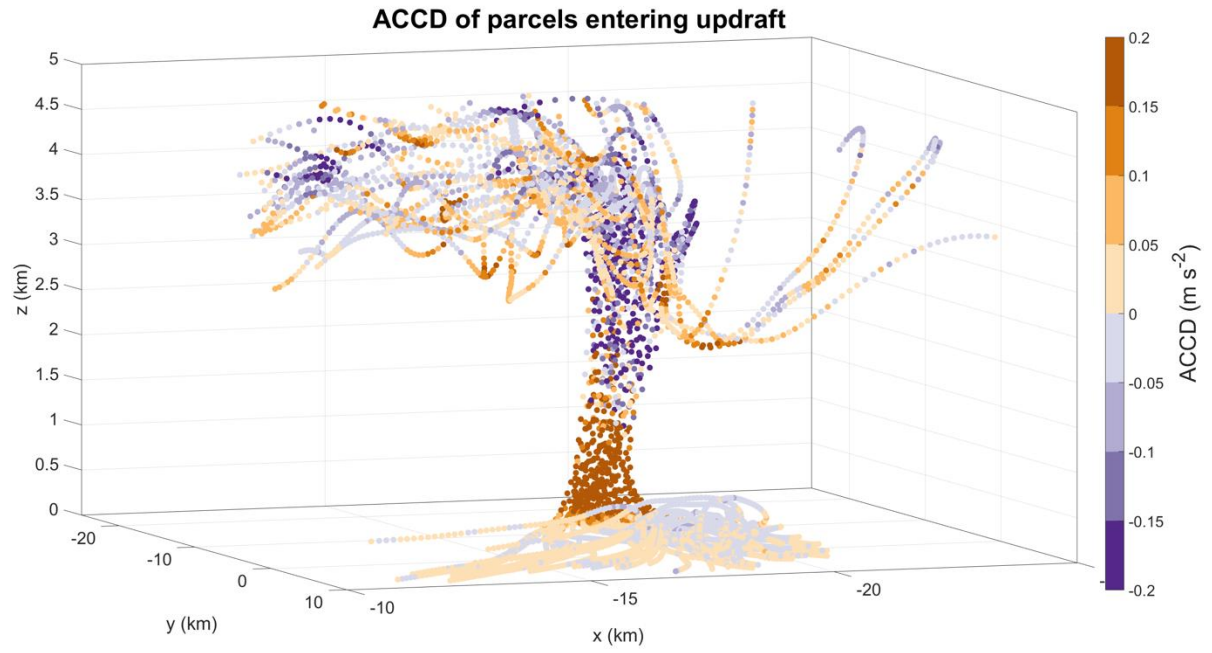


Figure 3.17. ACCD (m s^{-2}) and trajectories of parcels entering the strongest updraft in the control simulation, looking south-southwest.

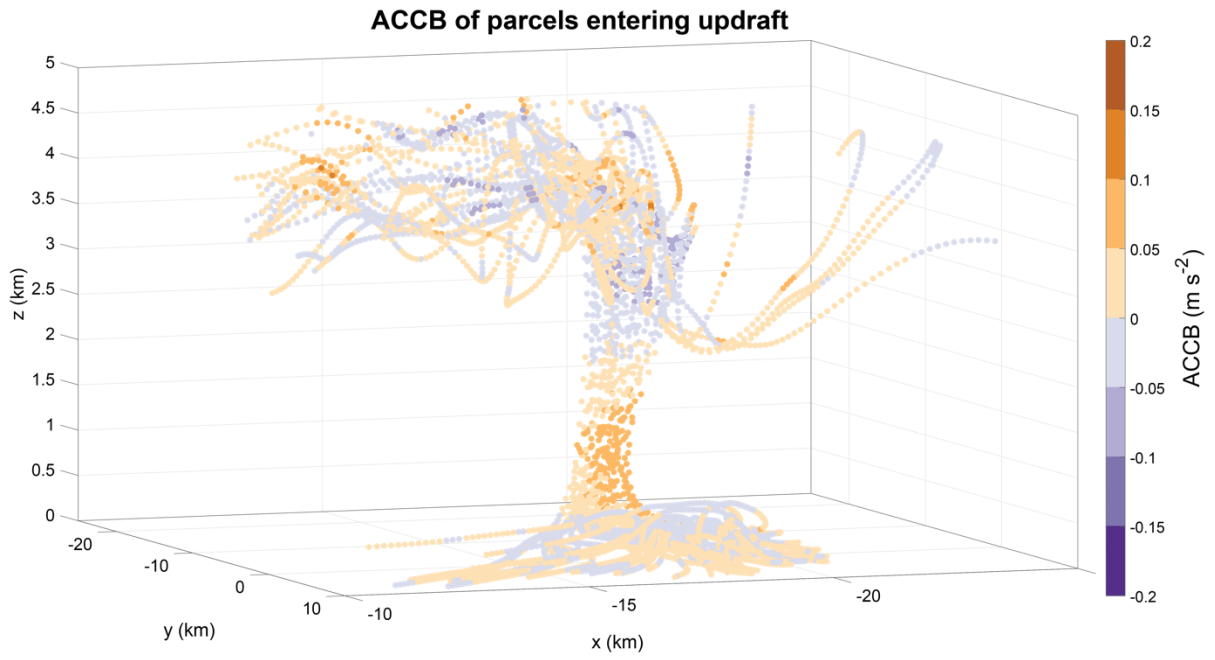


Figure 3.18. ACCB (m s^{-2}) and trajectories of parcels entering the strongest updraft in the control simulation, looking south-southwest.

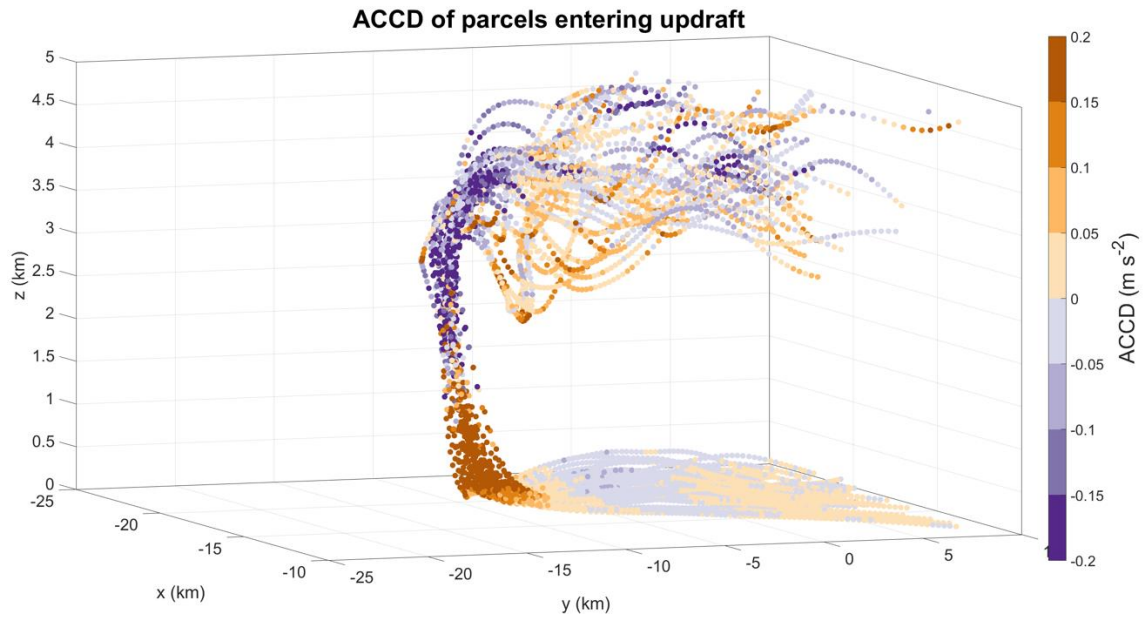


Figure 3.19. As in Fig. 3.17, but looking towards the west-northwest.

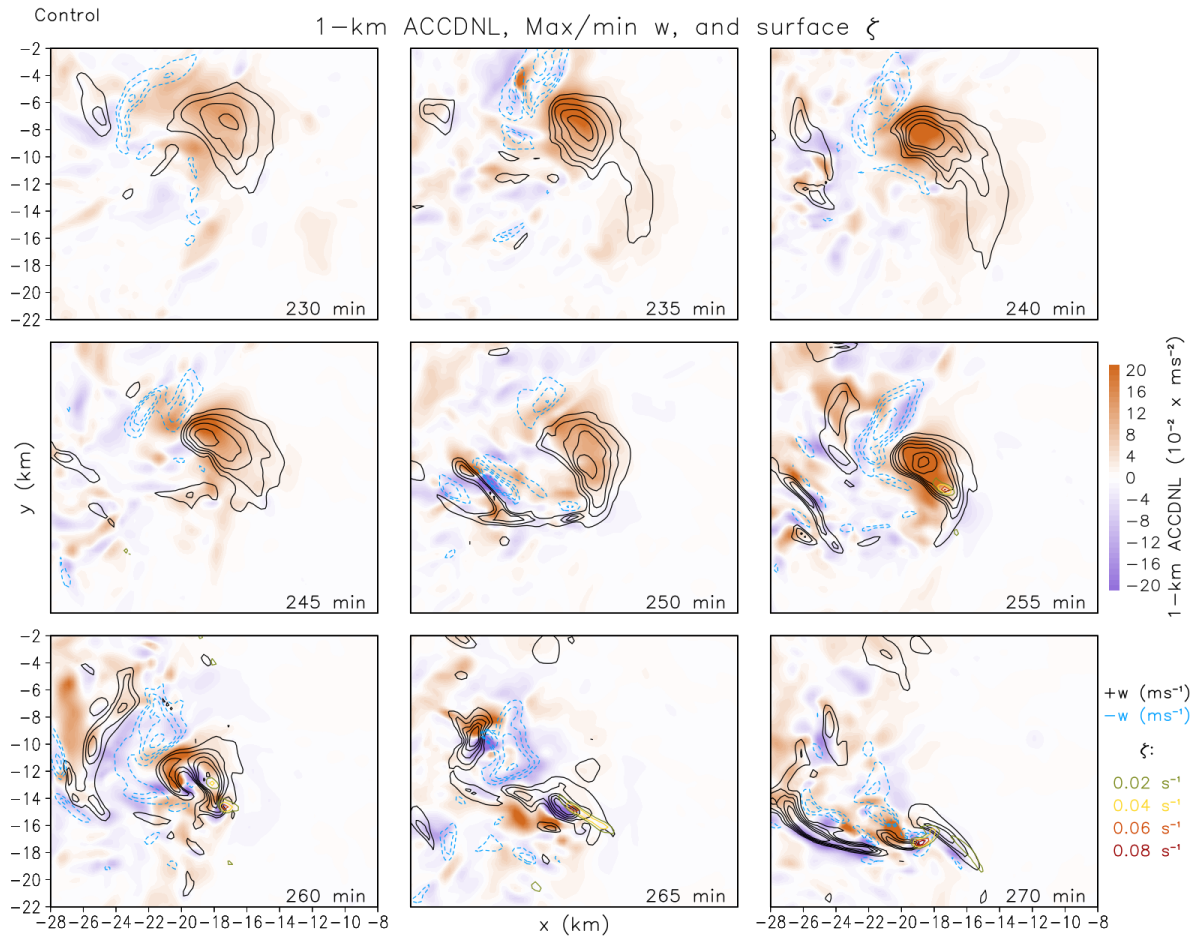


Figure 3.20. As in Fig. 3.14, but for 1-km ACCDNL ($10^{-2} \times \text{m s}^{-2}$; shading).

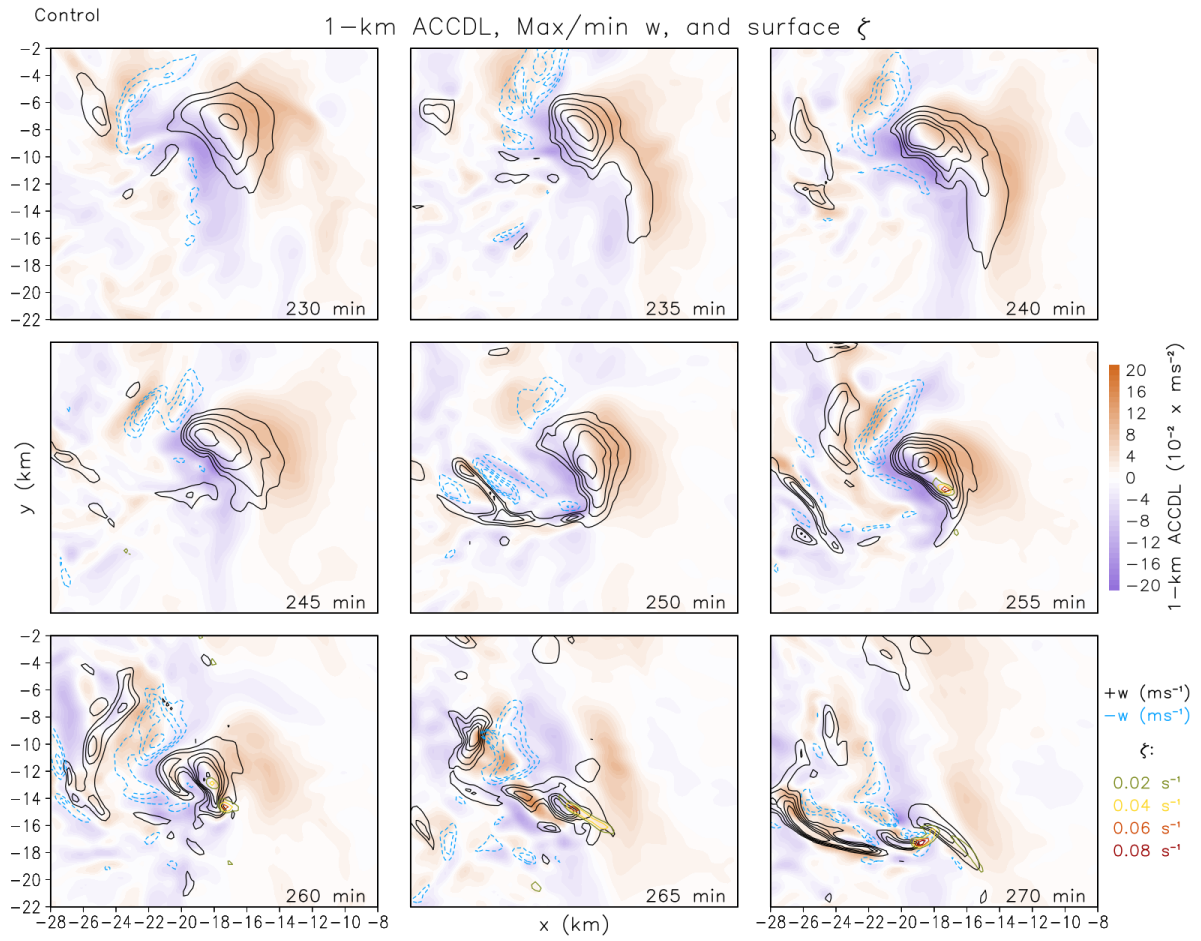


Figure 3.21. As in Fig. 3.14, but for 1-km ACCDL ($10^{-2} \times \text{m s}^{-2}$; shading).

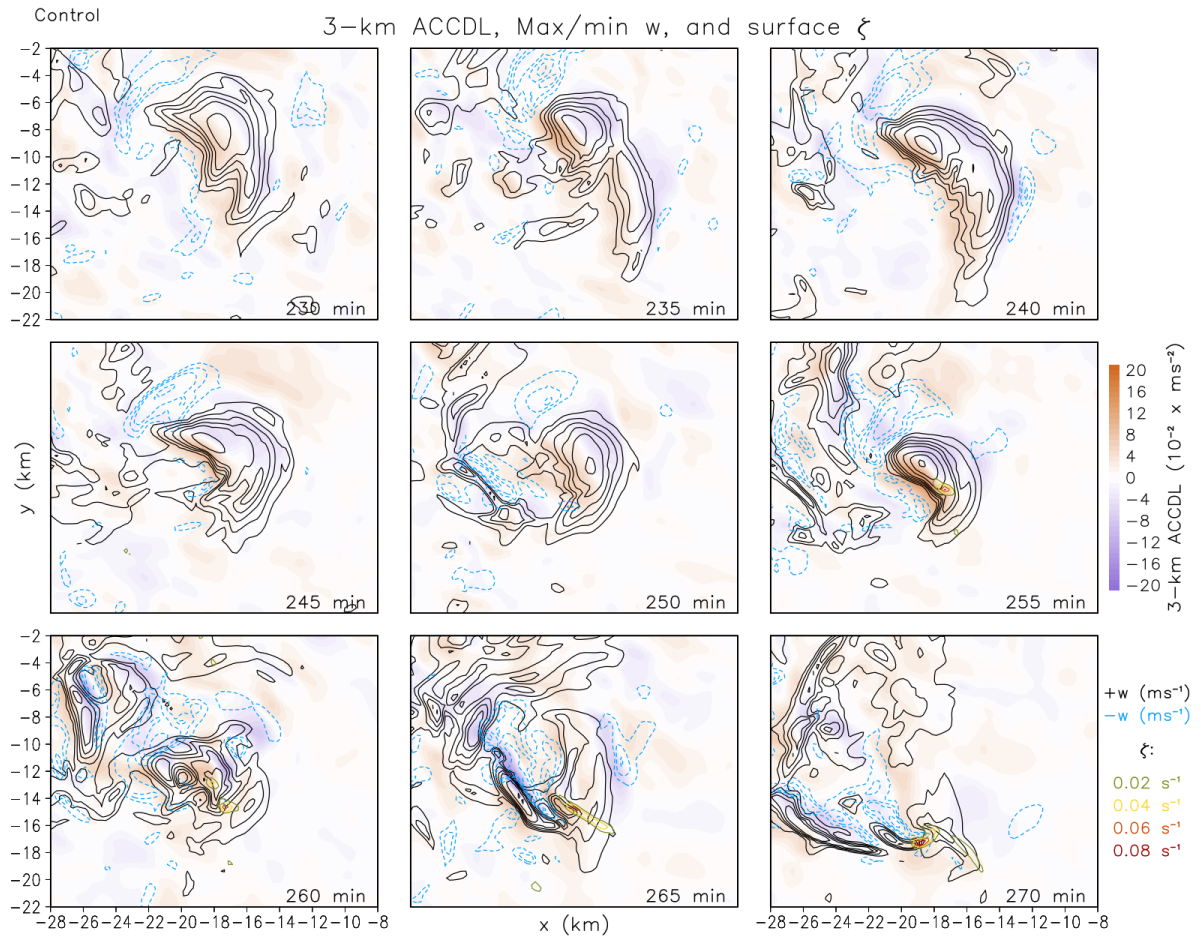


Figure 3.22. As in Fig. 3.21, but for 3-km ACCDL ($10^{-2} \times \text{m s}^{-2}$; shading).

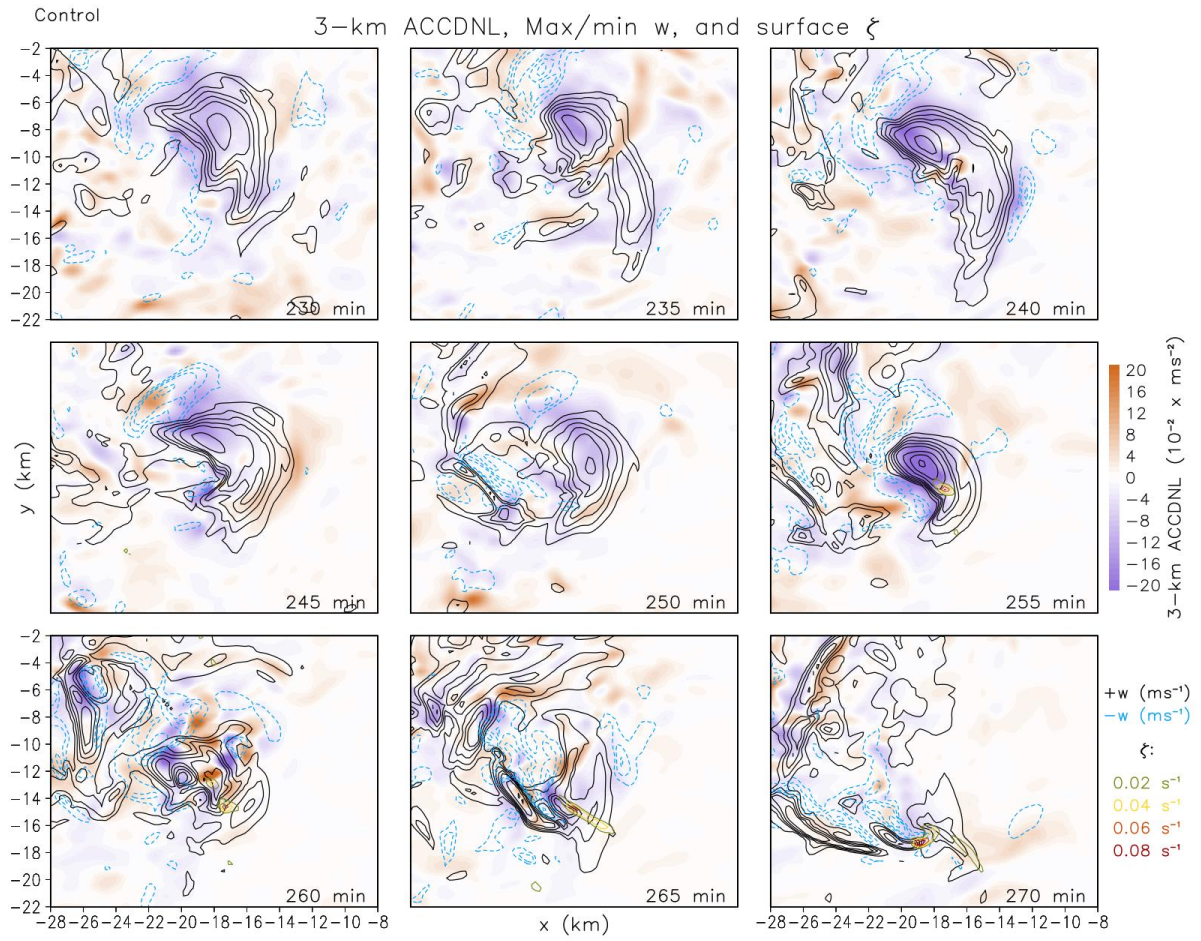


Figure 3.23. As in Fig. 3.20, but for 3-km ACCDNL ($10^{-2} \times \text{m s}^{-2}$; shading).

ξ , ACCDNL, and w for Control

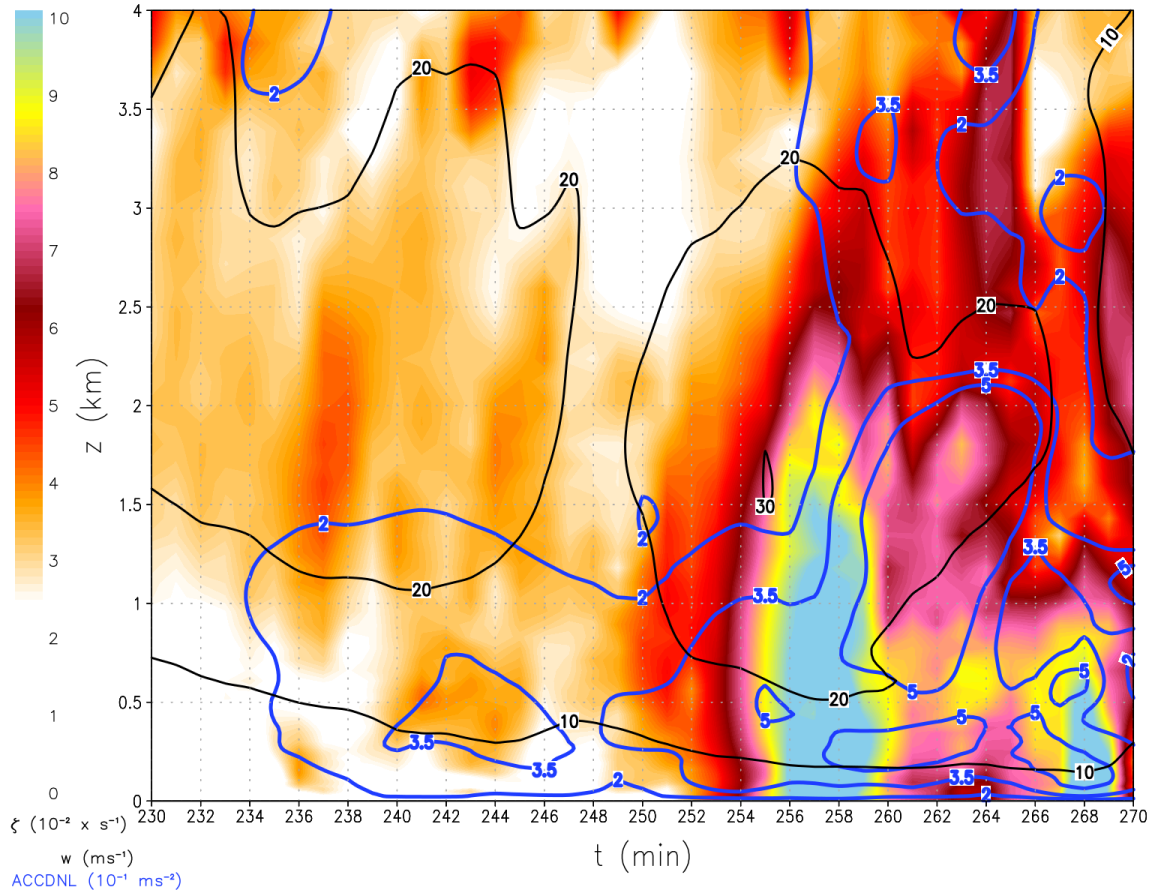


Figure 3.24. Vertical time series of maximum vertical vorticity ($10^{-2} \times \text{s}^{-1}$; shading), vertical velocity (m s^{-1} , black contours), and ACCDNL ($10 \times \text{m s}^{-2}$, blue contours) within a 10 km by 10 km box surrounding the strongest updraft, leading to the development of the strongest vortices in the control simulation.

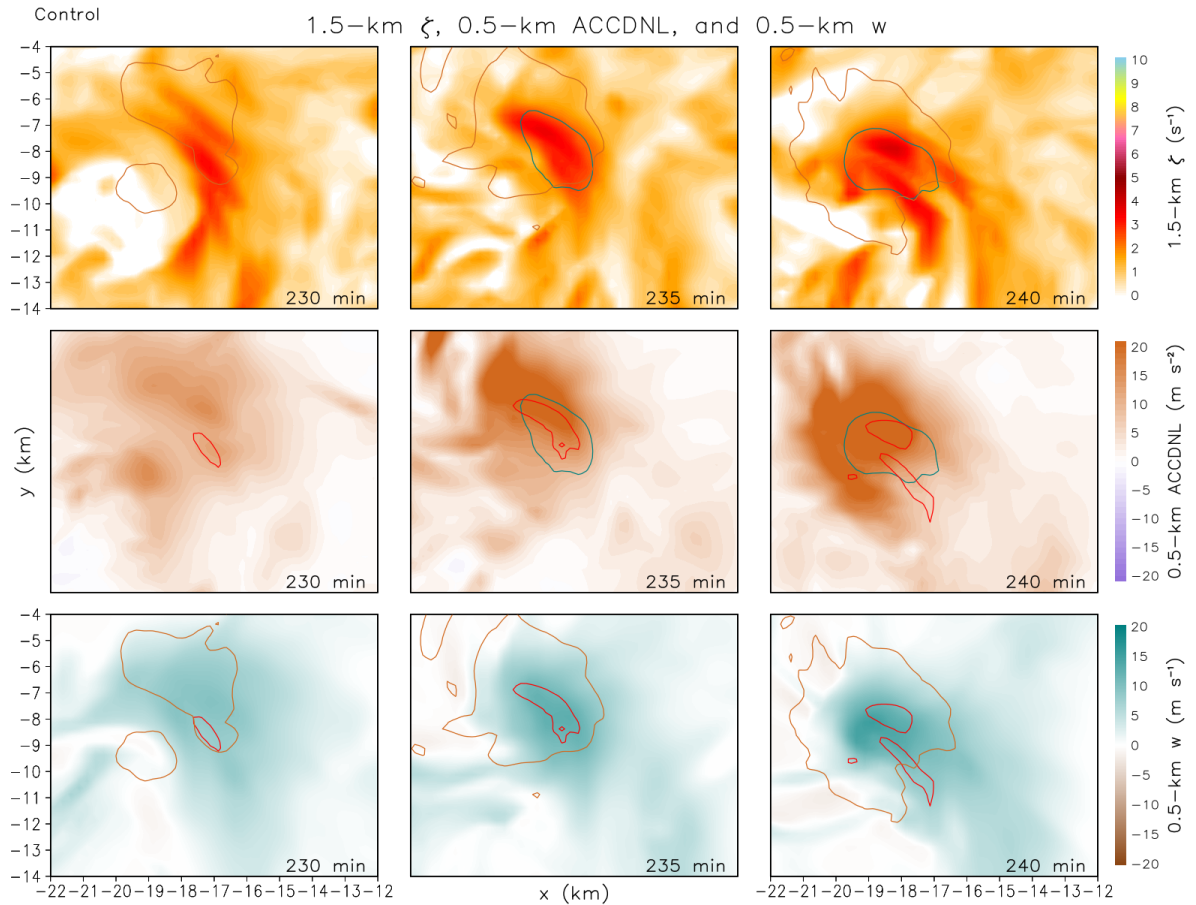


Figure 3.25. Plan-view images of (top row) low-to-midlevel vertical vorticity (shaded; 10^{-2} s^{-1}), (middle row) low-level ACCDNL (shaded; 10^{-2} m s^{-2}), and (bottom row) low-level vertical velocity (shaded; m s^{-1}) for the updraft and vortex shown in Fig. 3.24. Green, brown, and red contours show constant values of vertical velocity (10 m s^{-1}), ACCDNL (0.1 m s^{-2}), and vertical vorticity (0.03 s^{-1}), respectively. Times shown are $t=230 \text{ min}$, $t=235 \text{ min}$, and $t=240 \text{ min}$ from left to right, respectively.

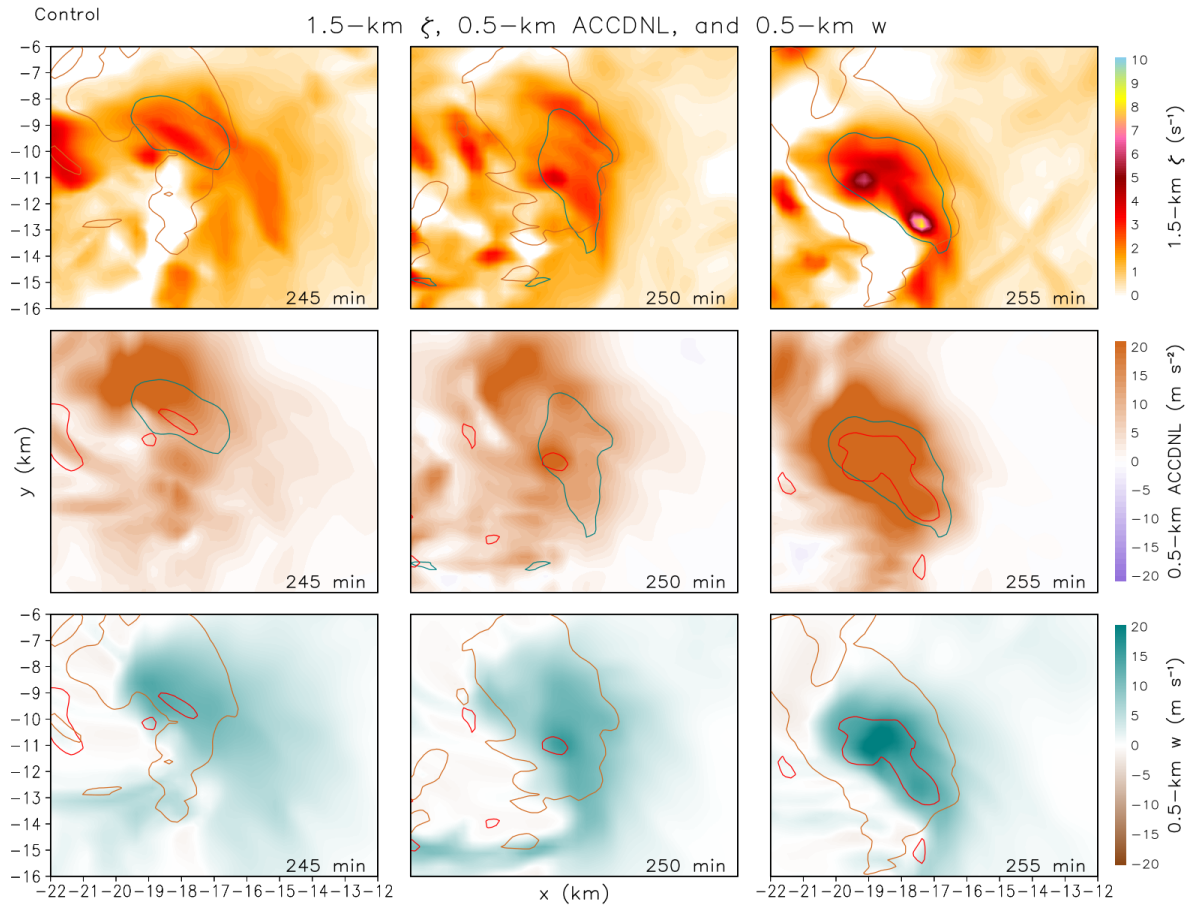


Figure 3.26. As in Fig. 3.25, but for $t=245$ min, $t=250$ min, and $t=255$ min from left to right, respectively.

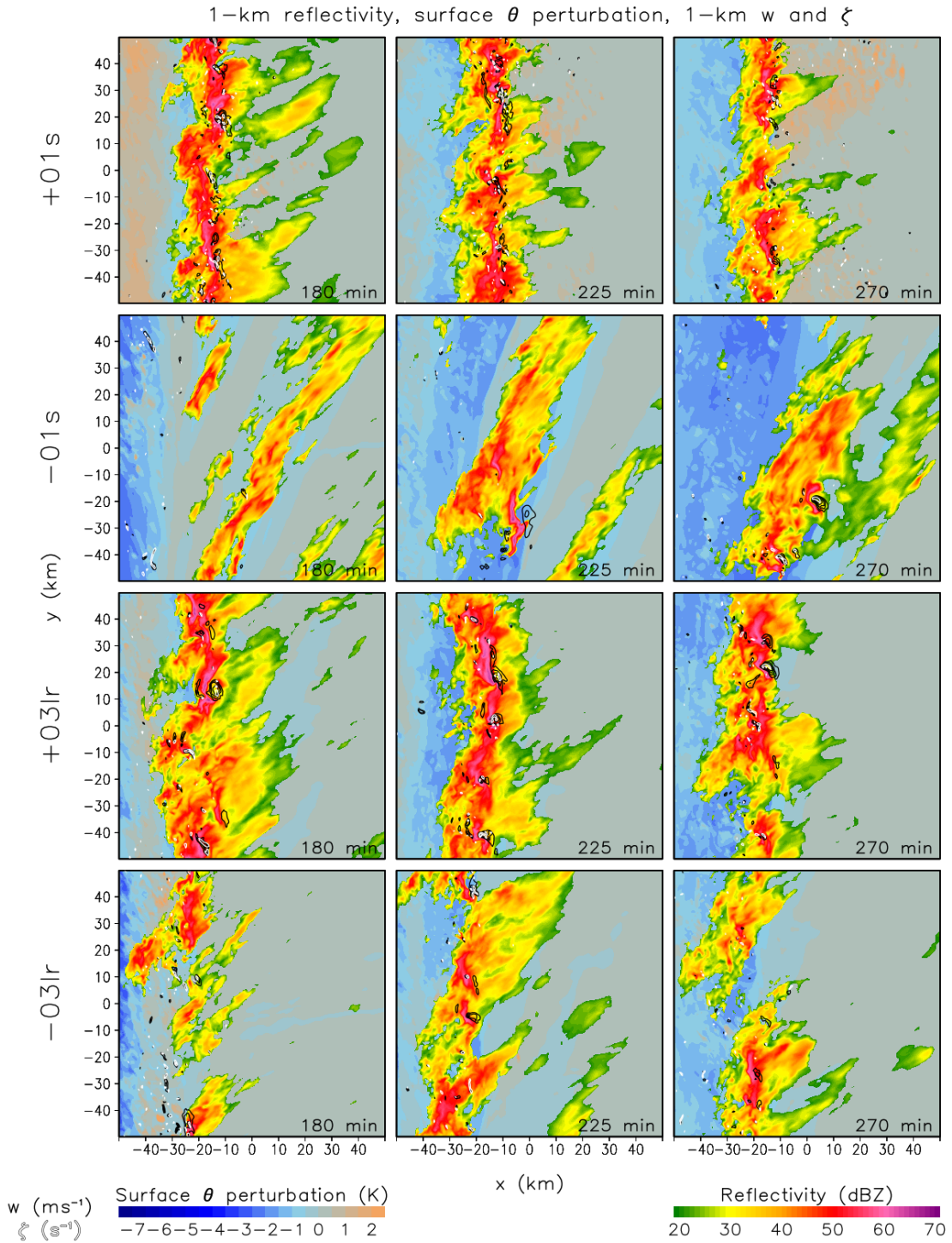


Figure 3.27. As in Fig. 3.2, but for (top row) +01s, (second row) -01s, (third row) +03lr, and (bottom row) -03lr for (left to right columns) $t=180$ min, 225 min, and 270 min.

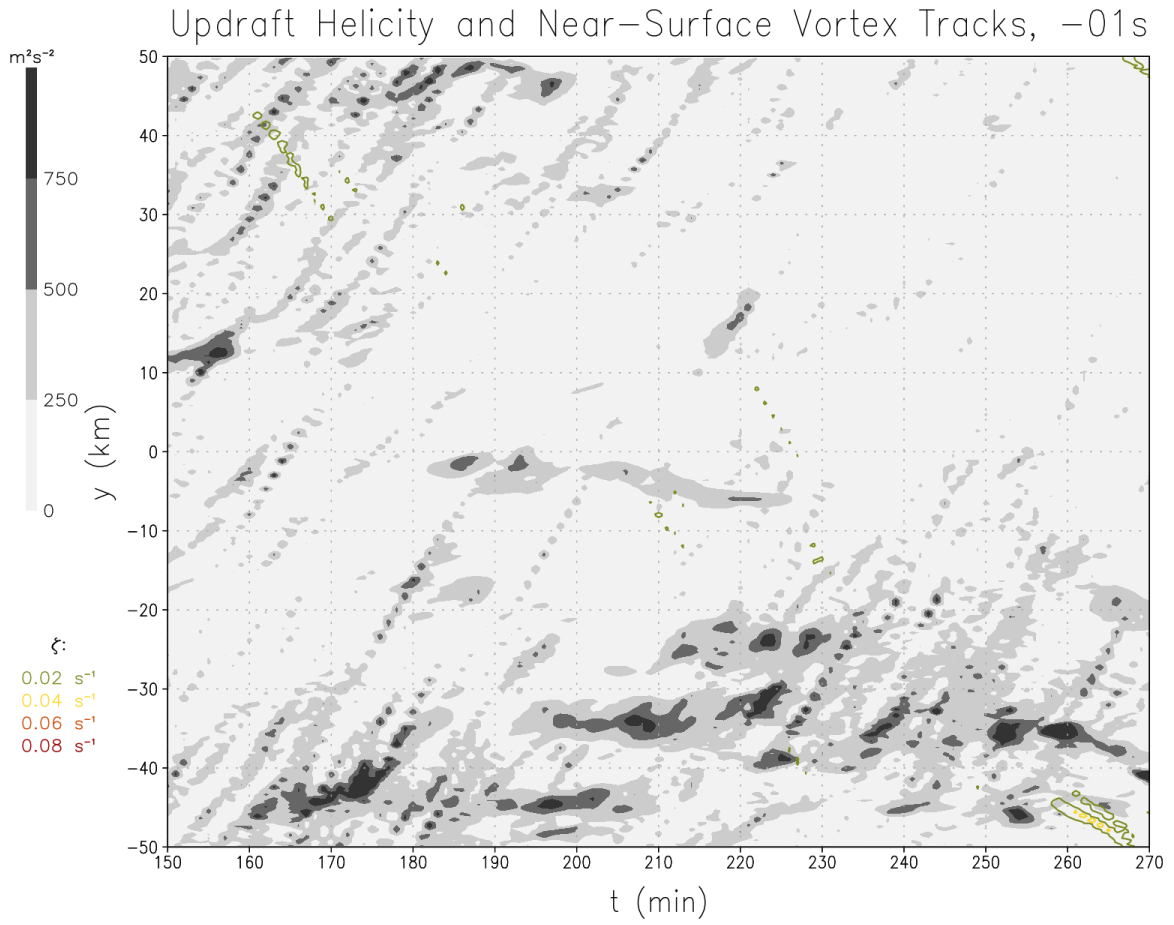


Figure 3.28. As in Fig. 3.4, but for -01s.

Updraft Helicity and Near-Surface Vortex Tracks, +01s

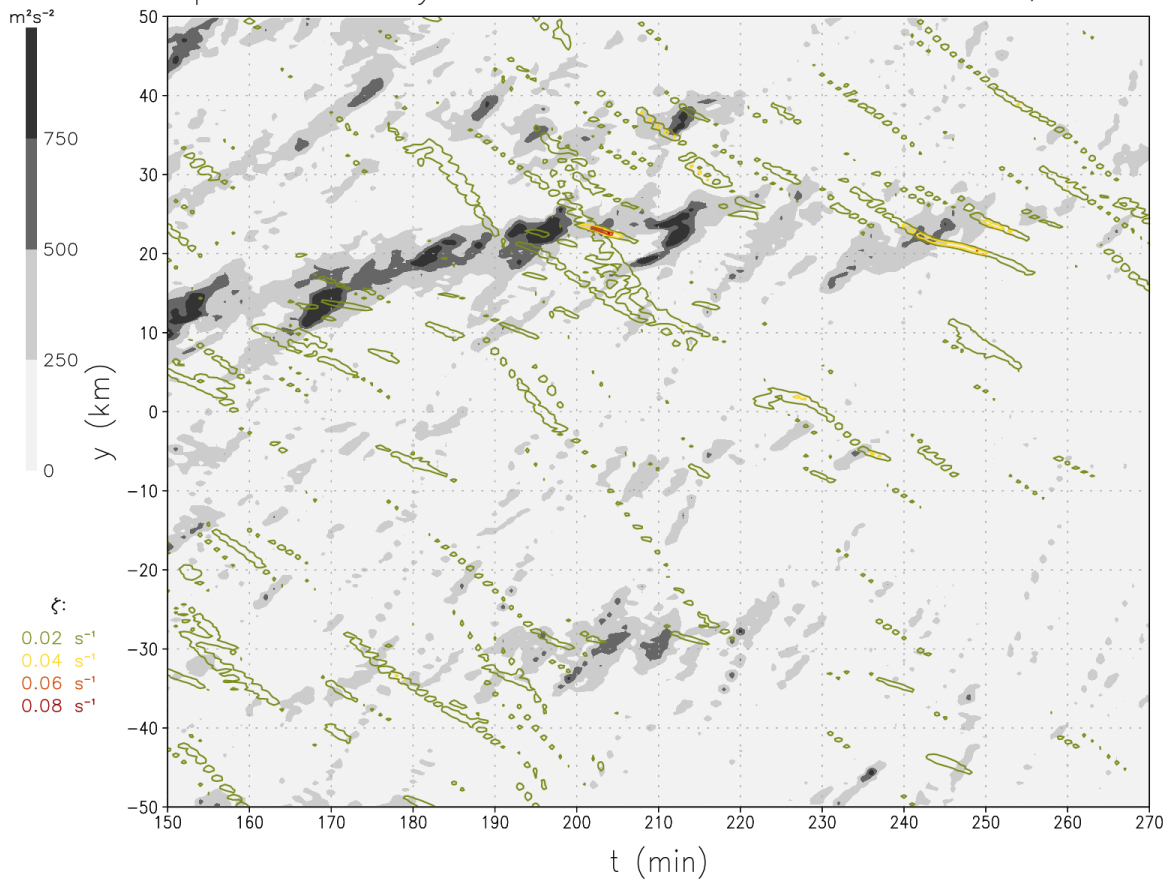


Figure 3.29. As in Fig. 3.4, but for +01s.

Updraft Helicity and Near-Surface Vortex Tracks, -03lr

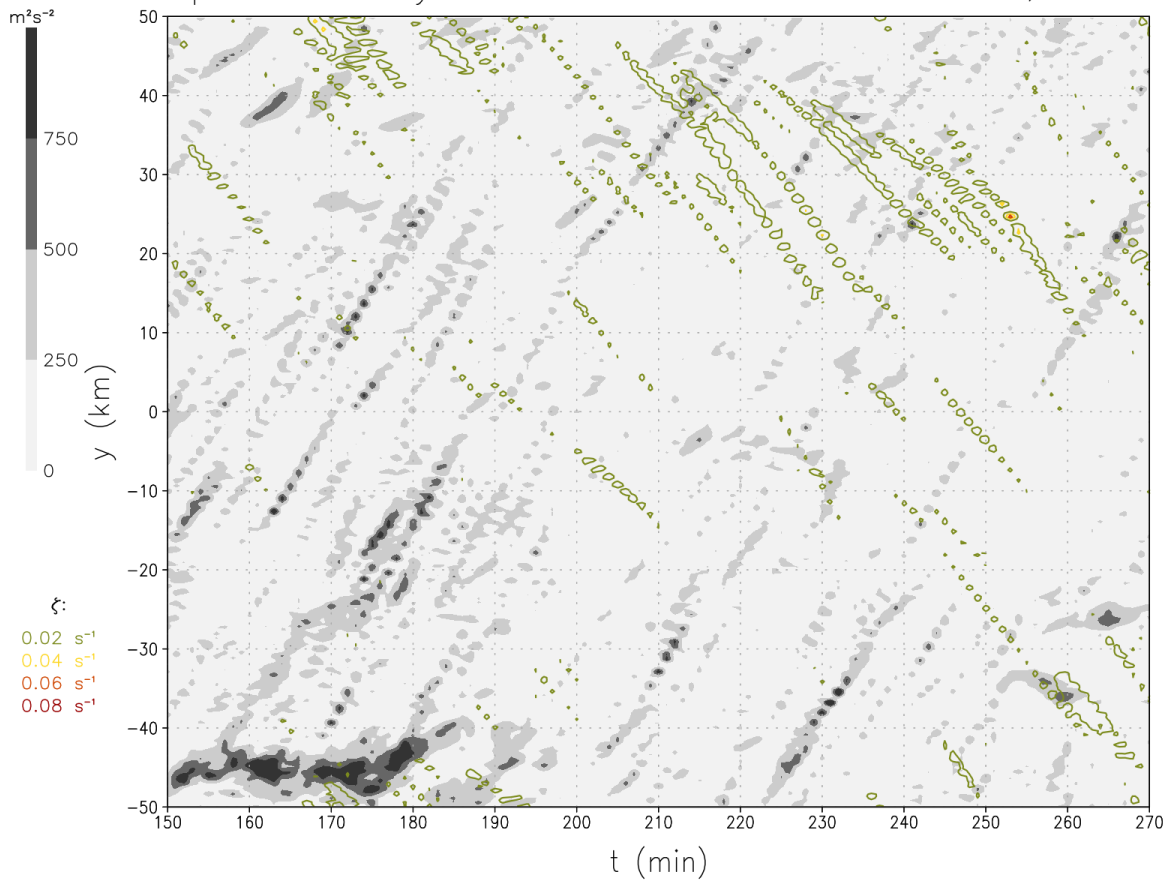


Figure 3.30. As in Fig. 3.4, but for -03lr.

Updraft Helicity and Near-Surface Vortex Tracks, +03lr

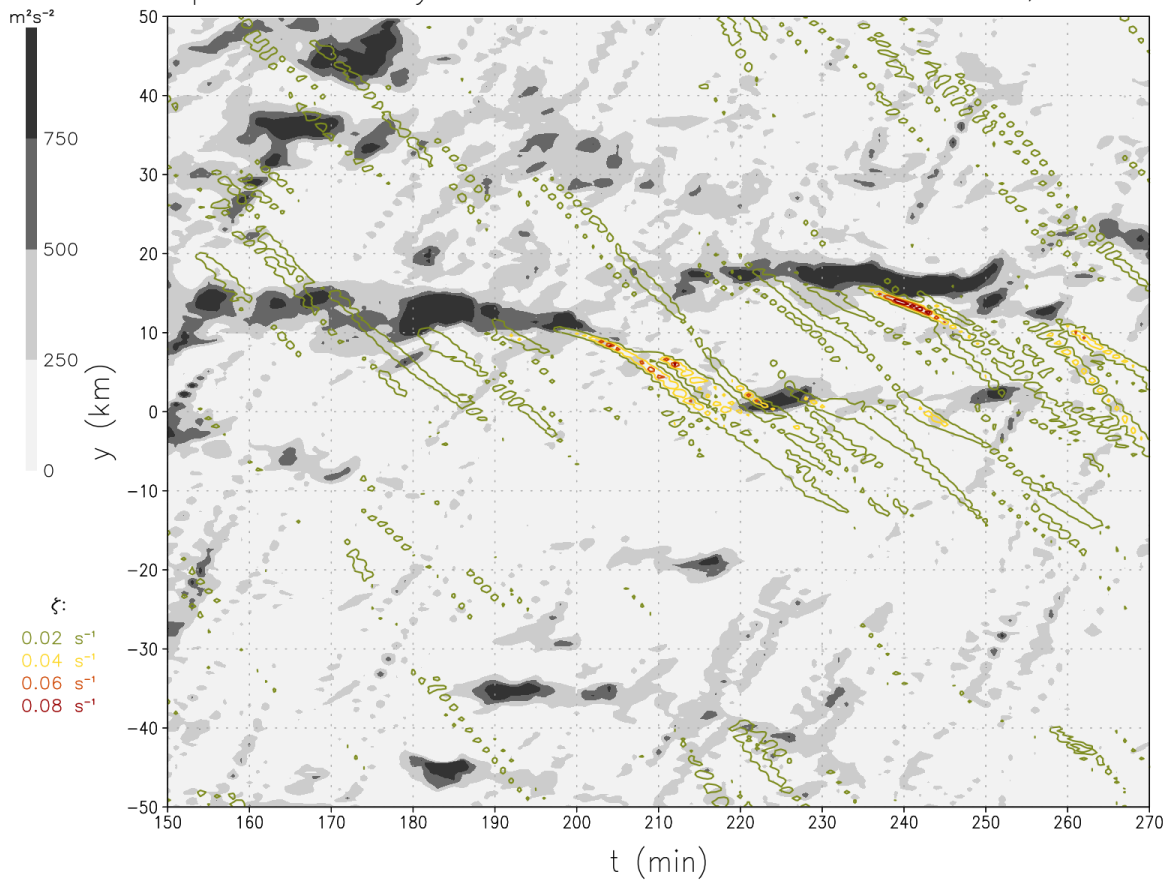


Figure 3.31. As in Fig. 3.4, but for +03lr.

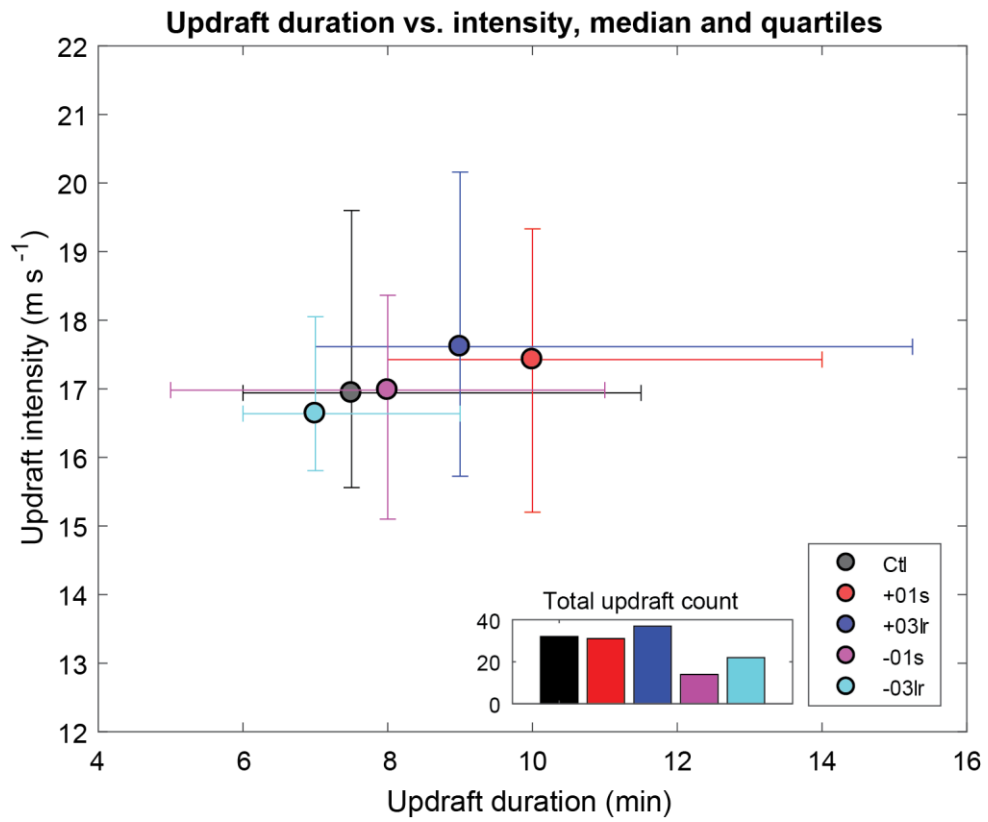


Figure 3.32. Scatter plot of median updraft duration (min) against median maximum updraft intensity (m s^{-1}) for the tracked updraft features in each simulation. Error bars extend to the 25th and 75th percentiles of each distribution.

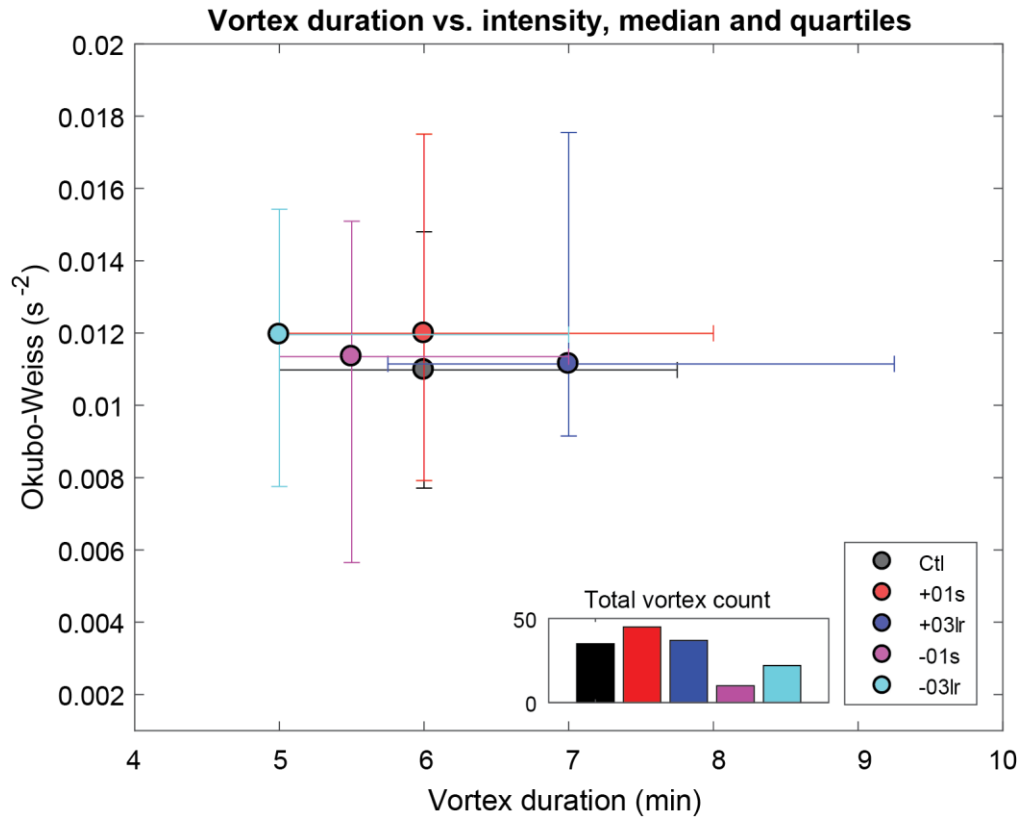


Figure 3.33. As in Fig. 3.32, but for duration and intensity (Okubo-Weiss parameter, s^{-2}) of tracked vortex features in each simulation.

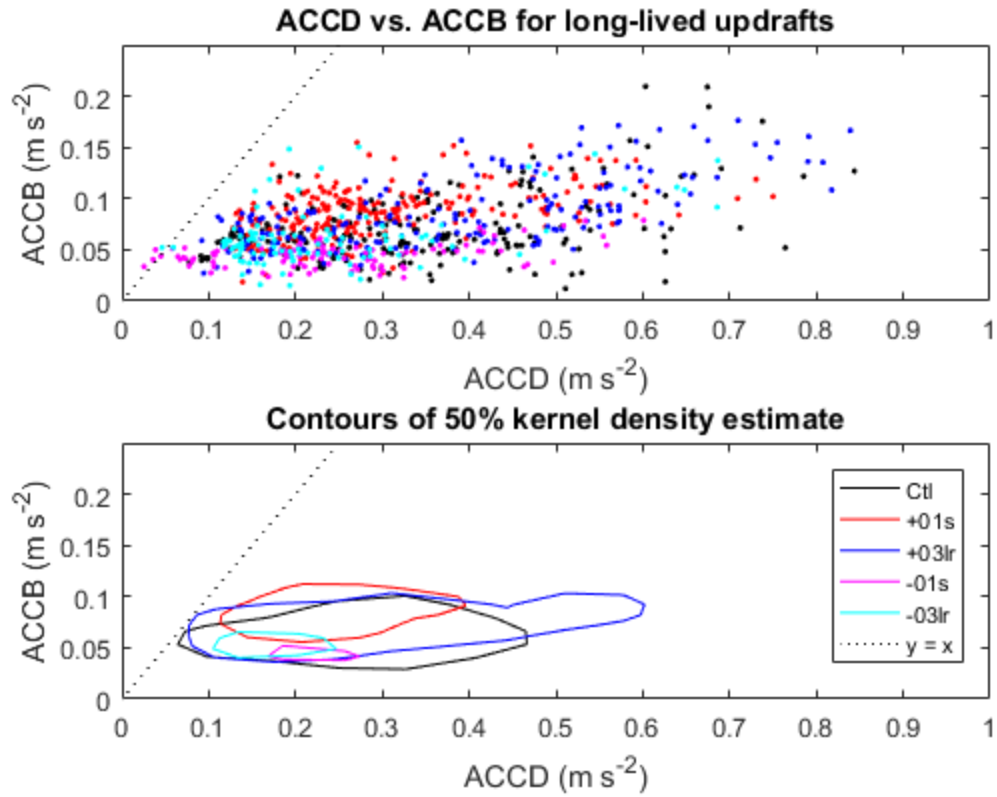


Figure 3.34. (Top) Scatter plot of ACCD and ACCB for each minute of tracked long-lived updrafts within the respective simulations. (Bottom) A kernel density estimate encompassing 50% of the total distribution, extending from the densest bin.

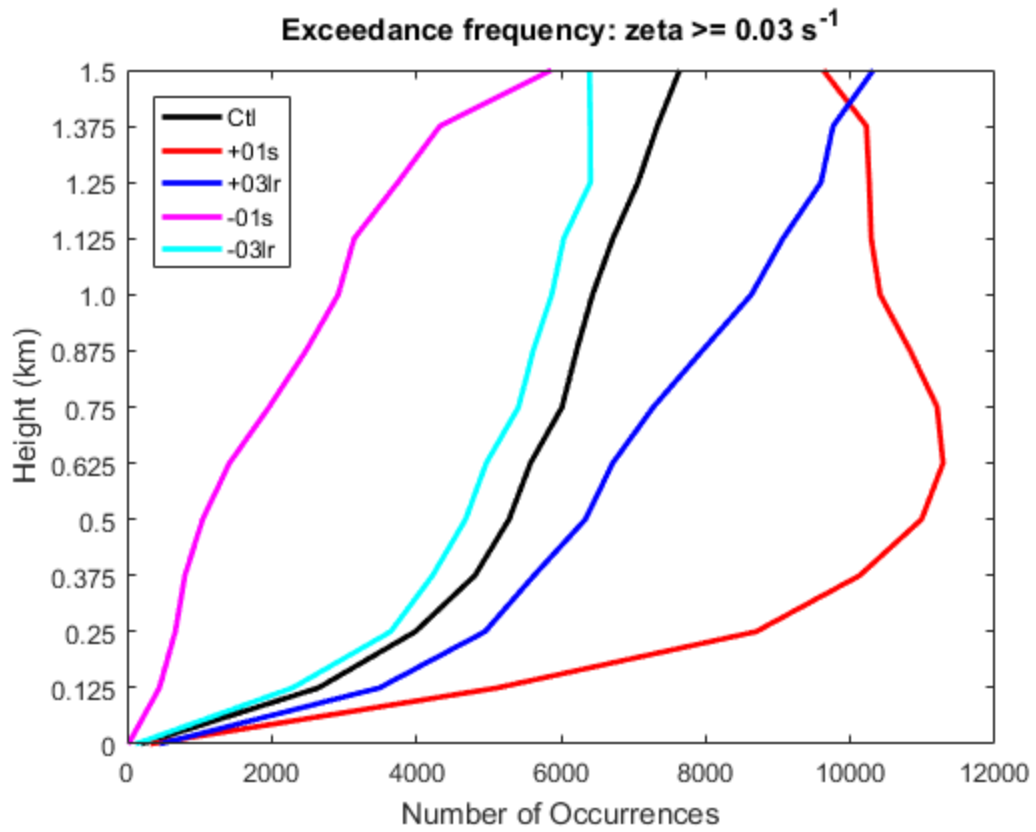


Figure 3.35. Exceedance frequency for vertical vorticity of 0.03 s^{-1} for all simulations.

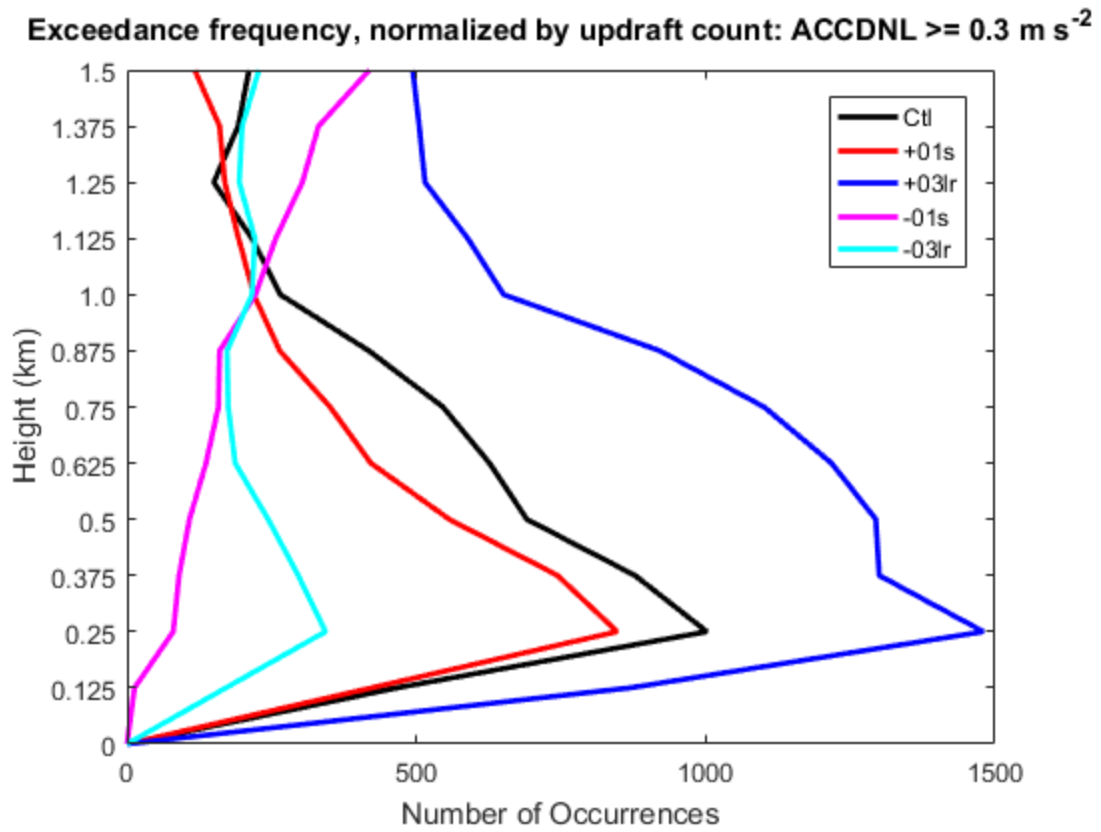


Figure 3.36. Exceedance frequency for ACCDNL of 0.3 m s^{-2} for all simulations.

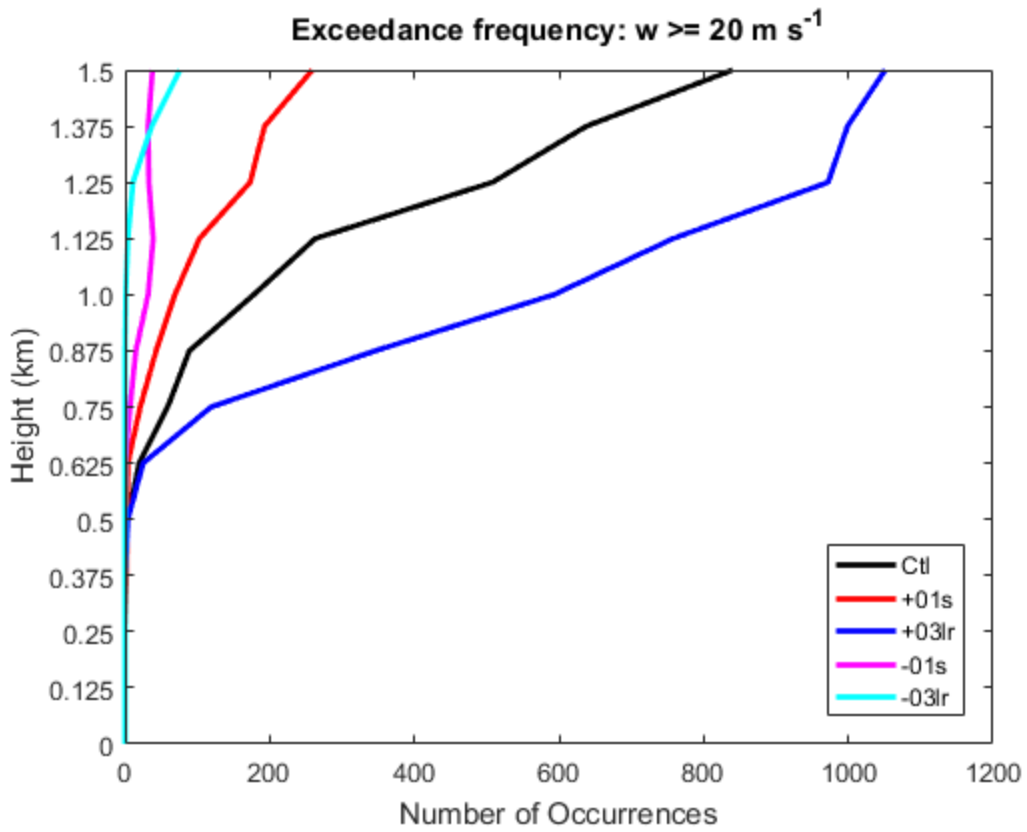


Figure 3.37. Exceedance frequency for vertical velocity of 20 m s^{-1} for all simulations.

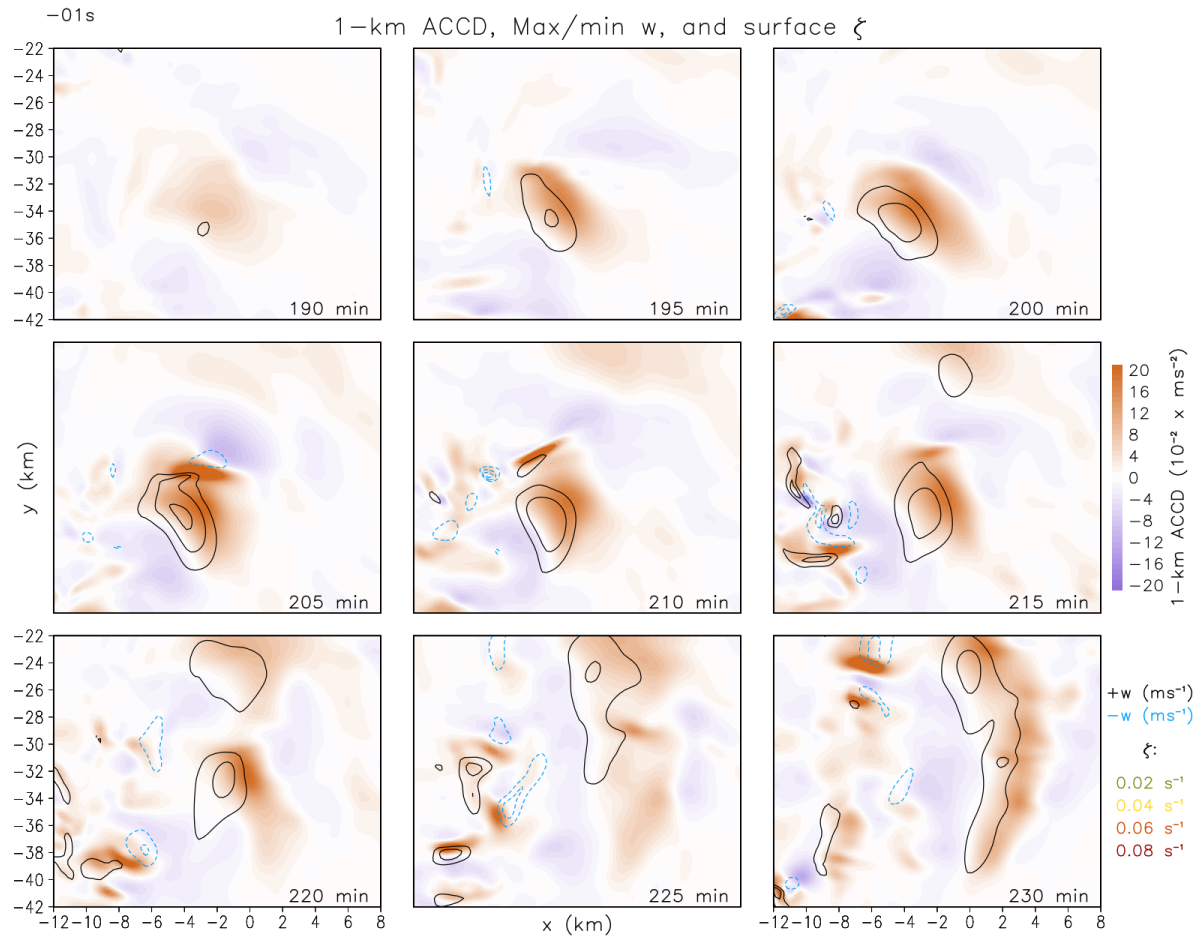


Figure 3.38. As in Fig. 3.14, but for -01s.

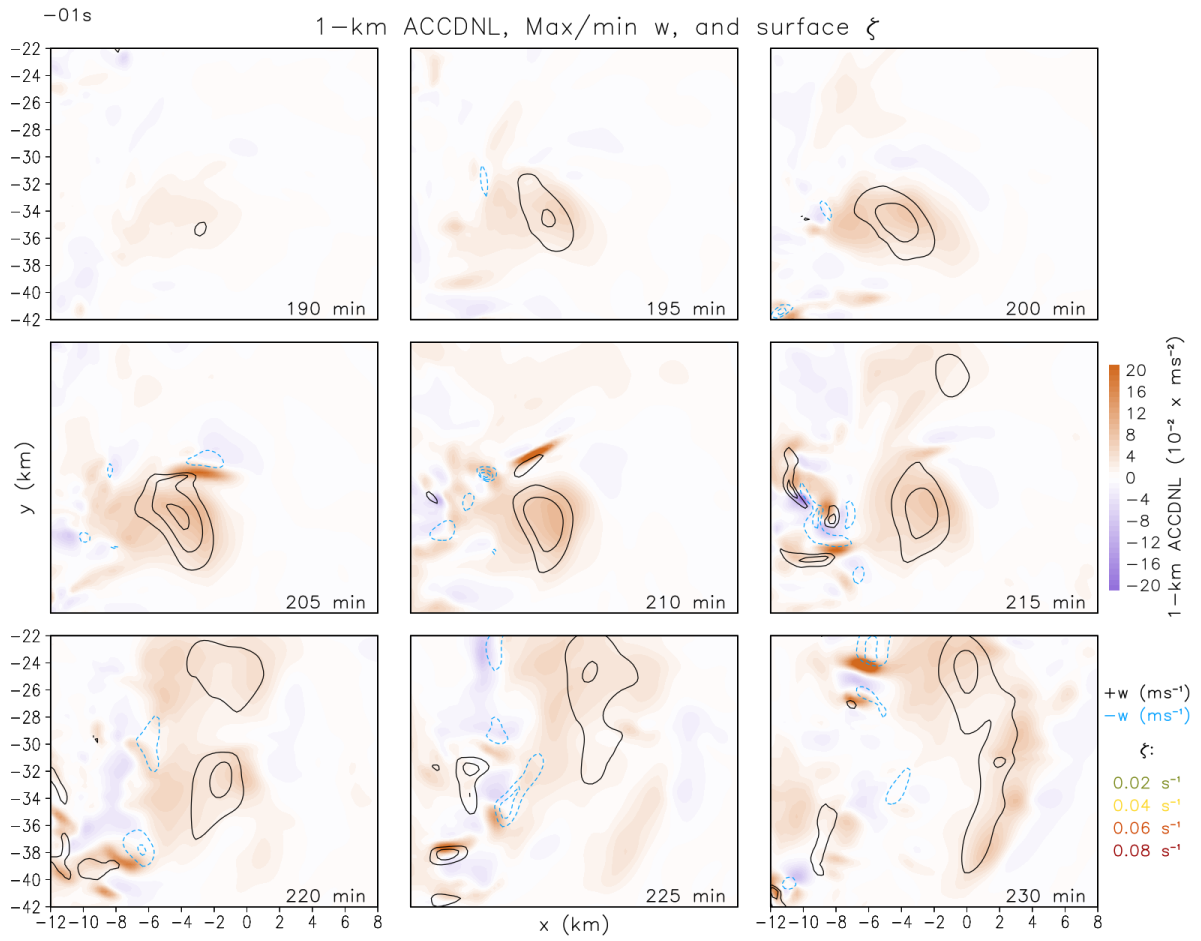


Figure 3.39. As in Fig. 3.20, but for -01s.

ζ , ACCDNL, and w for -01s

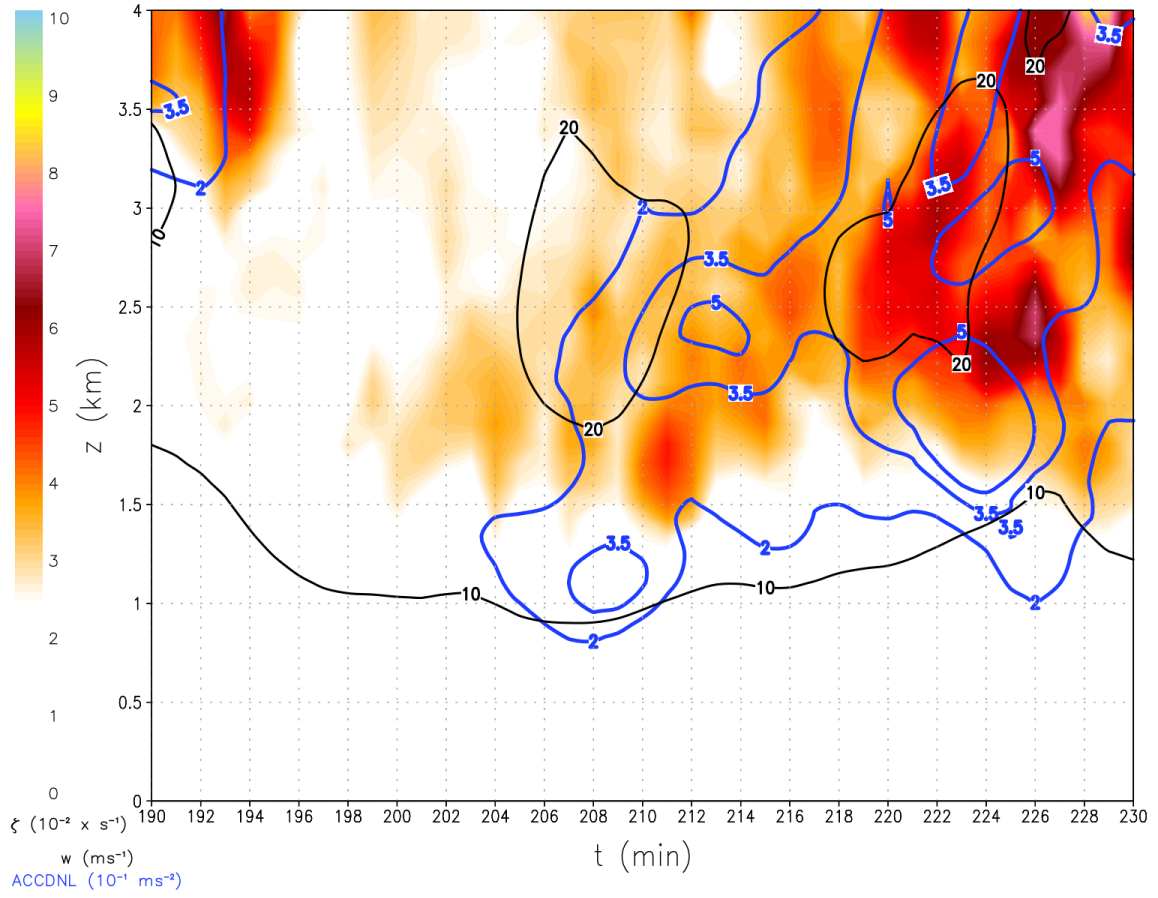


Figure 3.40. As in Fig. 3.24, but for -01s.

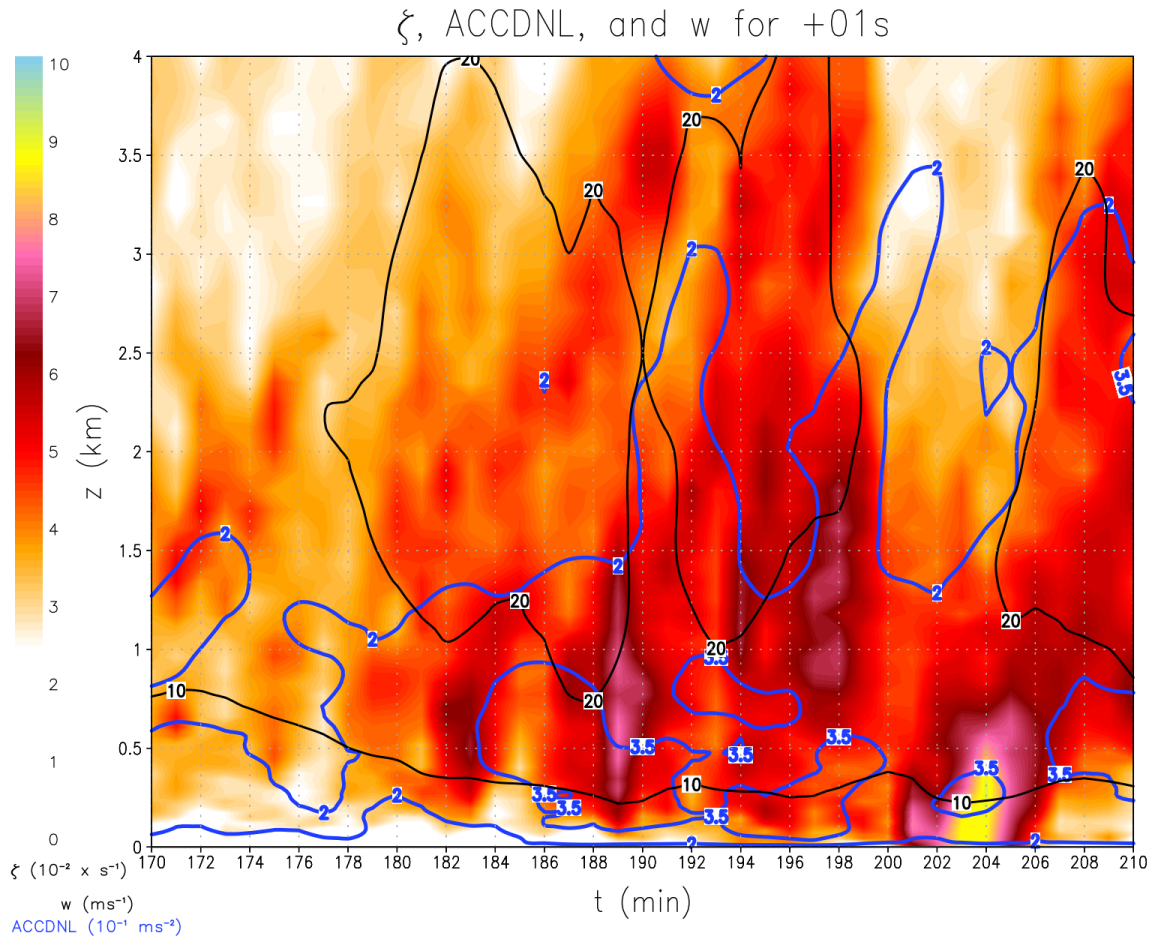


Figure 3.41. As in Fig. 3.24, but for +01s.

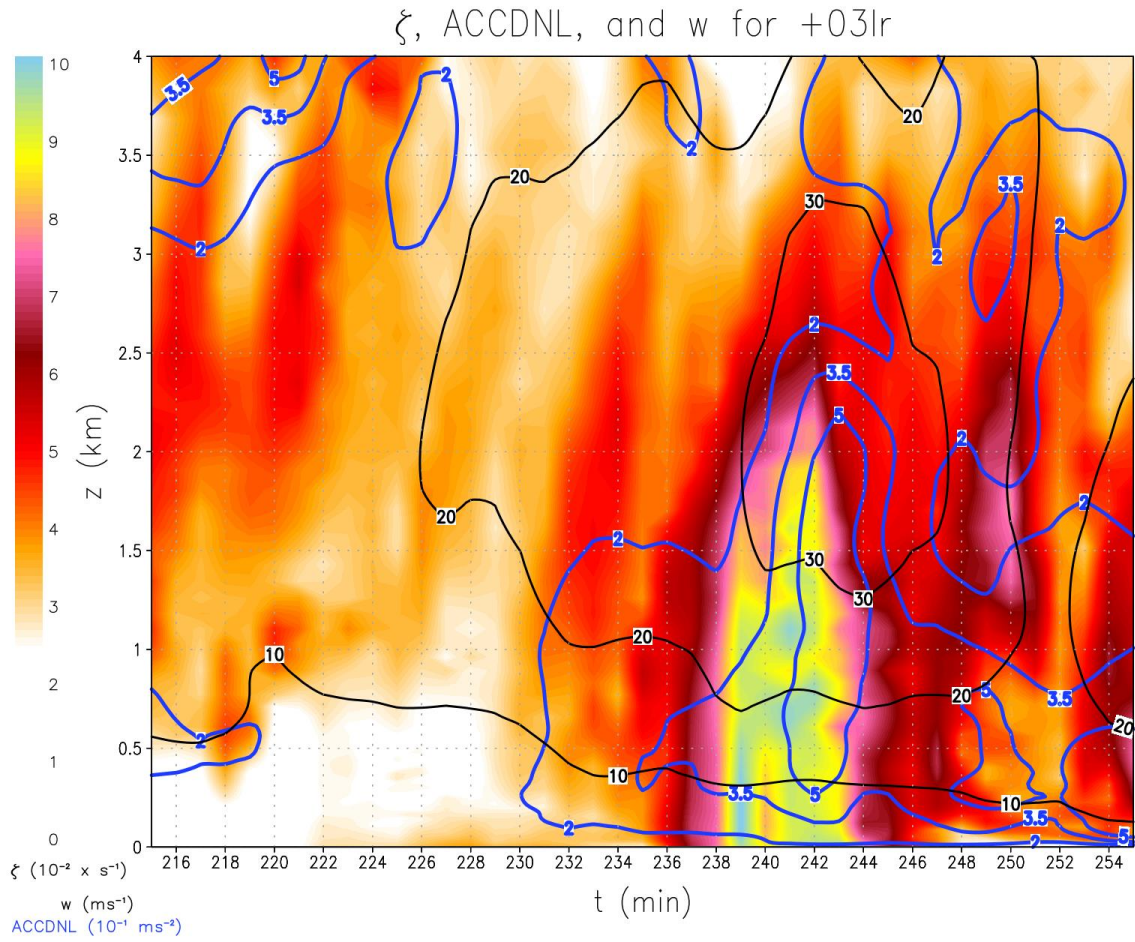


Figure 3.42. As in Fig. 3.24, but for +03lr.

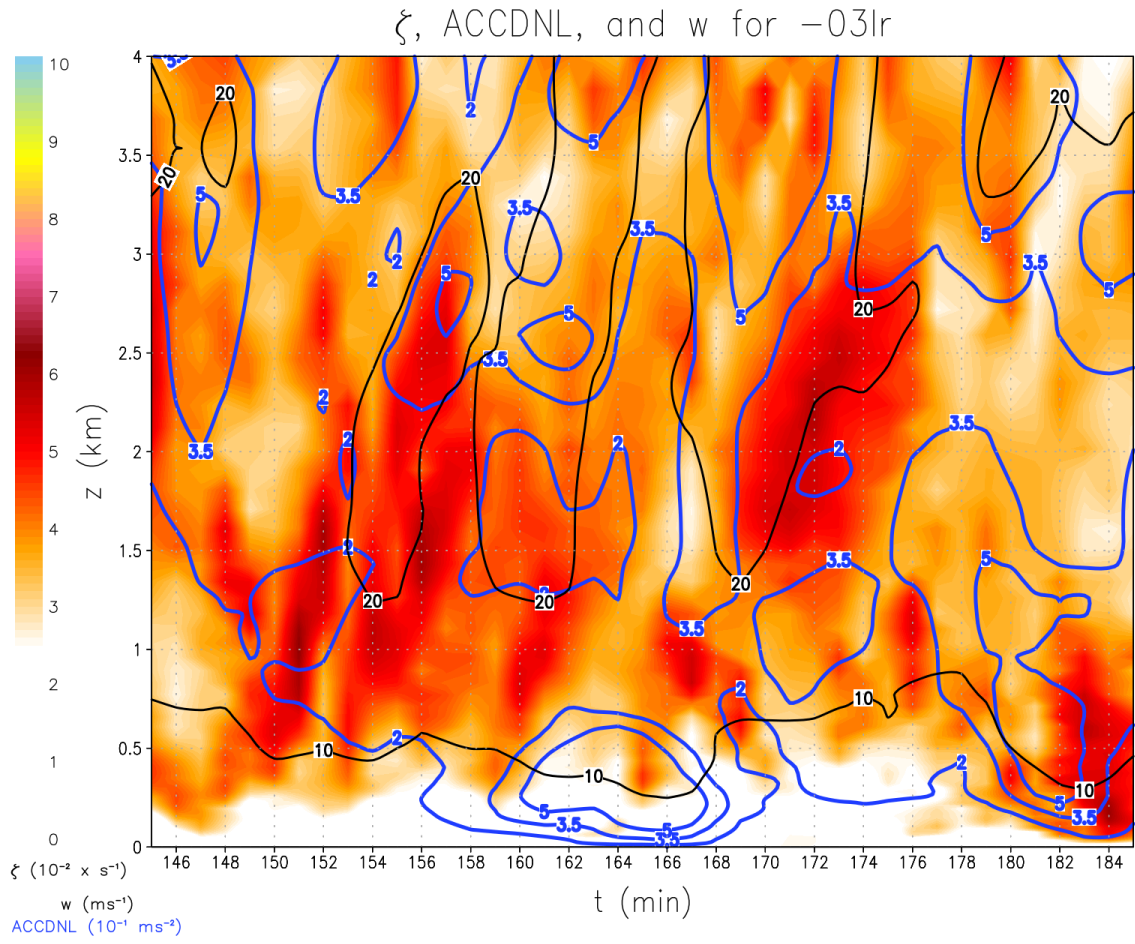


Figure 3.43. As in Fig. 3.24, but for -03lr.

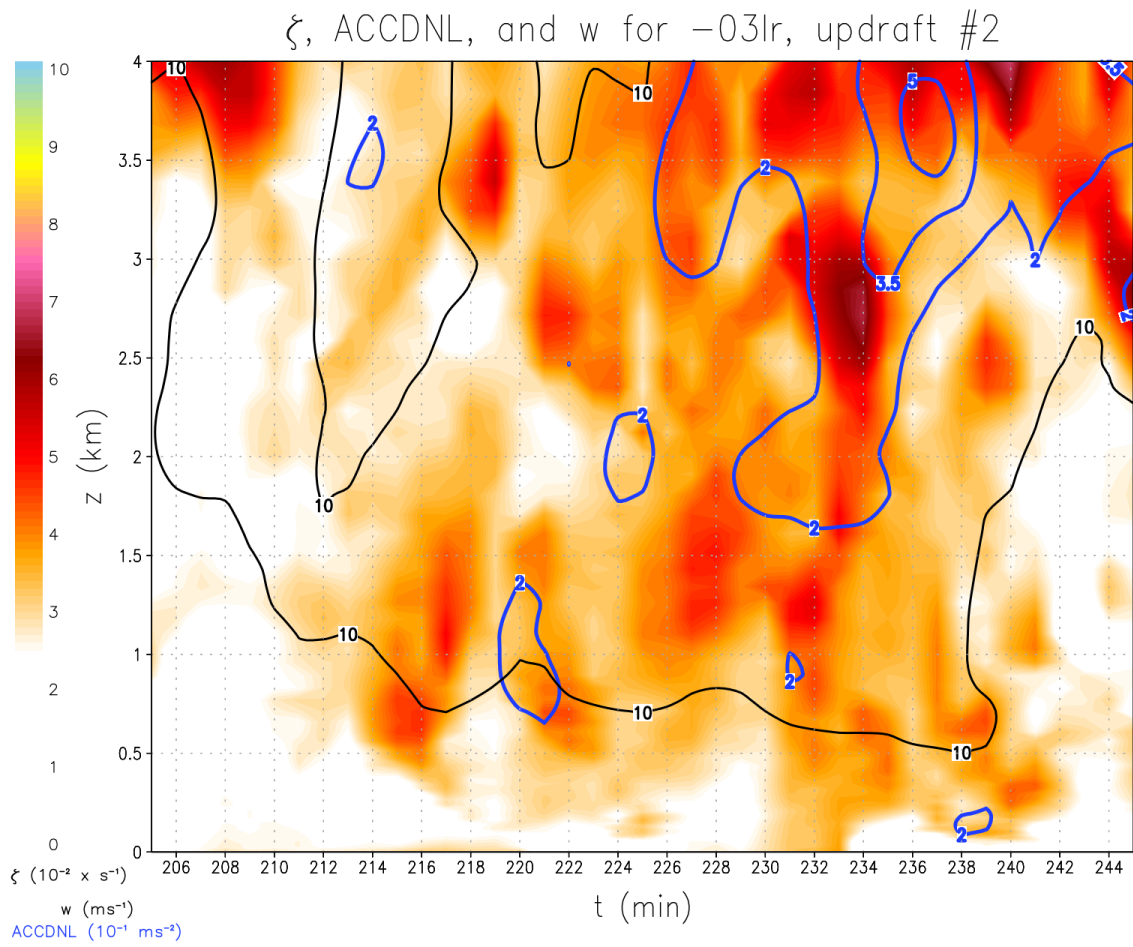


Figure 3.44. As in Fig. 3.24, but for a second $-03lr$ updraft that occurs at a closer simulation time to that in Fig. 3.42 for a more direct comparison between $-03lr$ and $+03lr$.

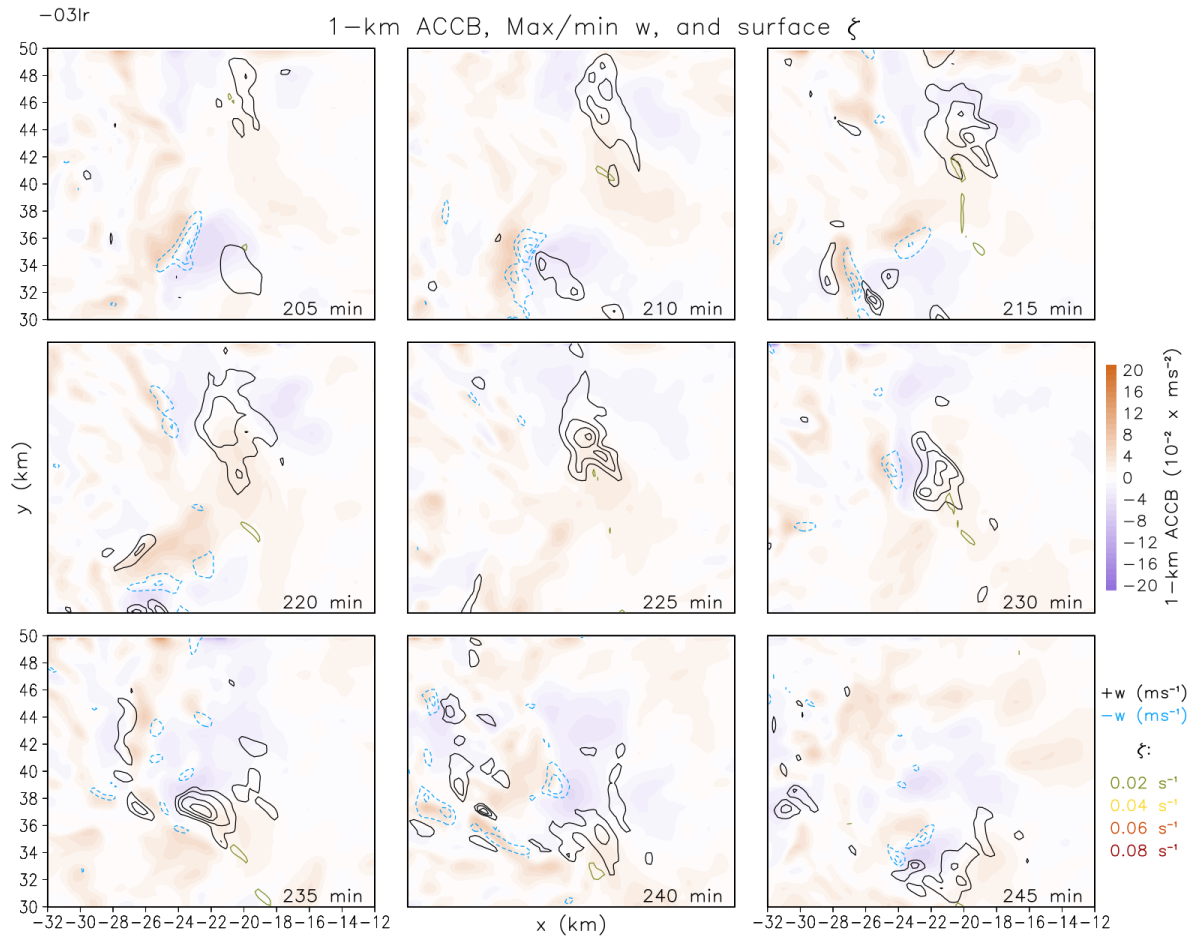


Figure 3.45. As in Fig. 3.15, but for -03lr.

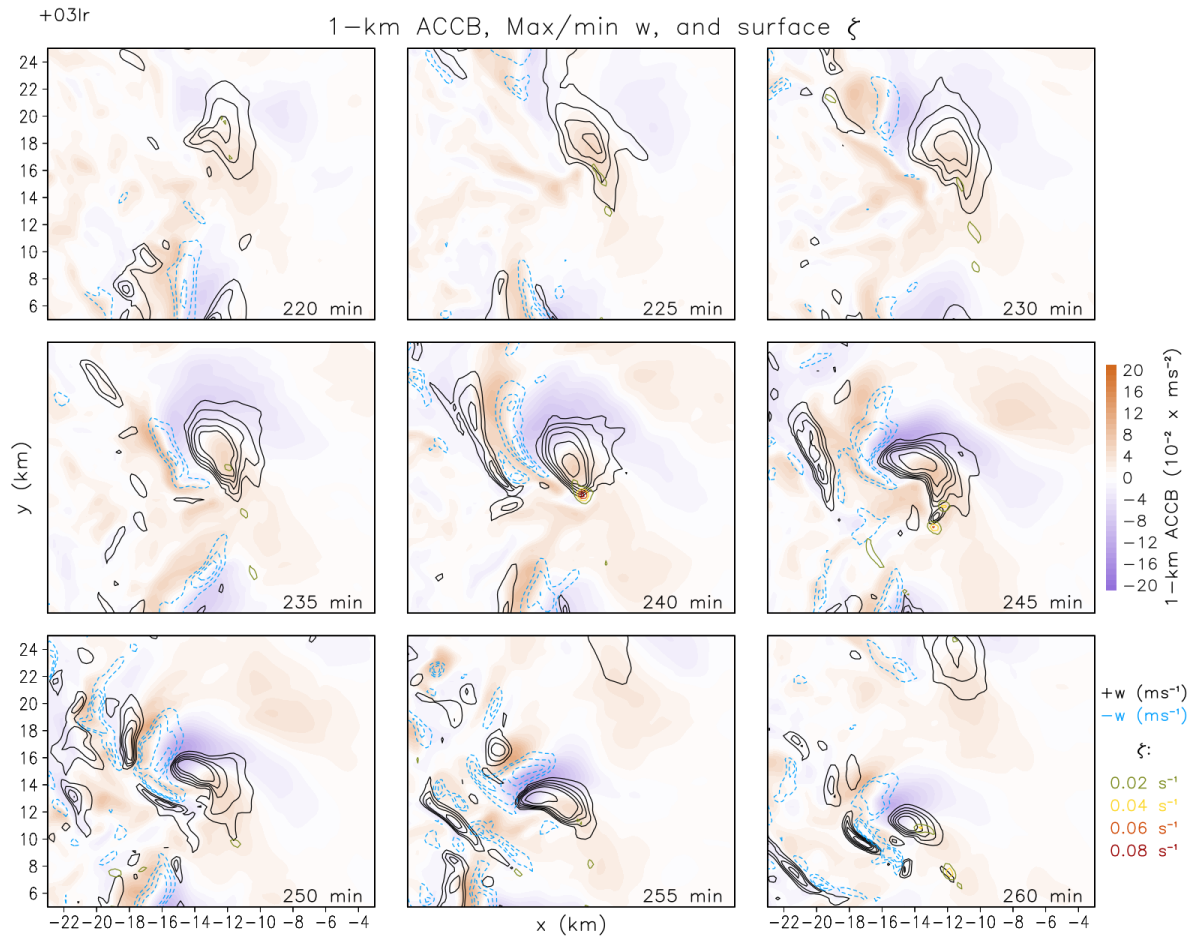


Figure 3.46. As in Fig. 3.15, but for +03lr.

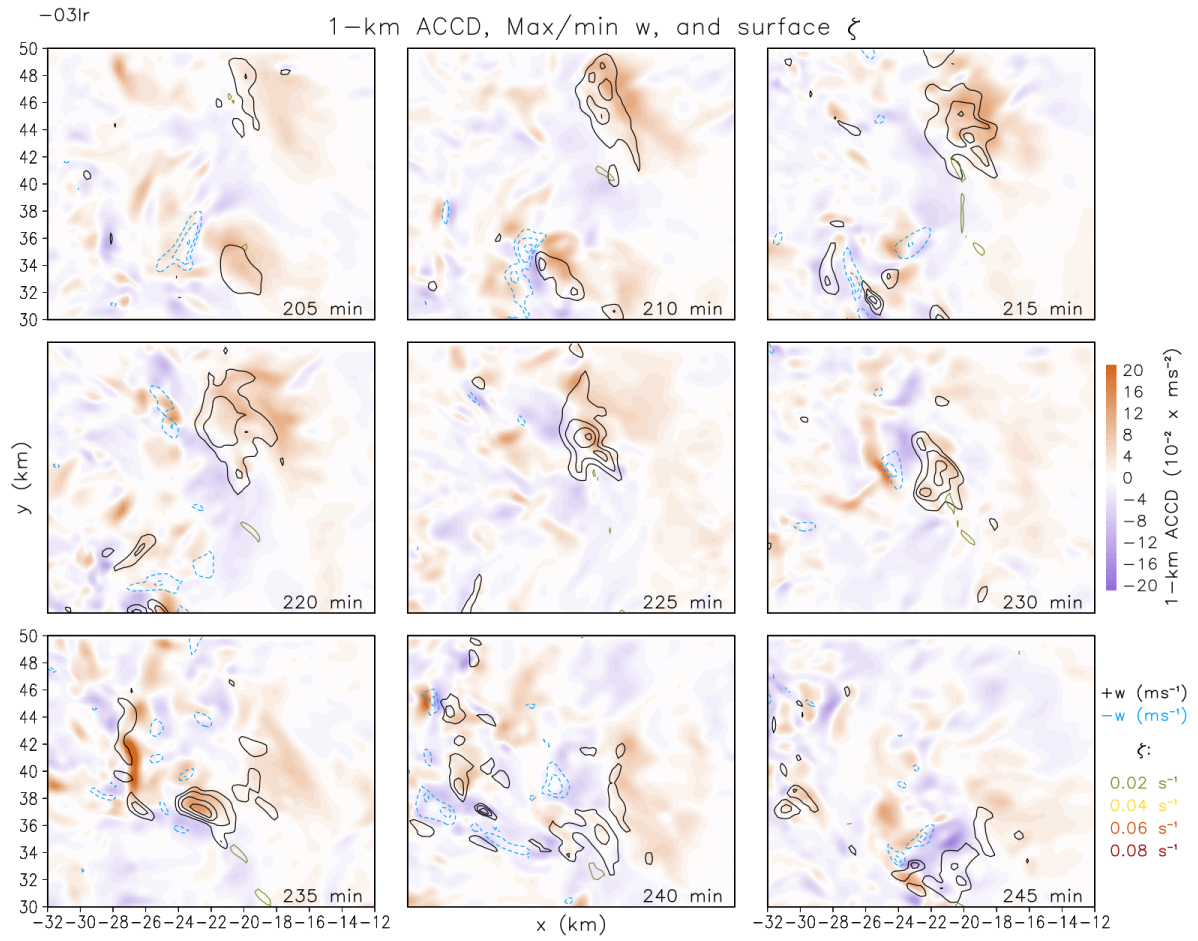


Figure 3.47. As in Fig. 3.14, but for -03lr.

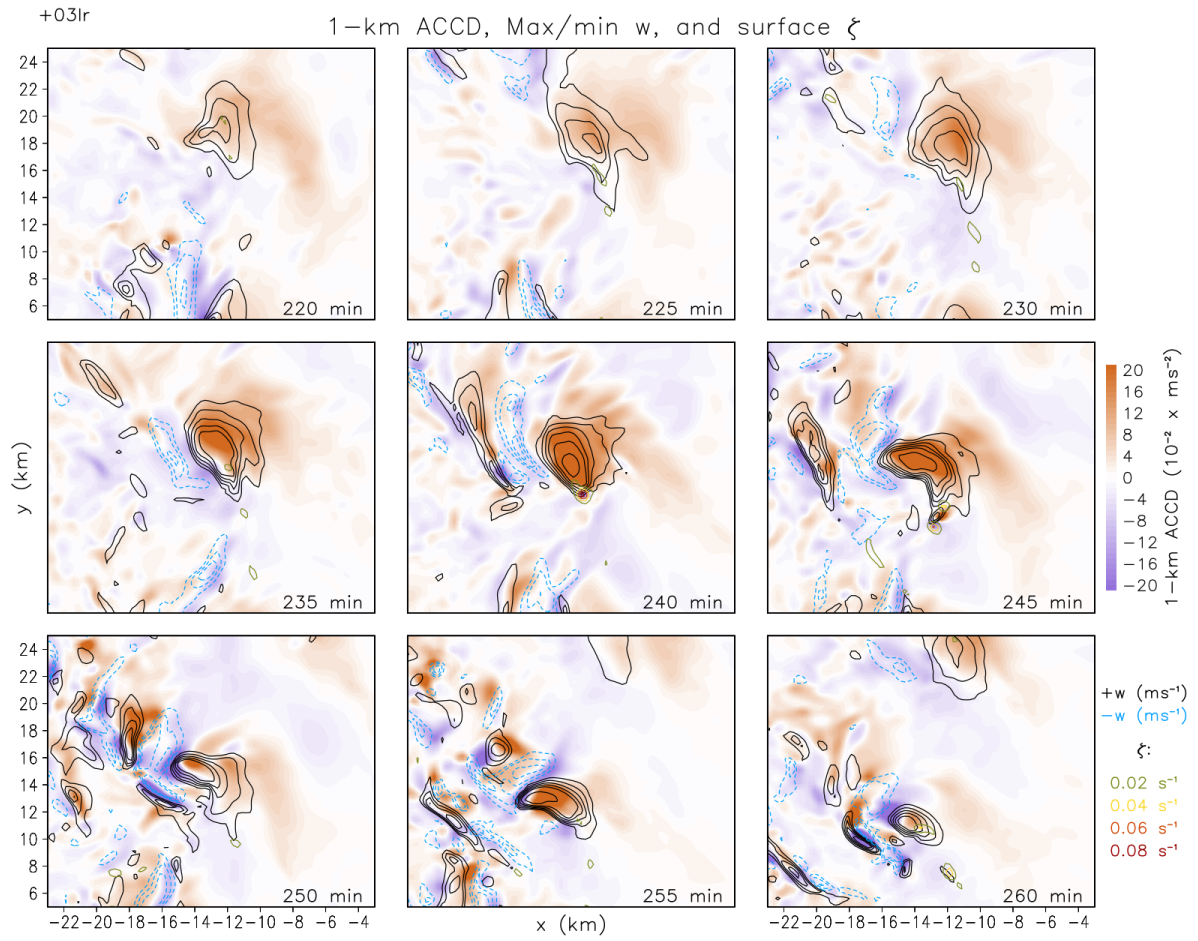


Figure 3.48. As in Fig. 3.14, but for +03lr.

Updraft Helicity and Near-Surface Vortex Tracks, Control

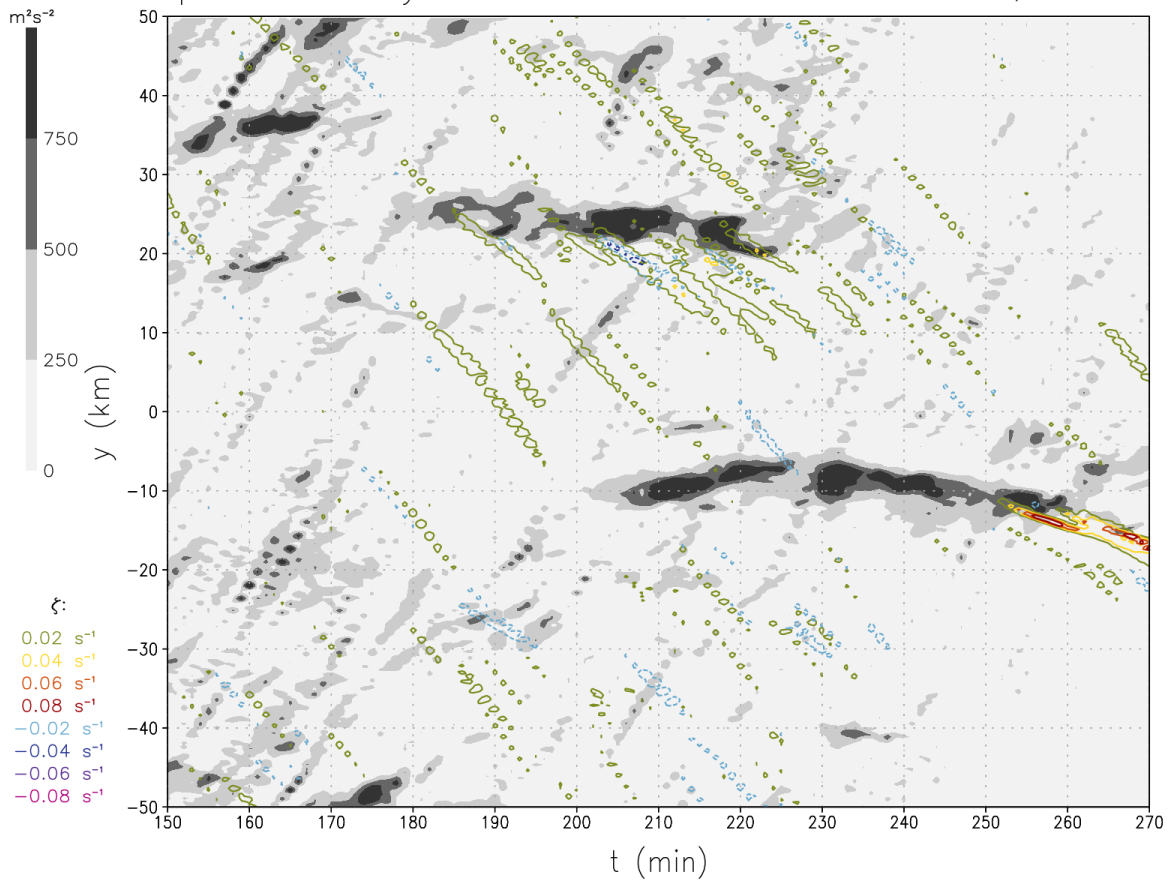


Figure 3.49. As in Fig. 3.4, but including anticyclonic lowest-level vortices.

Updraft Helicity and Near-Surface Vortex Tracks, Ctl No Cor

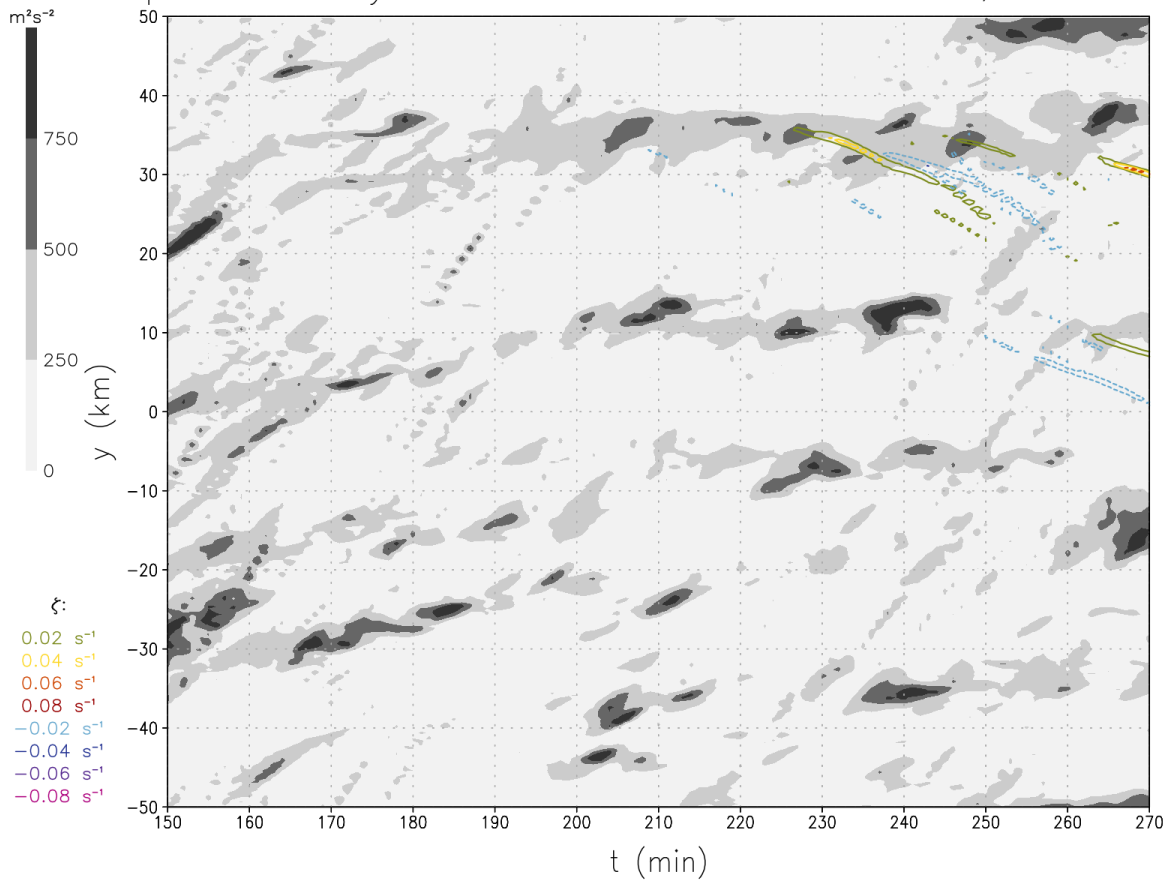


Figure 3.50. As in Fig. 3.49, but for the non-Coriolis control simulation.

Near-Surface Vorticity and 1-km updraft, Control

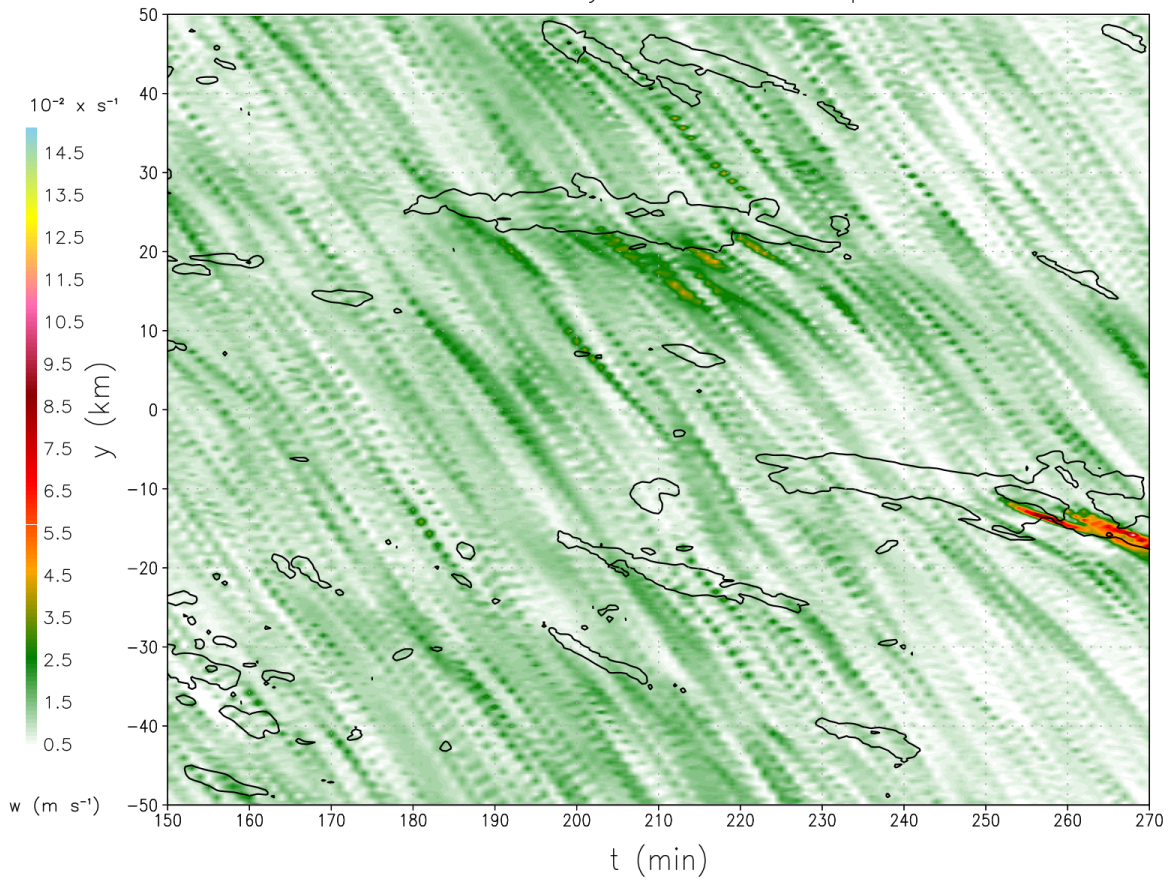


Figure 3.51. Hovmöller plot of near-surface vertical vorticity (s^{-1} ; shaded) and 1-km vertical velocity (m s^{-1} ; contours) tracks for the control simulation over the time period $t=150$ min to $t=270$ min.

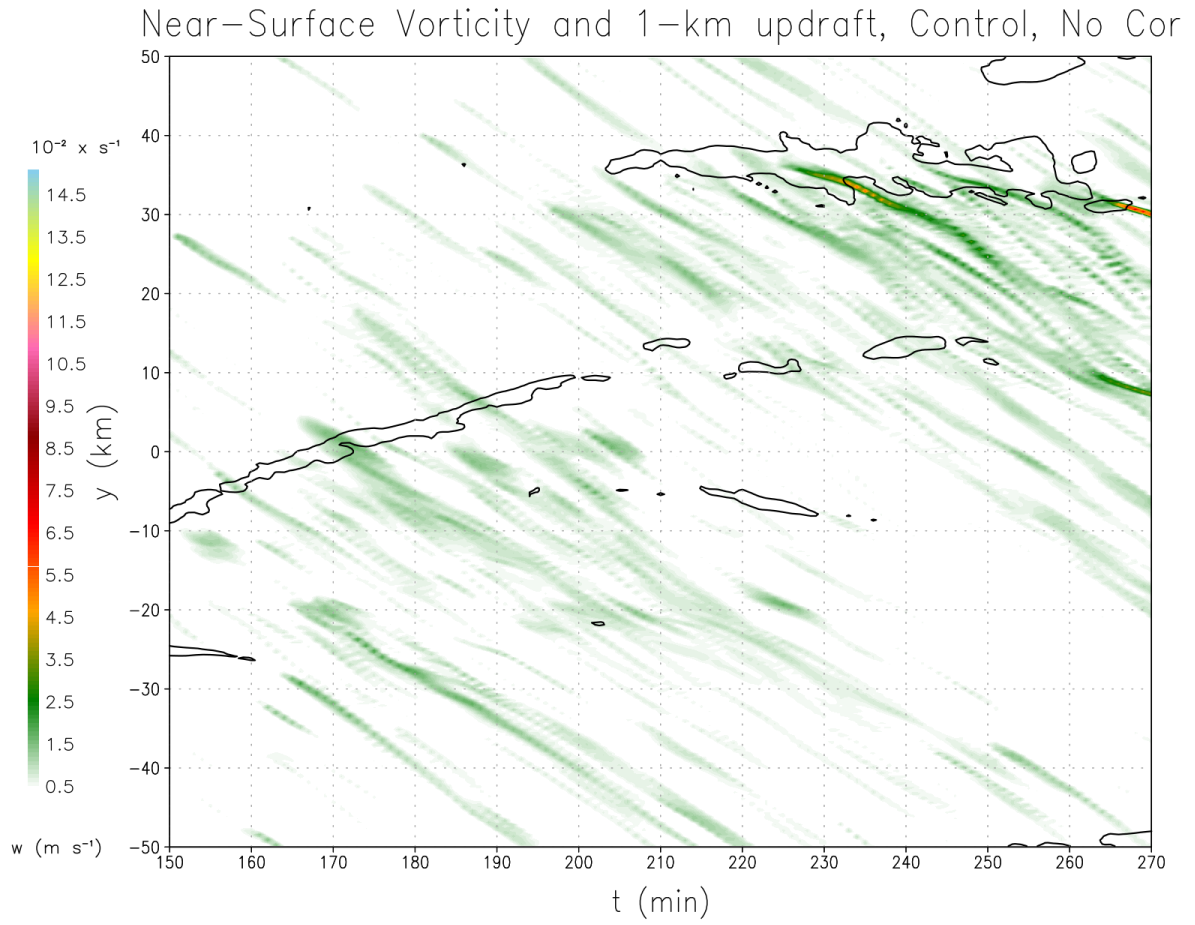


Figure 3.52. As in Fig. 3.51, but for the non-Coriolis control run.

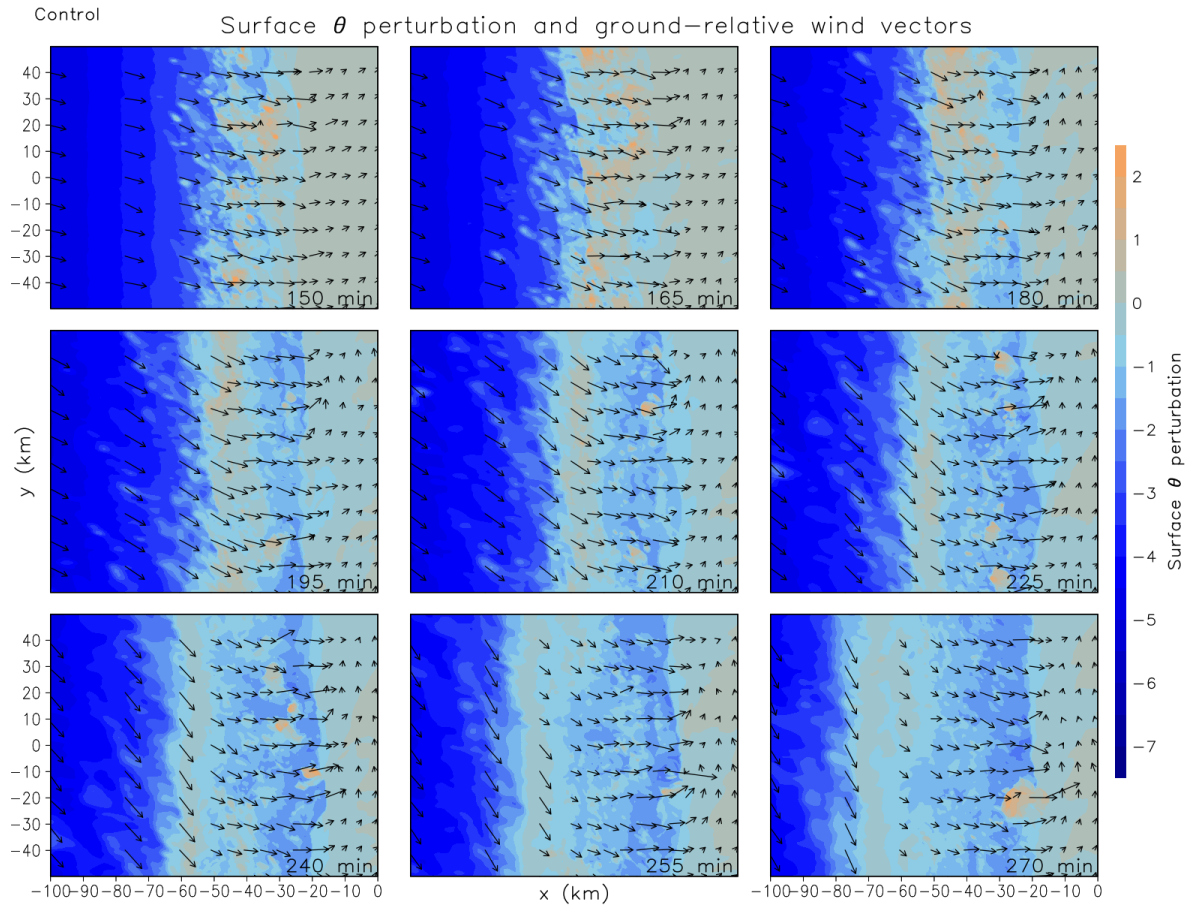


Figure 3.53. As in Fig. 3.2, but showing surface potential temperature perturbation (K; shaded) and surface wind vectors.

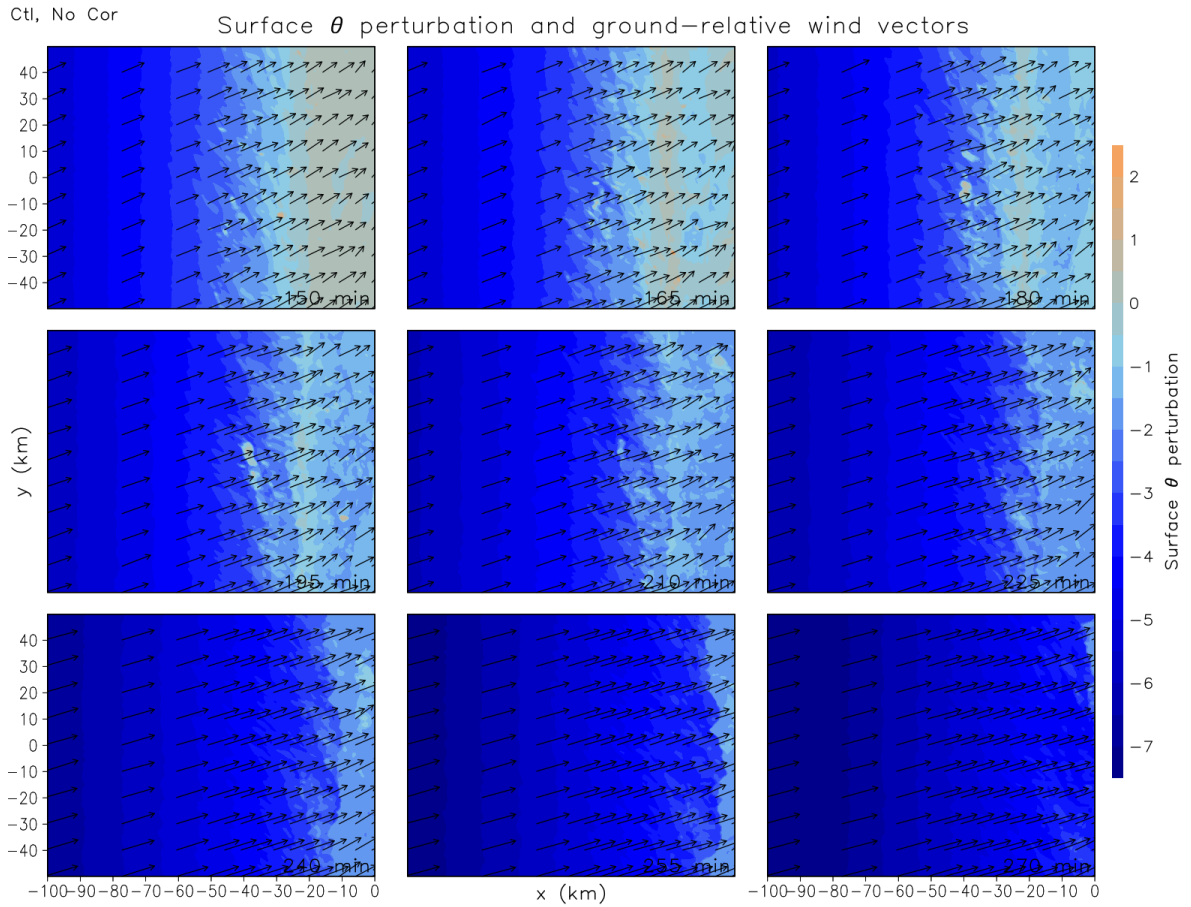


Figure 3.54. As in Fig. 3.53, but for the non-Coriolis control simulation.

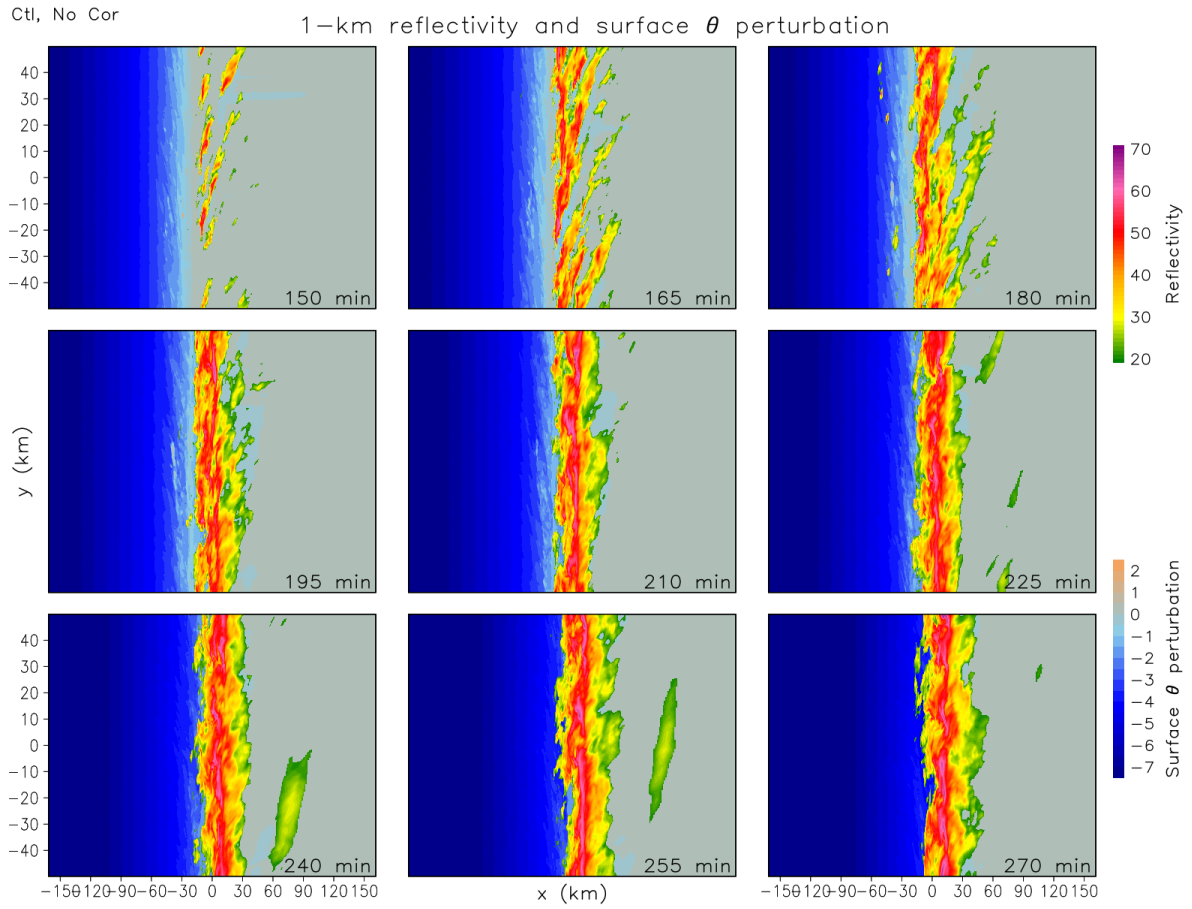


Figure 3.55. As in Fig. 3.3, but for the non-Coriolis control simulation.

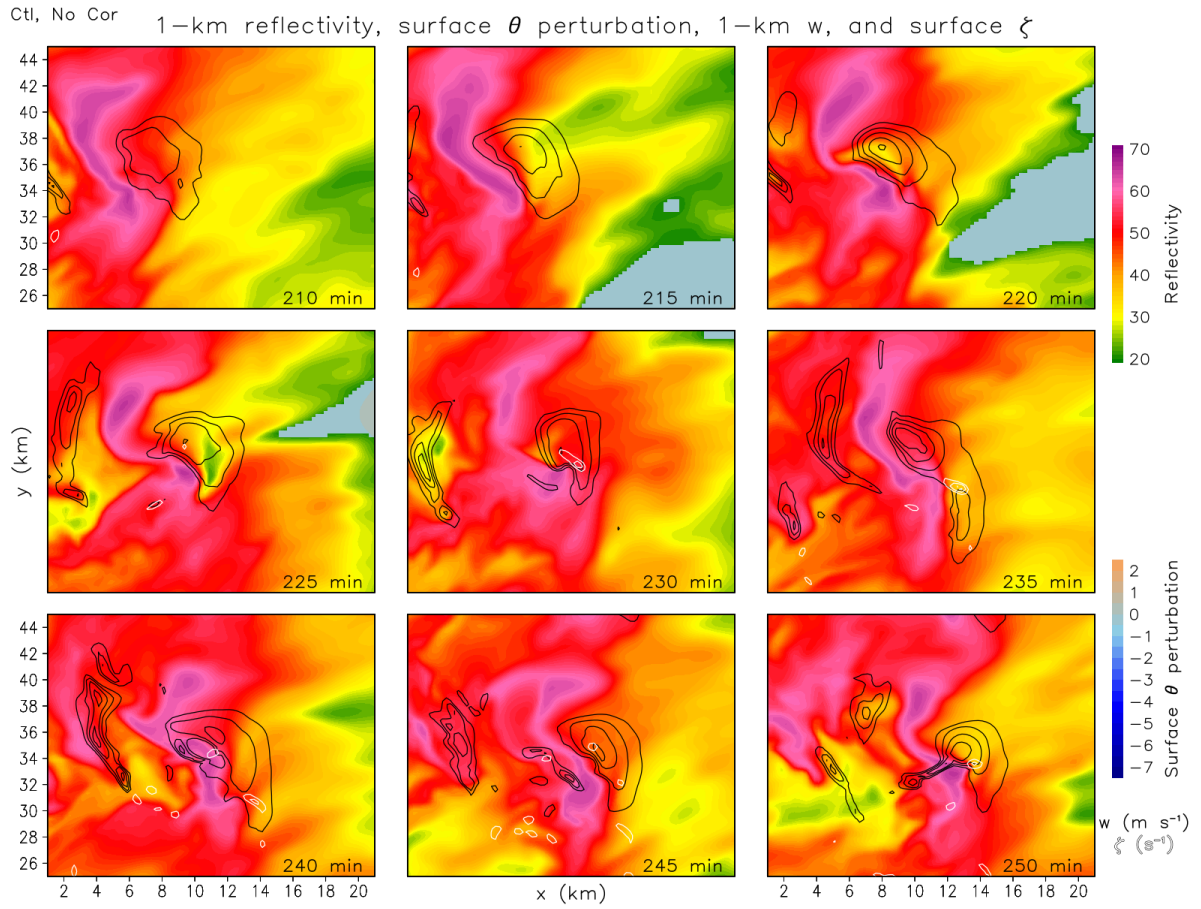


Figure 3.56. As in Fig. 3.5, but for the control, no Coriolis run.

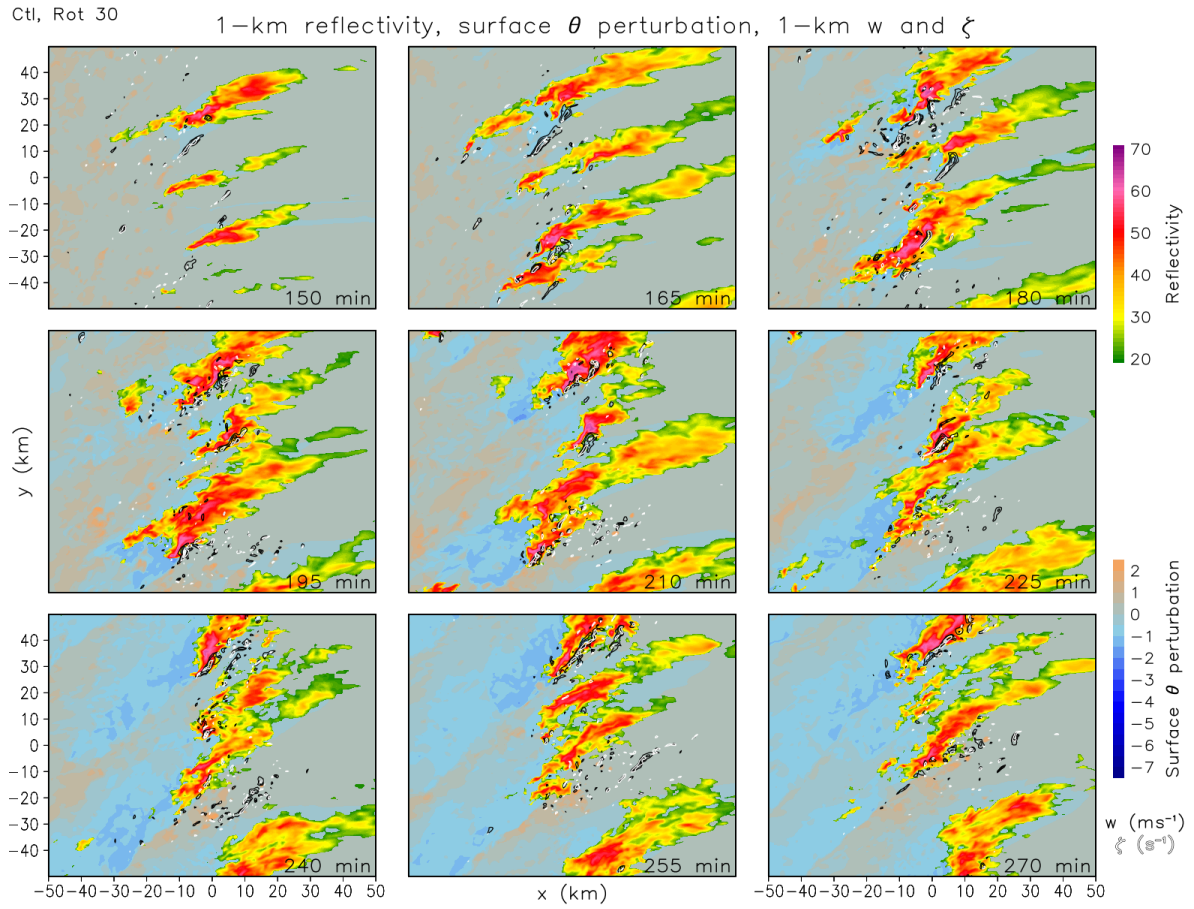


Figure 3.57. As in Fig. 3.2, but for the control simulation with the hodograph rotated 30° clockwise.

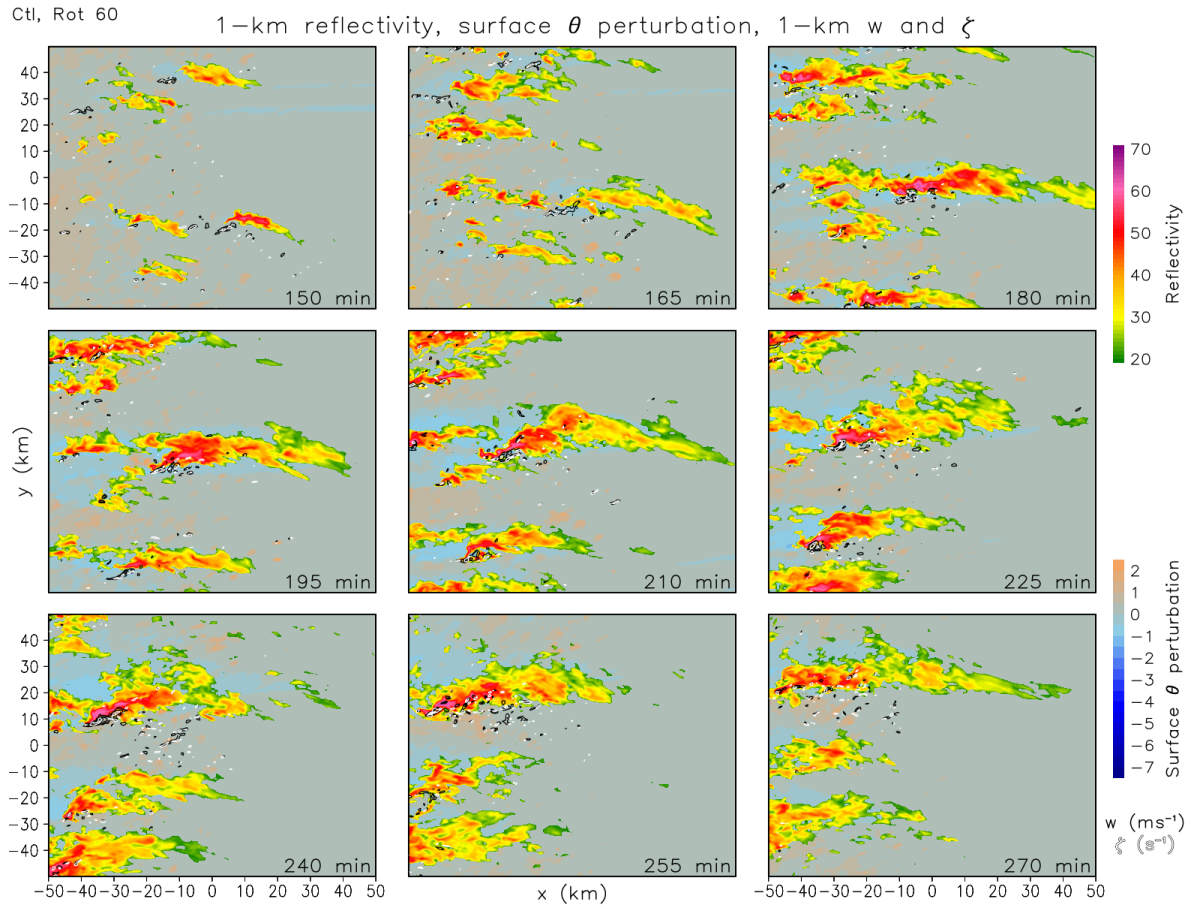


Figure 3.58. As in Fig. 3.2, but for the control simulation with the hodograph rotated 60° clockwise.

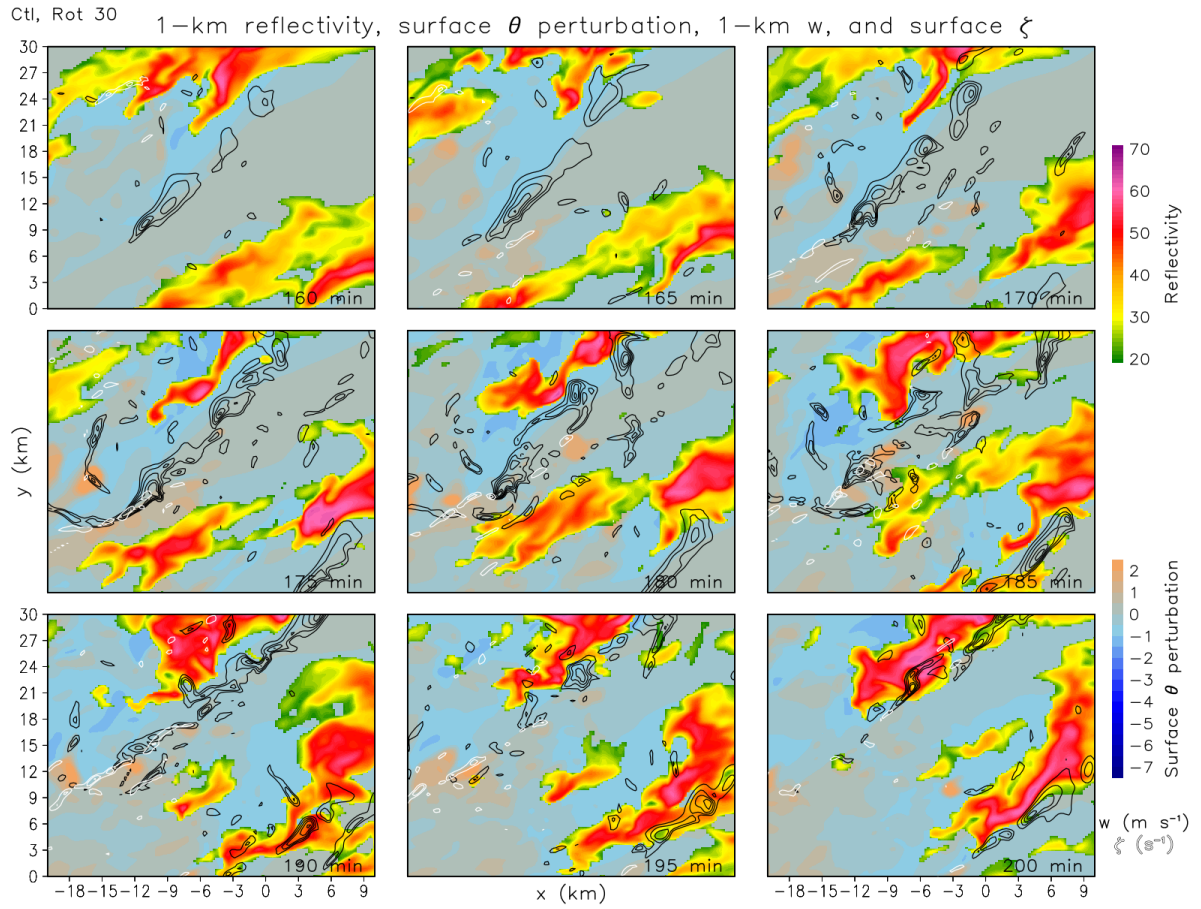


Figure 3.59. As in Fig. 3.57, but zoomed in on the development of an updraft and zone of near-surface vertical vorticity between two discrete convective cells.

Updraft Helicity and Near-Surface Vortex Tracks, Ctl, Rot 60

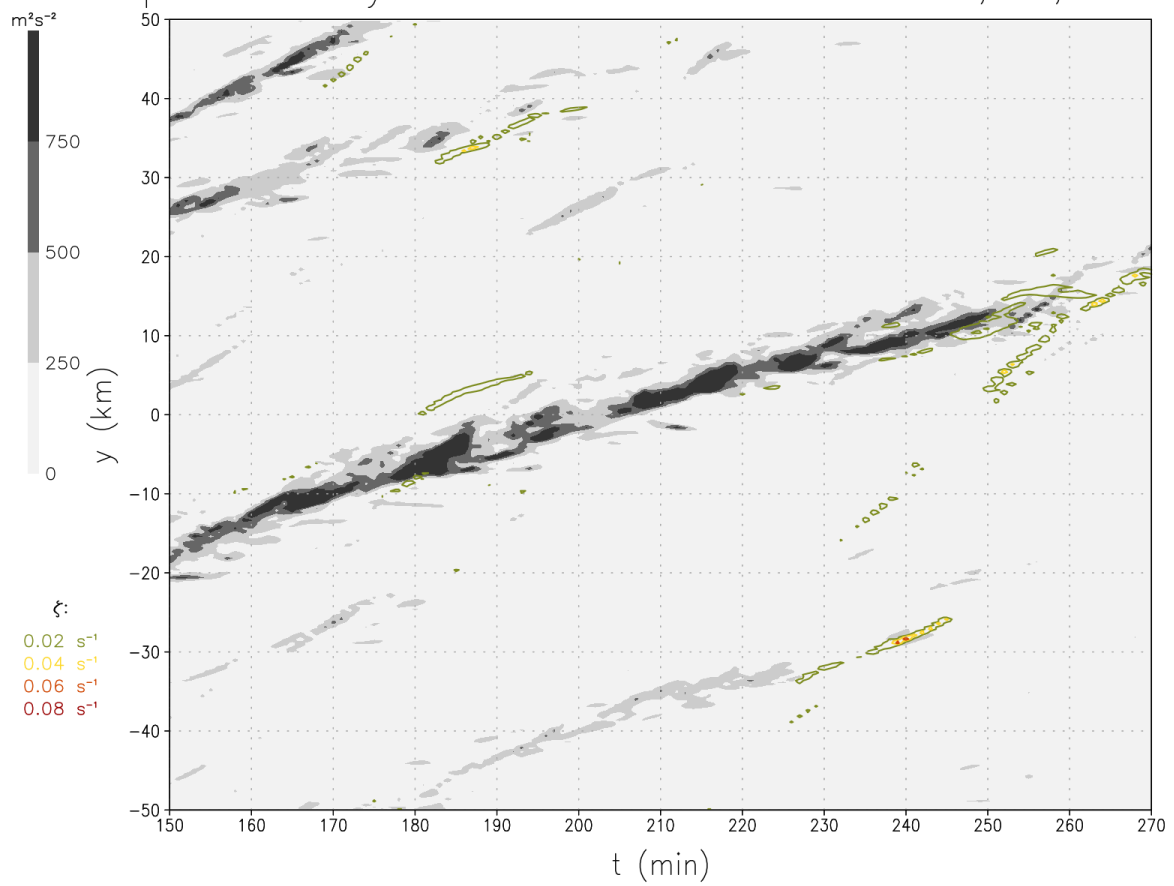


Figure 3.60. As in Fig. 3.4, but for the rotated 60° control simulation.

Control, Rot 60

Surface ξ and 1-km reflectivity (40 dBZ) and w

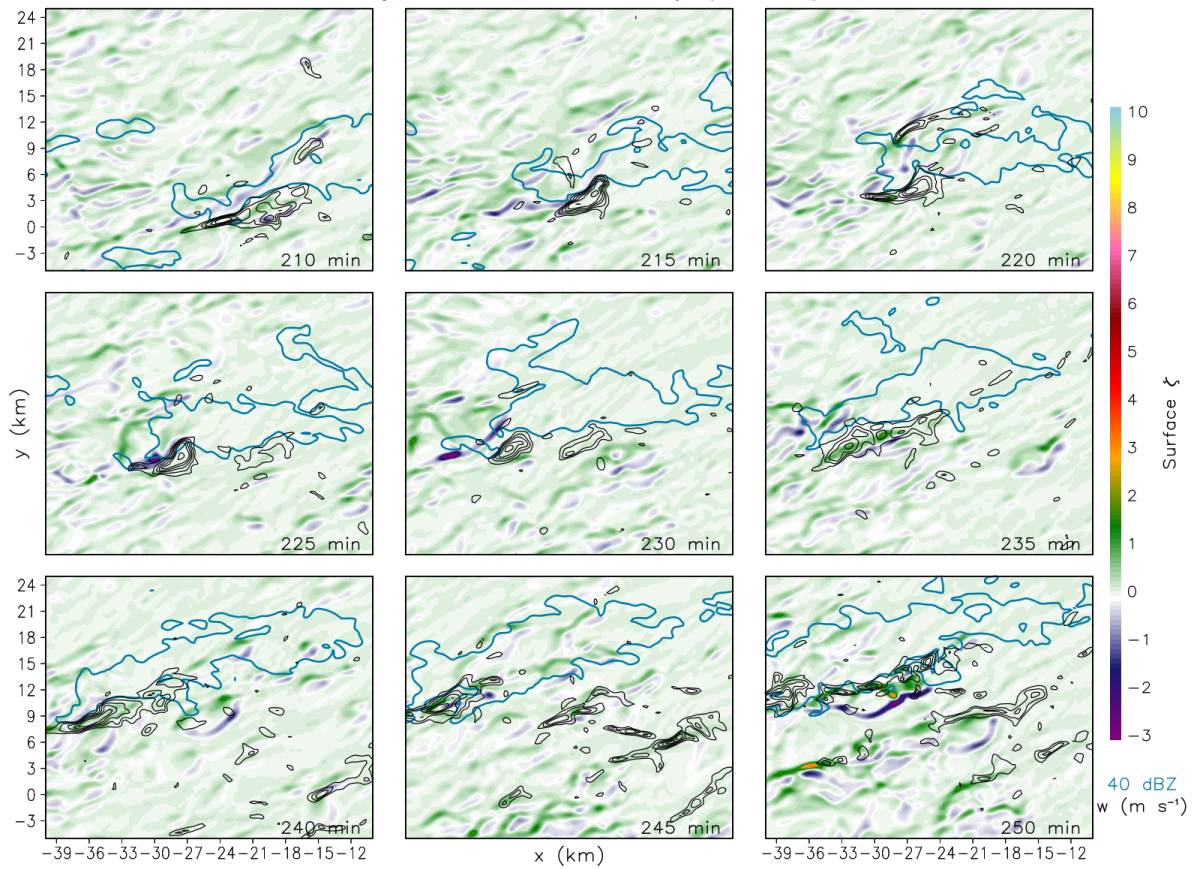


Figure 3.61. Lowest level vertical vorticity (s^{-1} ; shaded), 1-km updraft ($m s^{-1}$; black contours), and 40-dBZ simulated reflectivity contour (blue) for the strongest updraft in the rotated 60° control simulation from $t=210$ min through $t=250$ min.

CHAPTER 4

Summary and Conclusions

Investigations into severe and nonsevere high-shear, low-CAPE (HSLC) convection have identified key discriminators between their environments. In particular, low-level lapse rates and shear vector magnitudes—along with the strength of synoptic scale forcing for ascent—have been shown to differentiate well between those HSLC environments supporting severe convection and those that are limited to nonsevere convection. The idealized simulations herein have identified the physical explanations behind these sensitivities while providing an overview of the processes leading to the development of strong, near-surface vortices within HSLC environments that are capable of producing tornadoes or damaging straight-line winds.

Given a sufficiently strong initial updraft, the following processes lead to the development of a strong, near-surface vortex:

1. Low-to-midlevel vertical vorticity increases as the midlevel updraft develops and intensifies;
2. In response to the increase in vertical vorticity, upward-pointing accelerations via the nonlinear dynamic terms in the vertical perturbation pressure gradient acceleration (ACCDNL) increase in low levels;
3. Due to increased accelerations in low levels, low-level vertical velocities (i.e., updrafts) intensify; and
4. Increased low-level vertical velocities provide increased potential for tilting and especially stretching of near-surface vorticity, most of which occurs in the lowest 0.5-1 km above ground. This facilitates the development of a strong, near-surface vortex. Note that this step will only succeed if there is nontrivial vertical vorticity at the ground and this vertical vorticity is spatially collocated with the overlying updraft.

These processes provide the potential for a positive feedback, and it may be that any one of the first two or three takes the initial lead in various scenarios. Following the identification of these processes in a control simulation, sensitivity tests were used to determine how these processes were affected as either 0-1 km shear vector magnitude or 0-3 km lapse rates were decreased or increased.

Decreasing 0-1 km shear vector magnitude to 20 kt (-01s) led to an overall drop in the strength and organization of convection. The production of near-surface to midlevel vertical vorticity was considerably diminished, which largely limits step 1 of the above process. Unsurprisingly, -01s produced the fewest appreciable low-level updrafts and vortices of the tested environments. Despite few features of interest compared to other environments, local increases in low-level hodograph length and curvature late in the simulation did provide a suitable environment for the development of embedded rotating updrafts, implying that operational forecasters should be aware of any potential small-scale environmental changes (e.g., localized backing that could enhance low-level hodograph length and curvature) that could turn an innocuous near-storm environment into one capable of supporting severe weather. As 0-1 km shear vector magnitude increased to 40 kt (+01s), low-to-midlevel vertical vorticity developed much more readily, while a significant number of incipient, near-surface vortices were produced. Thus, the environment was suitable for the chain of processes outlined above to succeed.

As low-level lapse rates decrease to 6.0 K km^{-1} (-03lr), the primary limit on the development of near-surface vortices appears to be weaker initial updrafts, which limits the effectiveness of the chain of processes. Accordingly, despite producing a larger *number* of updrafts and vortices than -01s, those that are produced tend to be weaker and shorter-lived. Investigation of updrafts early in the evolution of the simulated convective system in -03lr also suggest that it may take time for sufficient vertical vorticity to develop at the surface. The environment with lapse rates steepened to 6.5 K km^{-1} (+03lr) unequivocally produced the most impressive convection and vortices across the primary set of simulations, suggesting it represented the best combination of lapse rates and shear among the five environments.

Regardless of environment, dynamic vertical accelerations, rather than buoyant vertical accelerations, were dominant in forcing updrafts. This is no surprise, given previous research indicating that dynamic accelerations dominated in both convection with rotating updrafts and in HSLC environments. However, it is important to reiterate that ACCDNL, in particular, is the critical factor in determining whether an updraft will support a strong, near-surface vortex. This implies that HSLC environments incapable of producing sufficient low-to-midlevel vertical vorticity—i.e., those with meager low-level shear—will have a much lower potential of producing strong near-surface vortices, as found here. Furthermore, it also suggests that the potential for the development of a strong surface vortex could be evaluated to some degree in real-time with radial velocity products, assuming sufficient radar coverage. Indeed, in the simulations presented here, nearly 20 minutes of time passed between the initial intensification of midlevel (1-to-2-km) vertical vorticity and the development of the near-surface vortex. Future work should continue to assess potential precursors to the development of low-level and near-surface vortices, particularly in simulations with finer horizontal resolutions that ensure the vortices are sufficiently resolved. The identification of any precursors could subsequently be used in operational settings to potentially improve upon the poor probability of detection, high false alarm rate, and limited lead time of HSLC tornado warnings.

Coriolis forcing and shear vector orientation relative to boundaries were also assessed here through a handful of additional simulations. Including Coriolis on the perturbation winds with the given control environment augments near-surface vertical vorticity through the convergence of planetary vorticity (by the perturbation winds). However, Coriolis forcing within the model is *not* necessary for cyclonic vortices to dominate, contrary to prior QLCS research. Environments with large ambient streamwise vorticity (such as in our simulations) appear to be quite effective at producing low-level cyclonic vortices, although that streamwise vorticity itself may, in nature, be partly attributable to the combination of boundary layer drag and Coriolis. Furthermore, the non-Coriolis QLCS still produced an embedded rotating updraft and a shorter-lived, weaker near-surface vortex.

Although a larger cross-boundary component of low-to-midlevel shear vectors generally led to more discrete updrafts, the overall strength of updrafts and their rotational characteristics did not change considerably as the hodograph was rotated relative to an initial boundary. However, the ability to produce a strong, near-surface vortex decreased as the cross-boundary component of the flow aloft (relative to the initiating boundary) was increased. Despite strong, rotating updrafts and the development of near-surface vorticity, the region of near-surface vertical vorticity was offset spatially from the potential updraft stretching. In essence, these more discrete cells were spatially removed from the source of vorticity along the leading edge of system-generated cold pools, which precluded intensification of any incipient vortices. These tests underscored the point that even when the key ingredients are in place for the development of a strong, near-surface vortex (strong low-level ACCDNL and updrafts, along with sufficient near-surface vorticity), they are insufficient to produce a vortex unless they are spatially and temporally collocated.

Although the particular matrix of simulations conducted here investigated only a small portion of the HSLC parameter space, the values for shear vector magnitudes and lapse rates tested represent a realistic sampling of environments near the most discriminatory values of these fields according to Sherburn and Parker (2014) and the results of Chapter 1. Thus, we are confident in the following summary of sensitivities:

- The primary impact of decreasing 0-1 km shear vector magnitude is decreasing the production of low-to-midlevel vertical vorticity via tilting by the developing updrafts. This subsequently limits low-level ACCDNL and, thus, low-level vertical velocities.
- The primary impact of decreasing 0-3 km lapse rates is decreasing the initial strength of updrafts. This limits the potential for tilting and stretching of vorticity in low levels.
- Decreasing either 0-1 km shear vector magnitudes or 0-3 km lapse rates limits the potential for the development of near-surface vortices capable of producing severe hazards. Either situation prevents the chain of processes extending from the

development of a strong updraft to the eventual development of a strong, near-surface vortex from being successful.

Note that these findings are not necessarily a surprise when viewed in the context of existing research on tornadogenesis. A key discovery here is that the same processes appear to be at work regardless of the magnitude of CAPE in the near-storm environment, and the same sensitivities to low-level shear and lapse rates hold. Additionally, the shallowness of the layer over which these key processes occur is eye-opening. Many of the processes that precede tornadogenesis within low-topped HSLC convection occur in the lowest few hundred meters above ground—well below that which is observable in many locations given the current operational radar network. The results of this work could be used as impetus for improving the spatial coverage of operational radars within the U.S., particularly in locations where severe HSLC convection is common.

There is no shortage of additional work on HSLC environments to be undertaken. Future work should continue to test the sensitivities of HSLC convection to additional environmental characteristics, such as midlevel shear vector magnitudes (which were also shown by Sherburn and Parker 2014 to be skillful discriminators), hodograph shapes, forcing mechanisms and strengths, and the orientation and strength of nearby boundaries. Further work at higher resolutions where low-level vortices are guaranteed to be adequately resolved would be especially useful in analyzing sources of vorticity and how HSLC vortices differ from those in higher-CAPE convection. Additionally, studies comparing observational data and model output, particularly with tools such as a radar emulator, would be helpful in identifying precursors to low-level vortexgenesis, which could improve detection and lead time of severe hazards in real cases. In spite of the lingering questions and abundant potential future work, the simulations herein provide detailed conclusions on why two of the most skillful environmental parameters, low-level shear vector magnitudes and lapse rates, discriminate well between severe and nonsevere HSLC convection.

REFERENCES

- Adlerman, E. J., and K. K. Droegemeier, 2005: The Dependence of Numerically Simulated Cyclic Mesocyclogenesis upon Environmental Vertical Wind Shear. *Mon. Wea. Rev.*, **133**, 3595-3623.
- Anderson-Frey, A. K., Y. P. Richardson, A. R. Dean, R. L. Thompson, and B. T. Smith, 2016: Investigation of Near-Storm Environments for Tornado Events and Warnings. *Wea. Forecasting*, **31**, 1771-1790.
- Ashley, W. S., A. J. Krmenc, and R. Schwantes, 2008: Vulnerability due to nocturnal tornadoes. *Wea. Forecasting*, **23**, 795–807.
- Atkins, N. T., J. M. Arnott, R. W. Przybylinski, R. A. Wolf, and B. D. Ketcham, 2004: Vortex Structure and Evolution within Bow Echoes. Part I: Single-Doppler and Damage Analysis of the 29 June 1998 Derecho. *Mon. Wea. Rev.*, **132**, 2224-2242.
- Atkins, N. T., C. S. Bouchard, R. W. Przybylinski, R. J. Trapp, and G. Schmocker, 2005: Damaging Surface Wind Mechanisms within the 10 June 2003 Saint Louis Bow Echo during BAMEX. *Mon. Wea. Rev.*, **133**, 2275-2296.
- Atkins, N. T., and M. St. Laurent, 2009a: Bow Echo Mesovortices. Part I: Processes That Influence Their Damaging Potential. *Mon. Wea. Rev.*, **137**, 1497-1513.
- Atkins, N. T., and M. St. Laurent, 2009b: Bow Echo Mesovortices. Part II: Their Genesis. *Mon. Wea. Rev.*, **137**, 1514-1532.
- Bluestein, H. B., and M. L. Weisman, 2000: The interaction of numerically simulated supercells initiated along lines. *Mon. Wea. Rev.*, **128**, 3128-3149.

Bothwell, P. D., J. A. Hart, and R. L. Thompson, 2002: An integrated three dimensional objective analysis scheme in use at the Storm Prediction Center. Preprints, *21st Conf. on Severe Local Storms*, San Antonio, TX, Amer. Meteor. Soc., J117-J120.

Brooks, H. E., C. A. Doswell, and M. P. Kay, 2003: Climatological estimates of local daily tornado probability for the United States. *Wea. Forecasting*, **18**, 626-640.

Brotzge, J., and S. Erickson, 2010: Tornadoes without NWS warning. *Wea. Forecasting*, **25**, 159-172.

Brotzge, J., S. Erickson, and H. Brooks, 2011: A 5-yr climatology of tornado false alarms. *Wea. Forecasting*, **26**, 534-544.

Bryan, G. H., J. M. Fritsch, 2002: A Benchmark Simulation for Moist Nonhydrostatic Numerical Models. *Mon. Wea. Rev.*, **130**, 2917-2928.

Bryan, G. H., and R. Rotunno, 2009: Evaluation of an Analytical Model for the Maximum Intensity of Tropical Cyclones. *J. Atmos. Sci.*, **66**, 3042-3060.

Bunkers, M. J., B. A. Klimowski, J. W. Zeitler, R. L. Thompson, and M. L. Weisman, 2000: Predicting supercell motion using a new hodograph technique. *Wea. Forecasting*, **15**, 61-79.

Bunkers, M. J., D. A. Barber, R. L. Thompson, R. Edwards, and J. Garner, 2014: Choosing a universal mean wind for supercell motion prediction. *J. Operational Meteor.*, **2** (11), 115-129.

Clark, M. R., 2009: The southern England tornadoes of 30 December 2006: Case study of a tornadic storm in a low CAPE, high shear environment. *J. Atmos. Res.*, **93**, 50-65.

Clark, M. R., 2011: Doppler radar observations of mesovortices within a cool-season tornadic squall line over the UK. *J. Atmos. Res.*, **100**, 749-764.

Clark, M. R., and D. J. Parker, 2014: On the Mesoscale Structure of Surface Wind and Pressure Fields near Tornadic and Nontornadic Cold Fronts. *Mon. Wea. Rev.*, **142**, 3560-3584.

Coffer, B. E., and M. D. Parker, 2015: Impacts of increasing low-level shear on supercells during the early evening transition. *Mon. Wea. Rev.*, **143**, 1945–1969.

Coffer, B. E., and M. D. Parker, 2017: Simulated supercells in nontornadic and tornadic VORTEX2 environments. *Mon. Wea. Rev.*, **145**, 149-180.

Coffer, B. E., M. D. Parker, J. M. L. Dahl, L. J. Wicker, and A. J. Clark, in press: Volatility of tornadogenesis: An ensemble of simulated nontornadic and tornadic supercells in VORTEX2 environments. *Mon. Wea. Rev.*, accepted in final form, September 2017.

Cope, A. M., 2004: An early morning mid-Atlantic severe weather episode: short-lived tornadoes in a high-shear low-instability environment. Preprints, *22nd Conf. on Severe Local Storms*, Hyannis, MA, P1.4.

Craven, J. P., and H. E. Brooks, 2004: Baseline climatology of sounding derived parameters associated with deep, moist convection. *Nat. Wea. Digest*, **28**, 13-24.

Dahl, J. M. L., 2015: Near-Ground Rotation in Simulated Supercells: On the Robustness of the Baroclinic Mechanism. *Mon. Wea. Rev.*, **143**, 4929-4942.

Dahl, J. M. L., M. D. Parker, and L. J. Wicker, 2014: Imported and Storm-Generated Near-Ground Vertical Vorticity in a Simulated Supercell. *J. Atmos. Sci.*, **71**, 3027-3051.

Davenport, C. E., and M. D. Parker, 2015: Impact of environmental heterogeneity on the dynamics of a dissipating supercell thunderstorm. *Mon. Wea. Rev.*, **143**, 4244-4277.

Davies, J. M., 1993: Hourly helicity, instability, & EHI in forecasting supercell tornadoes. Preprints, *17th Conf. on Severe Local Storms*, St. Louis, MO, Amer. Meteor. Soc., 107-111.

Davies-Jones, R., 2015: A review of supercell and tornado dynamics. *Atmos. Res.*, **158-159**, 274-291.

Davies-Jones, R., and H. Brooks, 1993: Mesocyclogenesis from a theoretical perspective. *The Tornado: Its Structure, Dynamics, Prediction, and Hazards*, C. Church et al., Eds., Amer. Geophys. Union, 105-114.

Davis, J. M., and M. D. Parker, 2014: Radar climatology of tornadic and non-tornadic vortices in high shear, low CAPE environments in the mid-Atlantic and southeastern U.S. *Wea. Forecasting*, **29**, 828-853.

Dean, A. R., and R. S. Schneider, 2008: Forecast challenges at the NWS Storm Prediction Center relating to the frequency of favorable severe storm environments. Preprints, *24th Conf. on Severe Local Storms*, Savannah, GA, Amer. Meteor. Soc., 9A.2.

Dean, A. R., and R. S. Schneider, 2012: An examination of tornado environments, events, and impacts from 2003-2012. Preprints, *26th Conf. Severe Local Storms*, Nashville TN, Amer. Meteor. Soc., P6.0.

Dean, A. R., R. S. Schneider, R. L. Thompson, J. A. Hart, and P. D. Bothwell, 2009: The conditional risk of severe convection estimated from NWS Storm Prediction Center mesoscale objective analyses: Potential uses in support of forecast operations and verification. Preprints, *23rd Conf. on Weather Analysis and Forecasting*, Omaha, NE, 6A.5.

Dial, G. L., J. P. Racy, and R. L. Thompson, 2010: Short-term convective mode evolution along synoptic boundaries. *Wea. Forecasting*, **25**, 1430-1446.

Doswell, C. A. III, R. Davies-Jones, and D. L. Keller, 1990: On summary measures of skill in rare event forecasting based on contingency tables. *Wea. Forecasting*, **5**, 576-585.

Doswell, C. A. III, H. E. Brooks, and M. P. Kay, 2005: Climatological Estimates of Daily Local Nontornadic Severe Thunderstorm Probability for the United States. *Wea. Forecasting*, **20**, 577-595.

Evans, J. S., and C. A. Doswell III, 2001: Examination of derecho environments using proximity soundings. *Wea. Forecasting*, **16**, 329-342.

Evans, M., 2010: An examination of low CAPE/high shear severe convective events in the Binghamton, New York county warning area. *Nat. Wea. Digest*, **34**, 129-144.

French, A. J., and M. D. Parker, 2008: The initiation and evolution of multiple modes of convection within a meso-alpha scale region. *Wea. Forecasting*, **23**, 1221-1252.

Fujita, T. T., and R. M. Wakimoto, 1981: Five scales of airflow associated with a series of downbursts on 16 July 1980. *Mon. Wea. Rev.*, **109**, 1438-1456.

Galway, J. G., and A. D. Pearson, 1979: Winter tornado outbreaks. Preprints, *11th Conf. on Severe Local Storms*, Amer. Meteor. Soc., pp. 1-6.

Gatzen, C., T. Púčik, and D. Ryva, 2011: Two cold-season derechos in Europe. *J. Atmos. Res.*, **100**, 740-748.

Gensini, V. A., and W. A. Ashley, 2011: Climatology of potentially severe convective environments from the North American Regional Reanalysis. *Electronic J. Severe Storms Meteor.*, **6** (8), 1-40.

Gensini, V. A., T. L. Mote, and H. E. Brooks, 2014: Severe-thunderstorm reanalysis environments and collocated radiosonde observations. *J. Applied Meteor. and Climatology*, **53**, 742-751.

Guyer, J. L., and A. R. Dean, 2010: Tornadoes within weak CAPE environments across the continental United States. Preprints, *25th Conf. on Severe Local Storms*, Denver, CO, Amer. Meteor. Soc., 1.5.

Guyer, J. L., D. A. Imy, A. Kis, and K. Venable, 2006: Cool season significant (F2-F5) tornadoes in the Gulf Coast states. Preprints, *23rd Conf. on Severe Local Storms*, St. Louis, MO, Amer. Meteor. Soc.

Hanstrum, B. N., G. A. Mills, A. Watson, J. P. Monteverdi, and C. A. Doswell III, 2002: The cool-season tornadoes of California and southern Australia. *Wea. Forecasting*, **17**, 705-722.

Henry, N. L., 2000: A static stability index for low-topped convection. *Wea. Forecasting*, **15**, 246-254.

Hobbs, P. V., J. D. Locatelli, and J. E. Martin, 1990: Cold fronts aloft and the forecasting of precipitation and severe weather east of the Rocky Mountains. *Wea. Forecasting*, **5**, 613-626.

Inoue, H. Y., K. Kusunoki, W. Kato, H. Suzuki, T. Imai, T. Takemi, K. Bessho, M. Nakazato, S. Hoshino, W. Mashiko, S. Hayashi, T. Fukuhara, T. Shibata, H. Yamauchi, and O. Suzuki, 2011: Finescale Doppler Radar Observation of a Tornado and Low-Level

Misocyclones within a Winter Storm in the Japan Sea Coastal Region. *Mon. Wea. Rev.*, **139**, 351-369.

Johns, R. H., 1993: Meteorological conditions associated with bow echo development in convective storms. *Wea. Forecasting*, **8**, 294–299.

Johns, R. H., J. M. Davies, and P. W. Leftwich, 1993: Some wind and instability parameters associated with strong and violent tornadoes. 2: Variations in the combinations of wind instability parameters. *The Tornado: Its Structure, Dynamics, Prediction, and Hazards, Geophys. Monogr.*, No. 79, Amer. Geophys. Union, 583-590.

Johnson, J. T., P. L. MacKeen, A. Witt, E. D. Mitchell, G. J. Stumpf, M. D. Eilts, and K. W. Thomas, 1998: The Storm Cell Identification and Tracking Algorithm: An enhanced WSR-88D algorithm. *Wea. Forecasting*, **13**, 263-276.

Kelly, D. L., J. T. Schaefer, R. P. McNulty, C. A. Doswell III, and R. F. Abbey, 1978: An augmented tornado climatology. *Mon. Wea. Rev.*, **106**, 1172-1183.

Kennedy, P. C., N. E. Westcott, and R. W. Scott, 1993: Single-Doppler radar observations of a minisupercell tornadic thunderstorm. *Mon. Wea. Rev.*, **121**, 1860-1870.

King, J. R., M. D. Parker, K. D. Sherburn, and G. M. Lackmann, 2017: Rapid Evolution of Cool Season, Low CAPE Severe Thunderstorm Environments. *Wea. Forecasting*, **32**, 763-779.

Kis, A. K., and J. M. Straka, 2010: Nocturnal tornado climatology. *Wea. Forecasting*, **25**, 545-561.

Klemp, J. B., 1987: Dynamics of tornadic thunderstorms. *Ann. Rev. Fluid Dyn.*, **19**, 369-402.

Konarik, S. B., and S. E. Nelson, 2008: Cool season tornadoes in the southeast U.S. Preprints, *24th Conf. on Severe Local Storms*, Savannah, GA, Amer. Meteor. Soc., P8.2.

Lackmann, G. M., 2002: Cold-frontal potential vorticity maxima, the low-level jet, and moisture transport in extratropical cyclones. *Mon. Wea. Rev.*, **130**, 59-74.

Lane, J. D., 2008: A sounding-derived climatology of significant tornado events in the Greenville-Spartanburg, South Carolina county warning area (1948-2006). Preprints, *24th Conf. on Severe Local Storms*, Savannah, GA, Amer. Meteor. Soc., P12.14.

Lane, J. D., and P. D. Moore, 2006: Observations of a non-supercell tornadic thunderstorm from terminal Doppler weather radar. Preprints, *23rd Conf. on Severe Local Storms*, St. Louis, MO, Amer. Meteor. Soc., P4.5.

Lee, W.-C., R. M. Wakimoto, and R. E. Carbone, 1992: The evolution and structure of a “bow-echo-microburst” event. Part II: The bow echo. *Mon. Wea. Rev.*, **120**, 2211-2225.

Leslie, L. M., and R. K. Smith, 1978: The effect of vertical stability on tornadogenesis. *J. Atmos. Sci.*, **35**, 1281-1288.

Mansell, E. R., C. L. Ziegler, and E. C. Bruning, 2010: Simulated electrification of a small thunderstorm with two-moment bulk microphysics. *J. Atmos. Sci.*, **67**, 171-194.

Markowski, P. M., 2002: Hook echoes and rear-flank downdrafts: A review. *Mon. Wea. Rev.*, **130**, 852–876.

Markowski, P. M., 2016: An Idealized Numerical Simulation Investigation of the Effects of Surface Drag on the Development of Near-Surface Vertical Vorticity in Supercell Thunderstorms. *J. Atmos. Sci.*, **73**, 4349-4385.

Markowski, P. M., and G. H. Bryan, 2016: LES of laminar flow in the PBL: A potential problem for convective storm simulations. *Mon. Wea. Rev.*, **144**, 1841-1850.

Markowski, P. M., and Y. P. Richardson, 2010: *Mesoscale Meteorology in Midlatitudes*. Wiley-Blackwell, 372 pp.

Markowski, P. M., and Y. P. Richardson, 2014: The Influence of Environmental Low-Level Shear and Cold Pools on Tornadogenesis: Insights from Idealized Simulations. *J. Atmos. Sci.*, **71**, 243-275.

Markowski, P. M., and J. M. Straka, 2000: Some observations of rotating updrafts in low-buoyancy, highly-sheared environments. *Mon. Wea. Rev.*, **128**, 449-461.

McAvoy, B. P., W. A. Jones, and P. D. Moore, 2000: Investigation of an unusual storm structure associated with weak to occasionally strong tornadoes over the eastern United States. Preprints, *20th Conf. on Severe Local Storms*, Orlando, FL, 182-185.

McCaul, E. W., Jr., 1987: Observations of the Hurricane "Danny" Tornado Outbreak of 16 August 1985. *Mon. Wea. Rev.*, **115**, 1206-1223.

McCaul, E. W., Jr., 1993: Observations and simulations of hurricane-spawned tornadoes. *The Tornado: Its Structure, Dynamics, Prediction, and Hazards*, *Geophys. Monogr.*, No. 79, Amer. Geophys. Union, 119-142.

McCaul, E. W., Jr., and M. L. Weisman, 1996: Simulation of shallow supercell storms in landfalling hurricane environments. *Mon. Wea. Rev.*, **124**, 408-429.

McCaul, E. W., Jr., and M. L. Weisman, 2001: The sensitivity of simulated supercell structure and intensity to variations in the shapes of environmental buoyancy and shear profiles. *Mon. Wea. Rev.*, **129**, 664-687.

Mesinger, F., G. DiMego, E. Kalnay, K. Mitchell, P. C. Shafran, W. Ebisuzaki, D. Jović, J. Woollen, E. Rogers, E. H. Berbery, M. B. Elk, Y. Fan, R. Grumbine, W. Higgins, H. Li, Y. Lin, G. Manikin, D. Parrish, W. Shi, 2006: North American Regional Reanalysis. *Bull. Amer. Meteor. Soc.*, **87**, 353-360.

Mulder, K., and D. Schultz, 2015: Climatology, Storm Morphologies, and Environments of Tornadoes in the British Isles: 1980-2012. *Mon. Wea. Rev.*, **143**, 2224-2240.

Okubo, A., 1970: Horizontal dispersion of floatable particles in the vicinity of velocity singularities such as convergences. *Deep-Sea Res.*, **17**, 445-454.

Parker, M. D., 2007b: Simulated convective lines with parallel stratiform precipitation. Part II: Governing dynamics and associated sensitivities. *J. Atmos. Sci.*, **64**, 289-313.

Parker, M. D., 2010: Relationship between system slope and updraft intensity in squall lines. *Mon. Wea. Rev.*, **138**, 3572-3578.

Parker, M. D., 2012: Impacts of lapse rates on low-level rotation in idealized storms. *J. Atmos. Sci.*, **69**, 538-559.

Parker, M. D., 2017: How much does “backing aloft” actually impact a supercell? *Wea. Forecasting*, **32**, 1937-1957.

Parker, M. D., and R. H. Johnson, 2004a: Simulated convective lines with leading precipitation. Part I: Governing dynamics. *J. Atmos. Sci.*, **61**, 1637-1655.

Parker, M. D., and R. H. Johnson, 2004b: Structures and dynamics of quasi-2D mesoscale convective systems. *J. Atmos. Sci.*, **61**, 545-567.

Rasmussen, E. N., and D. O. Blanchard, 1998: A baseline climatology of sounding-derived supercell and tornado forecast parameters. *Wea. Forecasting*, **13**, 1148-1164.

Roberts, B., M. Xue, A. D. Schenkman, and D. T. Dawson II, 2016: The Role of Surface Drag in Tornadogenesis within an Idealized Supercell Simulation. *J. Atmos. Sci.*, **73**, 3371-3395.

Romero, R., M. Gayà, and C. A. Doswell III, 2007: European climatology of severe convective storm environmental parameters: A test for significant tornado events. *J. Atmos. Res.*, **83**, 389-404.

Rotunno, R., and J. B. Klemp, 1982: The influence of the shear-induced pressure gradient on thunderstorm motion. *Mon. Wea. Rev.*, **110**, 136-151.

Rotunno, R., P. M. Markowski, and G. H. Bryan, 2017: "Near ground" vertical vorticity in supercell thunderstorm models. *J. Atmos. Sci.*, **74**, 1757-1766.

Schaumann, J. S., and R. W. Przybylinski, 2012: Operational application of 0-3 km bulk shear vectors in assessing QLCS mesovortex and tornado potential. Preprints, *26th Conf. on Severe Local Storms*, Nashville, TN, Amer. Meteor. Soc., P9.10.

Schenkman, A. D., and M. Xue, 2016: Bow-echo mesovortices: A review. *J. Atmos. Res.*, **170**, 1-13.

Schenkman, A. D., M. Xue, and A. Shapiro, 2012: Tornadogenesis in a Simulated Mesovortex within a Mesoscale Convective System. *J. Atmos. Sci.*, **69**, 3372-3390.

Schenkman, A. D., M. Xue, and M. Hu, 2014: Tornadogenesis in a High-Resolution Simulation of the 8 May 2003 Oklahoma City Supercell. *J. Atmos. Sci.*, **71**, 130-154.

Schneider, R. S., and A. R. Dean, 2008: A comprehensive 5-year severe storm environment climatology for the continental United States. Preprints, *24th Conf. on Severe Local Storms*, Savannah, GA, 16A.4.

Schneider, R. S., A. R. Dean, S. J. Weiss, and P. D. Bothwell, 2006: Analysis of Estimated Environments for 2004 and 2005 Severe Convective Storm Reports. Preprints, *23rd Conf. on Severe Local Storms*, St. Louis, MO, 3.5.

Sherburn, K. D., 2013: Improving the Understanding and Forecasting of Severe High Shear, Low CAPE Environments. M.S. thesis, Dept. of Marine, Earth, and Atmospheric Sciences, North Carolina State University, 124 pp.

Sherburn, K. D, and M. D. Parker, 2014: Climatology and ingredients of significant severe convection in high-shear, low-CAPE environments. *Wea. Forecasting*, **29**, 854-877.

Sherburn, K. D., M. D. Parker, J. R. King, and G. M. Lackmann, 2016: Composite Environments of Severe and Nonsevere High-Shear, Low-CAPE Convective Events. *Wea. Forecasting*, **31**, 1899-1927.

Skamarock, W., J. B. Klemp, J. Dudhia, D. O. Gill, D. M. Barker, M. G. Duda, X-Y. Huang, W. Wang, and J. G. Powers, 2008: A Description of the Advanced Research WRF Version 3. NCAR Technical Note NCAR/TN-475+STR, 125 pp.

Smith, B. T., R. L. Thompson, J. S. Grams, C. Broyles, and H. E. Brooks, 2012: Convective modes for significant severe thunderstorms in the contiguous United States. Part I: Storm classification and climatology. *Wea. Forecasting*, **27**, 1114-1135.

Smith, B. T., T. E. Castellanos, A. C. Winters, C. M. Mead, A. R. Dean, and R. L. Thompson, 2013: Measured severe convective wind climatology and associated convective modes of thunderstorms in the contiguous United States, 2003-09. *Wea. Forecasting*, **28**, 229-236.

Stein, U., and P. Alpert, 1993: Factor separation in numerical simulations. *J. Atmos. Sci.*, **50**, 2107-2115.

Thompson, R. L., R. Edwards, J. A. Hart, K. L. Elmore, and P. M. Markowski, 2003: Close proximity soundings within supercell environments obtained from the Rapid Update Cycle. *Wea. Forecasting*, **18**, 1243-1261.

Thompson, R. L., R. Edwards, and C. M. Mead, 2004: An update to the supercell composite and significant tornado parameters. Preprints, *22nd Conf. on Severe Local Storms*, Hyannis, MA, Amer. Meteor. Soc.

Thompson, R. L., C. M. Mead, and R. Edwards, 2007: Effective storm-relative helicity and bulk shear in supercell thunderstorm environments. *Wea. Forecasting*, **22**, 102-115.

Thompson, R. L., B. T. Smith, J. S. Grams, A. R. Dean, and C. Broyles, 2010: Climatology of near-storm environments with convective modes for significant severe thunderstorms in the contiguous United States. Preprints, *25th Conf. on Severe Local Storms*, Denver, CO, Amer. Meteor. Soc., 16B.6.

Thompson, R. L., B. T. Smith, J. S. Grams, A. R. Dean, and C. Broyles, 2012: Convective modes for significant severe thunderstorms in the contiguous United States. Part II: Supercell and QLCS tornado environments. *Wea. Forecasting*, **27**, 1114-1135.

Trapp, R. J., and M. L. Weisman, 2003: Low-level mesovortices within squall lines and bow echoes. Part II: Their genesis and implications. *Mon. Wea. Rev.*, **131**, 2804-2823.

Trapp, R. J., D. M. Wheatley, N. T. Atkins, R. W. Przybylinski, and R. Wolf, 2006: Buyer beware: Some words of caution on the use of severe wind reports in postevent assessment and research. *Wea. Forecasting*, **21**, 408-415.

Trier, S. B., C. A. Davis, D. Ahijevych, M. L. Weisman, and G. H. Bryan, 2006: Mechanisms supporting long-lived episodes of propagating nocturnal convection within a 7-day WRF model simulation. *J. Atmos. Sci.*, **63**, 2437-2461.

Tuttle, J. D., and C. A. Davis, 2006: Corridors of warm season precipitation in the central United States. *Monthly Weather Review*, **134**, 2297-2317.

Tyrrell, J., 2007: Winter tornadoes in Ireland: The case of the Athlone tornado of 12 January 2004. *J. Atmos. Res.*, **83**, 242-253.

Vescio, M. D., and R. L. Thompson, 1998: Some meteorological conditions associated with isolated F3-F5 tornadoes in the cool season. Preprints, *19th Conf. on Severe Local Storms*, Minneapolis, MN, Amer. Meteor. Soc., 2-4.

Wakimoto, R. M., H. V. Murphey, A. Nester, D. P. Jorgensen, and N. T. Atkins, 2006: High winds generated by bow echoes. Part I: Overview of the Omaha bow echo 5 July 2003 storm during BAMEX. *Mon. Wea. Rev.*, **134**, 2793-2812.

Walters, C. K., J. A. Winkler, S. Husseini, R. Keeling, J. Nikolic, and S. Zhong, 2014: Low-Level Jets in the North American Regional Reanalysis (NARR): A Comparison with Rawinsonde Observations. *J. App. Meteor. Clim.*, **53**, 2093-2113.

Wasula, T. A., N. A. Stuart, and A. C. Wasula, 2008: The 17 February 2006 severe weather and high wind event across eastern New York and New England. Preprints, *24th Conf. on Severe Local Storms*, Savannah, GA, Amer. Meteor. Soc., 13B.3.

Weisman, M. L., and R. Rotunno, 2000: The use of vertical wind shear versus helicity in interpreting supercell dynamics. *J. Atmos. Sci.*, **57**, 1452-1472.

Weisman, M. L., and R. J. Trapp, 2003: Low-level mesovortices within squall lines and bow echoes. Part I: Overview and dependence on environmental shear. *Mon. Wea. Rev.*, **131**, 2779-2803.

Weiss, J., 1991: The dynamics of enstrophy transfer in two-dimensional hydrodynamics. *Physica D*, **48**, 273-294.

Weiss, S. J., J. A. Hart, and P. R. Janish, 2002: An examination of severe thunderstorm wind report climatology. Preprints, *21st Conf. on Severe Local Storms*, San Antonio, TX, Amer. Meteor. Soc., 11B.2.

Wilhelmson, R. B., and Y. Ogura, 1972: The pressure perturbation and the numerical modeling of a cloud. *J. Atmos. Sci.*, **29**, 1295-1307.

Wilks, D. S., 1995: *Statistical Methods in the Atmospheric Sciences: An Introduction*. Academic Press, 467 pp.

Xu, X., M. Xue, Y. Wang, 2015: The genesis of mesovortices within a real-data simulation of a bow echo system. *J. Atmos. Sci.*, **72**, 1963-1986.